Rational coherent control applied to Br_2 molecules and their solid Ar environment

im Fachbereich Physik
der Freien Universität Berlin
eingereichte Dissertation von

Monika Helena Hejjas

2012

Diese Arbeit wurde in der Zeit vom April 2006 bis Dezember 2011 unter der Aufsicht von Herrn Professor Dr. N. Schwentner am Fachbereich Physik der Freien Universität Berlin durchgeführt.

Erstgutachter: Prof. Dr. N. Schwentner
Zweitgutachter: Prof. Dr. J. Manz
Drittgutachter: Prof. Dr. G. Gerber

Disputationstermin: 30. April 2012

Abbreviations

BBO - Beta-Barium Borate

BO approximation - Born-Oppenheimer approximation

CARS - Coherent anti-Stokes Raman scattering

CPA - Chirped pulse amplifier

CT - Crossing time

CT states- Charge transfer states

CT1 - First charge transfer state manifold

CT2 - Second charge transfer state manifold

DE - Differential equation

DECP - Displacive excitation of coherent phonons

DIM - Diatomics in molecules

DVR - Discrete variable representation

FC factors - Franck-Condon factors

fcc - Face centered cubic

F-OMA - Fiber coupled optical multichannel analyzer

FP - Fourier plane

FT - Fourier transformation

FFT - Fast Fourier transformation

FV - Final value

X-FROG - Noncollinear frequency resolved optical gating

FWHM - Full width at half maximum

LC(D) - Liquid crystal (display)

LiF - Light induced fluorescence

MPB - Multi-phonon background

NOPA - Noncollinear optical parametric amplifier

PSB - Phonon sideband

RKR - Rydberg-Klein-Rees

SFB - Sonderforschungsbereich - collaborative research center

SLM - Spatial liquid crystal modulator

TDSE - Time dependent Schrödinger equation

Ti:Sa - Titanium sapphire amplifier

TISE - Time independent Schrödinger equation

UHV - Ultrahigh vacuum

UV - Ultraviolet

ZBP - Zone boundary phonon

ZPL - Zero phonon line

4f-setup - zero dispersion compressor

Unit conversions

This work comprises combined experimental and computational studies. In simulations atomic units are used. Their values in terms of SI units are given below.

Quantity	Atomic Units	SI value
Mass	m_e	$9.109382 \cdot 10^{-31}\,kg$
Action	$\hbar$	$1.054572 \cdot 10^{-34}\,J\,s$
Charge	e	$1.602176 \cdot 10^{-19}\,C$
Coulomb's constant	$1/4\pi\epsilon_0$	$8.987552 \cdot 10^{9}\,Nm^2/C^2$
Length	$a_0 := 4\pi\epsilon_0\hbar^2/m_e\,e^2$	$5.291772 \cdot 10^{-11}\,m$
Energy	$E_h := \hbar^2/a_0^2 m_e$	$4.359744 \cdot 10^{-18}\,J$
Time	$t_0 := \hbar/E_h$	$2.418884 \cdot 10^{-17}\,s$
Frequency	$f_0 := E_h/\hbar$	$4.134138 \cdot 10^{16}\,Hz$
Electric Field	$\varepsilon := E_h/ea_0$	$5.142206 \cdot 10^{11}\,V/m$

In the experimental parts the usual spectroscopic units are used. Hence, energies E, frequencies ν and angular frequencies $\omega = 2\pi\,\nu$, respectively, are all given in units of spectroscopic wavenumbers, i.e. reciprocal wavelengths, cm^{-1}. The following table collects unit conversion factors for the quantities used in this work.

Quantity	Spectroscopic Units	SI value*	Atomic Units
Energy	$E\,[cm^{-1}] = E\,[J]/hc$	$1.9864455 \cdot 10^{-23}\,J$	$4.556335 \cdot 10^{-6}\,E_h$
Frequency	$\nu\,[cm^{-1}] = \nu\,[Hz]/c$	$2.99792458 \cdot 10^{10}\,Hz$	$7.251582 \cdot 10^{5}\,f_0$
Length	$\mathring{A}$	$10^{-10}\,m$	$1.889726\,a_0$
	nm	$10^{-9}\,m$	$18.89726\,a_0$
Time	fs	$10^{-15}\,s$	$41.34138\,t_0$

*For the light velocity in vacuum $c = 2.99792458 \cdot 10^{10}\,cm/s$,
for Planck's constant $h = 2\pi\,\hbar = 6.626069 \cdot 10^{-34}Js$ were used.

Abstract

This PhD thesis was embedded in the collaborative research center SFB 450 "Analysis and Control of Ultrafast Photoinduced Reactions". Its main result is the first experimental realization of coherent control of phonon induced predissociation in the combined chromophore-bath system Br_2:Ar. The course of experiments was carried out in a systematic way in the sense of a bottom-up approach. Energetic regions of nonadiabatic crossings of the covalent molecular B state with dissociative states were first identified by means of conventional pump probe spectroscopy. Measurements with varying parallel and perpendicular relative linear polarizations of pump and probe pulses were recorded. Light induced fluorescence from two different emission bands, showing only B state wave packet dynamics or B overlaid by a dominant A state dynamics was detected. The variation of parameters allowed for a decomposition of the wave packets into A and B state contributions, according to the theoretical expectation from photoselection rules. The search for optimal pulse durations needed for the predissociation control was guided by numerical studies of B state wave packet dynamics of gas phase Br_2, however, on effective matrix potentials. The B wave packet dynamics was monitored in the spectral domain. An analytical expression for the spectral coefficients was derived in first order perturbation theory. Comparison of simulated pump probe spectra with measurements allowed to determine matrix induced predissociation effects in the measured spectra. The conventional pump probe spectra and their analysis were used in the following steps: (1.) to construct incoherent contributions to simulate the additive, incoherent parts in wave packet interferometric measurements with trains of ultrashort excitation pulses and to separate the coherence terms in this way, and (2.) to allow for a decomposition of coherent control spectra into contributions from different electronic states. Especially, the dynamics of predissociated fragments from the B state could be isolated from the other contributions. The relative phases of subpulses in excitation pulse trains were steered by shifting the positions of corresponding spectral combs generated in a pulse shaper. The combs were selected in order to match molecular vibrations with or without coupling to specific phonon modes. Thereby, zero phonon vibrations could be either amplified by constructive interference in the weak phonon coupling regime or canceled by destructive interference. In case of strong phonon coupling, where also in frequency resolved excitation spectra the spectral weight gets carried away from zero phonon lines to a rising multiphonon background, destructive interference was still achieved. Spectral selection of B vibrations coherently coupled to a high energetic local phonon mode led to a doubling of predissociation efficiency. This is in accordance with theoretical predictions of collaboration partners within the SFB 450.

Kurzfassung

Diese Doktorarbeit wurde im Rahmen des SFB 450 "Analyse und Kontrolle von ultraschnellen photoinduzierten Reaktionen" durchgeführt. Ihr Hauptergebnis ist die erstmalige experimentelle Realisierung der kohärenten Kontrolle phononinduzierter Prädissoziation am kombinierten Chromophor-Bad-System Br_2:Ar. Die Abfolge der Experimente wurde systematisch im Sinne eines Bottom-up-Ansatzes durchgeführt. Energetische Bereiche nichtadiabatischer Kreuzungen des kovalenten B-Zustandes mit repulsiven Zuständen wurden zunächst mit herkömmlichen Methoden der Pump-Probe-Spektroskopie untersucht. Die Messungen wurden polarisationsaufgelöst durchgeführt. Lichtinduzierte Fluoreszenz wurde von zwei verschiedenen Emissionsbanden detektiert, die entweder nur B-Zustands-Dynamik oder auch eine überlagerte, dominierende A-Dynamik zeigen. Durch Variation der Parameter konnten die Wellenpakete in ihre B- und A-Anteile zerlegt werden und die quantitative Übereinstimmung mit der Erwartung der Photo-Auswahlregeln gezeigt werden. Die Suche einer optimalen Anregungspulslänge für die Kontrolle der Prädissoziation wurde von numerischen Studien der Wellenpaketdynamik in der Energie-Darstellung am freien Molekül, aber in einem effektiven B-Zustand in der Matrix, begleitet. Für die spektralen Koeffizienten der B-Anregung wurde ein analytischer Ausdruck in erster Ordnung zeitabhängiger Störungstheorie hergeleitet. Durch Vergleich mit simulierten Pump-Probe-Spektren konnten Effekte der matrixinduzierten Prädissoziation in gemessen Spektren identifiziert werden. Die klassischen Pump-Probe-Spektren wurden benutzt, um: (1.) in interferometrischen Experimenten mit ultraschnellen Pulszügen, additive Überlagerungen zu konstruieren, und damit die Kohärenzterme zu isolieren; (2.) kohärente Kontrollspektren in Beiträge von verschiedenen elektronischen Zuständen zu zerlegen. Insbesondere konnten so die prädissoziierten B-Anteile isoliert von anderen Beiträgen untersucht werden. Die relativen Phasen der Unterpulse im Pulszug wurden durch spektrale Verschiebungen der entsprechenden Frequenzkämme in einem Pulsformer gesteuert. Ihre spektrale Lage entsprach molekularen Schwingungsniveaus ohne und mit spezifischen Phononenmoden. So konnten Nullphononen-Beiträge durch konstruktive Wellenpaketinterferenzen im energetischen Bereich schwacher Phononenkopplung verstärkt werden, im Falle starker Kopplung ausgelöscht werden. Destruktive Interferenz wurde in einem energetischen Bereich des B-Anregungsspektrums beobachtet, wo das spektrale Gewicht sich von Nullphononenlinien zu einem steigenden Multiphononenuntergrund hin verschiebt. Spektrale Selektion von Schwingungen des B-Zustandes, die mit einer lokalen Phononenmode kohärent überlagert wurden, führte zu einer Verdopplung der beobachteten Prädissoziationsausbeute. Dies stimmt mit theoretischen Vorhersagen von Kooperationspartnern im SFB 450 überein.

Contents

Chapter 1

Motivation

Why do physicists nowadays go crazy about entanglement? To be entangled is the most natural state of the constituents of a quantum system [1–3]. The other extreme, a quantum system describable in terms of product states, constituent states of the system which do not "know" each other, i.e. do not interact, is only fulfilled in very special situations. One of the most fundamental examples are electronic, vibrational and rotational states of molecules which can be factorized within the Born-Oppenheimer approximation, when modeling spectroscopic characteristics of the molecule [4]. In fact, one goes beyond the Born-Oppenheimer approximation already in case of a diatomic molecule, when one aims to model dynamically a vibrational wave packet induced by light in a vibronic excitation mechanism from an initial to another final electronic state [5].

In theory, entanglement is just a basic point of Schrödinger's wave mechanics. For the experimentalist, however, it is a real challenge to measure entanglement, especially in systems being more complex than an atom or a diatomic molecule. The reason is that with an increasing number of degrees of freedom physical systems are more difficult to be isolated from a surrounding environment. Being entangled with an uncontrolled environment, however, leads to a flow of phase information i.e. coherences away from the considered part of the system into the uncontrolled environment, the effect commonly known as decoherence [6–9]. Physical states of a system which are completely decohered, do not show any defined phase relations among their constituent states anymore and due to their random phases no quantum mechanical interference effects. This work presents a basic decoherence study of diatomics which couple to a surrounding solid state environment, in which the entangled molecular and environmental dynamics are controlled.

In the last years, the question about the border between quantum and classical mechanics, already challenging the founders of quantum mechanics about 80-90 years ago, received again significant interest and is studied in a wide range of exper-

iments and theories (at this point only a few selected examples: [7, 10–12]). While theoretical models for coherence times and spatial decoherence rates and their dependence on system size and de-Broglie-wavelength have been established already in the early 1980ies [13, 14], the first experiments monitoring decoherence dynamics were performed just in the mid-1990ies. They started with the demonstration of coherent superposition states of trapped ions [15] and coherent states of the radiation field[1] [19, 20].

The experimental challenge for measuring decoherence dynamics or just proving the existence of coherences in a complex physical system with many degrees of freedom comprises two aspects. First, the system under consideration has to be isolated in a best possible way from interactions with an uncontrolled environment. Second, appropriate experimental tools for monitoring the entanglement within the controlled part of a system-environment-interaction have to be established. In this work a diatomic molecule plays the role of the system, which is enbedded in a crystalline vicinity of rare gas atoms. The crystalline surrounding partly plays the role of the controlled part of the environment consisting of coherent phonon modes coherently coupled to the molecular motion. The uncontrolled part of the surrounding crystal plays the role of a bath leading to the decoherence of the system.

Taking the experimental challenge for monitoring the decoherence dynamics is worth the cost. The reason is of fundamental nature: For the understanding of a complex system's basic properties it is absolutely necessary to determine to which extent the system shows entanglement and therefore behaves and has to be treated quantum mechanically. The establishing of appropriate theoretical models for complex systems inevitably requires the knowledge about coherence and decoherence in the system. Even if characteristic properties of the system can be reproduced quantitatively within a classical or semiclassical model, by ignoring the coherence properties, the model may lose its predictive power. Indeed, during the time evolution of this PhD thesis other experimental decoherence studies have been extended to biologically relevant systems. Pioneering experiments pointed out the decisive role of quantum mechanical coherence in a light harvesting system being part of the photosynthesis process [21–25], one of the preconditions for the present form of life on earth. To be quantum mechanical or not to be quantum mechanical is also the essential question motivating the studies presented in this work.

In order to prove the existence of coherence, two types of experiments are commonly used: (1.) projective measurements directly carried out on the superposition

---

[1]In 2005 Roy Glauber received the Nobel Prize for Physics for theoretically formulating the coherent states of the radiation field, which were formally introduced by Schrödinger [16], and for working out their fundamental mathematical properties in second quantization [17, 18].

state, like in a Stern-Gerlach apparatus and (2.) interferometric measurements, like
in Young's famous double slit setup (for a relatively recent review see the book of
Schlosshauer [9]). An "entanglement-hype" started with the first type of exper-
iments, spectacularly demonstrating an experimental realization of the Einstein-
Podolsky-Rosen Gedankenexperiment in coincidence measurements of photon pairs
entangled in a nonlinear medium [26–28]. Interference experiments analogous to
Young's double slit experiment and their extension to multislit-type experiments
and corresponding theories established the today widely explored field of quantum
optics [29,30]. One of its most revolutionary and challenging goals is the realization
of quantum computers and their connection to decoherence is extensively stud-
ied [31–37]. Subsequent demonstrations of coherence properties of more and more
complex systems, like single C_{70} molecules, fluorinated $C_{60}F_{48}$ and the biomolecule
$C_{44}H_{30}N_4$ kept the ball rolling [38–40].

   In the meantime, the photochemistry field stepped into regions of femtochem-
istry[2] [41, 44–46]. Dynamical chemical and physical processes became accessible
for investigation on the femtosecond timescale ($1fs=1\cdot10^{-15}s$), which is the natural
timescale of nuclear motions in molecules. Measuring and modeling the making
and breaking of chemical bonds on their natural timescale is currently about to be
extended into the attosecond-regime ($1as=1\cdot10^{-18}s$), the characteristic timescale of
electronic motion in atoms and molecules [47–51]. A field combining methods of
quantum optics and femtochemistry had been established and was titulated quan-
tum or coherent control [52–54]. This work can be seen as a contribution to this
field, as well.

   The great amount of experimentally applied and/or theoretically proposed coher-
ent control scenarios can be divided into two main branches, optimal control [55–58]
and rational control [59–61], where the first one is much more extensively explored.
They are based on the same guiding idea, i.e. leading a quantum system in a desired
state by excitation with appropriately shaped laser pulses [52,62–64]. They concep-
tually differ, however, by the way of defining the appropriate parameters for the
excitation pulses. While in optimal control schemes field parameters like amplitude,
phase and also polarization are varied typically in a feedback loop setup in order to
optimize a desired outcome [65–73], in rational control schemes, like applied in this
work, ideally, the interference pathways which lead from the initial to the desired
state of the system are identified first and then imprinted into the pulse parameters.
The theoretical procedure for finding these pathways in case of a many-body-system
involving the motion of several hundreds of atoms, as considered in this work, is how-

---

[2]In 1999 Ahmed Zewail received the Nobel Prize for Chemistry for establishing basic methods
of experimental femtochemistry [41–43].

ever a complicated and even numerically often not manageable task. Therefore, our rational coherent control scheme proposes a method which avoids this complexity by directly using spectroscopic information which contains the necessary information about the optimal pulse shapes. They are applied in this work in order to induce particular many-body-specific effects, like coherent vibron-phonon-coupling and solvent induced predissociation, even in the presence of dissipation [74].

The extension of control schemes from systems with only a few to ones with many degrees of freedom goes along with an increasing tendency to decoherence [6, 9]. Decoherence times for electronic transitions on the order of 100fs were expected for chromophores in the condensed phase [75, 76]. These short times are comparable to typical periods of the vibrational degrees of freedom and they represent a severe challenge for the application of coherent control schemes. Furthermore, even if some degrees of freedom remain coherent for some periods, they can be buried in an overwhelming background of contributions which undergo quick decoherence. Indeed, optimal control experiments delivered successful optimization in systems with rather featureless spectra originating from congestion and damping [77]. In addition, parametrically programmed coherent pulse trains enabled amplification of individual vibrations [78, 79]. In this work, the programmable shaping of a spectrally dispersed light pulse generating pulse trains in the time domain, will turn out to be an appropriate tool to enable a systematic search for coherent traces and their amplification, in order to monitor the decoherence dynamics of a dihalogen in a rare gas crystal.

Because the pulse shaping techniques usually work in the frequency domain, the availability of the spectroscopic information highly facilitates the control. Indeed, optimal control experiments carried out in a feedback-loop setup, where in combination with evolutionary algorithms targets are optimized with subsequently optimized pulse shapes, pulses are usually implemented in the time domain. A transformation into the spectral domain has to be carried out with every single optimization step. Moreover, the optimal pulse shapes often show a complicated time structure, which is difficult to trace back to the processes generating the optimal outcome, thus keeping the nature of the control mechanism in a black box. To overcome these disadvantages, attempts have been made to extend the optimization mechanism to time-frequency phase space [80–82].

All this is avoided in our case, where the optimal pulse shapes are dictated by measured high resolution excitation spectra carried out already in frequency domain in a previous work in our group [83]. The rational coherent control mechanism presented in this work is based on complementary frequency resolved and time resolved pump probe measurements, which in combination, provide all necessary informa-

tion for coherent control of phonon induced predissociation. The efficiency of the predissociation rate has been controlled by selectively exciting the relevant vibrational modes of the combined molecular-solid-state-motion. The importance of high energetic coherent phonons for the efficient nonadiabatic population transfer from a bound to a dissociative potential has been predicted theoretically for Br_2:Ar by our collaboration partners A. Borowski and O. Kühn in the working group of Prof. Manz [84, 85]. They predicted a doubling of predissociation efficiently in case of the vibrational preexcitation of the essential linear vibronic coupling mode for the bound vibronic B to C state predissociation. As final result of our experiments, the simultaneous spectral selection of chromophore vibrations in the B state and high energetic phonons remaining localized at the chromophore, led to a predissociation increase by a factor of two. Another nonadiabatic crossing of the B state with repulsive states was treated in the experiments. Therefore, besides of the experimental proof of the theoretical prediction, the importance of the high energetic phonons for the efficient population transfer observed in the rare gas solid environment, can be considered as a general phenomenon.

Since the coherence properties of the exciting field are transferred to the matter under investigation, in order to achieve the desired control, the required coherence does not only refer to the excitation pulses but at least during the pulse duration, to the controlled system, as well. Therefore, additionally to the quantum control of a chemical reaction driven by the combined chromophore-lattice motion, a dynamical monitoring of the molecular vibronic decoherence will be presented and attributed to the coupling of specific phonon modes. The dependence of the vibronic coherence on the phonon coupling strength in different energetic excitation regions has been investigated and will be presented, too.

The work is organized as follows. The following Chapter 2 introduces the system Br_2:Ar, summarizing its most relevant properties for making the system an ideal candidate for quantum control of phonon induced predissociation. In Chapter 3 the theoretical concepts of molecular wave packet dynamics generated with ultrashort laser pulses and pulse trains will be established. Fundamental terms of coherence and decoherence, respectively, will also be supplied in this chapter. Afterwards, the experimental concept for the implementation of our rational coherent control scheme will be introduced in Chapter 4. Chapter 5 presents results of numerical investigations of B state vibrational wave packets of the free molecule Br_2, induced by laser pulses and pulse sequences. Since in the simulations only the molecular dynamics was considered, a comparison with experimental data will enable identification of environment induced effects. Here, the validity of time dependent perturbation theory in 1st order for the given experimental conditions will be verified and an

analytical expression for the excitation process in this limit will be derived for the spectral domain[3]. The experimental results will be presented, analyzed and discussed in Chapter 6. A decomposition of vibrational wave packet dynamics into contributions from different electronic states based on polarization sensitive pump probe spectroscopy will be presented and transferred from conventional pump probe spectra to the coherent control measurements. This way the dynamics of controlled predissociated parts of the wave packet will be analyzed. Interference terms in the wave packet excitation will be identified and attributed to couplings to different phonon modes. The last Chapter 7 summarizes the findings. A calculation of the Morse oscillator eigenstates used for the numerical studies and a gallery of pump probe spectra can be found in Appendix A and Appendix B, respectively.

---

[3]The investigations presented in this chapter are results of a fruitful collaboration of our group with PD Dr. Burkhard Schmidt within the cooperative research center SFB 450.

Chapter 2

Introducing Br$_2$ in solid Ar

All experiments carried out in this work were time resolved spectroscopic studies on Br$_2$ molecules acting as chromophores in a crystalline environment of Ar atoms. After introducing briefly the most relevant gas phase properties of Br$_2$ in Sec. 2.1, lattice structure and energetic properties of solid Ar will be summarized in Sec. 2.2. It shall be noted that only those characteristics will be presented, which are needed in upcoming chapters. Some properties of the isolated constituents of the combined molecular- solid state system will be used as a reference to identify environment induced effects. For a complete set of characteristic parameters of the molecule Br$_2$ and the rare gas crystal the reader is refered to standard literature [86, 87] or previous work on Br$_2$:Ar [84, 88, 89]. In the following Sec. 2.3 typical effects arising in chromophore-bath-systems and methods to monitor them will be introduced on a general level. Vibrational energy relaxation and matrix induced predissociation will be first presented formally in order to pave the way for the discussion of the results presented in the last chapters. Not only the system Br$_2$:Ar but other dihalogen - rare gas matrix - combinations were topic of detailed investigation in the Schwentner group and other experimental groups [90–93], as well as of theoretical investigation [45, 94–98] within the cooperative research center SFB 450 [99–101] and beyond [102–105]. Why just Br$_2$:Ar is an ideal choice for rational coherent control of matrix induced predissociation with the control scheme applied in this work, will be answered in Sec. 2.4. The last Sec. 2.5 summarizes the energetic properties from previous work on Br$_2$:Ar. Especially, high resolution excitation spectra will be discussed with regard to the spectroscopic information they contain about matrix induced predissociation and coherence times. They provide the prerequisites needed for the rational coherent control.

2.1 The chromophore Br_2

Being situated in the seventh main group of the periodic table of elements, Br atoms are halogens with one electron missing in the outer shell and therefore highly reactive. The corresponding ground state configuration is $[Ar]3d^{10}4p^5 4s^2$, where [Ar] denotes the structure of the 18 core electrons. The combination of the atomic electrons to the molecular orbitals of Br_2 leads to the electronic configuration $\sigma_g^2 \pi_u^4 \pi_g^4 \sigma_u^0$ given here in molecular orbital nomenclature. Like for all dihalogens, the ground state is a $^1\Sigma_{0g}$ state, where according to the standard nomenclature, the upper index 1 stands for the molecular spin (here S=0) multiplicity 2S+1, and Σ denotes the angular momentum Λ (here Λ=0). Accordingly, the combined angular momentum Ω is here Ω=0, as given by the first lower index. The even parity is denoted by the index g (for German "gerade", whereas for odd parities u stands for "ungerade"). Since the Br atom has two stable isotopes $^{79}_{35}Br$ and $^{81}_{35}Br$, both of them occurring with 50% natural abundance, three stable isotopomers of Br_2 can be found, namely $^{79}Br^{79}Br$, $^{79}Br^{81}Br$ and $^{81}Br^{81}Br$, where $^{79}Br^{81}Br$ is twice as often present as the other two isotopomers. The natural abundance was used in the experiments of this work. The corresponding isotopomer splittings of the vibrational eigenstates have been observed in excitation spectra and will be shown in Sec. 2.5 [83,89]. At room temperature, bromine is a brown-orange liquid with an intense smell. It has a relatively high vapor pressure of 220hPa. It is extremely toxic and corrosive, so that its treatment in the laboratory requires special care, which is described in more detail in Chapter 4 [106–108].

Gas phase potentials

The gas phase electronic potentials of halogen bromine are well characterized spectroscopically in the literature [109–117]. The ground state $X^1\Sigma_{0g}$ and the lowest lying covalent Π states A' $^3\Pi_{2u}$, A $^3\Pi_{1u}$, B $^3\Pi_{0u}$ and C $^1\Pi_{1u}$ are depicted in Fig. 2.1. Due to the spin-orbit coupling of the heavy Br_2, the B state dissociates into a $^2P_{3/2}$ and a $^2P_{1/2}$ Br atom. Therefore, the dissociation energy is shifted by 2660cm^{-1} with respect to the dissociation energy of the other shown covalent states dissociating into two $^2P_{3/2}$ atoms. For the investigations in this work the bromine molecules were caged in the argon lattice in the electronic ground state and the vibrational wave packet dynamics in the depicted bound triplet states was controlled with ultrashort laser pulse excitation. In Fig. 2.1 three ionic electronic states D', β and E corresponding to the first charge transfer state (CT) manifold and the f state, the energetically lowest lying state from the second CT manifold, are shown, as well. They will be used as upper states to probe excited wave
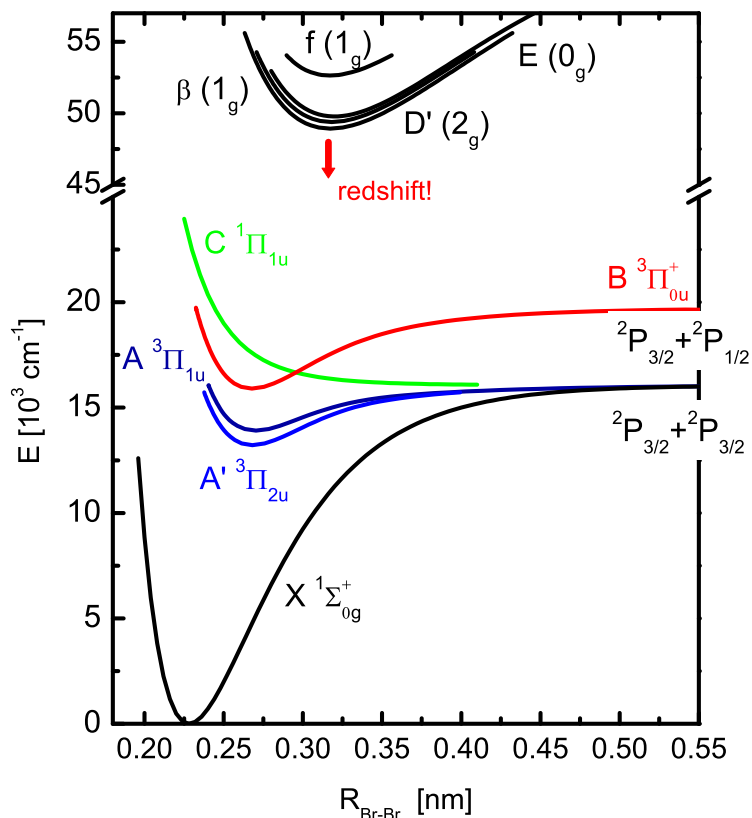
Fig.2.1. Gas phase potential curves of Br$_2$ involved in the coherent control experiments carried out in this work. The electronic states were obtained from absorption and emission spectroscopy in [109, 110, 114, 116, 117]. While the energetic positions of the lowest five covalent states are only slightly affected by the surrounding argon matrix, the charge transfer states experience a strong red shift (see also Sec. 2.3 where the matrix induced effects are discussed in detail).

packet dynamics on the covalent states by subsequent excitation with ultrashort probe pulses. A significant redshift of these states induced by the surrounding argon atoms is indicated. It has been observed and documented in [88]. Having the largest Franck-Condon (FC) factors in absorption (see Sec. 2.5.1), exemplary the spectroscopically best characterized dissociative singlet C $^1\Pi_{1u}$ state is shown in Fig. 2.1, too. Due to the large splitting of the dissociation energies caused by the strong spin-orbit coupling, this repulsive state crosses the electronic B state. The argon matrix induced predissociation to the C state was the topic of theoretical investigation carried out in [84]. The covalent states in Fig. 2.1 are only a small selection from in total 36 covalent states. In order to depict the entire manifold of covalent states of dibromide Br$_2$, besides of the spectroscopic potential data, ab initio calculations of the covalent electronic states carried
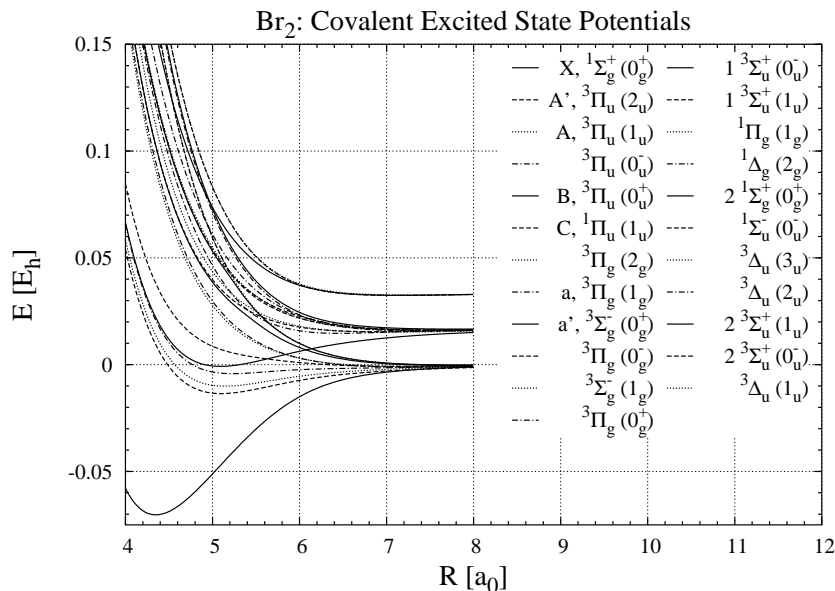
Fig.2.2. Ab initio potentials calculated by applying the spin-orbit coupled configuration interaction method from refs. [84, 118, 119].

out by S. Yabushita [118] are replotted in Fig. 2.2 from [84]. Borowski used these potentials for constructing effective chromophore-bath potentials for his theoretical investigations of Br$_2$:Ar. The effect of the potential curve crossing will be introduced on a general level and specified on the gas phase molecule in the following section.

Predissociation and curve crossings in the gas phase

When two electronic potentials cross, a population transfer from the initially populated to the initially not populated crossing potential may take place. A chemically interesting situation is given, if the molecule is initially excitated below the gas phase dissociation limit of the corresponding excited electronic state while the crossing state is a repulsive one, such that the molecule may dissociate by nonradiative transition to the crossing state. Therefore, for this type of molecular nonadiabatic interaction the term "predissociation" is commonly used. A special case is classified as a Landau-Zener-type nonadiabatic transition, where two one dimensional electronic curves with a variable energy gap avoid to cross and are coupled by a constant coupling parameter [120–123]. In contrast, a Rosen-Zener-type crossing describes a two state system with constant energy gap and time dependent coupling [124]. Rosen-Zener crosssings of covalent potential curves are shown for the calculated DIM potentials in [84] and will be important for the energy transfer processes investigated in this work, as well. Now we turn to the predissociation of molecular bromine.
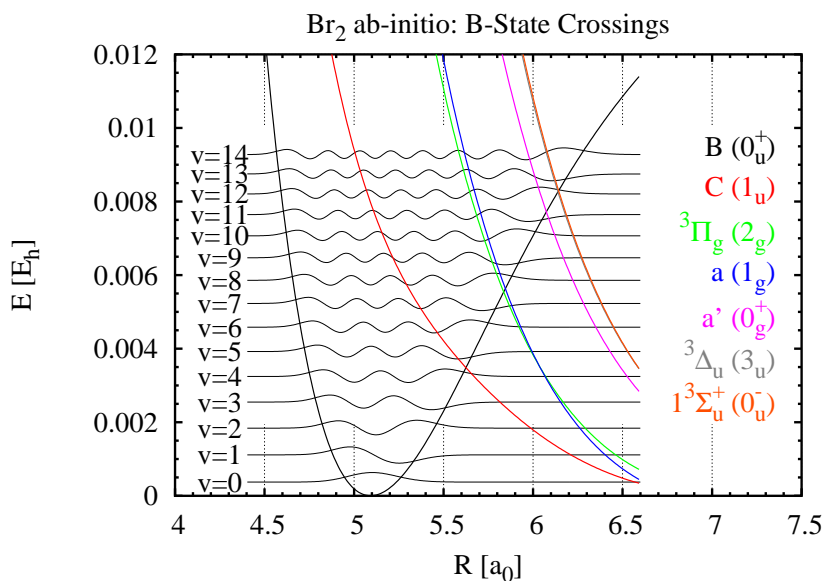
Fig.2.3. Low energetic part of the ab initio B state potential with first 15 vibrational eigenstates and crossings with dissociative states from [84, 118].

In the gas phase, no predissociation from the covalent B state to crossing repulsive states occur due to the orthogonality of the states. The transitions remain forbidden until a coupling to molecular rotations weakens the strict selection rules [111, 125–129]. Calculated nonadiabatic transition probabilities between selected ab initio potentials from Fig. 2.2 also report non vanishing values only for states sharing the same dissociation limit [119]. The treated crossings between the B (black line) and repulsive states (colored lines) are shown in Fig. 2.3 together with the ab initio B vibrational eigenstates and wave functions. The crossings lie between vibrational levels v'=4 and 5, v'=7 and 8 and v'=11 and 12. In Sec. 2.5, the energetic positions of these crossings are compared to those observed in excitation spectra of Br_2 in solid Ar. They were also used to address the observed predissociation to specific electronic states [83]. Before discussing the solvent induced effects on the gas phase crossings observed in frequency resolved spectroscopy, the solid state rare gas solvent will be briefly introduced.

2.2 The rare gas crystal ^{40}Ar

Being a noble gas, argon is located in the 8th main group of the periodic table of elements, having completely filled atomic shells in its ground state configuration. Therefore and as the name already suggests ($\alpha\rho\gamma\omega\varsigma$ means "inactive" in old greek), it is a chemically relatively inert element. This makes it an ideal candidate for isolating molecules in order to study their decoherence due to the vibronic coupling
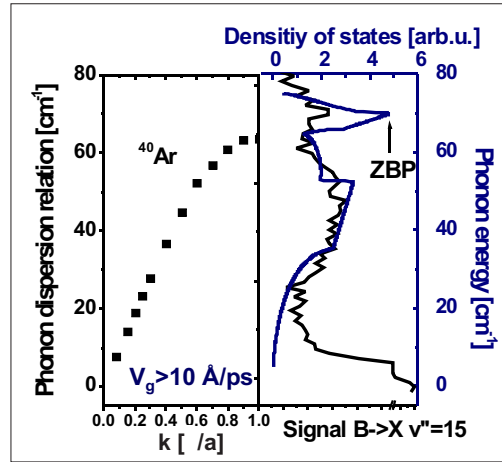
Fig.2.4. Phonon dispersion relation (left) and density of states (right) of solid argon, taken from [130] and scaled from ^{36}Ar to ^{40}Ar. A cut-out of the B state excitation spectrum of Br$_2$:Ar is added (blue line) [83]. The reduced wave vector k is given in units of π/a, where a=0.53nm is the lattice constant of the argon crytal.

of molecular and lattice motion. Argon has three stable isotopes, ^{36}Ar, ^{38}Ar and ^{40}Ar and the latter, the most abundant one, is used in the experiments of this work. Argon crystallizes at normal pressure at 83.9K into a face centered cubic (fcc) crystal lattice. Since it is only bound by van der Waals forces, it is theoretically well characterized. However, theoretically reproducing the fcc crystal structure observed in the experimental structure analysis, has been a challenging task for a long time period, since it necessitates the treatment of three body interactions. Without taking them into account, the hcp (hexagonal closest package) structure would be favored in theory [131, 132]. The energetic structure of Ar lattice phonons has been also well characterized and the data obtained from neutron scattering experiments by Fujii and coworkers are shown in the right side of Fig. 2.4. Since the measurements were carried out with ^{36}Ar, in order to allow for a comparison with the spectroscopic measurements carried out in our group, they have been scaled in energy by the mass ratio factor $\sqrt{36/40}$. The dispersion relation for the $\langle 100 \rangle$ branch of the acoustic phonons occurring in the rare gas crystal is shown on the left and its slope suggests phonon velocities around $10\mathring{A}$/ps in the linear region for small values of the reduced wave vector k. The applicability of the coherent control scheme proposed in this work requires an entanglement of Ar atoms and Br$_2$ vibronic wave packets in a time period of 1ps. A prove of this entanglement and the amount of atoms involved in this coherent motion will be estimated according to the velocities suggested by the dispersion curve in Sec. 6.3. On the right hand side of Fig. 2.4 the density of Ar lattice phonons is shown (black line) together with the phonon sideband structure

measured in excitation spectra of Br_2 doped Ar (blue line) [83]. In an energetic regime with moderate coupling of the dopant to the lattice motion, excitation spectra of the chromophore allow to reproduce the phonon state structure according to the agreement in Fig. 2.4. This means, that all phonons modes can be excited together with the color center, since not only the overall width is covered in the excitation spectrum but even the intensity distribution is satisfactorily reproduced [83]. The peak on the high energetic side, is even more pronounced in the high resolution excitation spectrum. It coincides with zero slope of the phonon dispersion relation i.e vanishing group velocity. It is attributed to the so-called zone boundary phonon (ZBP) which does not propagate away from the chromophore. It has been observed in a number of time resolved experiments on the Br_2:Ar [88] and before on the I_2:Ar [75, 133, 134] and I_2:Kr [135] systems. Its excitation with ultrashort laser pulses has been attributed to the displacive excitation of coherent phonon (DECP) mechanism, which is caused by the expansion of the molecular electron cloud during excitation [136–143]. In the last section of Chapter 6 it will be shown, that the combined selective excitation of the ZBP with the molecular vibrational modes amplifies the predissociation efficiency from B to a crossing repulsive state.

2.3 Rare gas matrix isolation

As the expression already suggests, originally rare gas matrices were applied in order to isolate single molecules within a chemically inert surrounding. Complementarily, doping of crystals with molecules finds technical application in solid state lasers, like for example the Ti:Sa laser used for the experiments presented in this work [144,145]. For special combinations of dihalogen and rare gas, the rare gas matrix can block translational as well as rotational molecular degrees of freedom. This allows for an effective one dimensional study of the vibronic properties of the dihalogen and the effects induced by the coupling to the matrix atoms. To achieve this specific type of isolation, both, van der Waals radius and equilibrium internuclear distance of the halogen are adapted to the nearest neighbor distance and van der Waals radius of the rare gas matrix. This is, e.g. the case for Br_2 molecules in solid Ar. To this end, the molecule occupies a double substitutional site in the fcc-structured Ar crystal, replacing two lattice atoms. This has been proven by means of Raman spectroscopy [146] and is schematically depicted in Fig. 2.5. The rare gas atoms are drawn in green and the Br_2 molecule in orange, as bigger balls, according to the atomic mass ratio. The freezing of the rotational motion has been verified by depolarization measurements in [88,147]. The fact that no ultrafast depolarization takes place in case of Br_2 in Ar will turn out to be a precondition for the control scheme
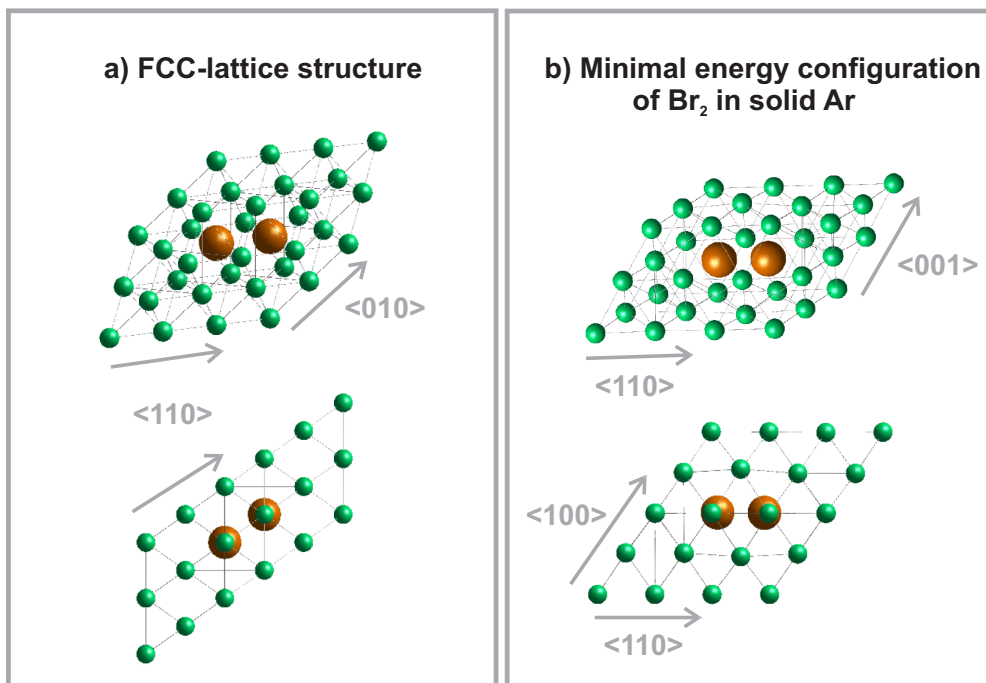
Fig.2.5. a) Scheme of the face centered cubic (fcc) lattice structure of 34 rare gas host atoms (green balls) and a diatomic guest molecule (orange balls) occupying a double substitutional site in the matrix being oriented in the $\langle 110 \rangle$-direction. On the bottom the view on the (111) plane is shown. b) Same as a) but now with realistic lattice structure with parameters resulting from energy minimization using pair potentials from Fig. 2.6 (see text). The (100) view reveals a deformation of the rigid fcc-structure in the neighborhood of the guest molecule Br_2.

applied in this work, since it allows the application of polarization sensitive pump probe spectroscopy[1] (see Sec. 4.2.1). For the simulation of Fig. 2.5 a) a rigid fcc lattice containing 36 sites[2] has been constructed and all atoms have been placed, artificially centered on the lattice sites. In order to draw a more realistic picture of the lattice distortion in the neighborhood of the molecular impurity, a minimal energy configuration of the 34 argon atoms surrounding a Br_2 molecule has been carried out under the guidance of Burkhard Schmidt and the result is shown in Fig. 2.5 b). A view on the (100) plane delivers a relatively weak deformation of the lattice structure. This is in qualitative accordance with the results from [154–156], where more sophisticated methods, involving the treatment of several hundreds of atoms have been used. For the calculation of the equilibrium

---

[1]Experimental study of the rotational motion leading to ultrafast depolarization is documented for ClF in Ar in [148] and investigated theoretically in [149–153].

[2]The first shell surrounding the molecule consists of only 18 atoms.
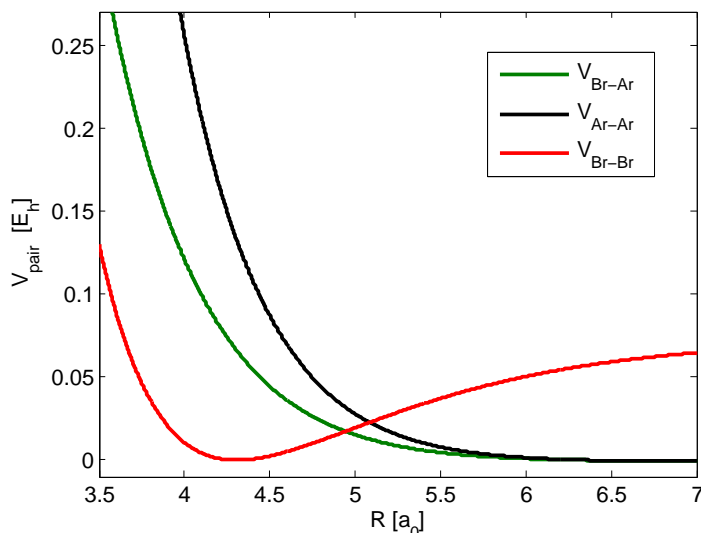
Fig.2.6. Pair potentials used for the simulating the geometrically relaxed latticed from Fig. 2.5 b). The electronic X state representing V_{Br-Br} (red) was taken from [109], V_{Br-Ar} (green) from [157] and V_{Ar-Ar} (black) from [158].

geometry depicted in Fig. 2.5 b) the interaction between the rare gas atoms and the molecule were modeled in terms of pair potentials, which are shown in Fig. 2.6. For the Br-Br interaction the electronic ground state with the Morse parameters from [109] has been used, the Ar-Ar pair potentials [158, 159] and the Ar-Br potentials [157, 160] are given in terms of Lennard-Jones potentials. In order to hinder an escape of atoms from the simulation box containing the 36 atoms during the energy minimization, periodic boundary conditions reflecting the fcc lattice periodicity have been applied [161]. Since a detailed, quantitatively more accurate analysis has been given in [84], here the displacement effects on specific atoms due to the perturbation by the chromophore will not be further discussed. Instead, we change again the perspective and report the interaction effects from the argon cage on the molecule Br_2.

Cage effects

As it has been already mentioned previously, the caging by the matrix influences the energetic structure of the hosted molecule. Since the rotational motion of the molecule is blocked, the multi-dimensional effects involving the interactions with each rare gas atom can be projected on the one dimensional internuclear distance dependent electronic potentials and discussed in terms of effective potentials. Two types of influences on the gas phase electronic structure can be distinguished: Inductive energetic shifts and geometrical shifts. In case of the CT states shown in

Fig. 2.1, the former dominates. Experimentally observed strong alterings of the CT states of I_2 embedded in different rare gas matrix environments was reported in [162]. Redshifts of the Br_2 ion pair states caused by the Ar matrix surrounding were observed in [88]. Having a large electric dipole moment, they polarize the surrounding crystal, which in turn enlarges the solvation energy, corresponding to a redshift of the charge transfer states. Theoretically, the establishment of molecular dipole moments in solvated ion-pair molecules was attributed to a local distortion of the polarizable rare gas matrix which breaks the symmetry of gas phase CT states and leads to charge localization [163]. Since the dipole moment of covalent states is much smaller, this effect is quite weak. Instead, a pronounced geometric modification of the covalent potential shapes is caused by the matrix atoms. Due to the rigid lattice structure and the comparable molecular and rare gas van der Waals radii, the molecules are hindered from permanent dissociation. This effect has been termed the "cage effect" already in 1934 [164]. In the shape of the effective covalent potentials it shows up in a bending up of the outer, repulsive wing as sketched in Fig. 2.7 b). Here, a binding potential is drawn, however, of course the same effect shows up in case of purely dissociative electronic potentials, too.

Vibrational energy relaxation

Indeed, even if being excited high above the dissociation limit, the molecules caged by the matrix usually recombine again. The recombination process is schematically exemplified for a wave packet excited above the gas phase dissociation limit in the inner turning point of a caged molecular potential in Fig. 2.7 b). The wave packet propagates outwards in the potential as long as, instead of dissociation in case of the free molecule, the caged molecule bumps in the surrounding matrix atoms. In a dissipation process analogous to an inelastic scattering, it transfers part of its kinetic energy to the matrix. While in the matrix phonons are induced, the wavepacket slides down the outer limb of the effective potential well and returns in the chemically bound part of the potential, where it oscillates again, energetically between inner and outer classical turning points. It has been shown in previous work, that vibrational wave packets experiencing such collisions with a strong energy loss to the matrix vibrations do not necessarily lose vibrational phase information [165]. The shape of the effective B state potential and the strong energy relaxation in the part of the B state potential of Br_2 in Ar which is bound by the matrix have been quantified by M. Gühr based on ultrafast dynamics studies [88, 166]. The results presented in this work analyze additionally to the vibrational coherence, the combined electronic and vibrational, i.e. vibronic coherence properties in the B state by means of coherent control experiments. The
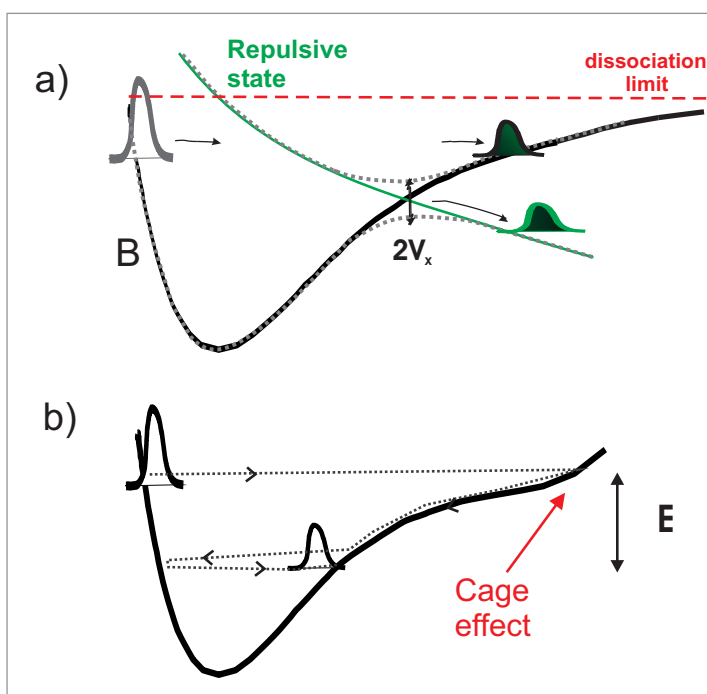
Fig.2.7. Schematic presentation of the dynamical processes investigated in terms of the corresponding wave packet dynamics: a) Predissociation and b) Vibrational energy relaxation. The cage effect is indicated in b) by the bending up of the potential near the dissociation limit and ΔE denotes the amount of energy transferred to the matrix atoms during the outward motion of the molecular wave packet, in an inelastic scattering-like process (see text). In a), the diabatic B potential (black) and a crossing repulsive potential (green) are depicted together with the corresponding adiabatic potentials (gray dotted lines). The gas phase dissociation limit of the B state is indicated by the dashed red line. V_X denotes the coupling matrix element between the B and the repulsive state and the adiabatic curves are split by $2 \cdot V_X$ according to the Landau-Zener model [167]. (See eq. (2.1) and text.)

vibrational relaxation process sketched here, will turn out to transfer predissociated population from the B state via a crossing repulsive state into the bound part of the A states, where it is detected and monitored by means of coherent control.

Matrix induced predissociation

A schematic representation of predissociation of a vibrational wave packet excited in the inner turning point of the electronic B state is drawn in Fig. 2.7 a). Although initially excited below the gas phase dissociation limit of the B state (red dashed line), the molecule may predissociate by radiation-less transition to a nona-

diabatically coupled repulsive state. The diabatic, uncoupled potentials are drawn as solid lines while the avoided crossing of adiabatic potentials is depicted with dotted lines. When passing the crossing, parts of the wave packet are transferred from the B state to the repulsive state while the remaining part still oscillates on in the B state. The transition probability P can be described by means of the well-known semiclassical Landau-Zener-formula, with a constant coupling strength V_X [121,167]:

$$P = 1 - exp[-\frac{2\pi V_X^2}{\hbar v_g \mid F_2 - F_1 \mid}] \tag{2.1}$$

where $F_2 - F_1$ denotes the force difference, i.e. the difference between the slopes of the B and the repulsive potential, and v_g the group velocity of the wave packet in the crossing point of diabatic potentials. The minimal gap of adiabatic potentials in the region of crossing diabatic states is given by $2V_X$, also indicated in Fig. 2.7 a) [167]. The Landau-Zener formula clearly displays the decrease of the transition probability with increasing group velocity v_g of the wave packet when passing the crossing. It delivers that for large transition probabilities an energetic region close to the crossing is favorable, where the wave packet is centered close to the classical turning points of the diabatic potentials corresponding to small group velocities. However, in order to achieve more accurate transition probabilities in the crossing region, the Landau-Zener formula has to be to extended, like it has been done for example within the quantum mechanical Zhu-Nakamura-model [168, 169].

In the gas phase, the population transfer from the B state of Br_2 to crossing repulsive states with the same irreducible representation is symmetry forbidden. A weakening of the radiation-less transition rules takes place, not only, as already mentioned in case of coupling to molecular rotations, but also in the presence of surrounding atoms [170]. In the group of A. Zewail the collisional induced predissociation of I_2 in a gaseous Kr surrounding has been investigated with respect to gas density dependence revealing a linear predissociation rate increase [171]. A further extrapolation would lead to even higher rates in the liquid and the highest ones in the solid phase. Lifetime measurements yield however another trend [172–174]. Theoretical investigations revealed, that a high symmetry of a crystal leads to a reduced coupling of electronic potentials [163, 175, 176]. The theoretical studies of our collaboration partners support this finding for the Br_2:Ar system. Projecting the coupling matrix elements of the B and C state on the normal mode phonon spectrum, which is similar to the phonon density shown in Sec. 2.2, they identified two pronounced phonon modes. They lie on the high energetic side of the spectrum and are responsible for the efficient matrix induced predissociation, one of which is needed to break the high symmetry of the cage [85, 177].

2.4   Why just Br$_2$:Ar?

The suggestion of coherently controlling matrix induced predissociation has been formulated already in the proposal for the first funding period of the collaborative research center SFB 450 in 1998. The reasons why its realization took so long will be discussed in the following. Combinations of dihalogen doped rare gas matrices different from Br$_2$:Ar have been investigated first in our working group.

Historically motivated by the great amount of available frequency and time resolved spectroscopic information and intensive theoretical treatments, iodine isolated in a krypton environment was the first dihalogen that served as a testing sample for the newly built up pump probe apparatus. Indeed, an efficient B state predissociation was observed and quantitatively analyzed in [135, 178]. However, the Apkarian group derived electronic coherence times around 100fs by means of coherent Anti-Stokes Raman Scattering (CARS) measurements. Therefore, I$_2$:Kr is not suitable for coherent control experiments with longer chirped pulses or sequences of pulses. As it has been already mentioned and will be explained in more detail in Sec. 4.3.1, the rational coherent control experiments carried out in this work receive their information about optimal pulse shapes needed for maximization of the target states from spectroscopic data. A prerequisite for its application is that structures being addressable to the different chromophore and lattice vibrational modes are accessible. In the case of iodine, no such structures appear in absorption or excitation spectra, which is another reason, most likely related to the short electronic coherence times, why I$_2$ is not the right candidate for the quantum control.

The lighter halogens ClF and Cl$_2$ embedded in an Ar matrix ware also matter of investigation in the Schwentner group [101, 179] and within the SFB 450. Combined experimental and theoretical studies reveald an ultrafast electronic spin-flip mechanism [180] which was related to cage exit dynamics by Korolkov and Manz on the theoretical side [100, 181], who also established schemes for coherent control of the electronic spin of both, ClF and Cl$_2$ isolated in solid Ar [182, 183]. In case of Cl$_2$:Ar, structured excitation spectra allow for an assignment of molecular and phonon modes. Indeed, also the electronic coherence times for the B state excitation last for about 600fs, which has been shown experimentally by excitation with phase locked double pulses from a Michelson-interferometer [76, 184, 185]. The coherent control with double pulses allowed for a selective excitation of Cl$_2$ vibrations and phonons and a lowering of vibrational energy relaxation rate could be induced this way [186]. However, due to a weaker spin-orbit coupling, as compared to the heavy molecules Br$_2$ and I$_2$, the dissociation limits for the B and repulsive states are only slightly shifted and predissociation takes place in the energetic region close to the
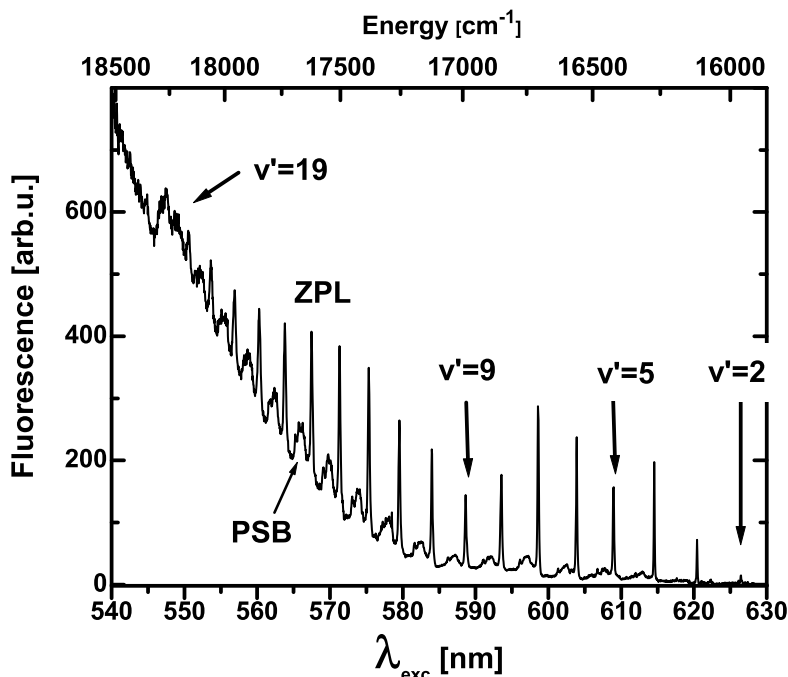
Fig.2.8. B state excitation spectrum measured in [83]. It shows a progression of sharp ZPL (zero phonon lines) and PSB (phonon side bands) that add up and form the unstructured background increasing with increasing excitation photon energy. The vibrational progression is observed from v'=2 up to v'=19 until it merges in an unstructured continuum, far below the gas phase dissociation limit at 500nm.

gas phase dissociation limit. In this energetic region the vibrational structures are seemingly buried in a continuum. Therefore, also Cl_2:Ar is not suitable for coherent control of matrix induced predissociation.

Br_2 in Ar matrix fulfills all required preconditions: The $X \to B$ transition shows a long vibrational progression in the suitable spectral region of 650nm to 500nm [187] and recent investigations with phase locked pulse pairs determined electronic coherence times for the X→B transitions of 1.5ps in the interesting region of B state crossings [188].

An improved investigation of the excitation spectra carried out in our group clarified the vibrational assignment in excitation spectra, the contribution of the $X \to A$ transition to excitation and fluorescence spectra and the population flow from B to A and A' via several crossings with repulsive states [83], which will be detailed in a following Sec. 2.5.3. The B state excitation spectrum is shown in Fig. 2.8. The B vibrational levels in excitation are characterized by zero phonon lines (ZPL) i.e. an exclusive excitation of the Br_2 chromophore vibrations without participation of

vibrations (phonons) in the surrounding lattice. The linewidth of the ZPL is small and essentially determined by the lifetime which indicates that indeed inhomogeneous broadening can be ignored. It additionally signalizes long coherence. The corresponding quantitative analysis will be shown in Sec. 2.5.3. The ZPL are accompanied on the blue side by broad phonon sidebands (PSB) which represent a simultaneous excitation of a Br$_2$ vibration and phonon modes of the environment. The PSB are structured and represent very well the matrix phonon density of states, as shown in Sec. 2.2. The structures have been reproduced convincingly in multidimensional quantum calculations of the normal mode spectrum [189]. The ZPL and PSB progressions will be the key features to be addressed in the present investigation by frequency combs in the molecule initiated by pulse trains. The first goal will be to separate out the ZPL coherences from the PSB part which is certainly more exposed to decoherence. The next step however will be a search for coherence in the PSB. To our surprise we find lasting coherences also in the PSB.

There is, however, a key problem also in the Br$_2$:Ar case, challenging both, experimental and theoretical investigations, i.e. the very small Franck-Condon factors for the B state excitation near the interesting crossings with repulsive states. Additionally, in the chosen spectral region for experiments, (around 585nm) the Franck-Condon factors of the X $\rightarrow$ A transition are several orders of magnitude larger than those of the X $\rightarrow$ B transition, which will be discussed in the next section. Furthermore, the X $\rightarrow$ A transition lies above the A state gas phase dissociation limit. Therefore, the A state is bound only by the matrix cage and the accompanied large energy due to vibrational relaxation leads to a structureless continuum in this spectral range. As a consequence, the B state ZPL around 585nm are hardly recognizable in absorption on the A state background and the PSB is not discernable at all [83]. This key problem has however been solved within our rational coherent control scheme (see Sec. 4.3). It was possible to enhance B state coherences by pulse trains to such an extent that not only ZPL but also PSB could be manipulated with molecular frequency combs [188, 190]. This finally allowed for a coherent control of matrix induced predissociation (see Chapter 6).

2.5   Energetic properties of Br$_2$ in solid Ar

In order to characterize the energetic properties of Br$_2$ in solid Ar, spectroscopic measurements have been carried out in [83, 88]. M. Gühr recorded the absorption spectrum from the electronic ground state to excited covalent states in the visible range, as well as the emission from charge transfer states in the ultaviolet. Both spectroscopic features are needed for the choice of proper wavelengths of ultrashort

laser pulses applied in time resolved pump probe experiments (see Sec. 6.1). The absorption spectrum, which will be presented next, specifies the pump pulse wavelengths needed for the excitation of vibrational B state wave packets. The emission from charge transfer states, which will be discussed in Sec. 2.5.2, characterizes the wavelength region for light induced fluorescence (LiF), needed for detection of pump probe spectra. It also determines the required probe pulse wavelengths. The excitation spectra provide information on the energy flow between different electronic states via nonadiabatic processes, as well as on lifetimes and coherences of vibrational features. They also contain the necessary information on the energetic region where crossings of the B state with repulsive states are located. Thus, their discussion will be summarized in the last part of this section [83, 89].

2.5.1   Absorption Spectrum

The absorption spectrum was taken by recording the transmission of a Br_2:Ar sample in the wavelengths range from 650 to 300 nm, covering the three major valence transitions from the ground state $X^1\Sigma_{0g}$ to the excited electronic states $A\,^3\Pi_{1u}$, $B\,^3\Pi_{0u}$ and $C\,^1\Pi_{1u}$ which are shown in the gas phase potential energy diagram of Fig. 2.1. The absorption $I(\lambda)$ obeys the Lambert-Beer law:

$$I(\lambda) = I_0(\lambda)e^{-\mu(\lambda)x}, \qquad\qquad (2.2)$$

with x being the sample thickness and $\mu(\lambda)$ the extinction coefficient. The light from a high pressure Xe lamp, delivering a continuum of radiation in the visible (VIS) and ultraviolet (UV) light range, was focused on the 1:500 Br_2:Ar mixture, kept at a temperature of 20K. It served as the reference spectrum $I_0(\lambda)$ (sample). The normalized transmission is displayed in Fig. 2.9 (thick black line). Good accordance with gas phase absorption spectra [191] and with matrix spectra measured at a higher Br_2:Ar concentration [192] could be observed [88]. The reason is, that the absorption process takes place on the inner limbs of the potential curves, which are least exposed to interactions with the cage atoms.

    The maximum of the absorption around 415 nm corresponds to the only fully dipole allowed transition from the $X^1\Sigma_{0g}$ to the $C\,^1\Pi_{1u}$ state, which has the largest oscillator strength. Involving a spin flip, the transitions to $A\,^3\Pi_{1u}$ and $B\,^3\Pi_{0u}$ states are weaker. The shoulder around 500 nm displays the Franck-Condon (FC) maximum of the transition to B. The transition to A is buried in the red wing of the absorption, where it dominates the spectrum, as also visualized in the insert of Fig. 2.9. The relative contributions of the A and B state transitions to the absorbance in this wavelength region between 600nm and 550nm are important to
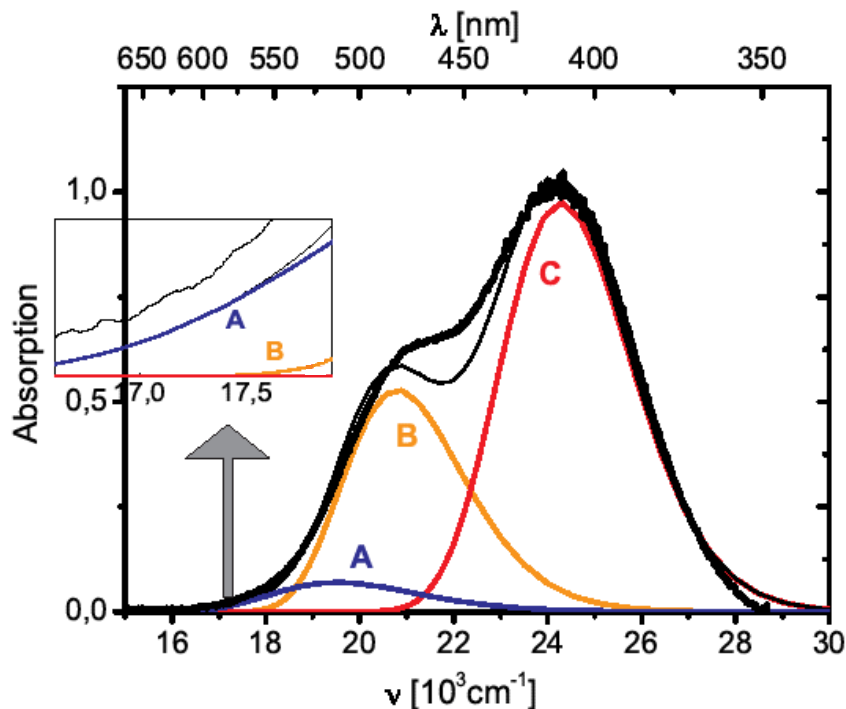
Fig.2.9. Absorption spectrum of Br$_2$:Ar recorded at 20K (thick black line) in [88]. Blue, orange and red parts show the contributions from the covalent A, B and C states, respectively. They were determined by applying the projection method (see text, [193]). The thin black line depicts the sum of the three contributions calculated with the projection method and is compared here with the experimental absorbance. In the insert an enlarged view of the interesting spectral region covering the B state crossings with repulsive states is shown in an enlarged view (compare Fig. 2.3 and Fig. 2.13).

determine the electronic composition of time resolved and coherent control spectra, respectively. Thus, using a classical projection method, a decomposition into the different electronic states has been carried out in [88]. The square of the ground state wave function $|\Psi_X(R)|^2$, which is in our case the $v'' = 0$ wave function in the X state, is projected onto the repulsive potential wing $V_Y(R)$ of the excited (Y=A, B or C) state to simulate the FC factors. Multiplication with the square of the electronic transition dipole $|\mu_{XY}(R)|^2$ with yields the Y-contribution to the absorption spectrum $\sigma_{abs}(R)$ according to

$$\sigma_{abs}(R) = |\Psi_X(R)|^2 \left| \frac{dV_Y}{dR} \right|^{-1} |\mu_{XY}(R)|^2 . \qquad (2.3)$$

The R-dependence implicitely includes the frequency dependence via $R(V_Y))=R(h\nu)$

and allows for a construction of the absorption spectrum. Usually, the projection method is used in the case of continuum transitions, since scattering states are mainly centered around the inner limb of the potential curves, what makes the projection a good approximation, for a detailed descrition the reader is referred to [193]. The contributions of the A (blue), B (orange) and C (red) state absorption constructed this way in [88] are shown in Fig. 2.9. The applied potential parameters and the $\mu_{XY}(R)$ value for B and C were taken from [109, 113, 194], respectively. In Condon approximation, μ is a constant and due to the lack of data and potential parameters the value from Ref. [116] was taken in [88]. Adding up the three contributions with optimized ratios for the maxima of C:B:A results in the thin black line in Fig. 2.9. The ratios agree quite well with intensity ratios calculated for the gas phase absorption [119]. In the gas phase, the C state represents a repulsive continuum of states, in the matrix, however, it is bound by the cage. The equilibrium internuclear distance of the bound A and B-states is much larger than that of the X state (see potentials in Fig. 2.1). The most intense vertical transitions terminate on the repulsive inner limb of the A and B states, again above the gas phase dissociation limit in the continuum. The absorption region, where B state crossings with repulsive states occur is shown in the insert of Fig. 2.9 in an enlarged view. The problems concerning time resolved coherent control experiments in this energetic region (also marked by the arrow in Fig. 2.9), which have been named in the previous section, are thus, obvious: We have to deal with challengingly small optical densities, as well as with a dominant contribution of the A state continuum in order to carry out the coherent control of the B state predissociation.

2.5.2   Emission Spectrum

The ultraviolet (UV) emission of LiF from charge transfer states of Br$_2$ in Ar has been first recorded in [88] and has been reproduced routinely during preparation of time resolved measurements in this work in order to check the sample quality. Two ultrashort pulses were focused on the sample. The fluorescence induced by excitation with a visible ultrashort pump pulse centered at a wavelength of 498nm, followed by a second UV pulse centered at 267nm wavelength was detected after amplification in a photomultiplier positioned behind the exit slit of a 25cm monochromator. The amplified, boxcar integrated signal is shown in Fig. 2.10 as a black line. Two broad emission bands labeled 1 and 2 are observed. The most intense band 2 has its maximum at a wavelength of 322nm, while band 1 is centered at around 340nm. These two emission bands also appear for an excitation with two visible pulses of 550nm, shown as the cyan line in Fig. 2.10, indicating a two photonic excitation
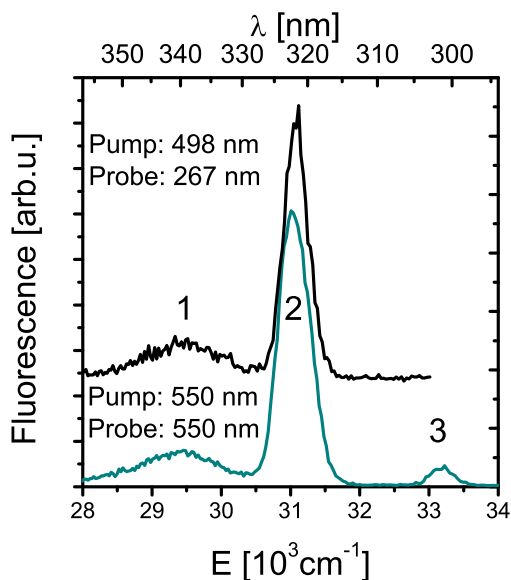
Fig.2.10. UV emission bands of Br$_2$:Ar from [88] detected after excitation with a visible ultrashort pump pulse centered at a wavelength of 498nm, followed by a second UV pulse of 267nm wavelength (black line, offset added for better visibility). For excitation with two visible pulses of 550nm, in addition to emission bands labeled 1 and 2, a third band, labeled 3, on the high energy side of the spectrum shows up (cyan line).

with the second pulse. In addition, a third band 3 appears in this case, with its maximum at 300nm. The fluorescence from this band will be indispensable in order to monitor nearly pure B state wave packet dynamics in the time resolved measurements presented in Chapter 6. In contrast, the LiF from the most intense band 2 monitors a combined wave packet dynamics on the B and A state, at selected pump and probe photon energies. Apart from the importance of the accessibility of band 3 for the decomposition of pump probe spectra into contributions from the A and B state, the choice of a two photonic probe step for the pump probe experiments carried out in this work also has a technical reason. When probing in a one photon process, with UV pulses, a separation of straightlight from these pulses from the LiF-signal is hard to manage. For both, visible pump and probe pulses, respectively, appropriate filtering is easily achievable. It will also turn out in the analysis of pump probe spectra to be presented in Sec. 6.1 that the LiF signal collected from band 3 corresponds to a two photonic probing to the 2nd manifold of ionic states of Br$_2$, while the emission from band 2 is decomposed of directly excited states from the 1st charge transfer manifold and relaxed population from the 2nd .

In the next part, the near infrared emission from the covalent states will be presented.

2.5.3 Excitation Spectra

A complete spectroscopic characterization of the B state of Br$_2$ in solid Ar has been carried out by H. Ibrahim [83]. To this end, emission from the A, A' and B states in the spectral range from 600 to 1100 nm was recorded. A triplet of lines is observable,
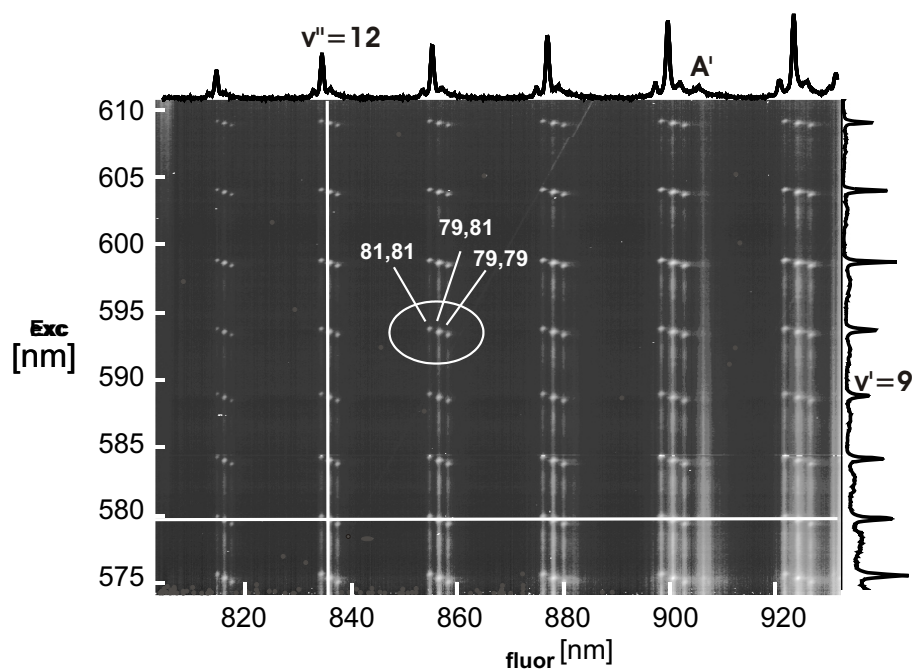
Fig.2.11. Fluorescence from the covalent states B, A and A' to different vibrational states of the X state recorded for excitation wavelength covering almost the whole bound area of the B state [83].

representing the emission from the three isotopomers $^{79}\text{Br}^{79}\text{Br}$, $^{79}\text{Br}^{81}\text{Br}$ and $^{81}\text{Br}^{81}\text{Br}$. In addition to the detected fluorescence wavelength, also the excitation wavelength has been scanned and the successive emission spectra were stored, as reproduced in the two dimensional false color plot of Fig. 2.11. Horizontal cuts, like for example along the white line at an excitation wavelength of 580nm, shows the B and A'-state emissions from the vibrational ground states to different vibrational states of the electronic X state, with the characteristic isotopomer splittings. Vertical cuts, like for example along the central isotopomer $^{79}\text{Br}^{79}\text{Br}$ of a B state emission indicated by the vertical white line provide excitation spectra consisting of sharp zero phonon lines (ZPL) and broad phonon sidebands (PSB), like the one already shown in Fig. 2.8. This excitation spectrum is replotted from [83] in Fig. 2.12 d), now versus the B state vibrations v'. In the following it will be discussed in more detail with respect to the information contained on matrix induced predissociation. All relevant parameters are collected in Fig. 2.12. The sharp ZPL in Fig. 2.12 d) originate from the excitation of the chromophore together with the ground state of the phonon spectrum, therefore, they characterize an effective bromine B state potential in the argon matrix, which is also shown in Fig. 2.13 (black solid line). The PSB in 2.12 d) originate from a combined excitation of Br$_2$ with one phonon of the bath. With increasing vibrational energy the number of excited phonons increases, too, and they
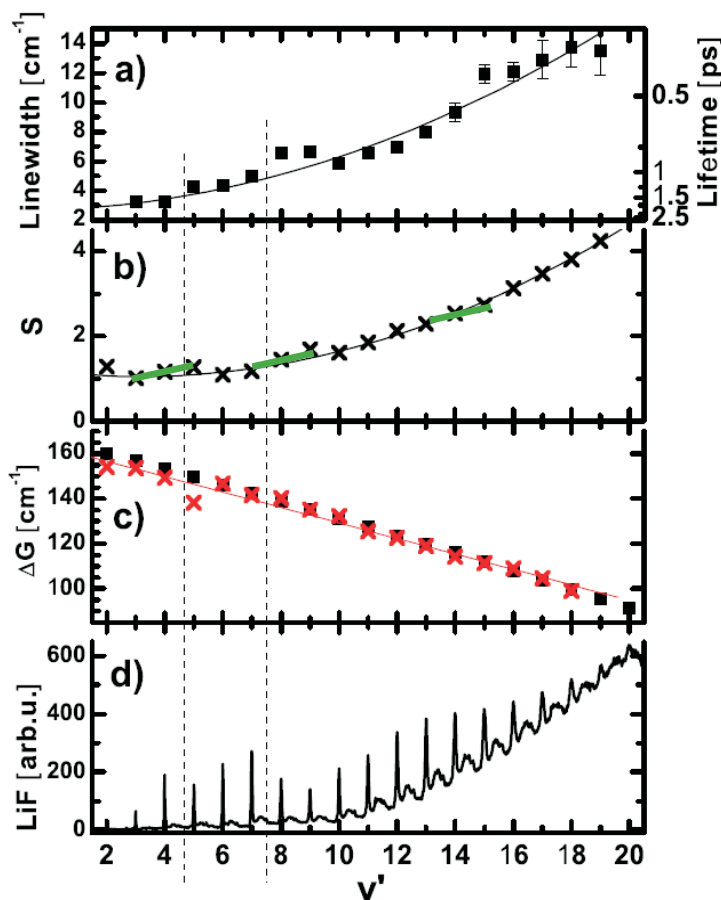
Fig.2.12. a) Integrated linewidths of ZPL from the B state excitation spectrum shown in d). The vertical axis on the right hand side displays the corresponding bandwidth limited lifetimes. In b), calculated Huang-Rhys coupling constants S are shown (see text). c) displays the vibrational spacings ΔG of subsequent ZPL [83].

add up and form the increasing multiphonon-background. A closer look on the progression of ZPL shows an increase in intensity from v'=2 to 3 and to 4 and then a drop between v'=4 and 5. Afterwards, from v'=5 to 6 and to 7 the intensity increases again, until another drop from v'=7 to 8 and 9 occurs. Then the intensity of the ZPL increases on, until the spectral weight shifts to the multiphonon background and the ZPL are not discernible anymore. The increasing trend is compatible with the increasing FC factors in this energetic region of the absorption spectrum shown in Fig. 2.9. The intensity drops, however, are signatures of population loss due to matrix induced predissociation from B to crossing repulsive states. In Fig. 2.12 a) the widths and corresponding lifetimes of the ZPL from d) are shown. An increasing trend is observable, according to increasing phonon couplings, which

have been parametrized in terms of the Huang-Rhys coupling[3] constant S and are
shown in Fig. 2.12 b). Significant jumps of the coupling constant (marked with
green bars) occur in the same energetic regions, where also intensity drops of the
ZPL are observed (vertical dashed lines), emphasizing the matrix induced nature
of the predissociation. These jumps are also present in the behavior of linewidths
in a). The broadening is a typical spectroscopic effect characterizing predissocia-
tion processes [170]. A corresponding lifetime shortening with a jump from about
1.7 to 1.3ps is observable between v'=4 and 5 and a jump from 1.2 to 0.8ps from
v'=7 to 8. In Fig. 2.12 c) gas phase vibrational spacings ΔG (black squares) are
shown together with ZPL spacings (red crosses). The gas phase spacings show the
smooth and linear behavior expected for a Morse oscillator. Between v'=4 and
5, however the spacing is lowered in the matrix. This indicates the position of a
first crossing of the B state with the dissociative C state between these vibrational
levels. The nonadiabatic crossing is most likely located closer to v'=5 such that
it pushes level 5 closer to 6 and thus reduces the spacing. For the second nona-
diabatic crossing between v'=7 to v'=9 only weak deviations from the gas phase
appear, indicating that it is located just in the middle of levels v'=7 and 8. We
are not able to assign this crossing uniquely to a specific dissociative state, since
also in the gas phase ab initio calculations shown in Fig. 2.3, two of them are lying
very close to each other. A third nonadiabatic crossing can be assumed between
v'=14 to 15 due to the observation of a further lifetime jump. Since it is not suf-
ficiently supported by the behavior of the other parameters, it remains a tentative
one. These three crossings are shown together with those from the gas phase cal-
culations in Fig. 2.13. They are labeled 1,2,3 and marked by thick black lines,
while the gas phase crossings are drawn in gray and labeled with the denotations of
corresponding crossing repulsive states. The potential derived from the ZPL posi-
tions in [83] is also shown (black line) in comparison with the RKR potential (red
dotted) derived from pump probe spectra [166] and the gas phase molecular B state
(black dashed) [86]. In the experiments performed in this work, the matrix induced

---

[3]The Huang-Rhys model is a linear coupling model using configuration coordinates [144, 195, 196]. Lattice changes induced by the excitation of the chromophore are modeled in a single configuration coordinate as one displaced harmonic oscillator. For the zero transition the excited lattice is kept in the ground state configuration, and no displacement occurs. The FC factors of these transitions are given by the Huang-Rhys coupling constant S [197], being the phonon number with the largest FC factor. It describes the relative intensity distribution I_n among n phonon states by $I_n = e^{-S}S^n/n!$. S increases with increasing shifts in the configuration coordinate, while the ZPL intensity decreases and a broad distribution of multiphonons is excited. The ratio $\sum_{n=0}^{\infty} I_n/I_0$ of the area of all phonon bands $\sum_{n=0}^{\infty} I_n$ is normalized to that of the ZPL, I_0. For a specific v' it corresponds to e^S. This way, the coupling constant in Fig. 2.12 b) were calculated by inserting in $S(v') = ln\left(\sum_{n=0}^{\infty} I_n(v')/I_0(v')\right)$ the area of the ZPL for $I_0(v')$ and the whole area between two subsequent ZPL for $\sum_{n=0}^{\infty} I_n(v')$.
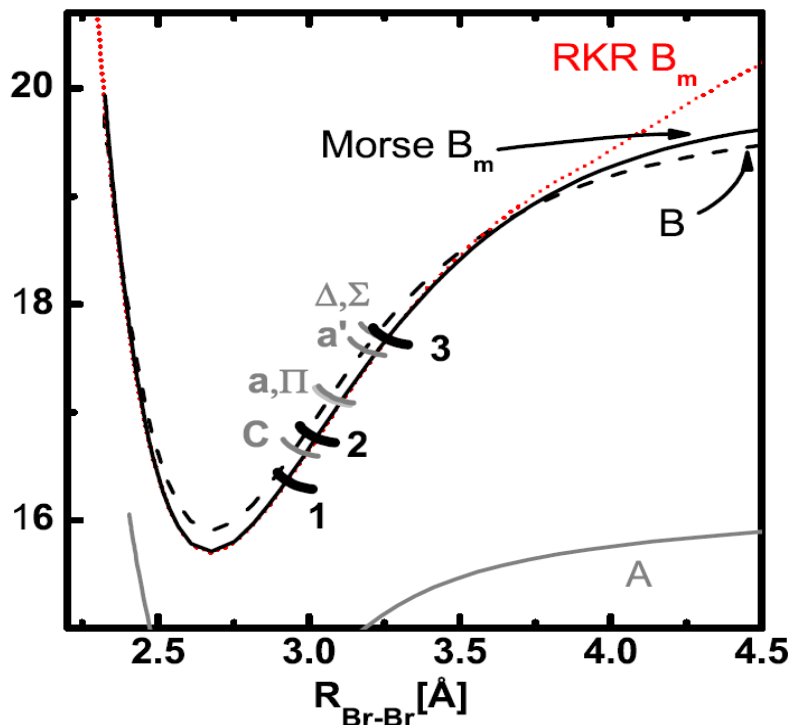
Fig.2.13. Gas phase B potential (dashed) from [86] together with calculated gas phase crossings (marked gray) with repulsive states from [118] plotted together with the effective Br$_2$:Ar B state from pump probe (red dotted) [166] and excitation spectra (black) [83]. The position of crossings determined from the excitation spectra are labeled with 1,2,3 (marked black).

predissociation at the second crossing 2 has been controlled coherently. We chose this specific crossing for the following reasons: First, simply because it is accessible with the FC factors, what is not the case for the lower lying C state crossing treated in the matrix calculations of Borowski [84, 85, 154, 189]. Second, the jump in the linewidth observed for this crossing in Fig. 2.12 a) expressed in terms of a predissociation lifetime, promises a loss of about 10% B state population per roundtrip of the vibrational wave packet excited just above the crossing. This is slow enough to be monitored dynamical and at the same time effective enough not to be buried in noise. Finally, the sharp localization of intensity drops of ZPL and the corresponding linewidth broadening in the crossing region indicates, that this efficient predissociation process is restricted to a narrow spectral region. Therefore, in the dynamical studies, the wave packet has to be excited close to the crossing and relatively long, i.e. spectrally narrow excitation pulses will be applied.

Finally, the detailed analysis carried out in [83] also allowed for following the predissociated population from B. To this end, another horizontal cut of the 2D plot from Fig. 2.11 is shown in Fig. 2.14, displaying the A' excitation spectrum.
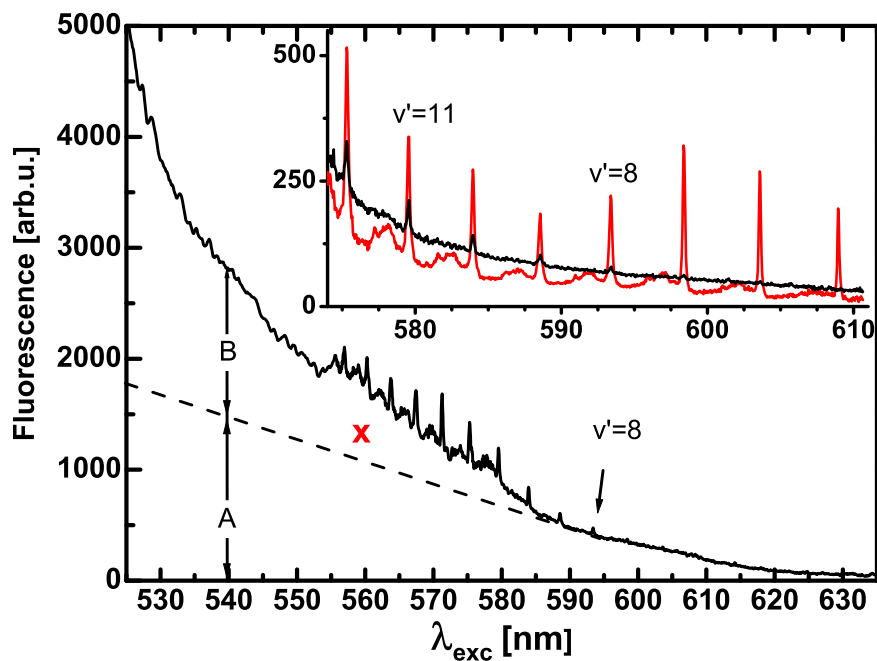
Fig.2.14. Excitation spectrum monitoring the A'→X transition [83]. The nonstructured part monitors the A state excitation above the gas phase dissociation limit on the low energetic side. On the high energy side (separated by the dashed line) the background results from multiphonon excitation of the B and A states. In the insert the structured part is shown, which coincides with the B state excitation (red line from Fig. 2.12 d) and thus can be identified with predissociated B population (see text).

It mainly shows a continuum with a rather weak vibrational structure between 595 and 550nm. In the insert, this part is compared with the B state excitation spectrum from Fig. 2.12 d), demonstrating that the structure corresponds to the B-state vibrational progression. One part of the continuum could be assigned to the absorption of the electronic A state in this energetic region, excited above the dissociation energy (compare Fig. 2.9). It is separated from the part attributed to the B state by the dashed line. Indeed, being a forbidden transition, the A' state only displays population excited on the B and A state. It will be shown in the dynamical studies performed in this work, that the B state contribution is transferred to A' via an intermediate crossing repulsive state and a tentative subsequent Rosen-Zener-type transition of the A, A' and repulsive state[4]. The efficiency of the predissociation will be coherently controlled by selectively steering the coupling of the molecular vibrations to specific phonon modes of the environment.

---

[4]Rosen-Zener type crossings are shown exemplary for the calculated gas phase potential in Fig. 2.2 and have been also observed for the matrix potentials calculated in [84].

Chapter 3

Theoretical background and concepts

This chapter provides the fundamental physical properties and mathematical description of ultrashort laser pulses, pulse sequences and their representation in time and frequency domain, as they are the "key" tool in the rational coherent control scenarios accomplished in this work. Being the precondition for the success of control in the experiments, the concept of coherence will be established in Sec. 3.1.2. Being the "probands", vibrational molecular wave packets will be introduced, as well as their dynamics on molecular electronic potentials coupled by the electric field via dipole interaction. Afterwards, the method to simulate vibronic excitation with ultrashort pulses and pulse sequences and the monitoring of the vibrational wave packet dynamics via simulated pump probe spectra will be explained in detail. The results of the application of these methods to the Br_2 molecular dynamics will be presented later in Chapter 5.

3.1 Vibrational wave packet dynamics

3.1.1 Vibrational wave packets

The eigenstates of the time independent Schrödinger equation (TISE), $|\psi_n(x)\rangle$, are also called stationary states since they do not show any dynamical behavior. Even under the influence of the time evolution operator, $\hat{U}_t = e^{-\frac{i}{\hbar}\hat{H}t}$, they "only" develop time dependent phases and their amplitudes remain stationary. This is in accordance with the energy-time uncertainty relation $\Delta E \cdot \Delta t \geq \hbar/2$: Since eigenstates belong to specific values of (eigen-)energies, they are infinitely extended in the time domain. Besides of energy and time, position and momentum are canonical conjugate variables, too. Thus, their standard deviations also obey the uncertainty

relation $\Delta x \cdot \Delta p \geq \hbar/2$. For eigenstates, the specific values of Δx and Δp are determined by the specific Hamiltonian under consideration.

Due to the linearity of the time dependent Schrödinger equation (TDSE) each linear superposition of the eigenstates of the Hamiltonian $\hat{H}$ with the corresponding dynamical phase factors is also a possible state of the considered quantum system:

$$|\Psi(x,t)\rangle = \sum_n c_n\, e^{-\frac{i}{\hbar} E_n t} |\psi_n(x)\rangle, \qquad (3.1)$$

where c_n are the excitation coefficients. For this superposition state, which is called a wave packet, the phase factors become crucial, leading to the dynamically changing amplitude pattern in position space, determined by the potential structure under consideration. As a prototype we remind of the textbook example of a harmonic oscillator. Here, Schrödinger already demonstrated that a special, Poissonian weighted superposition of the eigenstates of the harmonic oscillator leads to a Gaussian shaped wave packet in position and momentum space with the minimal uncertainty product $\Delta x \cdot \Delta p = \hbar/2$ [16]. These maximally localized wave packets are called coherent states and their quantum mechanical dynamics is as close as possible to that of a classical particle moving in a harmonic oscillator potential [17]. Indeed, their high localizability relies on their stable dynamical phase relations, supported additionally by the constant harmonic frequency spacing $\omega_n = E_n/\hbar = (n + 1/2) \cdot \omega_0$. In its general usage in quantum physics, the term "coherence" means nothing else than a stable phase relation between constituent states of a superposition state. Its loss is always due to a coupling of the system to an environment and is called decoherence. These fundamental terms will be explained in the following on the example of vibronic coherence of a molecular state coupled to a solid state environment, like treated in this work.

3.1.2   Vibronic coherence and decoherence

The general definition of a wave packet given in eq. (3.1) can be used in molecular physics in order to describe a superposition of either electronic, vibrational or rotational states of a molecule. Due to the different timescale of the motion of electrons and nuclei in the molecule, these states are treated independently within the Born-Oppenheimer (BO) approximation. In our coherent control experiments a coupled electronic and vibrational excitation, i.e. a vibronic excitation of the chromophore in a rare gas matrix with ultrashort pulses is performed. Thus, in our time resolved experiments we observe both, electronic and vibrational decoherence dynamics on the
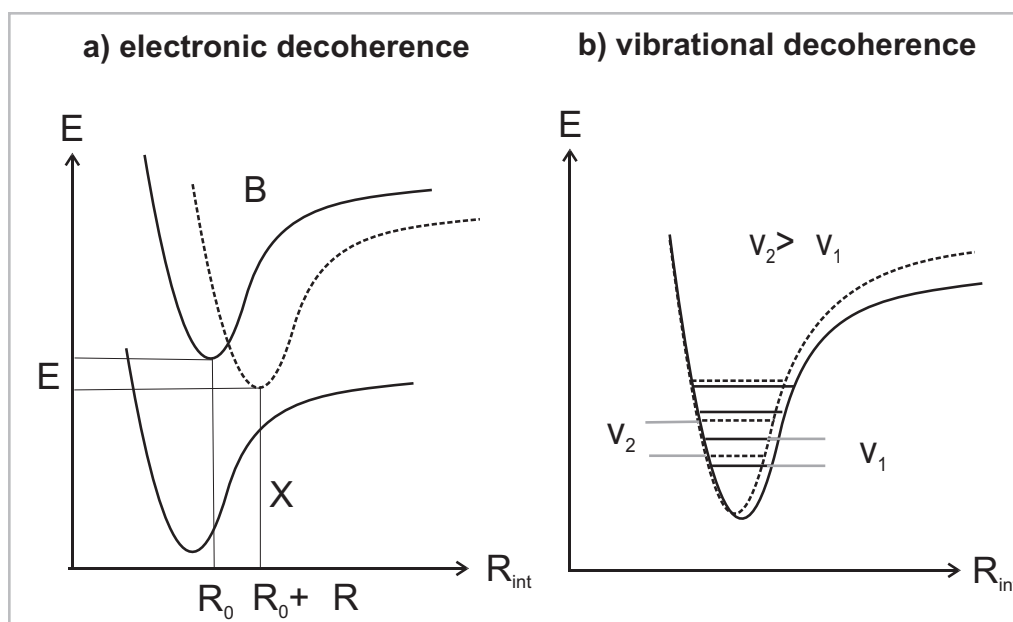
Fig.3.1. Schemes describing the effects on molecular potentials induced by couplings to a surrounding environment, which lead to a) electronic and b) vibrational decoherence (see text).

chromophore due to the coupling to the lattice. In terms of the BO approximation these processes are explained independently within the illustration given in Fig. 3.1. In a) the electronic molecular ground state and the excited covalent B state are drawn schematically (solid lines). Due to the interaction with the cage atoms, the potentials of the covalent states can be shifted (dashed line in a) energetically by an amount ΔE. Additionally, the equilibrium internuclear distance $R_{int}=R_0$ may change by ΔR. Indeed, a realistic picture of the multidimensional potential energy surfaces of the combined chromophore-bath system projected onto the internuclear molecular coordinate would involve dynamically changing potential structures on a femtosecond timescale. Fig. 3.1 a) illustrates that within a superposition state of X and B state vibrations, created in a dipole excitation, phase relations change, due to energy and internuclear distance shifts. Besides of the presented shifts of electronic potentials, also geometrical shifts, i.e. deformations of the potential shape (dashed) with respect to the gas phase structure (solid) occur, as illustrated in Fig. 3.1 b) (compare also Fig. 2.13). They cause pure vibrational decoherence. The potential deformation leads to a change in the spacings Δv of neighboring vibrational levels v. Thus, in the superposition state, i.e. the vibrational wave packet, the stable dynamical phase relations are changed. These geometrical shifts, like for example the cage effect introduced in Sec. 2.3, are in principle connected to dissipative processes

via creation of phonons in the surrounding lattice. Thus, additional vibrational states have to be included in the superposition state described by the vibrational wave packet, to model the vibrational motion of the combined molecule-matrix system. Then, during the ultrafast dynamics, the original phase information among the molecular vibrational states washes out and gets carried away from the molecule into the surrounding matrix atoms. Since electronic decoherence illustrated in Fig. 3.1 a) also changes the relative energies between vibrational levels in the electronic X and B states, they also contribute to the vibrational decoherence. Indeed, also electronic excitations with ultrafast laser pulses lead to impulsive excitations of phonons, like demonstrated for example within the DECP (displacive excitation of coherent phonons) scheme in [136–138].

In order to measure decoherence, the stability of defined dynamical phase relations between superimposed states has to be probed. One way to do this is by measuring interferences between these states. In this work, the electronic decoherence of the X→B transition of Br_2 in solid Ar is probed by the interference of subsequently excited vibrational wavepackets from the X to the B state. The vibrational decoherence dynamics has been investigated by the analysis of fractional revivals, i.e. interference patterns based on the anharmonicity of potentials, in the dynamics of vibrational B state wave packets of Br_2:Ar in [198].

Finally, it shall be mentioned that the theory of decoherence is not formulated in the wave packet picture given here. It is important to point out, that an isolated physical system, e.g. one ideally isolated molecule, does not decohere at all. We can go even one step further and consider a many-body-system with a large number of degrees of freedom. If it would be experimentally possible to completely isolate it from environmental interactions and in addition, numerically possible to take into account all electronic and vibrational couplings in this many-body system, a completely coherent dynamics would be observed. Thus, the whole system could be treated as a huge superposition state consisting of a huge number of eigenstates of the combined Hamiltonian. Then it would not make any sense to talk about decoherence. Instead, interference effects of the great number of constituent states would evolve dynamically. A separation of the system in a per se coherent part and an uncontrolled environment is necessary to define decoherence. Thus, the loss of defined phase relations from the point of view of the chosen coherent part of the system can be described in terms of a mixing with environmental states. To this end, usually, the density matrix formalism, allowing to distinguish between pure (always coherent superposition states) and mixed states is used and instead of the Schrödinger equation, its generalization to the Liouville-von-Neumann equation is applied to model decoherence dynamics [5, 9, 199–201].

In our experiments, the Br_2 molecules are treated as the originally coherent part of the system. Successively, distinct coherent phonon states of the environment will be included in this coherently controlled part. This way, we prepare coupled vibronic-phonon superposition states. Thus, we enlarge the coherent system by these specific environmental modes.

In addition to the discussed decoherence of molecules due to the coupling to an environment, which is identical for all molecules in the sample, decoherence for an ensemble of molecules can occur, due to their interactions. Then, the completely coherent reference system is the idealized ensemble of non-interacting molecules (i.e. it can be treated as just one molecule). This inhomogenous decoherence plays a crucial role in gas and liquid phase measurements, where collisions between molecules dictate the decoherence dynamics[1]. These stochastic processes leading to randomized phase relations, i.e. decoherence, are also modeled in the density matrix formalism. In order to avoid these inhomogenous contributions in our control experiments, we paid special attention to the preparation of clear, homogenous samples (see Sec. 4.2.2). Indeed, the spectral sharpness of zero phonon lines measured by excitation spectroscopy (see Sec. 2.5.3) indicates that these contributions to the decoherence process can be neglected in our case. Thus, the coupling to the lattice atoms plays the dominant role.

3.2   Simulating vibrational wave packet dynamics

In the following section those theoretical tools will be provided which underlie the numerical simulations carried out in this work for complementing the interpretations of our experimental results as presented in Chapter 5. We start with the mathematical description of ultrashort laser pulses followed by the introduction of the formalism used to simulate the vibrational wave packet dynamics in 1st order perturbation theory.

3.2.1   Ultrashort laser pulses and pulse sequences

Since they are closest to the excitation pulses used in our time resolved experiments, Gaussian shaped ultrashort laser pulses were used in the simulations, too. They are described by the time dependent electric field $\varepsilon(t)$, where actually only the real part has a physical meaning, but for mathematical convenience, the complex

---

[1]As an example, the recent study of rotational decoherence dynamics in an ensemble of gaseous N_2 molecules carried out in our working group shall be mentioned [202].

representation is given below:

$$\varepsilon(t) \quad = \quad \varepsilon_F \cdot e^{-\frac{(t-t_0)^2}{2\tau^2}} \, e^{-i\,\Phi(t)} \, . \tag{3.2}$$

Here, ε_F is the field amplitude, $e^{-\frac{(t-t_0)^2}{2\tau^2}}$ the Gaussian envelope peaked at t_0 and having the Gaussian width τ. The Taylor series of the phase $\Phi(t)$ around t_0,

$$\Phi(t) \quad = \quad \phi_0 + \omega_F \cdot (t - t_0) + \frac{\gamma}{2} \cdot (t - t_0)^2 + \mathcal{O}\left((t - t_0)^3\right) \, , \tag{3.3}$$

contains in the linear term the field carrier frequency ω_F and in the quadratic term, the so called linear chirp parameter γ. The latter linearly modifies the angular frequencies with time $\omega(t) = \dot{\Phi}(t) = \omega_F + \gamma\,(t - t_0) + \mathcal{O}\left((t - t_0)^2\right))$. It will play a crucial role in our coherent control experiments and has been also used to focus vibrational wave packets in an anharmonic potential and to advance the onset of fractional revivals [92, 198, 203]. A positive chirp is naturally induced when light traverses a dispersive medium with refractive index $n > 1$. Due to the dispersion relation for light, i.e. $k(\omega) = n(\omega) \cdot \omega/c$, a retardation for the high frequencies with respect to the lower ones is caused[2]. Negative chirps leading to the inverse order of frequencies have to be produced in prism or grating compressors. In our coherent control experiments the shaping of ultrashort laser pulses takes place in the frequency domain in a typical 4f-setup which will be introduced in Sec. 4.1.3. It is connected with the time domain representation via Fourier transformation (FT):

$$\begin{aligned}
\varepsilon(t) \quad &= \quad \varepsilon_F \, e^{-\frac{(t-t_0)^2}{2\tau^2}} \, e^{-i\,\omega_F\,(t-t_0) - i\frac{\gamma}{2}\,(t-t_0)^2} \\
\mathcal{F} \downarrow \qquad &\uparrow \mathcal{F}^{-1} \\
\tilde{\varepsilon}(\omega) \quad &= \quad \tilde{\varepsilon}_F \, e^{-\frac{(\omega-\omega_F)^2}{2\eta^2}} \, e^{i\frac{\beta}{2}\,(\omega-\omega_F)^2}
\end{aligned} \tag{3.4}$$

.

We perform optical Fourier transformations and shape the ultrashort laser pulses in such a way, that after the back transformation in time domain we achieve trains of ultrashort pulses, typically consisting of about five subpulses. For numerical studies

---

[2]In the Taylor series of the wave vector k, i.e. $k(\omega) = k(\omega_0) + k'(\omega - \omega_0) + k''/2 \cdot (\omega - \omega_0)^2 + \mathcal{O}\left((\omega - \omega_0)^3\right)$, the second order term defines the chirp parameter in frequency space $\beta(\omega) = k''(\omega) \cdot x$, while zeroth and first order terms lead to the well known definitions of phase and group velocity, respectively. The time domain chirp γ introduced in eq. (3.3) is connected with the spectral chirp parameter β by $\gamma = \beta \cdot \eta^2/\tau^2$, where τ and η are the Gaussian widths of the field envelopes in time and frequency domain, respectively.
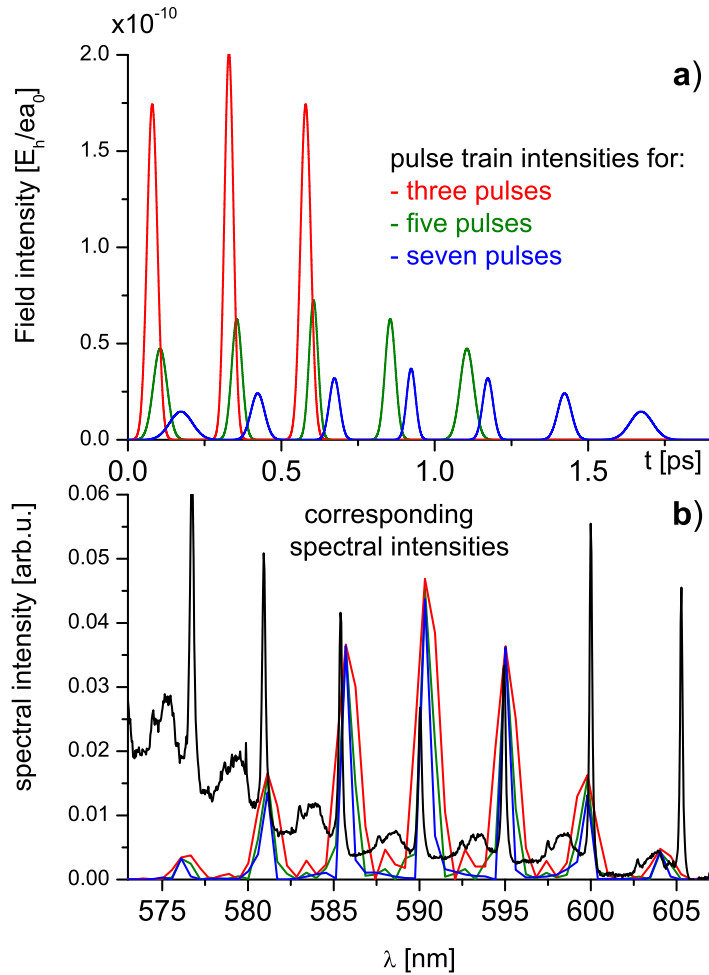
Fig.3.2. a) Three pulse trains with different overall durations consisting of three, five and seven subpulses, respectively. In b) their spectral representations calculated with FFT (Fast Fourier Transform [204–206]) are shown together with the B-state excitation spectrum (black) [83]. For parameters see text and eqs. (3.5) and (3.6).

of the pulse train excitation performed on the free molecule, the k-th subpulse has an individual set of parameters $\varepsilon_F^{(k)}, \tau^{(k)}, \gamma^{(k)}$ and additional phases $\varphi^{(k)}$ and is represented as:

$$\varepsilon^{(k)}(t) = \varepsilon_F^{(k)} \cdot e^{-\frac{(t-t_0-k\cdot T)^2}{2(\tau^{(k)})^2}} \cdot e^{-i\cdot\left(\omega_F\cdot(t-t_0)+0.5\,\gamma^{(k)}\cdot(t-t_0-k\cdot T)^2+\varphi^{(k)}\right)} \qquad (3.5)$$

Summation leads to the implemented pulse trains:

$$\varepsilon_{train}(t) = \sum_{k=0}^{n} \varepsilon^{(k)}(t) \qquad (3.6)$$

The subpulse parameters in the simulations which will be presented in Sec. 5.3 have been chosen such as to fit the experimentally generated pulse trains. In Fig.3.2 a) amplitude envelopes of pulse trains consisting of three (red), five (green) and seven (blue) subpulses are shown together with their Fourier transforms in the spectral domain (b). In the experiments their maxima are separated by the average vibrational period of wave packets excited from the ground state to the B state according to the pulse carrier frequency ω_F, here T=250fs. This way, a wave packet excited by one subpulse just returns in the excitation region after one vibrational period and thus spacially overlaps with the newly excited wave packet by the following subpulse. Thus, interference effects in the wave packet excitations can be used as a probe for vibronic coherence [184,185,207]. According to Fourier transformation the temporal separations of subpulses correspond to the inverse separation of teeth of spectral combs shown in Fig. 3.2 b). They match quite well the vibrational spacings from the B state excitation spectrum, which is also shown for comparison in Fig. 3.2 b) (black). The number of subpulses (i.e. for fixed subpulse separation T the overall pulse train duration) determines the sharpness of each tooth, and the more subpulses are added, the narrower spectral structures can be generated as shown in 3.2 b). In order to take into account the anharmonicity of the B state potential, besides of the central subpulse, all subpulses carry individual linear chirp parameters. They can compensate first order anharmonicities of a Morse oscillator. For a perfect Morse potential, the linear chirps also guarantee, that faster (low energetic) and slower (high energetic) vibrational constituent states of the wave packet, returning back in the excitation region, maximally overlap in time with the newly excited wave packet. As compared to a Morse oscillator, the vibratinal progression in the matrix is disturbed, especially in this selected energetic region of a nonadiabatic crossing (see discussion of Fig. 2.12 c). Therefore, no perfect matching of the experimental vibrational spacings can be expected. The application of these pulse trains in our coherent control scheme and their experimental realization will be further discussed in Sec. 4.3.1. In the following, the numerical method for the propagation of B state wave packets excited by these pulses and pulse sequences will be introduced.

3.2.2   1st order perturbation theory

Simulation of the B state wave packet dynamics for the gas phase molecule have been performed using an adapted code from Prof. D. J. Tannor [5,208]. It is based on time dependent perturbation theory and uses the first order term in the perturbation series

$$\psi_B(x,t) \;=\; \psi^{(0)}(x,0) \;+\; \psi^{(1)}(x,t) \;+\; \dots, \tag{3.7}$$

where the first order correction reads

$$\psi^{(1)}(x,t) \;=\; \frac{1}{i\hbar} \int\limits_0^t e^{-\frac{i}{\hbar} H_B \cdot (t-t')} \left\{ -\mu_{BX}\, \varepsilon(t') \right\} e^{-\frac{i}{\hbar} H_X \cdot t'} \psi_X(x,0)\, dt' \,. \quad (3.8)$$

It has an intuitively well accessible structure: The initial state is the vibrational ground state $\psi^{(0)}(x,0) = \psi_X(x,0)$ of the electronic ground state X, which is propagated via the time evolution operator $e^{-\frac{i}{\hbar} H_X \cdot t'}$ of the X state until time t'. At t', the transition dipole μ_{BX} and the ultrashort laser pulse $\varepsilon(t')$ couple the two electronic states X and B. The generated B state wave packet is further propagated according to the Hamiltonian H_B until the final time t. An integration over all intermediate time steps t' yields the excited B state wave packet at time t. For practical purposes this integral must be evaluated numerically. We look at the problem from the point of view of its implementation, i.e. given the functions $(\psi_X(x,t), \psi_B(x,t))$. We want to find a realization of the propagation from $t \;\mapsto\; t+dt$ which maps

$$(\psi_X(x,t), \psi_B(x,t)) \;\mapsto\; (\psi_X(x,t+dt), \psi_B(x,t+dt)) \,. \quad (3.9)$$

Then the function $\psi_B(x, t+dt)$ is obtained from one piece which is the results of the propagation of the wave function $\psi_B(x,t)$ at time t with the Hamiltonian H_B and one piece which corresponds to the contribution from the appropriate limit of the integral in eq. (3.8). This reads

$$\psi_B(x,t+dt) \;=\; e^{-\frac{i}{\hbar} H_B\, dt}\, \psi_B(x,t) \;+\; \frac{1}{i\hbar} \left\{ -\mu_{BX}\, \varepsilon(t) \right\} e^{-\frac{i}{\hbar} H_X(t)} \psi_X(x,0)\, dt \,. \quad (3.10)$$

A second significant simplification stems from the fact, that we assume $\psi_X(x,0)$ to be the ground state of the X potential. Then the following identity holds:

$$\psi_X(x,t) \;=\; e^{-\frac{i}{\hbar} H_X(t)} \psi_X(x,0) \;=\; e^{-\frac{i}{\hbar} E_0\, t} \psi_X(x,0) \,. \quad (3.11)$$

So we obtain as an intermediate result the following expression

$$\psi_B(x,t+dt) \;=\; e^{-\frac{i}{\hbar} H_B\, dt}\, \psi_B(x,t) \;+\; \frac{1}{i\hbar} \left\{ -\mu_{BX}\, \varepsilon(t)\, e^{-\frac{i}{\hbar} E_0\, dt} \psi_X(x,t)\, dt \right\} . \quad (3.12)$$

This is actually the mapping of eq.(3.9) we are looking for. We summarize it below:

$$\begin{pmatrix} \psi_X(x,t+dt) \\ \psi_B(x,t+dt) \end{pmatrix} = \begin{pmatrix} e^{-\frac{i}{\hbar} E_0\, dt} & 0 \\ -\frac{\mu_{BX}}{i\hbar}\, \varepsilon(t)\, e^{-\frac{i}{\hbar} E_0\, dt}\, dt & e^{-\frac{i}{\hbar} H_B\, dt} \end{pmatrix} \begin{pmatrix} \psi_X(x,t) \\ \psi_B(x,t) \end{pmatrix} . \quad (3.13)$$

3.2.3   Split operator method

Basically each of the operations in the matrix equation (3.13) is numerically easy to perform with one exception. This is the evaluation of the expression

$$e^{-\frac{i}{\hbar} H_B \, dt} \, \psi_B(x,t) \tag{3.14}$$

because $\psi_B(x,t)$ is not an eigenstate and therefore the propagation operator does not reduce to a multiplication operator as it was the case in eq. (3.11) for the wave function $\psi_X(x,t)$. The evaluation of eq. (3.14) uses the so called Split Operator method. The essential trick is to split $H_B = T + V$ according to a Baker-Campbell-Hausdorff-formula, which reads

$$e^{-\frac{i}{\hbar} H_B \, dt} \;\; = \;\; e^{-\frac{i}{\hbar} \frac{T}{2} \, dt} \, e^{-\frac{i}{\hbar} V \, dt} \, e^{-\frac{i}{\hbar} \frac{T}{2} \, dt} + \mathcal{O}(dt^3) \,. \tag{3.15}$$

The advantage of this type of splitting compared to others also discussed in [5] is a better degree of convergence. Furthermore, in this representation each of the three terms of the product on the right hand side of eq. (3.15) acts as pure multiplication operator on the wave function, when applied in the appropriate Fourier space. To this end, the term containing the potential V is applied in position space while the kinetic term containing T is treated in momentum space. The evaluation works like this

$$
\begin{aligned}
\psi_B(x,t) \quad &\overset{\mathcal{F}}{\mapsto} \quad e^{-\frac{i}{\hbar} \frac{\tilde{T}}{2} \, dt} \left[\tilde{\psi}_B(p,t) \right] \\
&\overset{\mathcal{F}^{-1}}{\mapsto} \quad e^{-\frac{i}{\hbar} V \, dt} \left[e^{-\frac{i}{\hbar} \frac{T}{2} \, dt} \, \psi_B(p,t) \right] \\
&\overset{\mathcal{F}}{\mapsto} \quad e^{-\frac{i}{\hbar} \frac{\tilde{T}}{2} \, dt} \left[e^{-\frac{i}{\hbar} \tilde{V} \, dt} \, e^{-\frac{i}{\hbar} \frac{\tilde{T}}{2} \, dt} \, \tilde{\psi}_B(p,t) \right] \\
&\overset{\mathcal{F}^{-1}}{\mapsto} \quad e^{-\frac{i}{\hbar} H_B \, dt} \, \psi_B(x,t) \,.
\end{aligned}
$$

To evaluate the integral in eq. (3.8) from time 0 to t, this algorithm is iteratively applied for each discrete timestep dt in a time grid $\{ t_k \}_{k=0\ldots n}$ with $dt = t/n$ and $t_k = k \cdot dt$. The Fourier transformations are done by using a MATLAB intern FFT algorithm.

Finally it shall be noted, that the dynamic Fourier method used here is only one among a number of tested numerical possibilities to solve the TDSE for the Hamiltonian considered in this work. Besides, discrete spectral and pseudospectral representations of the Hamiltonian, like e.g. done in the Fourier Grid Hamiltonian method or the DVR (Discrete Variable Representation) are widely used [209, 210], to

name only two. The latter is used, e.g. in the implementation of the "WavePacket"-project, which has been used to benchmark the 1st order propagation considered in this work [211].

3.2.4 Eigenstates of the Morse oscillator

In order to parametrize the gas phase X state potential and the effective B state potentials used in the simulations of wave packet dynamics excited from the X to the B state, measured data have been fitted to the mathematical structure of Morse potentials [83, 86, 166]. The three parameters from which it depends are molecule specific:

- Dissociation energy D

- internuclear distance R_0

- anharmonicity parameter β

The functional shape is given by[3]

$$V(R) \;=\; D \cdot \left[1 - e^{-\beta\,(R-R_0)} \right]^2 \tag{3.16}$$

This Morse function is well suited to describe binding electronic molecular states [86, 212] and has the advantage of analytically constructable eigenstates. Its minimum specifies the equilibrium internuclear distance R_0. For $R \rightarrow \infty$ it asymptotically approaches D. Above the dissociation limit D, scattering states solve the corresponding Schrödinger equation, while the quantized bound eigenenergies read:

$$E_n \;=\; \hbar\,\omega_e \left(n + \frac{1}{2} \right) \;-\; \hbar\,\omega_e\,x_e \left(n + \frac{1}{2} \right)^2 , \tag{3.17}$$

with the dimensionless anharmonicity parameter x_e as given in Appendix A. Expanding the Morse potential for elongations near the equilibrium position R_0 into a Taylor series, i.e.

$$\begin{aligned}
V(R) \;&=\; D \cdot \left[1 - 1 + \beta\,(R - R_0) + \mathcal{O}(\beta^2) \right]^2 \\
&\sim\; D \cdot \beta^2\,(R - R_0)^2 .
\end{aligned} \tag{3.18}$$

immediately displays the harmonic limit for small β parameters, where a harmonic frequency ω_e around the minimum is connected with β and D by $\frac{1}{2}m\omega_e^2 = D\beta^2$. In

---

[3]In the following considerations the abstract coordinate x from eq. (3.1) and following is assumed to denote the internuclear distance R.
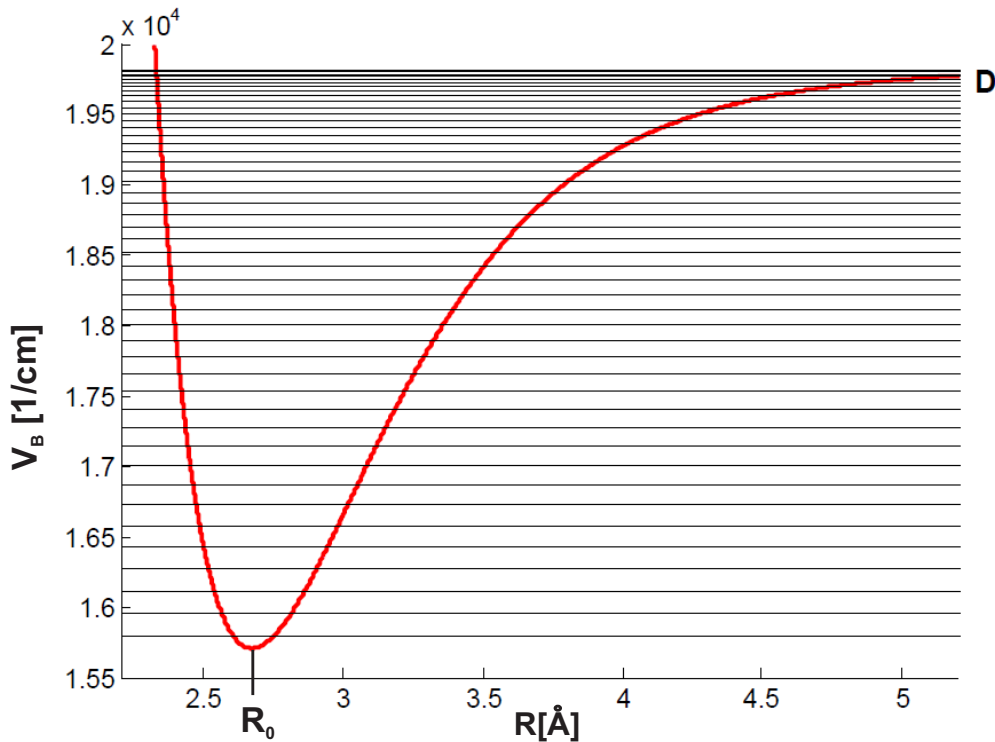
Fig.3.3. Morse potential (red) with bound eigenenergy levels (black) with parameters fitted for the effective electronic B state of Br_2 in solid Ar [83]. R_0 denotes the equilibrium internuclear distance and D the dissociation energy.

Fig. 3.3 the Morse fit of the B potential from [83] is depicted in red. The calculated bound eigenenergy levels, i.e. the vibrational levels in the B state are drawn as black horizontal lines. The anharmonicity causes a decreasing vibrational level spacing with increasing vibrational energy, that is linear in the quantum number n up to the dissociation energy D. According to eq. (3.17) it is given by

$$E_{n+1} - E_n = \hbar\omega_e - \hbar\omega_e x_e (2n + 4) . \tag{3.19}$$

For the matrix potential these spacings have been compared to those of the gas phase molecular B state in Fig. 2.12 c) in Sec. 2.5.3. (Here, for convenience, the spectroscopic notation, which will be used in Chapter 5 is replaced by the more general notation, v'$\rightarrow n$, with quantum number n). The corresponding bound eigenstates are well known from Morse's original work [212] and read

$$\psi_n(y) = \sqrt{\frac{2\lambda\beta n!}{\Gamma(n + 2\lambda + 1)}}\, y^\lambda\, e^{-y/2}\, L_n^{2\lambda}(y) \tag{3.20}$$
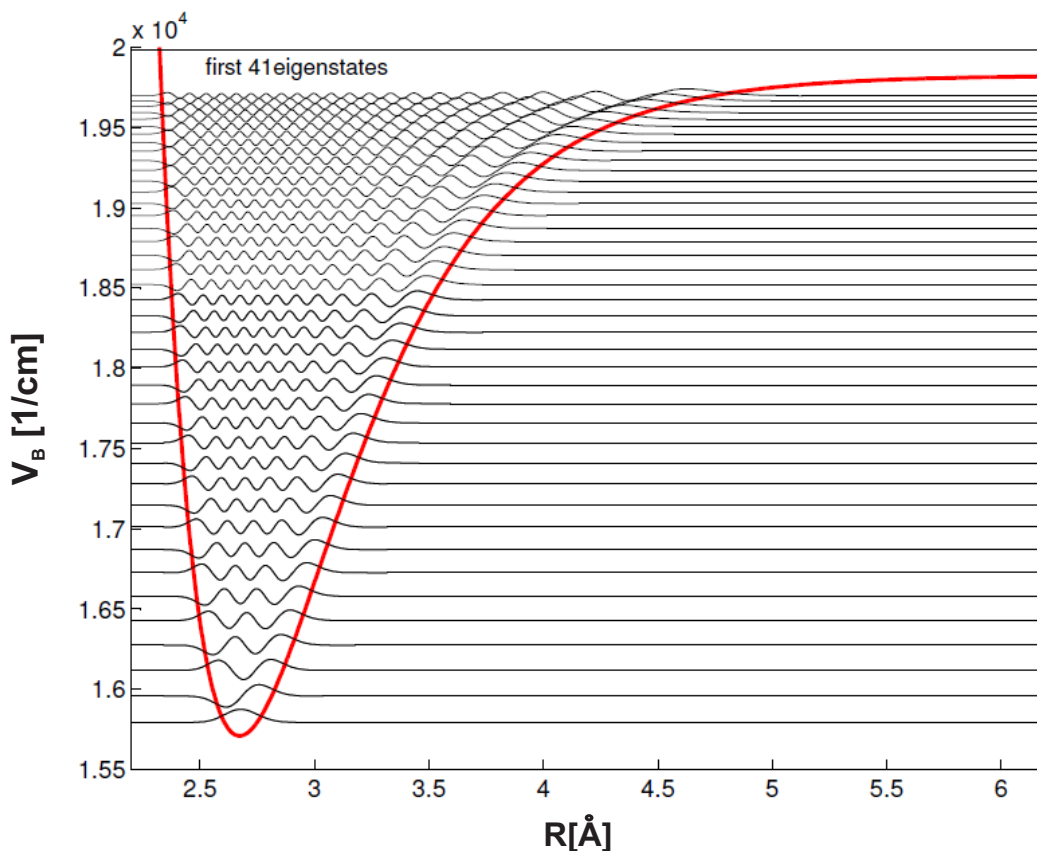
Fig.3.4. The effective B-state Morse oscillator from Fig. 3.3 with eigenstates corresponding to its first 41 vibrational states.

where $L_n^{2\lambda}(y)$ denote generalized Laguerre polynomials. They define the nodal structure of the eigenstates, shown in Fig. 3.4 for first 41 quantum numbers n. The set of the eigenstates of the effective B potential will be used as projectors to construct a spectral representation of excited B state wave packets. A very compact derivation of the eigenstates of the Morse oscillator as they were calculated and implemented in this work will be therefore given in Appendix A, where the definitions of y and λ are introduced, too.

3.3 Representations of wave packet dynamics

Now, the final step needed for the simulation of B wave packet dynamics, i.e. its representation will be introduced. In quantum mechanics, an abstract wave function, like a wave packet defined in eq. (3.1) can be cast in any desired representation of a Hilbert space. Here, we consider the position representation in order to draw an intuitive picture of the probability density of the excited wave packet. An example of a wave packet excitation with a train of ultrashort pulses (see eq. (3.6) and eq.

(3.5), respectively) will be discussed. Finally, the implemented pump probe picture will be introduced.

### 3.3.1   Position space representation

An informative picture of wave packet dynamics is drawn by recording its position density as a function of time, i.e.

$$\rho_B(R,t) \;\; = \;\; |\psi_B(R,t)|^2 \,. \tag{3.21}$$

In Fig. 3.5 a) and b), these densities are shown for the first 2ps of the propagation of a vibrational B state wave packet excited with a train of five ultrashort pulses shown as a green line in Fig. 3.2 a). In these false color plots, the intensity of the B state wave packet decreases from red to blue according to the color sequence of spectrally dispersed white light. Each of the five subpulses excites a particular amount of B state population around the inner classical turning points of the B potential around $4.3a_0$, depicted in Fig. 3.4 ($4.3a_0{=}2.27\text{Å}$). As compared to the intensity distributions from the pulse train (Fig. 3.2 a), for each of the subpulses, population increase takes place during the rising wings of the Gaussian subpulses. During their falling wings, the population decreases. After the termination of the pulse train, at 1.2ps, in Fig. 3.5 a) a significant amount of B state population oscillates between the inner and outer turning points of the B potential at $4.7a_0$ (i.e. 2.49Å) and $5.8a_0$ (i.e. 3.07Å), respectively. These correspond to the B state region around the 9th vibrational level (compare Fig. 3.3). Indeed, the selected excitation pulse carrier frequency ω_F in eq. (3.5) corresponds to the energy difference between the initial state, i.e. the ground vibrational state in the X state and the 9th vibrational level in the B state. Also the vibrational period of 250fs is the correct average vibrational period in this energetic region, corresponding to the separation of subpulses in the train. However, the center of the vibrational B wave packets during excitation is shifted to smaller internuclear distances. The reason is, that the wave packet excitation takes place far away from the Franck Condon maximum, in that sense, the excitation pulses have to force the wave packet in the energetic region selected by the carrier frequency. These observations have been analyzed in detail in the spectral representation and will be presented in Chapter 5.

In contrast to Fig. 3.5 a) in b) no significant amount of population remains in the B state after termination of the pulse train, although during the excitation process, up to 1.2ps, no obvious differences between a) and b) can be seen. Indeed, the intensity distributions of the applied excitation pulse trains as shown in Fig. 3.2 a),
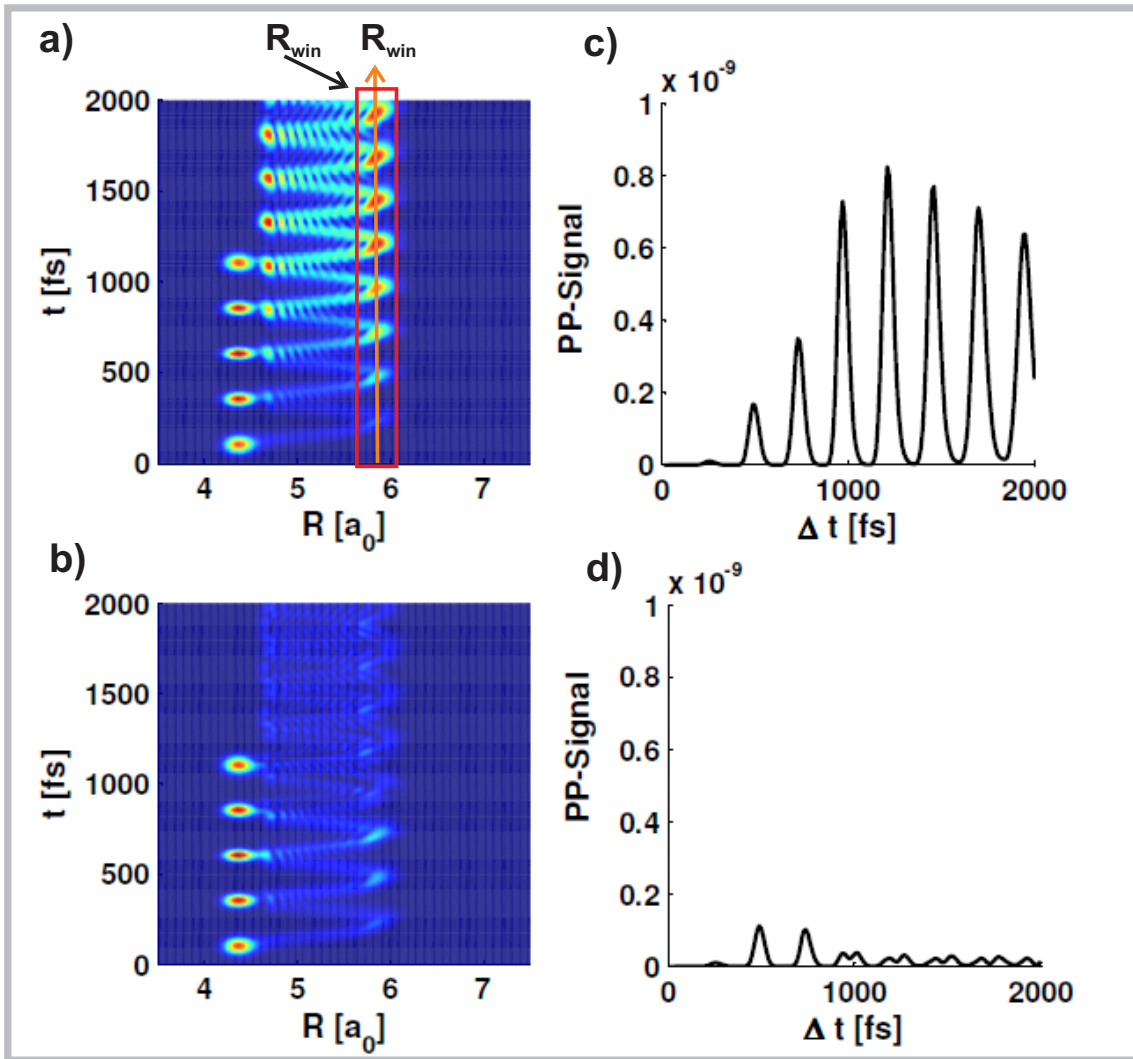
Fig.3.5. a) and b) show position space density functions of the vibrational wave packet dynamics excited from the X to the B state with a train of pulses from Fig. 3.2. c) and d) Simulated pump probe spectra with a Gaussian probe window (position R_{win} and width ΔR_{win} indicated in a). In a) and c) the relative phases of subpulses were set to zero, while in b) and d) respectively, they were tuned to destructive interference.

are the same for both simulations. However, in b) the phase parameters φ^k in eq. (3.5) were different. In a) all phases were set to zero with respect to pulse carrier phase corresponding to ω_F. Therefore, a constructive interference of subsequently excited wave packets can occur during the sequence of the five subpulses. In b), the relative phases of subsequent subpulses were chosen in such a way, as to completely cancel each other and thus lead to destructive interference of the wave packet. The method of wave packet interferometry exemplified here for the two extreme situations

of phases leading to destructive and constructive interference of a molecular wave packet will be applied in the experiments in order to steer the coupling between the B vibrational states and specific phonon modes in the matrix. The adapted experimental mechanism will be introduced in Sec. 4.3.

In the following the pump probe spectroscopy method used in the experiments to monitor the wave packet dynamics and its simulation will be introduced.

3.3.2   Pump probe picture

The basic ideas of pump probe spectroscopy as a method to monitor vibrational wave packet dynamics on the femtosecond timescale are sketched in Fig. 3.6 [41, 213, 214]. The ultrashort excitation pulse/pulse train pumps population from the initial X to the B state and creates the wave packet in the inner wing of the B potential. Around the outer turning point at the B state energy value labeled E_{win}, a second time delayed ultrashort pulse transfers portions of the propagating vibrational B wave packet to charge transfer states, if its average photon energy matches the energy gap between the outer turning point of the B state and charge transfer (CT) states. In the experiments the light induced fluorescence (LiF) from the CT states is then recorded as a function of time delay between pump and probe pulses. The simulation of the probe step is performed by using a Gaussian model probe window in position space. The window is centered at the internuclear distance R_{win} corresponding to the B state potential energy at E_{win}. The pump probe signal is modeled by calculating the spatial overlap of the B wave packet with this Gaussian probe window function as a function of time:

$$S(t) \; = \; \int\limits_{-\infty}^{\infty} |\psi_B(R,t)| \cdot e^{\frac{(R-R_{win})^2}{2\Delta R_{win}^2}} \; . \tag{3.22}$$

R_{win} is also marked in the position density plot of Fig. 3.5 a) by the orange arrow and the width of the probe window ΔR_{win}, i.e. the Gaussian width of the window function is indicated by the red box.

In Fig. 3.5 the corresponding simulated pump probe spectra for the constructive (c) and destructive (d) interference case are shown. According to the density plot in b), when the relative phases of subpulses in the train are tuned to destructive interference, only a weak pump probe signal is observable, almost vanishing after termination of the excitation pulse train. In contrast, the pump probe signal of the constructive interference case in c) monitors pronounced B state wave packet dynamics. It consists of two characteristic processes. In the first part, up
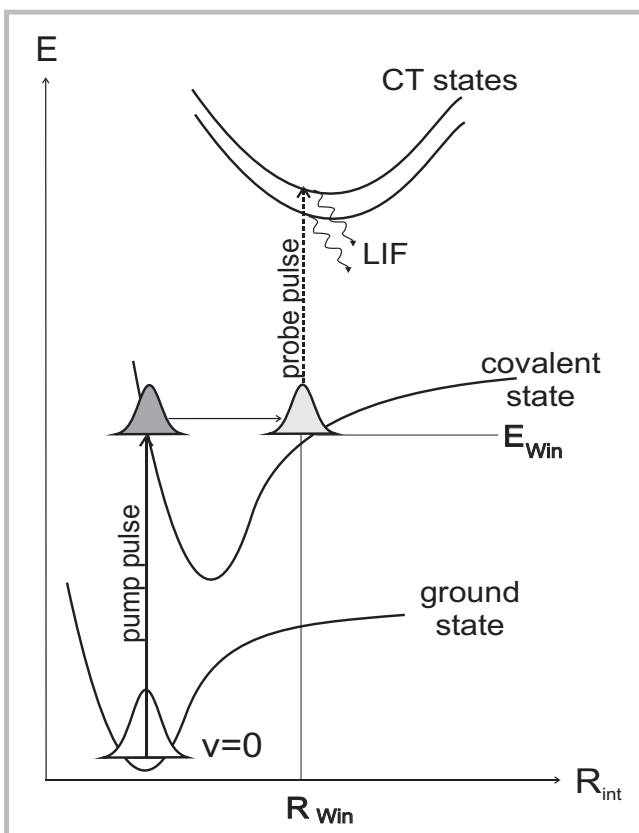
Fig.3.6. Experimental pump probe scheme depicting the excitation of a wave packet around the inner turning point of the covalent B state of Br_2:Ar from the electronic ground state with an ultra-short pump pulse and subsequent probing around the outer turning points with a second time delayed probe pulse to charge transfer states. R_{win} and E_{win} denote the probe position and energy, respectively.

to 1.4ps the interferometric wavepacket excitation process is monitored. With each subpulse the B population is increased. The pronounced maxima are shifted in time by half a vibrational period with respect to the subpulse maxima (compare green line in Fig. 3.2 a). This is the time, the wave packets excited in the inner turning points of the B state needs to propagate into the probe window near the outer turning point. After termination of the train, oscillations with the same period of 250fs occur. At this point, the excitation process is completed, therefore, no population and thus, no signal increase occurs anymore. Instead, a decreased modulation contrast sets in. This is due to a reversible dephasing of vibrational constituent states forming the wave packet. It is caused by the anharmonicity of the B potential, leading to increased vibrational periods of the higher energetic vibrations. In the density plot of Fig. 3.5 a) this dispersion of the wave packet shows up in a tilted, asymmetric spatial-temporal distribution, as compared to harmonic potential wave packets, where the maxima of the probability densities around the turning points would lead to symmetric, elliptical structures. The previous observations are essential in our coherent control experiments and will be therefore further analyzed numerically in Chapter 5. The experimental method for the wave packet intereferometry will be explained in the following Chapter 4.

Chapter 4

Experimental concept and setup

The experiments carried out in this work were all designed as typical pump probe experiments in order to monitor and coherently control vibrational wave packet dynamics on covalent states of Br_2 molecules, coupled to the surrounding Ar lattice. First, a brief overview of the experimental setup will be given. In a next step, the constituent parts of the setup will be treated in more detail. The methods applied for the generation, characterization and tailoring of ultrafast laser pulses will be provided. Polarization sensitive pump probe experiments and their usefulness for decomposing pump probe signals into their contributions from different electronic states will be introduced. The tasks concerning the preparation of clear Br_2 doped Ar crystals and their deposition conditions during the experiments will be summarized. Finally, the idea and concept of our rational coherent control scheme will be presented and related to the available spectroscopic information on Br_2:Ar (summerized in Sec. 2.5).

The experimental setup is shown schematically in Fig. 4.1. The primary light source is a commercial Ti:Sa (titanium sapphire) amplifier which pumps two (or three) non collinear parametric amplifiers (NOPA), one of which, NOPAI acts as a pump pulse, the other one, NOPAII, as a probe pulse. The pump pulse passes a standard pulse shaper unit consisting of a pair of polarizers, gratings and focusing mirrors with a liquid crystal display (LCD) as the active device. The pulse shaping mechanism will be explained in detail in Sec. 4.1.3. In order to compensate and precompensate for the positive chirp due to material dispersion caused by the optical elements and sample chamber window in front of the sample, the pump pulses were compressed by a grating compressor being part of the pulse shaper [89, 215]. Its polarization relative to the probe beam was optionally modified from parallel to perpendicular by a $\lambda/2$ plate. The probe pulses were compressed to a duration being close to the Gaussian limit in a prism compressor (PC) [216]. The spectral profile of pump and probe pulses was measured with a fiber coupled optical multichannel
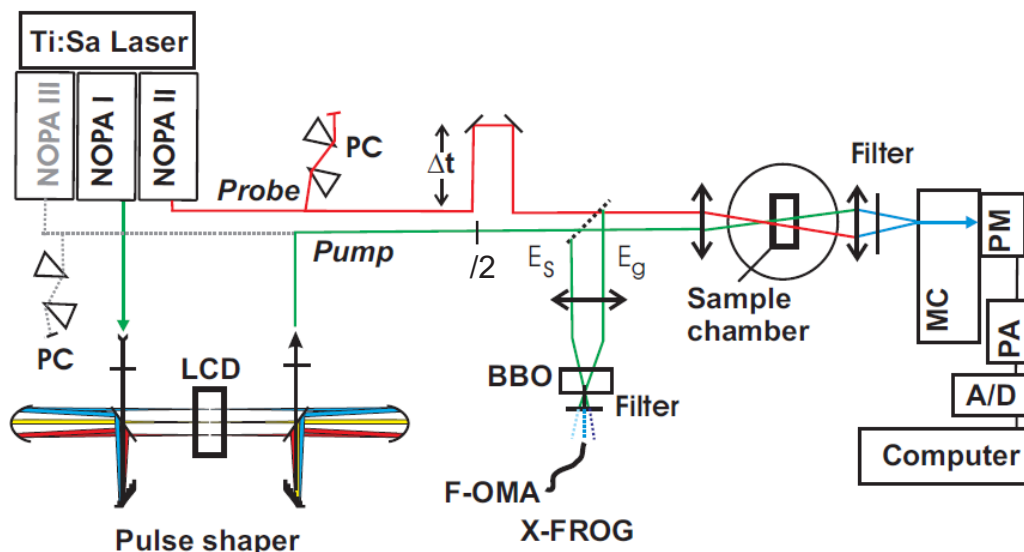
Fig.4.1. Experimental setup for pump probe spectroscopy and coherent control experiments (see text).

analyzer (F-OMA: Ocean Optics 2000). The temporal characterization of the shaped pump pulse was carried out within an X-FROG (Non collinear Frequency Resolved Optical Gating) geometry, by cross correlating the pump beam with the probe beam in a BBO (Beta-Barium Borate) crystal and detecting the phase matched second harmonic [217, 218]. The single short probe pulse serves as a fast gate to record the time dependent amplitude and phase (chirp) in the pulse sequence of the pump beam. The X-FROG setup was also used to predefine the temporal overlap between pump and probe pulses already outside the sample chamber, in order to facilitate the search of the overlap on the sample. To this end, by using a flipping mirror, it was built up with the same optical path length of the pulses to the sample. Finally, both pulses were focused and superimposed spatially and temporally on the sample. In order to control the delay time Δt between pump and probe, the probe pulse passed a delay stage which can be controlled both, electronically and mechanically, and allows for a maximal time resolution of 3fs. After appropriate filtering of the visible beams and stray light from the sample and an additional wavelength selection achieved by a 1/4m single monochromator (MC, Oriel Cornerstone), some of the UV fluorescence signal from the sample was collected by a f=10cm fused silica lens and detected by a photomultiplier (PM), preamplified and subsequently converted from an analog to a digital signal (A/D). Afterwards, in order to minimize electronic noise, the signal was integrated in a boxcar, which was coordinated with the 1kHz repetition rate of the Ti:Sa laser and opened for a duration of 30ns, in accordance

with the fluorescence lifetime. Finally, the pump probe signal was accumulated by a computer as a function of the time delay Δt between pump and probe pulses. The data were recorded with a time separation of 10fs. Each data point was averaged over 3000 or 4000 shots, in order to maximize the signal to noise ratio.

First coherent control experiments, which will be presented in Sec. 6.2, were designed as one-color pump probe experiments and used as the ultrashort pulse source NOPAI for both, excitation and probing. The setup was systematically extended, first by integrating NOPAII in order to allow for a greater wavelength flexibility in the combination of pump and probe and the results will be presented and discussed in sections 6.2.2-6.4.3. Additionally, a third NOPAIII has been integrated into the setup in order to be able to easily switch between coherent control experiments and classical two-color pump probe experiments, without changing the pump wavelength of NOPAI and thereby avoiding a realignment of the shaper setup. Corresponding data are presented in Sec. 6.1 and Appendix B.

4.1 Generation of ultrashort laser pulses and pulse sequences

Now the experimental method for generation and manipulation of ultrashort laser pulses will be provided. The CPA system will be explained briefly and for further details the reader is referred to the standard literature [219–222]. The guiding ideas of optical parametric amplification can be found in [223–226]. The NOPA setup used in our experiments will be presented in Sec. 4.1.2. In Sec. 4.1.3 an overview of the applied pulse shaping technique will be given. The setup was build up first by H. Ibrahim with my assistance and a more detailed overview can be found in [89].

4.1.1 The chirped pulse amplifier system

The femtosecond laser system pumping the NOPAs was a commercial Ti:Sa regenerative amplifier (Clark-MXR, CPA 2001). In the first experiments, it was seeded by an integrated erbium doped quartz fiber oscillator, which generates the ultrashort pulses and emits at 1550nm. The short pulses are generated by passive mode locking. They are frequency doubled to 775nm and positively chirped in a stretcher to a duration of some ps, in order to protect the optical components from high intensity damages [227–229]. In a regenerative amplifier consisting of a cavity and the Ti:Sa crystal as active medium, the stretched pulses are amplified. The pump laser is a Q-switched frequency doubled Nd:Yag (neodymium doped yttrium aluminium garnet) laser working at 1kHz repetition rate. The amplified pulses are switched out

by a Pockels cell and are recompressed by gratings to an output duration of 110fs. The pulses are emitted at a 1kHz repetition rate and are linearly polarized, parallel to the optical table.

For the last experiments, the internal fiber oscillator was replaced by an external fiber oscillator (IMRA femtolite 780) providing higher seed intensities. The replacement led to a better output stability with pulse-to-pulse fluctuations reduced from above 5 percent to 1 percent. The power was increased from 900mW to 1W. The central wavelength of 775nm, the width of 8nm and the corresponding duration of 110fs remained.

4.1.2   Noncollinear parametric amplifiers

Parts of the fundamental of the Ti:Sa laser (Clark-MXR CPA 2001) were used to pump the three non collinear optical parametric amplifiers (NOPAs in 4.1). The generation of the ultrashort NOPA pulses involves nonlinear optical processes [221, 222, 230]. In Fig. 4.2 the setup used for our experiments is depicted. It consists of three parts, (1.) the white light generation for seeding the NOPA, (2.) the frequency doubling of the fundamental for generating the pump light and (3.) the parametric amplification [223, 231]. For the seed light generation 4% of the incoming fundamental is reflected by a beam splitter BS and focused by a lens L1 into a 1mm thick sapphire plate. Here, a strongly positively chirped whitelight continuum is generated. This high order optical process is very sensitive to the incoming pulse intensity which is regulated together with the beam profile by a gray wedge G and an aperture A, respectively. The remaining fundamental light is filtered out by a glass filter F. A second lens L2 regulates the focusing of the seed in the amplifier crystal BBO2 via aluminum coated mirrors M1 and M2. For the pump light generation in step (2.), the remaining fundamental light (around 150 μJ) transmitted by the beam splitter BS was directed via mirror M3, after passing a retroreflector RR, to a telescope setup consisting of two lenses L3 and L4. It narrows the beam diameter before reaching the SHG (second harmonic generation) crystal BBO1, where under the right phase matching angle, the fundamental is frequency doubled to 387.5nm in a second order optical process. Finally, in step (3.), pump and seed are overlapped spatially under a non collinear angle in a second BBO crystal BBO2. The noncollinear angle is generated by a vertical tilt of mirror M4, such that the second harmonic reaches M5 and the overlap with the seed in BBO2 from below. In order to realize the parametric amplification, an overlap of the two beams in time domain is required, as well. It is controlled via the retroreflector RR which is mounted on a μm-delay stage. Since the whitelight is chirped positively, its red components advance
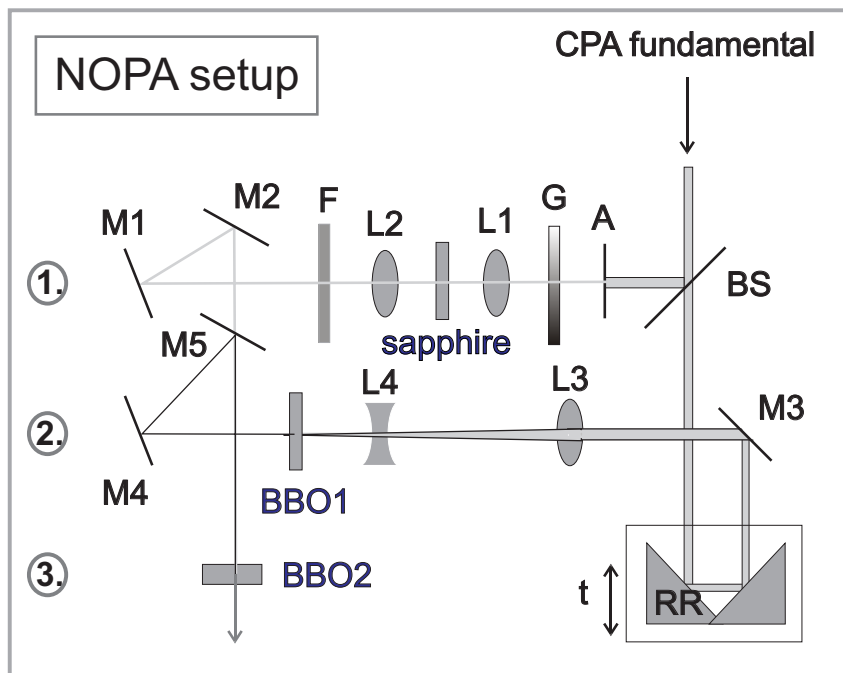
Fig.4.2. Schematic setup of the noncollinear optical parametric amplifier consisting of the three main parts: (1.) seed light generation, (2.) pump light generation and (3.) parametric amplification [88, 223, 232]. (See text for details.)

the blue ones, and the time overlap controlled via the delay stage defines the central wavelength of the amplified light. For maximally effective amplification of a chosen central wavelength, the right phase matching angle has to be adjusted at BBO2 in order to reassure momentum conservation for a great number of photons created in the parametric process. The three NOPAs used in our experiments are tunable between 460-650 nm and deliver typically 50 fs pulse duration with 5-7 μJ per pulse. For the coherent control experiments, short probe pulses centered at 590nm were used. For the excitation pulses, central wavelengths between 590-570nm and durations up to 80fs turned out to be appropriate, which will be further motivated in Chapters 5 and 6, respectively.

4.1.3 The pulse shaper unit

Among the wide range of possibilities for tailoring ultrashort laser pulses, their modulation by computer controlled liquid crystal arrays was chosen in our experiments [233–235]. The pulse shaper unit consists of two parts, a 4f-setup and the spatial liquid crystal modulator (SLM), which are depicted in Fig. 4.3. The 4f-setup allows for an optical forward and subsequent backward Fourier transformation (FT) of the incoming light pulse from time to frequency domain and vice versa.
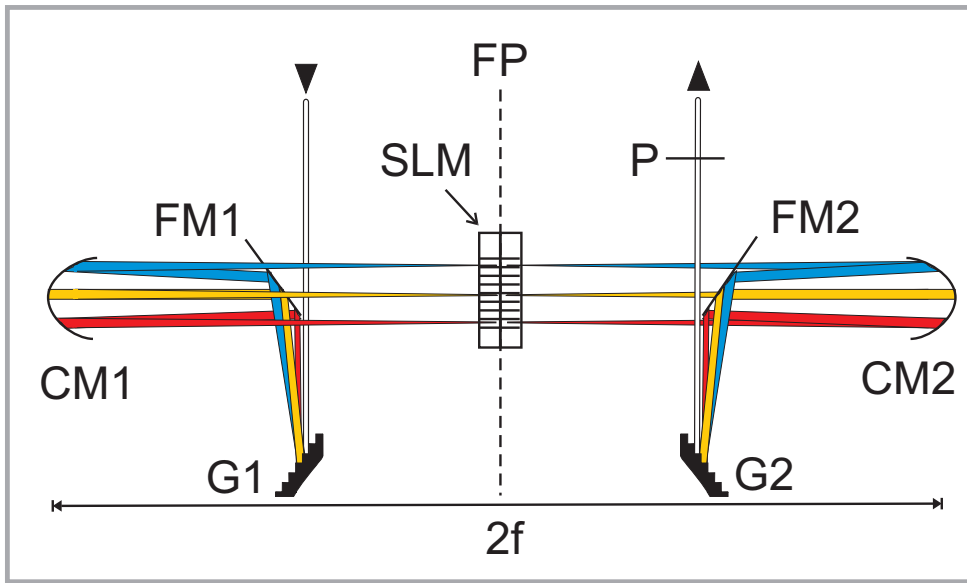
Fig.4.3. Symmetrical 4f-setup consisting of two gratings G1 and G2, focusing mirrors CM1 and CM2 and folding mirrors FM1 and FM2, realizing optical Fourier transformation of a NOPA pulse from time to frequency domain and back transform into time domain). The frequency modulation takes place in the Fourier plane FP, where a spatial liquid crystal modulator (SLM) as the active device is placed [233, 234]. (See text for details.)

The spectrally broad incoming pulse is dispersed by a grating G1 (2000l/mm), which is located in the focal plane of a cylindrical mirror C1 (f=13cm) where it is reflected by a folding mirror FM1 after spectral dispersion. Concerning the height, the cylindrical mirror is optically inactive, thus, it is vertically tilted, such that the dispersed beam passes above FM1 and its spectral components are focused in the Fourier plane FP, where the pulse modulation takes place. A second cylindrical mirror CM2, positioned one focal length away from the Fourier plane in a symmetrical geometry, focuses the dispersed components onto a grating G2, identical to G1. Now, the vertical tilt of CM2 was chosen such, that the second folding mirror FM2 and grating G2 are reached by the beam again parallel to the optical table, however, now in a greater height as compared to the incoming beam. This tilted geometry leads to a tilted Fourier plane in height with respect to the plane perpendicular to the optical table. On grating G2 the spectral components are merged again spatially and a spatial chirp of the outcoming beam is eliminated. However, besides of the function of the 4f-setup as a zero dispersion compressor, we used the setup to compensate and precompensate for temporal positive chirp
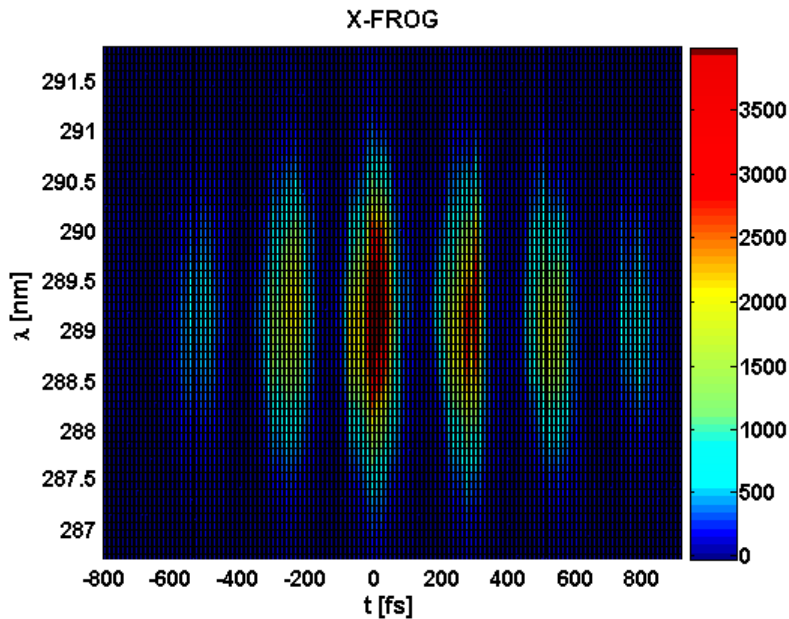
Fig.4.4. X-FROG trace of a pulse train generated in the pulse shaper unit depicted in Fig. 4.3.

of the NOPA pulse originating from other optical components. To this end, the distance of grating G2 from the Fourier plane was slightly enlarged from 2f. This way, the setup acted as an additional grating compressor in order to avoid intensity losses by an additional prism compressor. As a result, the spatial chirp of the outcoming beam could not be eliminated completely, was however negligibly small. In order to complete the shaping process, a polarizer P acts as an analyzer and filters out the spectrally chosen amplitude components of the pulse. As the active device of the pulse modulation process, a liquid crystal spatial light modulator (LC SLM type CRI-SLM-256-GPIB) is placed in the Fourier plane [64, 234, 236]. It consists of two LC arrays, each with 128 pixels of 97μm width separated by 3μm wide gaps. Liquid crystals are nematic, birefringent crystals consisting of rodlike molecules oriented along the optically active extraordinary axis. By a variable voltage connected to the LC arrays the original orientation of the molecules and the extraordinary axis is tilted. This way, the polarization of electric field components of an incoming electric field, originally polarized parallel to the optical table, is changed. Thus, the arrays act as electrically variable wave plates. The analyzer P is finally responsible for the filtering.

Exemplarily, the temporal structure of a pulse train generated by amplitude shaping in the just described setup is shown in Fig. 4.4. It depicts the X-FROG trace recorded by cross-correlating the shaped pulse with a 50fs short gate pulse in a BBO crystal and recording the spectral intensity of the sum frequency with a fiber spectrometer as a function of time delay between pulse train and gate pulse. Its temporal structure represents a reference for the simulated pulse trains in Fig. 3.2 used for the numerical studies. High accuracy measurements of the temporal
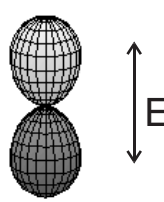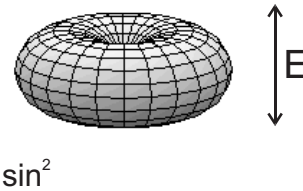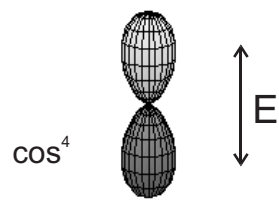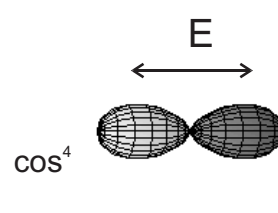
structure of pulse trains will turn out to be also indispensable for separating inco-
herent contributions from coherence terms in our control spectra in Sec. 6.3 and for
the identification of predissociated parts of wave packets in Sec. 6.4. The intensity
distribution among the subpulses is used as a reference to estimate the amount of
incoherent accumulations in the wave packet interferometric pump probe spectra.

4.2   Pump probe experiment

Our control experiments with ultrashort pulse trains were all designed as pump
probe experiments based on the pump probe scheme introduced in Sec. 3.3.2. With
this method, we monitored wave packet dynamics on different covalent states of
Br_2 in solid Ar. In order to assign the observed wave packet dynamics to different
electronic states, we varied the relative polarizations of pump and probe pulses. The
guiding ideas of polarization sensitive pump probe spectroscopy will be summarized
in the following Sec. 4.2.1. By increasing the number of performed measurements
with different relative polarizations, the continuous cooling time for stable samples
was increased, as well. The tasks concerning high quality sample preparation and
long time deposition will be provided in Sec. 4.2.2.

4.2.1   Polarization sensitive pump probe spectroscopy

Polarization sensitive pump probe spectroscopy is based on the rules of photose-
lection [237–239]. In the Schwentner group, e.g., the method has been applied to
measure ultrafast depolarization of matrix isolated light ClF molecules [148, 240].
For the case of heavier matrix isolated I_2 and also Br_2 molecules a reorientation
of molecules could be shown to be negligible on the ultrafast timescale [88] since
rotations are hindered by the matrix atoms. To this end, the method can be used
to decompose the pump probe spectra into contributions resulting from excitation
of different electronic states. In the excitation region selected for our control exper-
iments, dipole transitions from the electronic ground state to the covalent A and B
states occur, according to the absorption spectrum from Fig. 2.9 in Sec. 2.5.1. The
molecule Br_2 follows Hund's case c and the angular momentum quantum number
Ω is only allowed to change by $\Delta\Omega = 0, \pm 1$ (see e.g. [86]). In the surrounding of
matrix atoms, the Br_2 molecular axes are fixed and in general randomly oriented
in the sample. Thus, linearly polarized excitation pulses and pulse trains, respec-
tively, select an ensemble of excited molecules in the electronic B state in a $\Delta\Omega = 0$
transition. According to the transition dipole matrix element, such an excitation
with linearly polarized pulses selects a $\cos^2\theta$ distribution of excited molecules with

a) Pump	b) two-photonic probe	
B state =0 $\cos^2$	parallel	perpendicular
	$S_0{}^{\parallel}=5$	$S_0 =1$
A state: =1 $\sin^2$	$\cos^4$	$\cos^4$
	$S_1{}^{\parallel}=1$	$S_1 =3$

Fig.4.5.   a) Dipole excitation of samples consisting of randomly oriented Br_2 molecules with orientations fixed by the matrix atoms spanning an angle θ with the direction of a linearly polarized excitation field E, selects ensembles of $\cos^2\theta$ and $\sin^2\theta$ molecular distributions in case of $\Delta\Omega = 0$ and $\Delta\Omega = 1$ transitions, respectively. (b) Their overlap with $\cos^4\theta$ distributions belonging to a two-photonic probe step, yields relative contributions of the two different contributions from A to pump probe signals $S_{0,1}{}^{\parallel}$ with parallel and $S_{0,1}{}^{\perp}$ for perpendicular relative orientations of pump and probe pulse polarizations.

a parallel orientation with respect to the electric excitation field direction, with θ being the angle between the electric field direction and the internuclear molecular axis, as indicated in the first row of Fig. 4.5 a). In the second row, the case of a $\sin^2\theta$ distribution belonging to an A state excitation in a $\Delta\Omega = 1$ transition is displayed. In the experiments a linear superposition of both transitions is selected. The probing of the covalent wave packet dynamics goes to charge transfer states according to the pump probe scheme of Fig. 3.6. Thus the probe step is a parallel, $\Delta\Omega = 0$ transition involving a charge separation between the Br atoms. Because in this work two-photonic probe steps with visible probe pulses have been carried out, an even sharper $\cos^4\theta$ distribution is selected in the probe step. By changing the relative polarization of excitation pulses with respect to the probe pulses from parallel to perpendicular, the relative contributions of the A and B state molecules to the corresponding pump probe signals $S_1{}^{\parallel,\perp}$ and $S_0{}^{\parallel,\perp}$ can be determined, respectively. The results from the relative overlap of normalized pump distributions

with probe distributions are collected in Fig. 4.5 b). In case of parallel probe and pump orientations, the B state contributions to the signal are five times stronger than those from the A state (left column of Fig. 4.5 b), while in the perpendicular a three times larger A state contribution dominates the pump probe signal (right column). These ratios predicted by photoselection rules for an idealized model of a non-depolarizing sample consisting of an ensemble of randomly oriented molecules served as a testing ground for our decomposition method of measured signals into the A and B state contributions. The results of these decompositions will be presented in detail in Sec. 6.1.1. It will be demonstrated, that this simple model predicts the measured relative contributions with high accuracy. Besides of the variation of relative polarization we also varied the fluorescence wavelength of UV signals by considering signals from different emission bands, as already mentioned in Sec. 2.5.2. We were able to measure the B state dynamics without contributions from the A state molecules, by reducing their probe efficiency to a negligible amount in detection. This allowed for an independent determination of relative weights of A and B contributions in the combined spectra, well matching the values collected in Fig. 4.5 b). This agreement supports on the one hand our decomposition method relying on both polarization and detected fluorescence band variation. On the other hand, it shows, that photoselection rules can be applied as a tool to decompose the involved molecular dynamics in different electronic states for molecular ensembles with blocked rotational degrees of freedom. In our case of a combined signal consisting of $\Delta\Omega = 0$ and $\Delta\Omega = 1$ transitions the relative polarization variation leads to a set of equations for the A and B contributions

$$
\begin{aligned}
A &= \frac{1}{14\alpha} \cdot \left(3\, S^{\parallel} - S^{\perp} \right) \\
B &= \frac{1}{14\beta} \cdot \left(5\, S^{\perp} - S^{\parallel} \right) ,
\end{aligned}
\tag{4.1}
$$

that follows when including the relative weights from Fig. 4.5 b) in the pump probe signals:

$$
\begin{aligned}
S^{\parallel} &= S_1{}^{\parallel}\, \alpha\, A + S_0{}^{\parallel}\, \beta\, B \\
S^{\perp} &= S_1{}^{\perp}\, \alpha\, A + S_0{}^{\perp}\, \beta\, B .
\end{aligned}
\tag{4.2}
$$

In order to keep the equations on a general level at this point and allow to take into account different probe sensitivities for the A and B state molecules, the parameters α and β have been included. However, they turned out to be close to unity, which will be shown in Sec. 6.1.1.
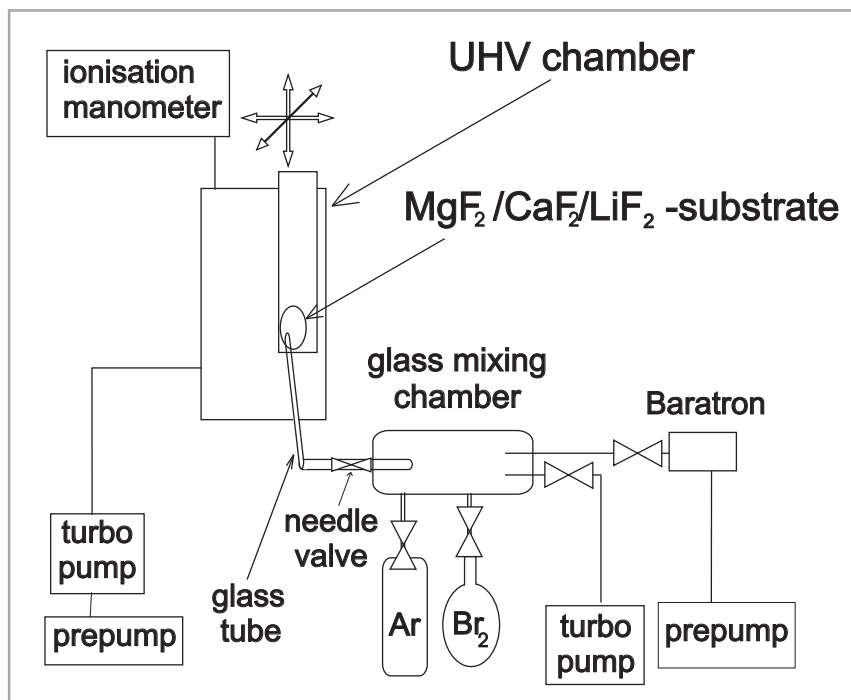
Fig.4.6. Sample deposition chamber displaying the setup built up in [88] (see text).

4.2.2   Sample preparation and cooling

The polarization sensitive measurements with varying fluorescence wavelengths had
to be carried out under identical conditions concerning both, the laser system and
the sample. Thus, high quality crystals had to be prepared and kept stableized for
several days in order to allow to record complete and comparable data sets. The
Br_2:Ar setup build up by M. Gühr has been adapted to the new requirements. In
Fig. 4.6 the sample preparation and deposition chamber, as it was build up in [88]
is sketched. (A more detailed description can be found in [88].) It consists of two
main parts, a mixing chamber and an UHV (ultrahigh vacuum) cryostat chamber.
Since Br_2 corrodes stainless steel, the whole mixing apparatus, seals and transfer
tubes were made of glass, teflon and viton. In a glass vessel, gaseous Ar (99.9999
% purity, Linde) and Br_2 with isotopomers in natural abundance (purity 99.99 %,
Sigma Aldrich) were mixed at room temperature in concentrations between 1000:1
and 500:1. Before preparation of the gas mixture, the glass mixing chamber, as well
as the Br_2 containing glass vessel were evacuated by a turbo pump to 10^{-7}mbar.
To this end, the bromine liquid, having a vapor pressure of 200mbar at room tem-
perature, had to be frozen with liquid nitrogen during the cleaning process. The
concentrations were prepared in two steps, controlled by measuring the pressure

Fig.4.7. Photo showing a 250l liquid He tank (right) used for long time stabilization of the samples together with the earlier used typical 100l tank (left) during refilling by a coworker of the Low Temperature Laboratory of the Institute for Experimental Physics. (Many thanks to Mr H. Streuber, Mr C. Christiansen and to Mr R. Matte for the strong support.)

inside the mixing chamber with a baratron while Ar and Br_2 were induced, respectively. To avoid excessive contact with Br_2, the baratron could be separated from the mixing chamber by a glass valve and connected to the prepump. Finally the gas mixture was sprayed on a cooled substrate in the cryostat chamber. The gas flow was regulated by a needle valve placed between the glass chamber and a glass tube connecting to the cryostat chamber. The glass tube is positioned around 5cm in front of the sample during the crystal growth. To allow for a variable positioning of the sample, the cryostat was placed on an UHV manipulator, hand movable from outside the chamber in all three space dimensions. During the gas flow a vapor pressure of $5 \cdot 10^{-5}$mbar measured by an ionization gauge inside the UHV chamber, was kept constant. Around 70 μm thick, rather clear polycrystalline films were grown this way within 3 hours on MgF_2/CaF_2 or LiF_2 substrates placed on the copper rod of a liquid He flow cryostat kept at 20K (in case of MgF_2/CaF_2 substrates) or 10K (for LiF_2) during preparation and cooled to 6K for the measurements. The actual temperature of the sample was measured by a temperature diode connected to the copper rod on the cryostat and controlled by regulating the liquid He flow and an additional electric heating during sample preparation. Since the MgF_2 substrates used in the first coherent control measurements are birefringent, they destroy the linear polarization of laser pulses. Therefore, it has been replaced by a LiF_2 substrate, which has a simple cubic crystal structure, like the CaF_2 substrate originally used in [88] (see also Chapter 6).

Finally, to obtain one complete set of measurements, the sample had to be kept at 6K for around 40h. To this end, a $100l$ liquid He tank used for the cooling of the substrate in the first control measurements has been replaced by a $250l$ tank, which is shown in Fig. 4.7. This allowed for a stabilization of the sample for up to 4 days . This way, reference measurements could be carried out during the recording of spectra with varying parameters, in order to cross check required laser setup stabilities. In case of instabilities, complete sets could be repeated and reproduced, with the same sample, respectively. In the following section the guiding ideas of our coherent control scheme applied to Br_2:Ar will be introduced. Pulse trains with different relative phases between the subpulses will turn out to be the key tools in steering the coupling of molecular vibrations to different phonon states of the matrix. This increased number of parameters to be varied in independent measurements, enforces the necessity of long time sample cooling.

4.3 Coherent control experiment

Intuitive coherent control scenarios were first introduced in 1986 by theoretical chemists [52,63] and experimentally realized for diatomic gas phase molecules [241–243]. In the Brumer-Shapiro-scheme two-path interferences analogous to Young's double slit experiments are induced by controlling the relative phases between two CW (continuous wave) laser pulses in order to steer the excitation coefficients of a final electronic molecular superposition state. [52]. In the Tannor-Rice-Kosloff or pump-dump scheme an initially excited molecular wave packet is transferred to another electronic state by a second time delayed laser pulse in a multiple-slit-like interference process [63,242]. Chirped pulse excitations were proposed by Ruhmann and Kosloff to manipulate vibrational wave packets and were applied, e.g. also in our working group [92,198,244,245]. These intuitive schemes have been developed further and led to experimental realization in nowadays widely used closed loop experiments [58,246]. While the original intuitive schemes were most often used for control of relatively simple systems, closed loop experiments are favored for more complex and also biologically relevant systems. In our case an intuitive scheme is tailored for a combined diatomic-solid state system which will be described now.

4.3.1 Rational control scheme

In order to control the coupling of vibrational B state wave packets to the phonon modes of the surrounding Ar matrix, an excitation method allowing for a sharp spectral selection is necessary. On the one hand, the creation of a vibrational
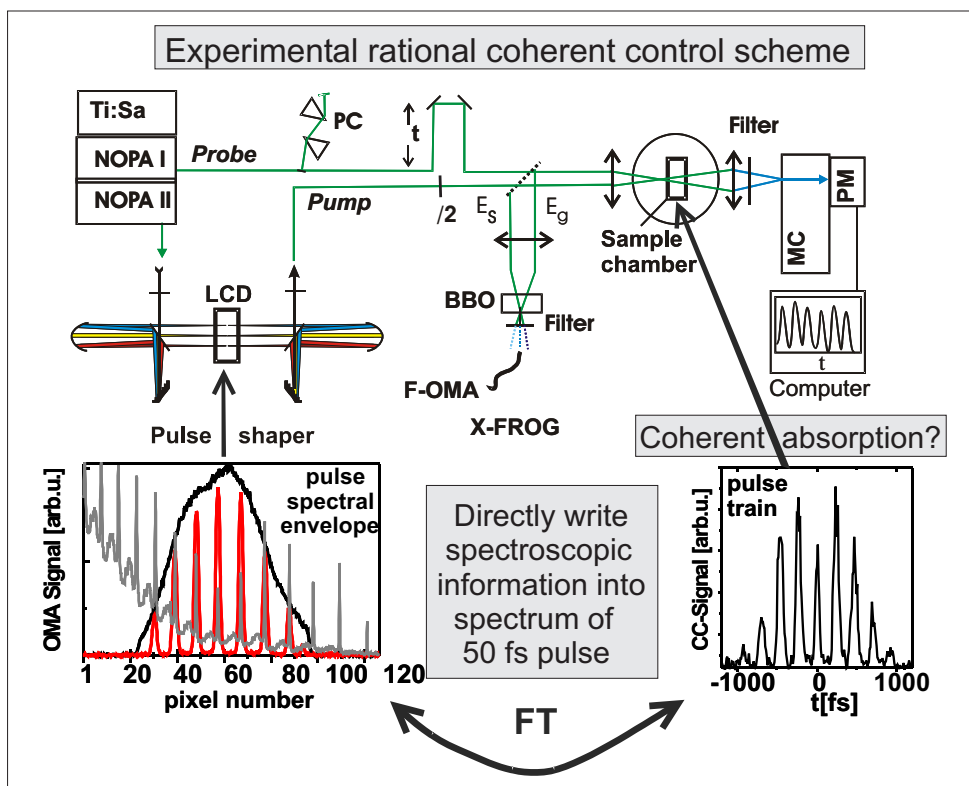
Fig.4.8. Experimental setup including the guiding ideas of our rational coherent control scheme. The spectroscopic information contained in the excitation spectra from [83] is pixel by pixel, directly written into the spectrum of an ultrashort laser pulse on a liquid crystal display (LCD) placed in the Fourier plane of a pulse shaper setup. By pure amplitude filtering, the Fourier transformed pulse in the time domain has a pulse train structure measured in cross-correlation with a short gate pulse. If the whole pulse train is absorbed by the sample in a phase-stable way, the sharp spectral features selected from the excitation spectrum develop in the constituent states forming the excited vibrational wave packet. The coherent absorption requires preservation of electronic coherence for at least up to 1.5ps.

superposition state of molecular and lattice vibrations requires a spectrally broad excitation. These seemingly contradictory requirements can be achieved by excitation with a sequence of ultrashort pulses, where each subpulse in the train is short, thus, spectrally broad enough to prepare vibrational wave packets. On the other hand, the wave packets created by time delayed, phase controlled subpulses, interfere with each other in such a way, that sharp spectral features can develop in the course of time. To achieve the desired spectral selection of specific phonons coupling to the molecular vibrations, we make use of the spectroscopic information contained in the excitation spectra (introduced in Sec. 2.5.3). They contain all necessary

information about spectral positions of zero phonon lines (ZPL) and combined excitations of the chromophore's B state vibrations with Ar lattice phonons within the phonon sidebands (PSB). The positions of ZPL and their spacing, respectively, already reflect matrix induced potential energy changes and nonadiabatic crossings with dissociative states. Therefore, directly writing the spectral features into the spectrum of an ultrashort laser pulses allows to select out the desired superposition states in excitation and no further optimization of excitation pulses is necessary. Furthermore, an intuitive interpretation of the temporal structure of the excitation pulse trains created this way and their action on the combined chromophore-bath system is provided within this control scheme. The experimental realization of this control scheme is sketched in Fig. 4.8. The desired spectral features in the excitation spectra are directly selected out from the broad spectrum of a NOPA pulse by pixelwise amplitude filtering of the unwanted features in the pulse shaper. This way, we generate sharp spectral combs reflecting the vibrational spacing in the exciation spectra (shown in red on the left side bottom of Fig. 4.8). After the spectral filtering, the pulses are back-Fourier transformed into time domain by the second grating and their temporal structure is measured by X-FROG. The resulting time domain intensity distribution is a pulse train (right side, bottom of Fig. 4.8) consisting of five strong subpulses. They are separated by the average vibrational period determined by the average spacing of teeth forming the corresponding spectral comb. The pulse train is finally sent on the sample to excite the selected spectral superposition state. In order to achieve this, the whole phase-stabilized pulse train has to be absorbed by the Br_2:Ar system in a coherent way. Only if the time domain phase information is transferred and preserved in the system during excitation, the dynamically evolving interference processes lead to the desired spectrally structured absorption according to the spectral combs measured with the fiber-spectrometer. This, however requires not only vibrational but especially also electronic coherence to be preserved during the excitation process (see Sec. 3.1.2). The spectral sharpness of ZPLs already indicates electronic coherence times of around 1ps in this spectral region, just fulfilling the requirements of our control scheme (compare Fig. 2.12 a). The necessity of applying such long pulse trains, consisting of more than 2 subpulses has been already mentioned in Sec. 3.2.1 and will be explained in detail in the following part.

4.3.2   Wave packet interferometry with two and more pulses

We started the measurements in a systematic way with first generating double pulses in the pulse shaper to display the trend [188]. The two pulses were separated by the average vibrational period in the B state and led to an interference of two vibrational
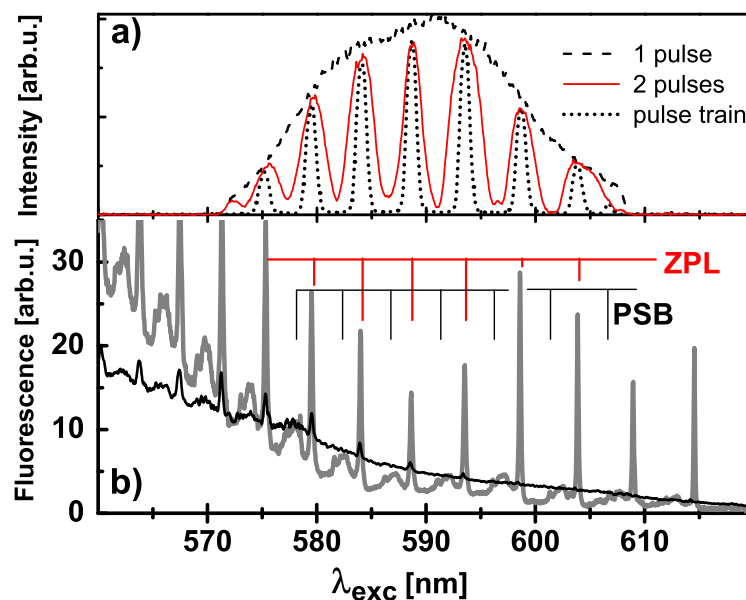
Fig.4.9. a) Spectral representation of a single pulse (dashed line), two pulses (solid line) and a pulse train (dotted line) matching the ZPL. b) Excitation spectrum of the B state (thick gray line) and the A' state (thin black line) with indicated positions of the ZPL and the PSB [188].

wave packets. Programming the ZPL center positions with a sinusoidal amplitude modulation and appropriate phases into the LCD leads to the two-pulse spectrum shown as solid line in Fig. 4.9 a). Programming sharper ZPLs with a period of 3 open ZPL pixels and around 14 closed pixels between the ZPL leads to the dotted comb with a ZPL contribution now well separated from PSB. This comb can be tuned to ZPL, PSB and also to the low intensity intervals just in front of ZPL, called "A" position in the following. In this way, well defined wave packets with the underlying Br_2 vibrations decoupled or coupled to the lattice phonons are prepared. The shift of the comb from the ZPL position to spectral positions covering parts of the PSB or the "A" position are shifts in frequency domain. According to the rules of Fourier transformation they correspond to phase shifts of the subpulses in time domain. The resulting pulse sequences in time space and their phase distributions will be analyzed at the end of this section.

In 4.9 b), the excitation spectrum of the A' fluorescence (already discussed in Fig. 2.14) is shown as black solid line. It is similar to an absorption spectrum and shows the dominating A state continuum excitation with hardly discernible small spikes from the weak, however well resolved B state vibrational progression. The small fraction of B state population surviving matrix induced predissociation relaxes to B(v'=0) from where it radiates well separated from A and A' fluorescence. There-

fore, in the B-state excitation spectrum shown in gray, the A background is suppressed. Exclusively the B state vibrational progression is obtained with sharp ZPLs, blue shifted broad PSBs and an accumulated MPB (multi-phonon background) at shorter wavelength, as discussed in detail in Sec. 2.5.3. The dashed line in Fig. 4.9 a) shows the spectral envelope of one unshaped pulse after passage of the fully transmitting pulse shaper unit. This allows for amplitude and phase shaping. For the pulse train experiments only amplitude shaping is applied by keeping the phase retardances of the sum of both arrays fixed and varying only the differences. The phase-voltage calibration was adapted for each pixel and a contrast of 200:1 was achieved for transmission maximum to minimum. The whole unit covers a spectral range of 40nm and each pixel corresponds to 0.3 nm (see also discussion of Fig. 4.3). For single pulse experiments all pixels were set to full transmission (dashed envelope in Fig. 4.9 a). Programming of double pulses was started with a sinusoidal pattern and optimization of phase and amplitude to achieve spectral coincidence of the shaped spectrum with the excitation spectrum (solid comb in Fig. 4.9 a). The spectral sharpness of the comb indicates that selection is possible with two pulses, but the spectral resolution is not sufficient to separate ZPL and PSB contributions. For the pulse train, the ZPL comb was programmed (Fig. 4.9 a) dotted comb) as an exact copy of the excitation spectrum and then shifted to PSB and "A" positions. It leads to five strong pulses in time frame. We want to point out again, that despite the exclusive amplitude shaping in frequency domain the pulse train acquires the necessary relative phase pattern in time domain, which will be derived later on.

Now, pump probe spectra resulting from the single and double pulse spectra with the corresponding combs from Fig. 4.9 a) will be discussed [188]. In Fig. 4.10 a) the result of a typical pump probe experiment with 590nm single pump and probe pulses detected at 322nm fluorescence wavelength is shown. The first two pronounced peaks are marked by A1 and A2 since they originate from a wave packet in the A state. A detailed explanation of the A state dynamics will be provided in Sec. 6.1. Simultaneously to the A state, a B state wave packet is excited. It oscillates with a period of 250 fs and it should be seen once per roundtrip in its probe window. Indeed, a progression of 5 recurrences can be identified in Fig. 4.10 a) as marked by ticks labeled B. Oscillations 1 and 3 coincide with A1 and A2 and are hardly visible in these strong A peaks. The second one is marked with B. The weakness of the B amplitude compared to A is consistent with the small B contribution to the absorption (compare A' excitation in Fig. 4.9 b). Thus, the first goal in the control experiments is to amplify B with respect to A so that a detailed B investigation is feasible.
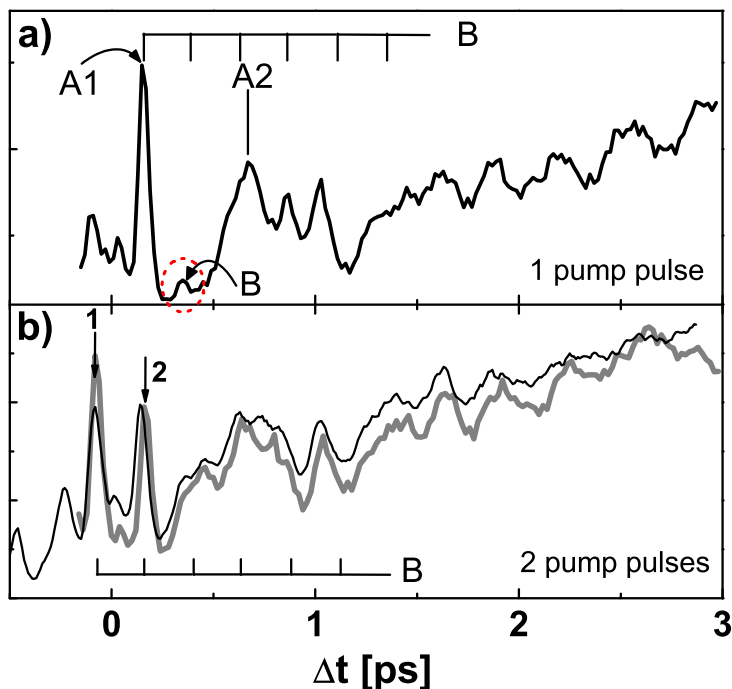
Fig.4.10. Comparison of single pump and double pump probe spectra recorded at $\lambda_{fl} = 322$nm. a) Single pump probe spectrum (solid line) with first and second passage A1 and A2 of the A state wave packet through its probe window. The B vibrational period is indicated by ticks. The second recurrence of the B wave packet is marked by the dashed ellipse. b) Reconstruction of double pump probe spectrum (thick gray line) by adding a) and its copy shifted by 250fs. Arrows 1 and 2 indicate the two positions of A1. The measured spectrum with double pulse excitation, reconstructed this way is shown as the thin black line [188].

The pump probe spectrum in Fig. 4.10 b) taken for otherwise comparable conditions as in 4.10 a) shows the result of the double pulse excitation. The first two strong pulses 1 and 2 are just replica of the probe window A1 separated by T_{vib} due to the time separation of the two excitation pulses. A2 has merged to a broad structure since T_{vib} does not match with its time delay. The B period shown by ticks matches with peaks in the spectrum but the complexity would put question marks on such an assignment. If we repeat the single pump probe spectrum from a) with a shift in Δt by T_{vib} and add these two spectra we end up with the gray line spectrum in b). It contains all features of the measured double pulse spectrum within the reproducibility of these two independent measurements. There is some progress towards our aim. The A state structures have somewhat lower amplitudes compared to B and have a trend to wash out after the first recursion due to the timing mismatch. The progress is however insufficient. Thus, it is obvious that a
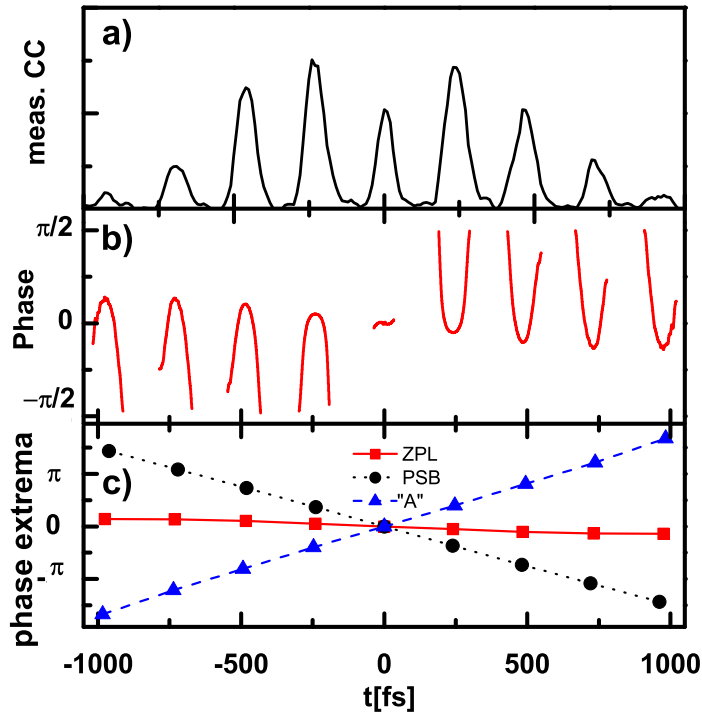
Fig.4.11. Reconstruction of phases from Fourier transformation of measured frequency resolved spectra. a) Experimental cross correlation of the pulse train. b) Plot of the relevant phase information calculated for ZPL position. The phases show a quadratic dependence, corresponding to a linear chirp with changing sign around time zero. c) Unwrapped extrema values from b) for ZPL (squares), PSB (circles) and "A" (triangles) positions (phases not shown) [188].

sharper spectral selection is required already to achieve this first goal of control and the results of excitation with more than two pulses will be presented in Sec. 6.2 and following.

Now, the detailed discussion of the time structure of excitation pulse trains corresponding to the dotted comb in Fig. 4.9 a) will follow. The intensity distribution in the pulse trains is identical for the "A", PSB and ZPL comb locations and is shown in Fig. 4.11 a). The difference is contained in the relative phases, despite the fact that only amplitudes were shaped. To retrieve the phase relations the spectral fringe patterns recorded with a F-OMA are exploited. The measured fringes were Fourier transformed from frequency domain into time domain for the three chosen comb positions. The measured cross correlation shown in 4.11 a) is compared with the phase information within the subpulses obtained from the Fourier transformation. The central peak in frequency domain for ZPL was taken as a reference phase with $\phi=0$ and the further phases for this fringe are reproduced in 4.11 b). The early

peaks (at negative times) have a quadratic phase with negative curvature which corresponds to a negative linear chirp. For peaks at positive times the sign is switched to positive and this coincides with the expectation for a pulse train, where the chirp of subsequent pulses should compensate for the molecular anharmonicity. Measured X-FROG traces confirm this change in sign and the trend of an increasing positive chirp with positive times away from the center. The unwrapped phase values for the position of the maxima at negative times and minima at positive times respectively are displayed in Fig. 4.11 c) for the three spectral comb positions. All these phase values follow a linear trend and cross at zero. For ZPL (squares) a horizontal line is observed, as expected, since it is the center of reference. By changing the relative phase between subsequent pulses the spectral comb can be shifted relative to the envelope and this was done for the PSB (circles) and for the "A" excitation (triangles). In both cases the extrema lie on a straight line covering 3π. They are tilted with opposite sign, since the comb was shifted from ZPL position to higher energies for PSB excitation and to lower energies for the "A" position. Thus, this method of phase reconstruction fully reproduces the expectation from the phase shift picture of spectral combs.

The crucial question is to which extent these phases are conserved in the accumulation of molecular wave packets. The population $P_3{}^c$ for three pulses for example with electric fields ε_1 to ε_3 scales for constructive interference, i.e. $\phi=0$ with

$$P_3{}^c(\phi = 0) \sim \varepsilon_1{}^2 + \varepsilon_2{}^2 + \varepsilon_3{}^2 + 2\left(\varepsilon_1\varepsilon_2 + \varepsilon_1\varepsilon_3 + \varepsilon_2\varepsilon_3\right). \qquad (4.3)$$

The first three terms $P_3{}^{inc}$ are insensitive to the phase and are present in the coherent and incoherent case. The term in brackets would be canceled in the incoherent case with statistical phases and $P_3{}^{inc} \sim n \cdot \varepsilon^2$ for pulses with equal field amplitudes ε. It changes sign for coherence with $\phi=\pi$. It compensates the first one and leads to $P_3{}^c(\phi = \pi) = 0$. In contrast, it has positive sign for $\phi = 0$ and the population $P_n{}^c(\phi = 0)$ for constructive interference of n pulses with equal field amplitude ε will scale with

$$P_n{}^c(\phi = 0) \sim n^2 \cdot \varepsilon^2 \qquad (4.4)$$

and the ratio to the incoherent statistical part is given by

$$\frac{P_n{}^c(\phi = 0)}{P_n{}^{inc}} = n. \qquad (4.5)$$

Simulations of the pulse train excitation for gas phase Br_2 will show these interference effects in the spectral domain in Sec. 5.3. They will be compared with results of our control experiments in Sec. 6.2.

Chapter 5

Theoretical/numerical results

In the present chapter a detailed analysis of the excitation mechanism of a vibrational wave packet with ultrashort laser pulses and trains of pulses will be presented. As already mentioned in Chapter 1, the excitation process involves coupled dynamics on several potential energy surfaces and therefore the corresponding spectral problem goes beyond the Born-Oppenheimer approximation. The time dependence of the electric field is treated explicitly and the developing phases in the wave functions are kept. Here, simulations of the coupled wave packet dynamics in first order time dependent perturbation theory and numerically exact solutions of the time dependent Schrödinger equation (TDSE) will be discussed and compared, respectively. The central findings provide a dynamical picture of an ultrashort excitation processes in the spectral domain, taking place in the far falling wing of the Franck-Condon (FC) factors. They represent the experimental situation in the energetic region of interest, i.e. the one where crossings of the B state with repulsive states occur. The results reveal, that in the extreme situation of an absorption in the far red wing of the spectrum, in addition to the problem of small optical densities, another problem appears: The spectral weight of an excited wave packet gets shifted within the spectral width of the excitation pulses in direction of growing FC factors, in our case corresponding to a blueshift with respect to the central wavelength of excitation pulses. In order to assign measured wave packet dynamics to the energetic region, in which they take place, the problem has been investigated numerically and analytically and the results will be presented in the following sections. The magnitudes of this blueshift have been calculated for the experimental parameters. They mainly depend on the spectral width and corresponding duration of single excitation pulses and the spectral width of envelopes of spectral combs in case of excitation pulse trains, respectively. It was pointed out first by J. A. Wheeler, that in position-momentum phase space, the excitation process shows a sensitive dependence on phase differences of quantum states involved, [247, 248]. The time resolved

study of the spectral representation of the mechanism presented in this work will confirm these fundamental findings.

The analysis presented here has been performed on a gas phase potential for the electronic ground state and the effective matrix potentials derived from pump probe and excitation spectra presented in Fig. 2.1 and Fig. 2.13 in Chapter 2 [83, 166]. No additional matrix induced environmental effects are included. Since the excitation takes place to the inner limb of the B state, the interaction with the surrounding can be further neglected for this purpose (see discussion of the absorption spectrum in Sec. 2.5.1). A detailed and much more sophisticated theoretical analysis based full quantum calculations on the system Br_2:Ar has been carried out by A. Borowski with O. Kühn and A. Accardi. Using a dimensionality reduced DIM (Diatomics in Molecules) Hamiltonian, Borowski was able to construct potentials mirroring experimental reality, to reproduce in the Huang-Rhys coupling model the B state excitation in good agreement with our measured spectra and to simulate predissociation dynamics of the C ← B transition applying the Multi-Configurational-Time-Dependent-Hartree method [84, 85, 154, 177, 189]. Despite of the relative simplicity of the gas phase like studies presented in this work, they turned out to be appropriate as a reference in order to identify deviations due to matrix induced effects. In Sec. 5.4 of this chapter, examples of simulated gas phase pump probe spectra will be presented together with measured spectra using the same pulse parameters. A comparison will allow to identify the fingerprints of environment induced effects like vibrational energy relaxation and matrix induced predissociation in pump probe spectra.

5.1 Birth of a wave packet: Spectral picture

A central question one has to answer if one aims to monitor wave packet dynamics in the spectral domain is which basis set one has to choose to gain maximum of desired information. Here, the intuitively best accessible representation was chosen, by using the B potential's vibrational eigenstates as projectors. In order to stay as close as possible to the experimental situation, we project the dynamics on the set of Morse eigenstates of the effective experimental B state potentials. Thus, we consider only the two-state interaction between the chromophore's ground and $^3\Pi_{0u}$ state. The eigenstates have been presented in in Sec. 3.2.4 and the results of the projections will be discussed now in a time dependent framework. Finally, an analytical expression for the spectral coefficients will be derived in 1st order perturbation theory, inspired by similar calculations for ro-vibrational states carried out in [249].

5.1.1   Projection onto Morse eigenstates: Full quantum mechanical propagation

For the simulation of the B state wave packet dynamics, besides the numerical propagation in 1st order perturbation theory presented in Sec. 3.2, a numerically exact fully quantum propagation using the "WavePacket" MATLAB-code package developed by B. Schmidt and U. Lorenz has been adapted to the Br_2 case with the experimentally relevant parameters under the supervision of B. Schmidt [211]. Using both propagation methods allows for a cross-check for the extent of validity of the 1st order perturbation and a discussion of the validity will follow in the next sections. As a first example, the spectral decomposition of a wave packet is shown in Fig. 5.1, which was excited with a pulse centered at $16949 cm^{-1}$, which corresponds to 590nm, close to the B state vibrational level v'=9, and has an autocorrelation full width at half maximum (FWHM) duration of t_{FWHM}=80fs[1]. The Gaussian shaped pulse has been centered at a propagation time of t_{propa}=160fs, so that the simulation starts earlier than two FWHM of the laser pulse, which will be motivated in the following Sec. 5.1.2. Fig. 5.1 shows the time evolution of the spectral coefficients of the B state vibrations v' for four different propagation times. At t_{propa}=100fs the excitation pulse's Gaussian temporal envelope is still increasing, but it is already within its FWHM. The corresponding spectral representation of the excited wave packet shows a broad distribution on the high vibrational levels between v'=10 and 45 on the high energetic side, and spectral coefficients in the order of 10^{-9}. Even when the excitation pulse has reached its maximum at t_{propa}=160fs, the spectral weight is still remaining in the far blue wing of the spectrum. However, a second maximum starts to arise around v'=10 in the energetic region of the excitation pulse center and the coefficients increase by one order of magnitude. At t_{propa}=240fs the excitation pulse just leaves its FWHM on the falling wing of its envelope and the maximum shifts to the pulse center. No further spectral redistribution occurs (see t_{propa}=600fs) and the excitation process is completed. For this pulse duration, the wave packet is essentially composed of three vibrational states, and it will turn out in the following and will be also discussed in Chapter 6, that this is the optimal pulse duration to be used in order to perform the coherent control experiments. The reason for this characteristic time evolution of the spectral coefficients will be discussed now exemplarily for another excitation pulse duration. The spectral coefficients of

---

[1]In the following, pulse durations will be given in terms of intensity autocorrelation full width at half maxima t_{FWHM} of Gaussian shaped laser pulses (as defined in eq. (3.2) in Sec. 3.2.1), which is related to the Gaussian width τ of the electric field's envelope by $t_{FWHM}=\sqrt{8\,ln\,2}\,\tau$ and to the intensity FWHM $\Delta\tau$ by $t_{FWHM}=\sqrt{2}\Delta\tau$. [221]. The spectral width of the pulses can be computed by combining the time-frequency uncertainty-type relation $\Delta\nu\Delta\tau=4ln2/2\pi$ and the relation $\Delta\nu=c\Delta\lambda/\lambda_0^2$, where λ_0 is the pulse center wavelength.

excitation pulse of 80fs FWHM-duration,
pulse centred at 160fs
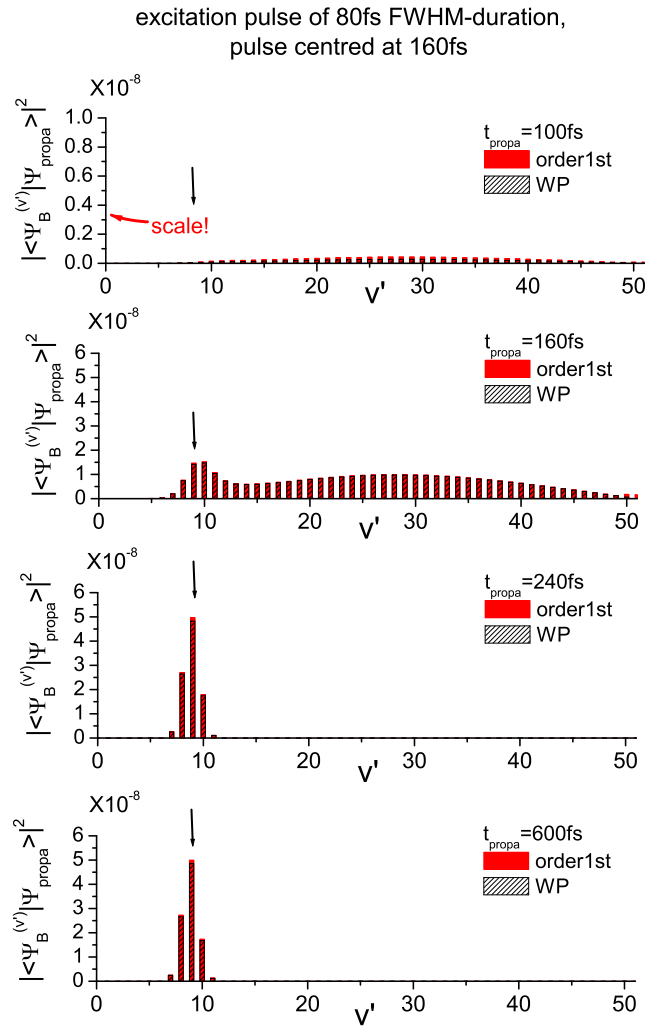
Fig.5.1.   Spectral coefficients of a simulated B state wave packet $|\psi_{propa}\rangle = \psi(R, t_{propa})$ excited with a 80fs long Gaussian laser pulse (corresponding spectral width $\Delta\lambda = 9$nm) with a carrier frequency of 16949cm^{-1} close to v'=9 as indicated by the arrows. The red bars show the results of a wave packet propagation in 1st order perturbation, while the black shaded bars depict numerically exact propagation. Snapshots at four different propagation times were chosen in order to illustrate characteristics of the excitation process. (Other simulation parameters see eq. (3.2): field amplitude $\varepsilon_F = 2 \cdot 10^{-4} E_h/ea_0$, transition dipole moment $\mu_{BX} = 0.15 ea_0$)

a wave packet excited with the same parameters as in Fig. 5.1 but with a duration of 20fs is shown in Fig. 5.2 for six different propagation times. Again, the Gaussian excitation pulse has been centered at two FWHM corresponding to $t_{propa} = 40$fs. For $t_{propa} = 30$fs in a) a broad distribution covering more than 30 vibrational levels, and with a maximum around v'=30 is observable. This early time behavior, also observed for the 80fs pulse can be explained with the time-energy uncertainty

excitation pulse of 20fs FWHM-duration, pulse centred at 40fs
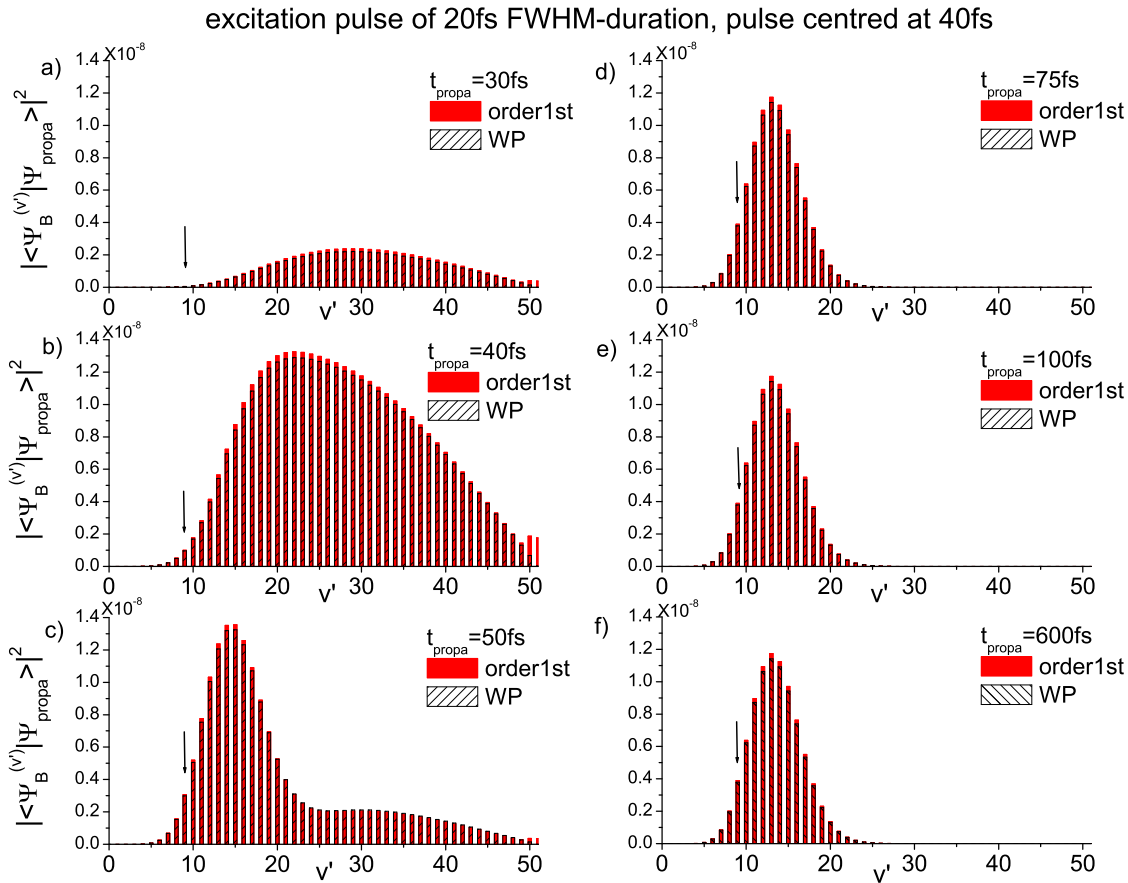
Fig.5.2. Same as Fig. 5.1 with an excitation pulse duration of 20fs (corresponding spectral width $\Delta\lambda=36$nm). Snapshots for 6 subsequent propagation times are shown in a)-f). The arrows indicate the excitation pulse's carrier frequency. (Other parameters: $\varepsilon_F=2\cdot10^{-4}E_h/ea_0$, $\mu_{BX}=0.15ea_0$)

principle: A short pulse covers a broad energetic region. With the first cycle of the electric field, a spectrally broad wave packet, displaying the largest FC factors is excited. Therefore, at this early stage the blue components with large FC factors dominate the spectral distribution. With subsequently following cycles of the electric field, the spectral weight shifts to smaller vibrational quantum numbers, in direction of the selected carrier frequency. In Fig. 5.2 b) the pulse has reached its maximum and the still very broad spectral distribution has experienced a shift of its maximum to around v'=22. The population, which is the integrated spectral density, has also reached its maximum. During the falling wing of the pulse's envelope, the blue wing starts to disappear and a spectral redistribution centered close to the excitation pulse's carrier frequency develops, at 50fs in c), peaked at v'=15. At this point, the pulse just leaves its FWHM and in contrast to the 80fs pulse excitation in Fig. 5.1, the excitation process is not completed yet. The blue wing is extinguished completely only at t_{propa}=75fs, shown in Fig. 5.2 d). The spectral coefficients do

not show any time dependence anymore for greater propagation times in e) and f).

In order to better understand the reason for this self-cleaning excitation process, we have to recall, that it is the result of interferences between all possible vibrational eigenstates of the B potential with the ground state wave function and the time dependent electric field. The broad spectral distribution, analogous to a whitelight-excitation, excited by the first cycles of the field interferes with the subsequently created, again, still broad distribution. During this interaction, the constituents of the broad wave packet which are not in phase with the pulse carrier frequency experience destructive interference, while the in phase contributions survive. To this end, for a fixed carrier frequency, the excitation cleaning process in case of a long pulse, consisting of a great number of optical cycles within its envelope, is completed already within its FWHM like in Fig. 5.1, while for a short pulse, at this point the interference process is still active, since less optical cycles have occurred. Indeed, no complete cleaning is achievable with extremely short pulses. For the 20fs pulse shown in Fig. 5.2 f) at t_{propa}=600fs the spectral distribution is still not centered, where one would eventually expect it to be, namely at v'=9 but blueshifted by four vibrational quanta to v'=13. The final shape of the spectral envelopes can be, however, very well fitted by a Gaussian function, mimicking the electric field's spectral envelope. In order to further exploit the nature of this characteristic far red wing excitation process, an analytical expression for the spectral coefficients will be derived in the following.

5.1.2 Analytical expression in 1st order perturbation theory

For the derivation of an analytical expression for the spectral representation of the excited B state vibrational wave packet we make use of the 1st order term in the perturbation series (see also Sec. 3.2.2 and note that molecular rotations have been neglected):

$$
\begin{aligned}
\psi^{(1)}(R,t) &= \frac{1}{i\hbar} \int_0^t e^{-\frac{i}{\hbar} H_B (t-t')} \left\{ -\mu_{BX}(R)\,\varepsilon(t') \right\} e^{-\frac{i}{\hbar} H_X t'} \psi_X(R,0)\, dt' \\
&= \frac{1}{i\hbar} \int_0^t \left\{ -\mu_{BX}\,\varepsilon(t') \right\} e^{-\frac{i}{\hbar} H_B (t-t')} \underbrace{e^{-\frac{i}{\hbar} H_X t'} \psi_X(R,0)}_{e^{-\frac{i}{\hbar} E_X t'}\, \psi_X(R,0)}\, dt' \quad (5.1)
\end{aligned}
$$

In general the transition dipole is a function of R, however, in the simulations the Condon approximation with a constant value μ_{BX}=0.15ea$_0$ was applied [250, 251]. Inserting the resolution of the identity operator in terms of projectors onto the

complete set of eigenstates of the B state Morse potential

$$\mathbb{1} \;=\; \sum_{v'=0}^{\infty} |\psi_B^{(v')}\rangle\langle\psi_B^{(v')}| \tag{5.2}$$

one obtains the action of the B state's time evolution operator $e^{-\frac{i}{\hbar}H_B(t-t')}$ onto the initial ground state wave function $|\psi_X^{(0)}\rangle$:

$$
\begin{aligned}
\psi^{(1)}(R,t) &= \frac{1}{i\hbar}\int_0^t \{-\mu_{BX}\,\varepsilon(t')\}\; e^{-\frac{i}{\hbar}E_X t'} e^{-\frac{i}{\hbar}H_B(t-t')}\sum_{n=0}^{\infty}\psi_B^{(v')}(R)\cdot\langle\psi_B^{(v')}|\psi_X^{(0)}\rangle\,dt' \\[2mm]
&= \frac{1}{i\hbar}\int_0^t \{-\mu_{BX}\,\varepsilon(t')\}\; e^{-\frac{i}{\hbar}E_X t'}\sum_{n=0}^{\infty} e^{-\frac{i}{\hbar}E_B^{(v')}(t-t')}\psi_B^{(v')}(R)\cdot\langle\psi_B^{(v')}|\psi_X^{(0)}\rangle\,dt' \\[2mm]
&= \frac{1}{i\hbar}\sum_{v'=0}^{\infty}\left\{\int_0^t \{-\mu_{BX}\,\varepsilon(t')\}\; e^{-\frac{i}{\hbar}E_X t'} e^{-\frac{i}{\hbar}E_B^{(v')}(t-t')}\psi_B^{(v')}(R)\cdot\langle\psi_B^{(v')}|\psi_X^{(0)}\rangle\,dt'\right\} \\[2mm]
&= \frac{1}{i\hbar}\sum_{v'=0}^{\infty}\left\{\int_0^t \{-\mu_{BX}\,\varepsilon(t')\}\; e^{-\frac{i}{\hbar}\left(E_X-E_B^{(v')}\right)t'}\langle\psi_B^{(v')}|\psi_X^{(0)}\rangle\,dt'\right\}\underbrace{e^{-\frac{i}{\hbar}E_B^{(v')}t}\,\psi_B^{(v')}(R)}_{\psi_B^{(v')}(R,t)} \\[2mm]
&= \sum_{v'=0}^{\infty}c_{v'}(R,t)\,\psi_B^{(v')}(R,t)\,. \tag{5.3}
\end{aligned}
$$

This leads to an expression for the spectral coefficients:

$$c_{v'}(R,t) \;=\; \left\{\frac{1}{i\hbar}\int_0^t \{-\mu_{BX}\,\varepsilon(t')\}\; e^{-\frac{i}{\hbar}\left(E_X-E_B^{(v')}\right)t'}\,dt'\right\}\langle\psi_B^{(v')}|\psi_X^{(0)}\rangle\,. \tag{5.4}$$

Defining

$$\tilde{\varepsilon}(\omega_0^{(v')}) \;=\; \int_0^t \varepsilon(t')\,e^{i\omega_0^{(v')}t'}\,dt' \tag{5.5}$$

where

$$\omega_0^{(v')} \;=\; \frac{E_B^{(v')}-E_X}{\hbar} \tag{5.6}$$

is the frequency difference between initial and excited vibrational states, the spectral distribution of the excited B state population is given by

$$|\tilde{c}_{v'}(R,\omega)|^2 \;=\; \frac{\mu_{BX}^2}{\hbar^2}\cdot|\tilde{\varepsilon}(\omega_0^{(v')})|^2\cdot|\langle\psi_B^{(v')}|\psi_X^{(0)}\rangle|^2 \tag{5.7}$$

with $|\langle \psi_B^{(v')} | \psi_X^{(0)} \rangle|^2$ being the Franck-Condon factors of the B ← X state absorption. Inserting in eq. (5.5) for $\varepsilon(t)$ a Gaussian shaped excitation pulse

$$\varepsilon(t') \quad = \quad \varepsilon_F \, e^{-\frac{(t'-t_0)^2}{2\tau^2}} \, \cos(\omega_F \, t') \tag{5.8}$$

with amplitude ε_F, Gaussian duration τ and carrier frequency ω_F, one obtains for $\tilde{\varepsilon}(\omega_0^{(v')})$

$$\tilde{\varepsilon}(\omega_0^{(v')}) \quad = \quad \int_0^t \frac{\varepsilon_F}{2} \, e^{-\frac{(t'-t_0)^2}{2\tau^2}} \left\{ \underbrace{e^{i\,(\omega_0^{(v')}+\omega_F)\,t'}}_{0 \ in \ RWA} + e^{i\,(\omega_0^{(v')}-\omega_F)\,t'} \right\} dt' \tag{5.9}$$

The fast oscillating term $e^{i\,(\omega_0^{(v')}+\omega_F)\,t'}$ can be neglected within the rotating wave approximation [5]. The spectral coefficients in eq. (5.7) can be obtained by evaluating eq. (5.9) in the limit where the two integration boundaries are taken to be $\pm\infty$. Then, eq. (5.9) becomes the Fourier transform of the electric field. Since the simulation of the 1st order wave function $\psi^{(1)}(R,t)$ always starts and ends at a finite time, it has to be shown, that a restriction to finite boundaries does not affect the numerical correctness of the results. To this end the decomposition of $\psi^{(1)}(R,t)$ into eigenstates of the B state was calculated and is shown in Fig. 5.3 for the two different pulse durations t_{FWHM}=80fs in the first column and t_{FWHM}=20fs in the second column. To check the influence of the time limits, the start and end points of the propagation were shifted by two full widths at half maxima $2t_{FWHM} = 2\sqrt{8\ln 2}\,\tau$ from the center of the laser pulse in time domain (black squares in Fig. 5.3). When increasing the integration boundaries to $4t_{FWHM}$ (magenta squares) no changes are visible on a linear scale in the first row of Fig. 5.3. On a logarithmic scale, shown in the second row of Fig. 5.3, non-monotonic structures in the outer wings of the spectral distributions can be observed that decrease with increasing integration interval around the pulse center. However, they do not exceed the order of magnitude of 10^{-16} and are only visible in the logarithmic representation. Therefore, the extension of the integration from $-\infty$ to $+\infty$ is also justified for the numerical treatment. With the definition of the Fourier transformation as

$$\mathcal{F}\,[\,f(t)\,]\,(\omega) \quad = \quad \frac{1}{\sqrt{2\pi}} \int_{-\infty}^{\infty} f(t)\,e^{-i\omega t}\,dt \tag{5.10}$$

and using the fixed point of the Fourier transformation, i.e.

$$\mathcal{F}\left[e^{-\frac{t^2}{2}}\right](\omega) \quad = \quad e^{-\frac{\omega^2}{2}} \tag{5.11}$$
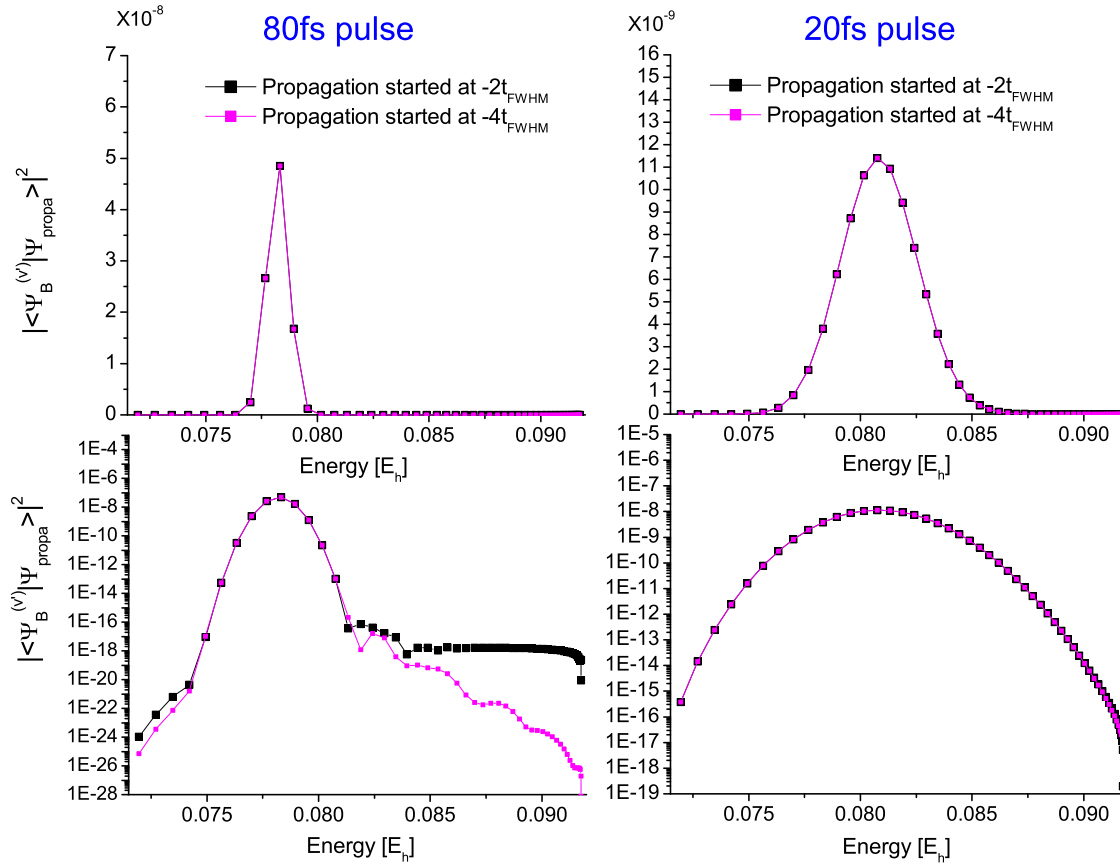
Fig.5.3.　　Spectral coefficients for two different excitation pulse durations (t_{FWHM}=80fs in the left, t_{FWHM}=20fs in the right panel) plotted on a linear (upper panel) and logarithmic (lower panel) scale to visualize the vanishing "cutoff-effects" in the simulations. The data displayed with black squares are the result of propagations started at $-2t_{FWHM}$, the magenta squares at $-4t_{FWHM}$ with respect to the Gaussian excitation pulses' maxima in the time domain. (Other simulation parameters: ε_F=2·10$^{-4}E_h/ea_0$, μ_{BX}=0.15ea_0)

the integral in eq. (5.9) can be solved analytically and reads

$$\tilde{\varepsilon}\big(\omega_0^{(v')}\big) \;\; = \;\; \frac{\sqrt{2\pi}}{2}\, \varepsilon_F\, \tau\, e^{i\,(\omega_0^{(v')}-\omega_F)\,t_0}\, e^{-\frac{(\omega_F-\omega_0^{(v')})^2\,\tau^2}{2}} \; . \tag{5.12}$$

Inserting this expression into eq. (5.7) leads to the spectral coefficients

$$|c_{v'}|^2 \;\; = \;\; \frac{\mu_{BX}^2}{\hbar^2}\cdot\frac{\pi}{2}\,\varepsilon_F^2\,\tau^2\, e^{-(\omega_F-\omega_0^{(v')})^2\,\tau^2}|\langle\psi_B^{(v')}|\,\psi_X^{(0)}\rangle|^2 \; . \tag{5.13}$$

The coefficients are Gaussian-like functions in the detuning $\Delta \;=\; \omega_F - \omega_0^{(v')}$ weighted by the FC factors $|\langle\psi_B^{(v')}|\,\psi_X^{(0)}\rangle|^2$ and the square of the Gaussian pulse duration τ.

Thus, eq. (5.13) directly displays that for decreasing (Gaussian) pulse duration τ the relative weight of the FC factors increases as shown by the numerical results presented in Fig. 5.2. Indeed, for even shorter excitation pulses, the spectral distribution approaches the envelope of the FC factors. In order to further explain the results for long pulse durations, we remind of the representation of the Dirac delta function as the limit case of a very sharp Gaussian function:

$$\delta(u) = \lim_{\varepsilon \to 0} \frac{1}{\sqrt{2\pi}\,\varepsilon} e^{-\frac{u^2}{2\,\varepsilon^2}} . \tag{5.14}$$

We use this relation to calculate the limit of the excitation coefficients from eq. (5.13) for spectrally sharp and correspondingly long excitation pulses with large τ, which can be rewritten as:

$$\lim_{\tau \to \infty} |c_{v'}|^2 = \frac{\mu_{BX}^2}{\hbar^2} \cdot \pi^2 \cdot \varepsilon_F^2 \left(\lim_{\tau \to \infty} \frac{1}{\sqrt{2\pi}} \tau\, e^{-\frac{(\omega_F - \omega_0^{(v')})^2 \tau^2}{2}} \right)^2 \cdot |\langle \psi_B^{(v')} | \psi_X^{(0)} \rangle|^2$$

$$= \frac{\mu_{BX}^2}{\hbar^2} \cdot \pi^2 \cdot \varepsilon_F^2 \cdot \delta^2(\omega_F - \omega_0^{(v')}) \cdot |\langle \psi_B^{(v')} | \psi_X^{(0)} \rangle|^2 .$$

Thus, for long excitation pulses and vanishing detuning $\Delta = \omega_F - \omega_0^{(v')}$ only exactly one FC factor contributes. In the case of nonvanishing Δ, which is the case treated in Fig. 5.1, the argument should be understood by replacing the delta function with its asymptotic representation from eq. (5.14) as a sharp but slightly smeared out Gaussian peaked around ω_F. This is just the spectral distribution observed in the last row of Fig. 5.1. In conclusion, the analytical expression for the excitation coefficients derived in time dependent 1st order perturbation theory allows to explain the results of the simulated excitation process.

In order to cross-check the validity of 1st order perturbation and for the applied parameters, the analytically derived spectral coefficients have been calculated and are shown in Fig. 5.4 (green triangles) together with a spectral decomposition of the numerically exactly calculated excited B state wave packet into eigenstates of the B state Morse potential (black squares), performed with the "WavePacket" code package provided by B. Schmidt [211]. The two different representations agree very well concerning their centers of mass and widths and the deviations are for both pulse durations smaller than 0.5%. The Fourier transformed electric fields are shown as well (red, scaled for comparability) to illustrate that increasing FC factors (right panel in Fig. 5.4) only slightly shift the spectral weight of the distribution for a long and therefore spectrally sharp excitation pulse of 80fs while the excitation with a 20fs short and correspondingly
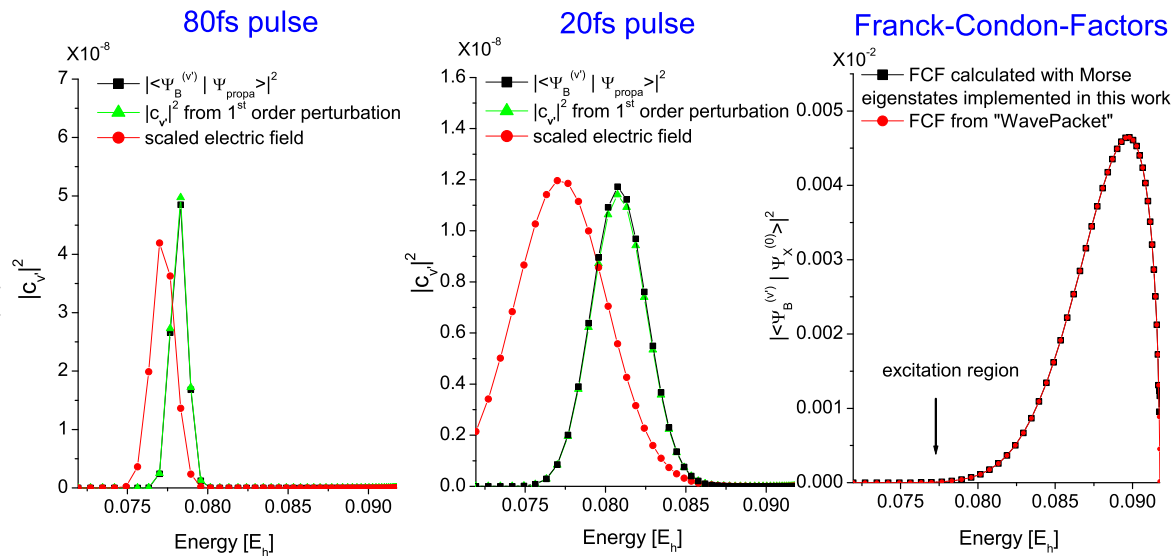
Fig.5.4. Comparison of spectral coefficients obtained from the first order perturbation term following eq. (5.13) (green triangles) and those obtained from the numerically exact simulation with "WavePacket" (black squares) [211] for an 80fs and a 20fs long excitation pulse. The electric field's spectral envelope is shown in red. The Franck-Condon factors calculated using the B eigenstates implemented in this work (see Sec. 3.2.4) are compared to those obtained with "WavePacket". The selected excitation region is marked by an arrow. (Other simulation parameters: $\varepsilon_F=2\cdot10^{-4}E_h/ea_0$, $\mu_{BX}=0.15ea_0$)

spectrally broad pulse results in a strong spectral shift into the blue wing of the field's spectral envelopes, according to the rapidly growing Franck-Condon factors in this energetic region (marked by the arrow in the last column of Fig. 5.4).

Finally, we provide a mathematical proof for the interference processes proposed for the explanation of the excitation mechanism presented in Fig. 5.1 and Fig. 5.2., respectively. It consists of the analysis of two limiting cases of a symmetric pulse $\varepsilon(t) = \varepsilon(-t)$ where either only half of the pulse or the complete pulse $\varepsilon(t) = \varepsilon^{(-)}(t) + \varepsilon^{(+)}(t)$ is known by the molecule. For these cases the FT can be calculated explicitly due to the symmetry properties of the Fourier transformation. Starting with the left half $\varepsilon^{(-)}(t)=\Theta(-t)\cdot\varepsilon(t)$ of a symmetric pulse one obtains:

$$
\begin{aligned}
\mathcal{F}[\varepsilon^{(-)}](\omega) &= \frac{1}{\sqrt{2\pi}}\int\limits_{-\infty}^{\infty} \Theta(-t)\cdot\varepsilon(t)\cdot e^{i\,\omega\,t}\,dt \\
&= \frac{1}{\sqrt{2\pi}}\int\limits_{-\infty}^{0} \varepsilon(t)\cdot e^{i\,\omega\,t}\,dt\,,
\end{aligned}
$$
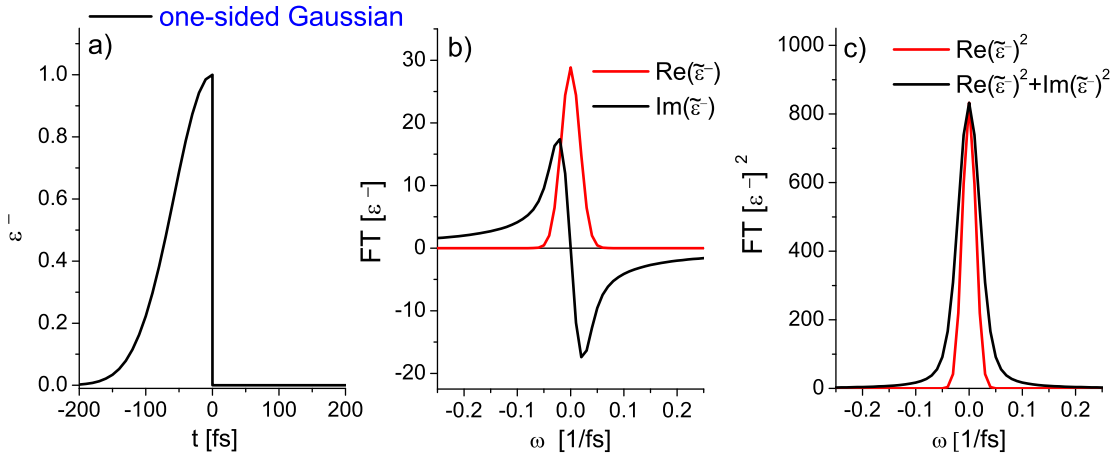
Fig.5.5. One sided Gaussian function (a) and its Fourier transform (b) decomposed into real (red) and imaginary (black) part. In c) the square of the FT from b) (black) is compared with the contribution from the real part (red).

and by using the Euler formula $e^{i\varphi} = \cos\varphi + i\sin\varphi$,

$$\mathcal{F}[\varepsilon^{(-)}](\omega) = \frac{1}{\sqrt{2\pi}} \int_0^\infty \varepsilon(t) \cdot \cos(\omega t)\, dt - i \cdot \frac{1}{\sqrt{2\pi}} \int_0^\infty \varepsilon(t) \cdot \sin(\omega t)\, dt$$

$$= \frac{1}{2}\mathcal{F}[\varepsilon](\omega) - i \cdot \frac{1}{\sqrt{2\pi}} \int_0^\infty \varepsilon(t) \cdot \sin(\omega t)\, dt. \tag{5.15}$$

The same calculation applied to the right half $\varepsilon^{(+)}(t)$ of the pulse leads to the complex conjugate of the above result. If one finally considers the complete pulse as the sum of its left and right wing, i.e. $\varepsilon(t) = \varepsilon^{(-)}(t) + \varepsilon^{(+)}(t)$, it becomes clear that the phases of the two halfs do exactly cancel producing thereby the real valued Fourier transform $\mathcal{F}[f](\omega)$ of the complete symmetric pulse, which is just twice the real part of eq. (5.15). This general and well-known symmetry property of the FT [252] explains why the far resonant excitation coefficients excited on the high energetic side during the rising wing of the excitation pulse experience destructive interference during the falling wing of the pulse due to the opposite signs of phases and are extinguished after termination of the pulse. In order to examine the widths of the real and imaginary parts, in the following, we consider a concrete example of a one-sided Gaussian function $\varepsilon^{(-)}(t) = \Theta(-t) \cdot e^{-\frac{t^2}{2\tau^2}}$ shown in Fig. 5.5 a). The FT can be computed explicitly and reads

$$\mathcal{F}[f^{(-)}](\omega) = \frac{a}{2} e^{-a^2\omega^2/2} \left[1 - i \cdot \mathrm{erfi}\left(\frac{a\,\omega}{\sqrt{2}} \right) \right] = \tilde{\varepsilon}(\omega), \tag{5.16}$$

where erfi is the imaginary error function. The real part (red line) and the imaginary part (black line) are shown in Fig. 5.5 b). Furthermore, as illustrated in Fig. 5.5 c), the imaginary part leads to a broadening of the spectrum which is $|\tilde{\varepsilon}(\omega)|^2 = Re(\tilde{\varepsilon})^2 + Im(\tilde{\varepsilon})^2$ (black line), as compared to the spectrum of the complete pulse, where only the real part (red line) of the FT survives[2]. Thus, the broad spectral distributions observed in Fig. 5.1 and Fig. 5.2 for propagation times corresponding to the center of the Gaussian excitation pulses in the time domain, can be attributed to the broadening of $|\tilde{\varepsilon}(\omega)|^2$ in eq. (5.13) due to the contribution of the imaginary parts.

5.2   Population dynamics in the far red wing of the Franck-Condon factors

In the following, the time evolution of the integrated spectral densities introduced in the previous section will be further analyzed. First, the range of electric field amplitudes in the linear regime, where first order perturbation is justified, will be identified. The population dynamics on the electronic X and B states will be monitored during the excitation process in order to quantify the underlying excitation process. The pulse duration dependence of the spectral distribution introduced in the previous section will be finally summarized in Sec. 5.2.2.

5.2.1   Nonlinear effects in 1st order perturbation?

The interference effects taking place in an excitation in the far red falling wing of the FC factors, are central for the dipole excitations considered in this thesis. From the behavior depicted in Fig. 5.2 naturally the question arises where the population in the blue part, which is deexcited from the B state remains? Therefore, in the first instance the dependence of the excited B state population on the electric field amplitude has been analyzed and is shown in Fig. 5.6 on a double logarithmic scale. The two extreme situations of an excitation close to the FC maximum at around 480nm (upper panel of Fig. 5.6) and an excitation in the far falling red wing of the spectrum (lower panel) at 590nm have been compared. As expected, when considering only the first order term in the perturbation series, a linear field dependence is observable, which has been fitted to the selected electric field amplitudes (red line), for which the given data points are shown with red circles. It has been

---

[2]Many thanks to Burkhard Schmidt for advicing me to this general property and calculating the FT of the one-sided Gaussian together with Jan-Hendrik Prinz from the DFG Research Center Matheon, FU Berlin.
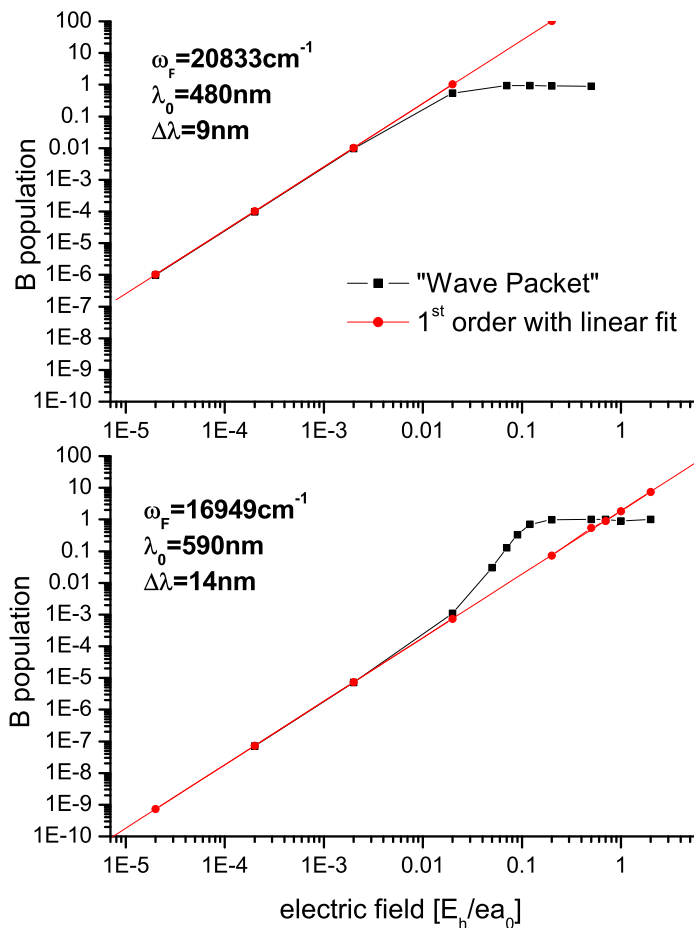
Fig.5.6. Comparison of the electric field dependence of excited B state population in first order perturbation theory (red) and in the numerically exact simulation with "WavePacket" (black) plotted on a double logarithmic scale. Field amplitudes are given in atomic units. In the upper panel the carrier frequency of the electric field was located close to the FC maximum of the B state excitation from the vibrational ground state of the X potential. The lower panel shows the result of the excitation with the carrier frequency corresponding to 590nm excitation pulse wavelength (close to v'=9). The excitation pulse duration was in both cases t_{FWHM}=50fs. Corresponding spectral widths are given in the Figure legend.

pointed out in Sec. 3.2.2, that the first order term in the perturbation series in eq. (5.1) only includes the excitation from the ground to the excited state, but neglects any back transitions onto the ground state. Nonlinear effects only show up for the full quantum mechanical calculations with "WavePacket", shown in Fig. 5.6 with black squares for the selected field amplitudes. Their connection only serves as a guide for the eye to follow the trend. In case of the near FC maximum excitation in the upper panel for electric fields greater than $0.01E_h/e·a_0$ the exact calculation clearly deviates from the linear behavior. Here, Rabi oscillations in the two state

system composed of the electronic X and B states come into play and decrease the B population. For the excitation wavelength region relevant for the experimental situation, shown in the lower panel, nonlinearities set in for the same order of magnitude of the electric field. The experimentally applied fields are, however, two orders of magnitude smaller than $0.01E_h/e{\cdot}a_0$. Indeed, in order to avoid destroying the samples, in the experiments, electric field strengths in the linear regime have to be chosen[3]. For the case of excitation in the far red wing of the FC factors, in the exact calculation, the B state population exceeds the linear dependence in a field region between $0.1E_h/e{\cdot}a_0$ and $0.8E_h/e{\cdot}a_0$, where it crosses the linear limit twice. For even larger fields, the population decreases just as in the upper panel. In this intermediate field region, the overall B state population can be increased, because the electric field induces a so called dynamical hole in the ground state wave function in the X state [253–256]. Since the maximum of the wave function then does not remain located around the potential minimum but also oscillates between the turning points of potentials, like superposition states do, the FC envelope also becomes time dependent. In this case, the FC envelope dynamics effectively increases the transition probabilities. Unfortunately, in the experiments we cannot make use of the dynamical hole burning method in order to increase the optical densities in the desired energetic regime, since a destruction of the sample sets in already in the linear regime of the X $\rightarrow$ B excitation.

Despite the fact, that in the first order term no back transitions from B to X are included, the spectrally resolved B state population dynamics shown in Figs. 5.1 and 5.2 agrees very well with the exact dynamics. Obviously, in addition to the amplification during the rising wing of the excitation pulse train a depopulation process is contained while the pulse envelope decreases. The nonresonant high energetic states develop a negative phase and since the phases are stored, a cancellation of earlier excitations in this part occurs. The symmetric pulse shape guarantees that the falling part completely cancels the nonresonant excitation in the rising part. The more resonant parts add up constructively and gain weight.

---

[3]The experimentally determined field energies E are connected with the field amplitudes ε_F by the relation $E = A\,c\,\epsilon_0\,\frac{\varepsilon_F^2}{4}\sqrt{\pi}\,\tau$, where $A = \pi\,d^2/4$ is the laser spot area with a typically used focus diameter of $d{=}100\mu$m on the sample. The above relation has been calculated for a Gaussian pulse $\varepsilon(t) = \varepsilon_F\,e^{-\frac{(t-t_0)^2}{2\tau^2}}\cos(\omega_F t) = \varepsilon_F\,e^{-\frac{(t-t_0)^2}{2\tau^2}}\left(e^{i\omega_F t} + e^{-i\omega_F t}\right)/2$ in the following way,

$$E_{el} \;=\; \frac{\epsilon_0}{2}\int_{\mathbb{R}^3}\varepsilon^2\,d^3r \;=\; \frac{\epsilon_0}{2}\int_{-\infty}^{\infty}\varepsilon^2\cdot A\cdot c\cdot dt \;=\; \frac{A\,c\,\epsilon_0}{2}\frac{\varepsilon_F^2}{4}\int_{-\infty}^{\infty}\left[2\,e^{-\frac{(t-t_0)^2}{\tau^2}}\;+\;\dots\right]d\tau\;,$$

where $d^3r = A\cdot c\cdot dt$. The dotted terms do not contribute to the integral since they are fastly oscillating. Evaluating the only remaining term produces the above relation.
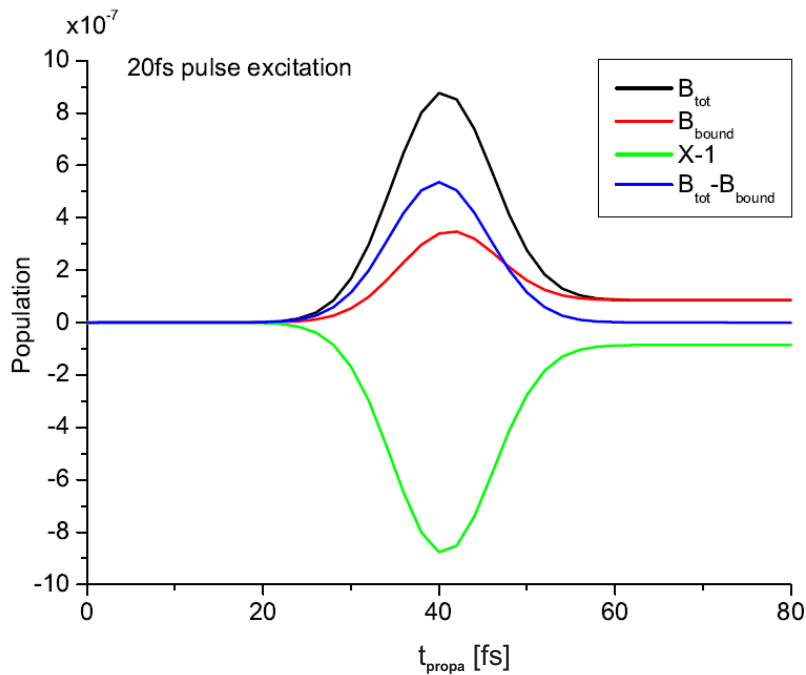
Fig.5.7. Simulations monitoring the time evolution of the B (black) and X-state population (X-1 green) performed with "WavePacket" on the effective B state Morse potential from [88] and X potential parameters from [109]. The B-state population has been decomposed into its bound (red) and scattering (blue) state components. (Parameters: $\varepsilon_F=2\cdot10^{-4}E_h/ea_0$, $\mu_{BX}=0.15ea_0$, $\omega_F=16949\text{cm}^{-1}$, $\Delta\lambda=36\text{nm}$)

Summed spectral densities of the excited B state wave packet have been calculated with "WavePacket" and the result is shown in Fig. 5.7 for a 20fs long excitation pulse as a function of propagation time (black line). The bound part of the total population (black) is depicted in red. The blue line shows the remaining B state population, which belongs to scattering states of the Morse potential. Indeed, during the excitation the continuum state contribution dominates the population according to the FC factors and only when the excitation pulse has left its FWHM, the continuum contribution approaches zero. The remaining population is transferred back to the X state. The calculated X state population has been shifted by just adding a negative offset of -1 for better visibility and is shown in green in Fig. 5.7. The observed nonlinear, antipodal time evolution of the X and B population again emphasizes, that constructive and destructive interference between the dipole interacting X and B states are the driving mechanism behind the depopulation and following repopulation of the X state for this excitation in the far falling red wing of the FC factors.

It is worth to note, that the first order propagation, which does not take into account explicitly the influence of the field on the X state population dynamics, implicitly includes the repopulation of the X state, too, by monitoring the antipodal

depopulation process of the B state. The reason is the choice of field amplitudes in the linear regime. It emphasizes the essential role of interference and phase relations between interacting states and electric field, respectively. This richness of information contained in the 1st order term clearly shows up for excitation processes far from the FC maximum.

5.2.2   Pulse duration dependence

Finally, an overview of spectral shifts of the excited wave packets' spectral maxima with respect to the excitation pulses' central photon energy is given in Fig. 5.8, for pulse durations of 80fs (blue), 60fs (red), 40fs (green) and 20fs (black). The spectral representations are given in terms of the RKR-B state potential constructed in [88] from time resolved data, and the excitation pulse carrier frequency was chosen in resonance with v'=9 of this potential. The projection of the wave packets on the eigenstates took place for a propagation time of $t_{propa} = 600fs$, in order to ensure, that no spectral redistributions occur for later times. Indeed, for 80fs and 60fs long pulses, the spectral distribution remains peaked at the spectral position selected by the carrier frequency. For shorter pulses, the maximum is blueshifted up to 4 vibrational quanta. In the calculation of the integrated spectral densities for the 4 different pulse durations, the maxima of the field amplitudes have been kept constant. Under these conditions, the integrated spectral density of the wave packet decreases, as well, with decreasing pulselength and fixed temporal field amplitude, as it is immediately observable when tuning the duration from 80fs (total population after excitation: $9.8 \cdot 10^{-8}$) to 60fs ($8.1 \cdot 10^{-8}$), due to the shortening of the dipole interaction's duration. For a 40fs short pulse, the excited population further decreases to $6.8 \cdot 10^{-8}$. With even shorter pulses, and therefore increasing spectral width, the overall population decrease can be compensated due to increasing FC factors for the higher energetic vibrations (compare eq. (5.13)). For a 20fs pulse duration it amounts $8.8 \cdot 10^{-8}$. However, the cost for the increased population is a very strong blueshift. In conclusion, for the coherent control experiments, which aim to monitor and control the dynamics in this energetic region of B state crossings with repulsive states, a choice of excitation pulse durations between 60fs and 80fs, i.e. relatively long ultrashort pulses turned out to be preferable.

To complete the explanation of the relative population increase when tuning the pulse duration from 40fs to 20fs the interference picture introduced in the previous section will be used. The total B state population dynamics for the 20fs pulse excitation has been already plotted in Fig. 5.7. In Fig. 5.9 the population dynamics for a 40fs long pulse excitation is shown (upper panel) together with the time dependent
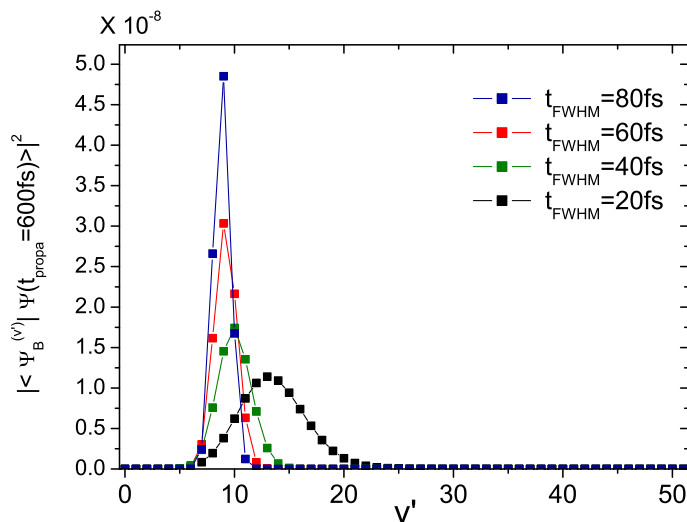
Fig.5.8. Spectral representations of excited B state wave packets are shown as a function of vibrational quantum number for 4 different excitation pulse durations. The decompositions of the wave packets into eigenstates of the B potential have been all performed for a propagation time of t_{propa}=600fs, after the termination of the excitation process. The trend of an increasing spectral blueshift with respect to the pulse carrier frequency (v'=9) can be observed for decreasing pulse durations. (Other simulation parameters: ε_F=2·10$^{-4}E_h/ea_0$, μ_{BX}=0.15ea_0)

electric field (lower panel). When the excitation pulse reaches its maximum, a total population of 8.46·10^{-7} has been excited. During the falling wing, the destructive interference cancels 92% of this population and after termination of the pulse only 6.83·10^{-8} remain. For a short pulse, the destructive interference due to the far wing excitation also acts strongly, however, still nearly 10% of the maximally excited population remain in the B state. This is because the falling wing of the excitation pulse is shorter, thus includes only half of the optical cycles of the field, namely 10 within one FWHM duration at the chosen fixed carrier frequency. The number of cycles is decisive for the efficiency of the interference, and 20 optical cycles in case of the 40fs pulse lead to a more effective depopulation process. Indeed, these observations of the interference effects taking place in the one pulse excitation of wave packets in the far red falling wing of the FC factors are analogous to the interference effects of a pulse train excitation process, which will be a matter of investigation in the next chapter. The optical cycles play the role of the subpulses in pulse trains, and just like here, the number of subpulses is decisive for the formation of sharp spectral features. This has been already emphasized within the presentation of our rational coherent control scheme in Sec. 4.3.1. The vibronic excitation mechanism presented here for optical cycles of 2fs period within an envelope of 80fs, will be transferred in
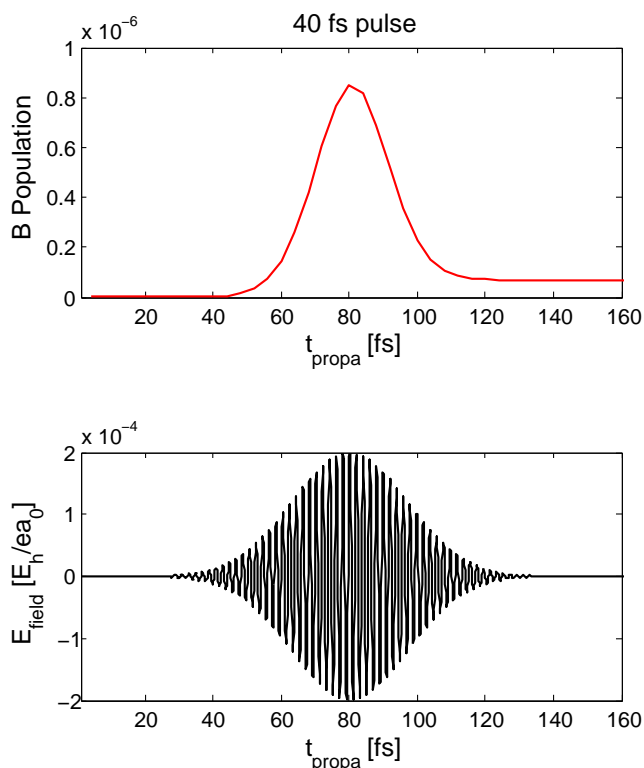
Fig.5.9.   a) Dynamics of the B state population during excitation with a t_{FWHM}=40fs pulse corresponding to a spectral width of $\Delta\lambda$=18nm with field amplitude ε_F=2·$10^{-4}E_h/ea_0$ shown in b) (μ_{BX}=0.15ea_0). The maximal population coincides with the pulse's temporal maximum at t_{propa}=80fs and amounts 8.46·10^{-7}. The final B state population amounts 6.83·10^{-8} after the excitation process.

the coherent control experiments to a train of around 80fs long pulses separated by the B state vibrational period of 250fs within an envelope of around 1.2ps. This way, besides of the spectral composition of the molecular wave packet concerning the molecular B state vibrations, the coupling of these vibrations to the phonon modes of the surrounding solid state environment will be controlled coherently. In order to further quantify the previously presented expected spectral blueshifts with respect to the experimental situation, besides of the RKR potential, the potential parameters derived from the spectral positions of the ZPL in the excitation spectrum (see Figs. 2.8 and 2.13 in Sec. 2.5.3) have been applied, too. Since the RKR potential was originally constructed in order to characterize the projection of the matrix B potential onto the Br_2 internuclear axis for high excitation energies, it is less appropriate for simulating the vibrational energies and eigenstates in the low energetic part of the B potential, respectively[4]. In Fig. 5.10 the positions of the spectral distributions' maxima of the excited wave packets, v'$_{max}$, are plotted as a function of vibrational numbers v'$_{exc}$ corresponding to carrier frequencies of pump pulses, which were again chosen in resonance with the vibrational eigenenergies of the corresponding potentials. The results for the RKR potential from [166] are compared to those for the

---

[4]The numerical treatments presented in the previous sections used the RKR potential. For the following simulations the B potential from the excitation spectra was used in order to allow for an accurate quantitative comparison of simulations and experiments in the low energetic part of the B state.
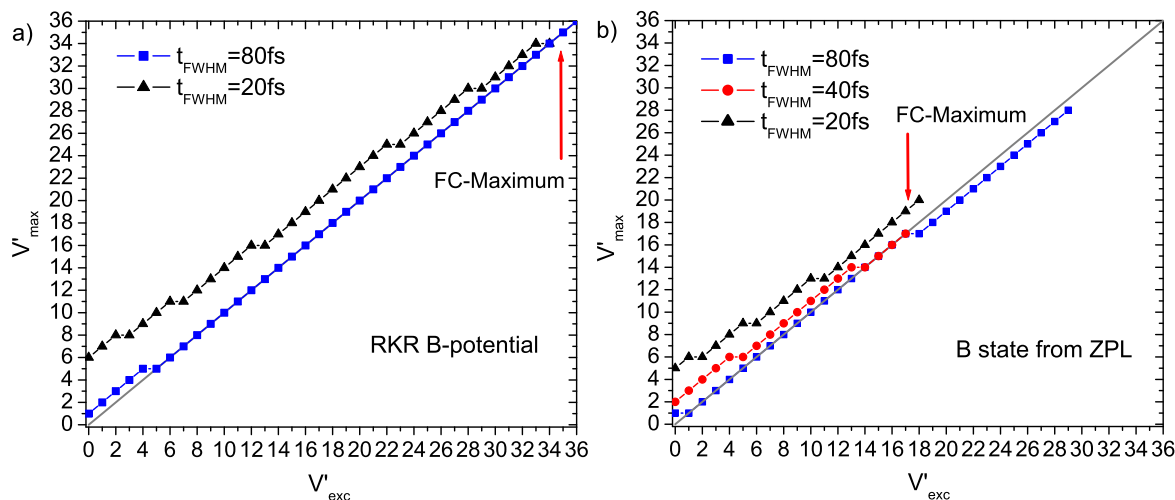
Fig.5.10. The vibrational numbers having maximal weight in the spectral representations of vibrational wave packets excited with Gaussian pulses of different durations on the effective B state potentials constructed a) from pump probe spectra and b) from the excitation spectra are plotted in dependence of the carrier frequency of the excitation pulses expressed in terms of B-state vibrational quanta. The Franck-Condon-Maxima are marked with arrows. (Other simulation parameters: $\varepsilon_F = 2 \cdot 10^{-4} E_h / e a_0$, $\mu_{BX} = 0.15 e a_0$)

Morse fit applied to the spectroscopy data in [83]. The shifts for the RKR potential are shown in Fig. 5.10 a) for an 80fs (blue squares) and a 20fs (black triangles) long excitation pulse. The FC maximum of this potential is marked by the red arrow. Here, a spectral shift only occurs for vibrational numbers smaller than $v'_{exc} = 4$ for 80fs long pulses. As already discussed before, much more drastic blueshifts occur for 20fs short pulses. Quantitatively, the observations also hold for the matrix potential used in b). Here, the spectral shifts are even less incisive, again for the 20fs long pulse, they extend up to 5 vibrational quanta close to the potential minimum and 3 quanta in the experimentally interesting region around $v' = 9$. The behavior for a 40fs long pulse is shown, too, in Fig. 5.10 b) (red circles). Also in this case a blueshift occurs and the deviation from the $v'_{max} = v'_{exc}$ line (gray line) is observable. Therefore, the choice of long pulse durations for the coherent control experiments remains reasonable for this potential, too. It shall be noted, that the potential used for b) is only a good effective matrix potential for the low vibrational quantum numbers. Its failing in the high energetic regime clearly shows up in the shift of the FC maximum around $v' = 17$ corresponding to 555nm, which is one of the last still resolvable zero phonon lines on the high energetic side of the excitation spectrum. Higher energetic zero phonon vibrations get more and more buried and shifted within a rising unstructured multiphonon background (compare Sec. 2.5.3).
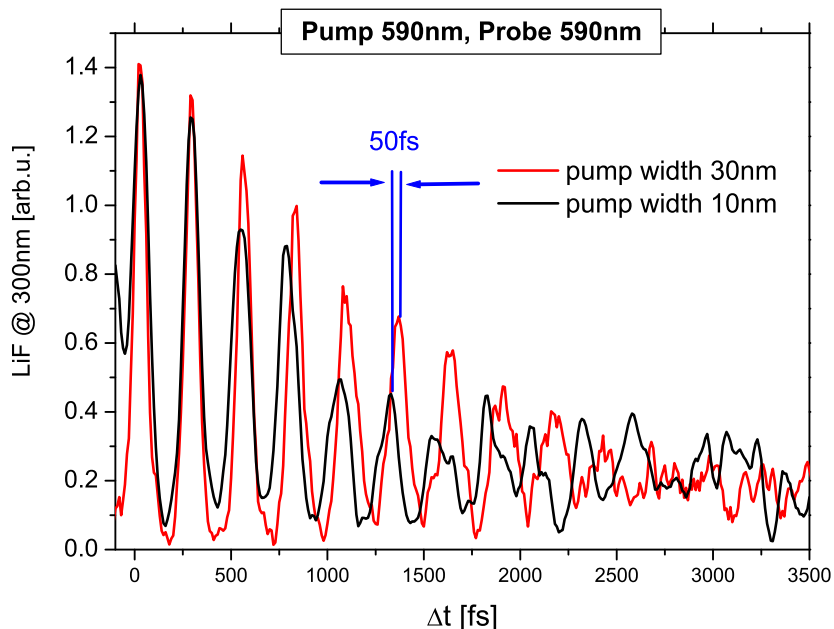
Fig.5.11. Comparison of measured pump probe spectra with short (t_{FWHM}=25fs and $\Delta\lambda$=30nm, red line, from [257]) and long (t_{FWHM}=75fs and $\Delta\lambda$=10nm, black line, this work) pump pulses. Excitations and probing was carried out at a central wavelength of 590nm in both pump probe spectra. Pump pulse energies (around 0.3μJ with a focus diameter of d=100μm on the sample) corresponding to field strengths in the linear excitation regime (see Fig. 5.6) were chosen. (For probe pulse energies (here around 0.5μJ) see discussion in Sec. 6.2.2).

For the RKR potential, an FC maximum at v'=35 is observed, i.e. $0.09E_h$ (compare Fig. 5.4) corresponding to 506nm, which is not very far from the gas phase value at 510nm from [109].

The spectral blueshifts presented here have been also observed experimentally and their signatures in pump probe spectra are shown in Fig. 5.11. The spectra were excited at a central pump pulse wavelength of 590nm and probed with a second short pulse centered at 590nm. The wave packet dynamics excited with a 25fs long pulse, having a spectral width of around 30nm is depicted in red and was measured by M. Gühr [257]. For the pump probe spectrum shown as a black line in Fig. 5.11, a 75fs long and correspondingly 10nm broad pump pulse was used (this work). The spectra have been shifted on the time axis in order to match in the first maximum, corresponding to the first excursion of the wave packet in the B potential. After five vibrational roundtrips of the wave packet an accumulated vibrational period deviation of 50fs is observable. Despite the same excitation pulse wavelength, the shorter pulse leads to the spectral blueshift of the excited wave packet. Due to the anharmonicity of the B potential, the blueshifted weight of the spectral distribution

corresponds to the vibrational period increase. The observed roundtrip time increase of 10fs per roundtrip corresponds to a spectral blueshift of around 10nm, thus to a shift by two or three vibrational quanta (compare Fig. 2.8). This is in quanitative agreement with the calculation presented in Fig. 5.10 b).

5.3 Spectral representation of the excitation with pulse trains

The spectral decompositions introduced for the single Gaussian excitation pulse in Sec. 5.1.1 will be applied to the excitation with trains of ultrashort Gaussian pulses, which is at the heart of the rational coherent control scheme presented in Sec. 4.3.1. An extension of simulations from single pulse excitation to the excitation with a train of pulses has been introduced in [89] and discussed in comparison with measured control spectra. Here, the successive enhancement of B state vibrational wave packets by constructive interference and their destructive extinction will be analyzed in the spectral domain. Our coherent control mechanism involves constructive and destructive interferences among the coherent constituent states of the combined chromophore-bath-system including phonon modes coupled to the vibronic molecular dynamics. In the simulations, however, again only the gas phase properties of the ultrafast vibronic excitation from the vibrational ground state of the molecular X state to vibrational states of the covalent B state are considered.

The in total 1.2ps long excitation pulse train is shown in Fig. 5.12 in the time domain. It consists of five subpulses, with their centers shifted by 250fs, which is the B wave packet's vibrational period at a central excitation at v'=9. As already discussed in Sec. 4.3.1, the subsequently following subpulses induce interference effects in the excitation region for the just created partial wave packets with previously created ones, which return into the excitation region at integer multiples of the roundtrip time. The different chirps of the subpulses compensate for the dispersion of the wave packet in the anharmonic potential and guarantee maximal overlap of subsequently created parts of the wave packet as discussed in Sec. 3.2.1. The central subpulse (centered at 600fs) remains unchirped and is thus the shortest one with its 50fs duration, while for the second and fourth subpulse negative and positive chirp parameters of ∓0.29fs·cm have been applied, respectively. The outer subpulses have chirps of ∓0.58fs·cm, respectively, and are therefore the longest ones. The arrows in Fig. 5.12 indicate propagation times at which spectral decompositions of the excited B state wave packets are shown in the following Figs. 5.13 and 5.14. In case of constructive interference all subpulses have the same temporal phase matching the
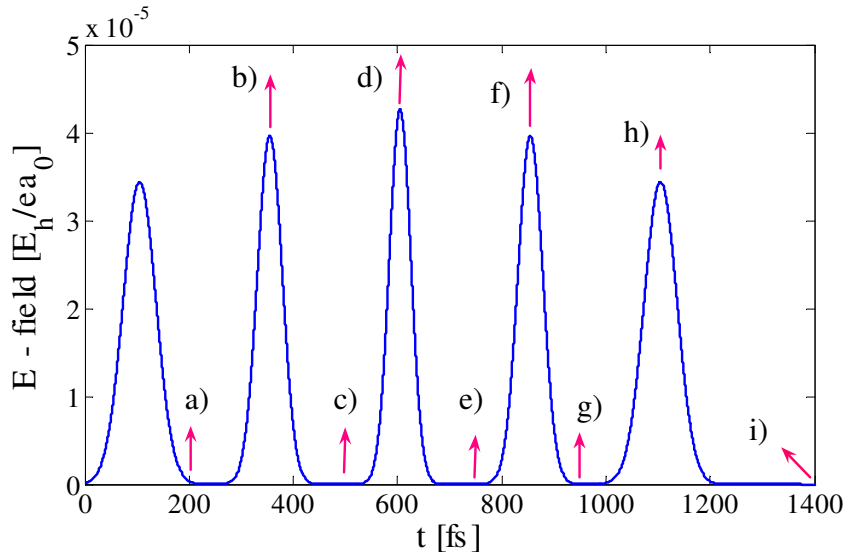
Fig.5.12. Envelope of excitation pulse train consisting of five 50fs long subpulses separated by the B state vibrational period of 250fs in the excitation region around 590nm (carrier frequency at v'=9). The overall pulse duration is 1.2ps. The arrows mark the propagation times at which spectral decompositions have been calculated and are shown in Fig. 5.13 and Fig. 5.14, respectively.

carrier frequency corresponding to v'=9. After termination of the first subpulse at 200fs a distribution of about 5 vibrations around v'=9 show up in Fig. 5.13 a). In b) the center of the second subpulse is reached and the excitation of the high energetic blue wing with high FC factors dominates the spectral distribution. In the falling wing of this subpulse, however, the blue wing is extinguished by destructive interference and does not show up after the termination of the pulse, as depicted in c). In contrast, the resonant parts of the wave packet interfere constructively with the wave packet in a) and a higher than linear increase can be observed when comparing the weights of v'=9 in a) and c). The third subpulse, i.e. the central one in the train, excites the blue wing again. However, its relative weight is strongly reduced in d) with respect to the nearly resonant part. The resonant part is increased due to its still ongoing constructive interference. The falling wing of this subpulse is again responsible for the excitation cleaning seen in e). With the following two subpulses the weight of the nonresonant blue wing further decreases at propagation times corresponding to the maxima of the pulses in f) and h). At the termination of the whole pulse train at t_{propa}=1.4ps shown in i), a spectral decomposition of the wave packet similar to that shown in a) remains, however, more intense by almost a factor 20. A trivial addition of the wave packets created by the five equally strong subpulses would lead to a population increase by a factor 5 with respect to the
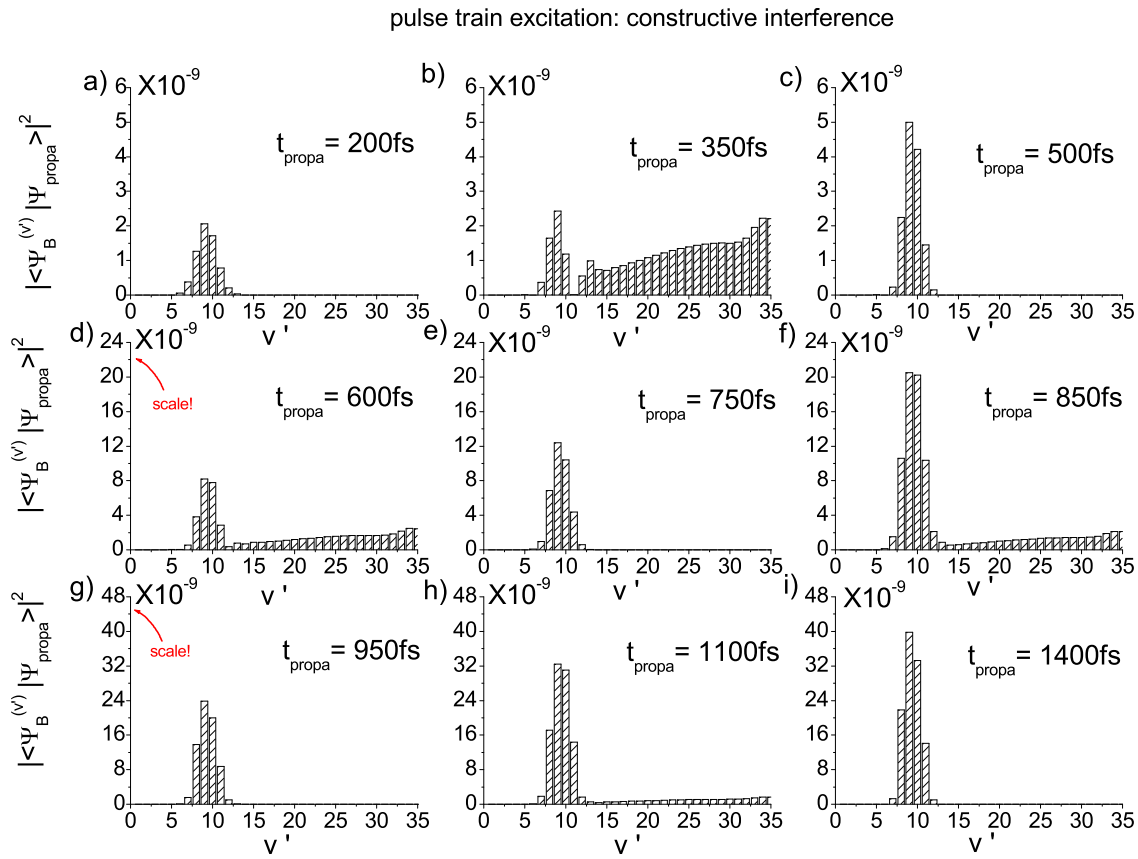
Fig.5.13. a)-i) Spectral coefficients of the vibronic B state wave packet excitation with the pulse train displayed in Fig. 5.12 for 9 different propagation times marked by the arrows in Fig. 5.12. In order to achieve constructive interference the relative phase of the subpulses was set to zero.

population excited by only one subpulse. Thus, the effect of constructive interference is obvious. According to eq. (4.4) in Sec. 4.3.1, the maximally achievable factor is 25, which requires optimized chirp parameters.

In order to simulate the destructive interference case, the relative phases of neighboring subpulses in the train have been set to $2\pi/n$, where n=5 is the number of subpulses. The spectral decomposition of the results is shown in Fig. 5.14 a)-i) for the selected propagation times from Fig. 5.12. At times after the termination of the first three subpulses, shown in a), c) and e), Gaussian-like distributions are observable. While after the second subpulse in c) the population still increases as compared to a), after the central pulse in e) a destructive interference sets in, first for the slow energetic parts (v'=7 and 8). After the last two pulses also the central vibrations at v'=9 and 10 experience destructive interference, as depicted in g) and i). At the termination of the pulse train in i), however, the outer, v'=8 and v'=11 contributions from the first excitation pulse shown in a) remain. On the one hand this indicates nonperfect chirp parameters. On the other hand, the
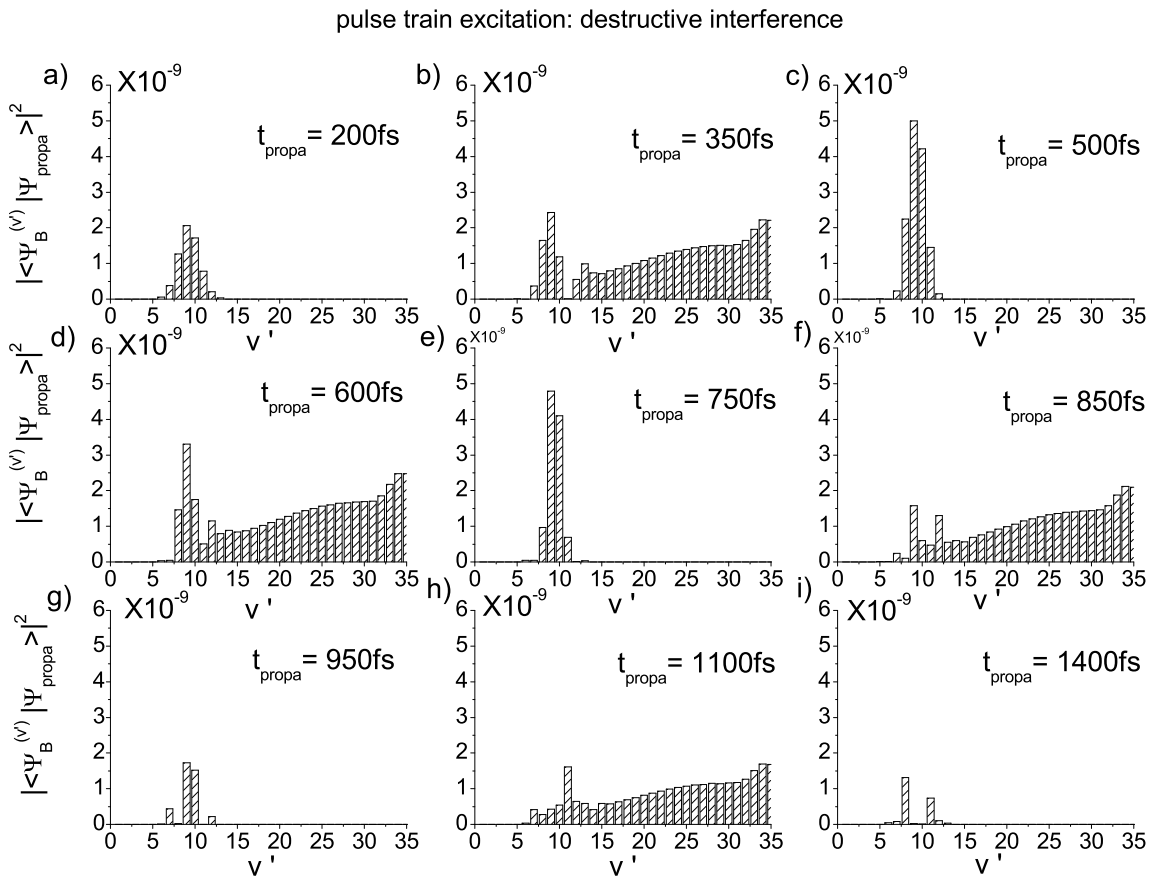
Fig.5.14. a)-i) Spectral coefficients of the vibronic B state wave packet excitation with the pulse train displayed in Fig. 5.12 for 9 different propagation times marked by the arrows in Fig. 5.12. In order to achieve destructive interference the relative phase of the subsequent subpulses was set to $2\pi/n$ where n=5 is the number of subpulses in Fig. 5.12.

number of subpulses required for complete extinction might not be reached with just five subpulses. Indeed, while the extinction of the nonresonant blue wing by the subsequent optical cycles within the envelope of each subpulse take place in a time interval of around 100fs ($2 \cdot t_{FWHM}$), for the extinction of the nearly resonant parts, more than 1.2ps are needed and only perfect phase relations guarantee complete cancellation. Especially, when comparing the energetic region around v'=9 from d) to e), one observes, that the negative interference of this part happens during the rising wing of the excitation pulse and shows maximal effect in the maxima, just when the new B wave packet is excited and overlaps with the formerly excited one returning back in the excitation region. The resonant part excited during the falling wing of the third, central subpulse has no temporarily and spatially overlapping excitation partners. Therefore, it further increases from c) to e). It has to wait to be extinguished in the rising wing of the following subpulse in f).

The interference mechanism presented here will be transferred to the phonon coupled molecular vibrations in the experiments presented in Chapter 6. A comparison of simulated pump probe spectra using the just discussed pulse train excitation with measured coherent control spectra will be provided later in Sec. 6.2.1.

5.4   Simulated pump probe spectra

In the present section we turn back to the single pulse excitation. Measured pump probe spectra on Br_2:Ar will be compared to simulated pump probe spectra using the B state potential from the excitation spectra. The deviation of experiment and gas phase dynamics will be attributed to vibrational energy relaxation in the higher energetic part of the potential, which shows increased matrix interaction, in Sec. 5.4.2. In the deeper energetic region of crossings with repulsive states the signatures of matrix induced predissociation will be identified in the pump probe spectra by comparison with the simulation for the free molecule in Sec. 5.4.1.

5.4.1   A matter of predissociation

The B state vibrational wave packet dynamics at an excitation wavelength of 590nm with a pump pulse duration of 60fs has been monitored by probing it in a two photonic excitation to charge transfer states with a second time delayed, 30fs short probe pulse also centered at 590nm. The pump probe spectrum was recorded as a function of time delay Δt by detecting the light induced fluorescence at 300nm (see Sec. 4.2 and Sec. 6.1). In Fig. 5.15 a comparison of the measured spectrum (black line) and a simulation (red solid line) for the gas phase molecule with adapted pulse parameters is shown. The simulation of the pump probe spectra for the free Br_2 wave packet has been carried out following the numerical method presented in Sec. 3.2 and Sec. 3.3.2, respectively. Both spectra show B state wave packet oscillations with an average vibrational period of T_{vib}=250fs. A strong decrease of modulation contrast is addressable to the dispersion of vibrational constituent states of the wave packet in the anharmonic B potential. However, in the simulation (red solid line) the mean value of the oscillations (red dotted line) remains constant, according to the population conservation. In contrast, the measured spectrum (black) shows a strong decrease of the mean value, which can be well fitted by multiplication of the simulated spectrum with a decaying exponential function with an inverse rate constant of 2.5ps (blue line in Fig. 5.15). The fitted inverse rate constant is in perfect agreement with the spectroscopic results for predissociation timescales determined for excitation spectra in [83] (see also discussion of Fig. 2.12 in Sec. 2.5.3).
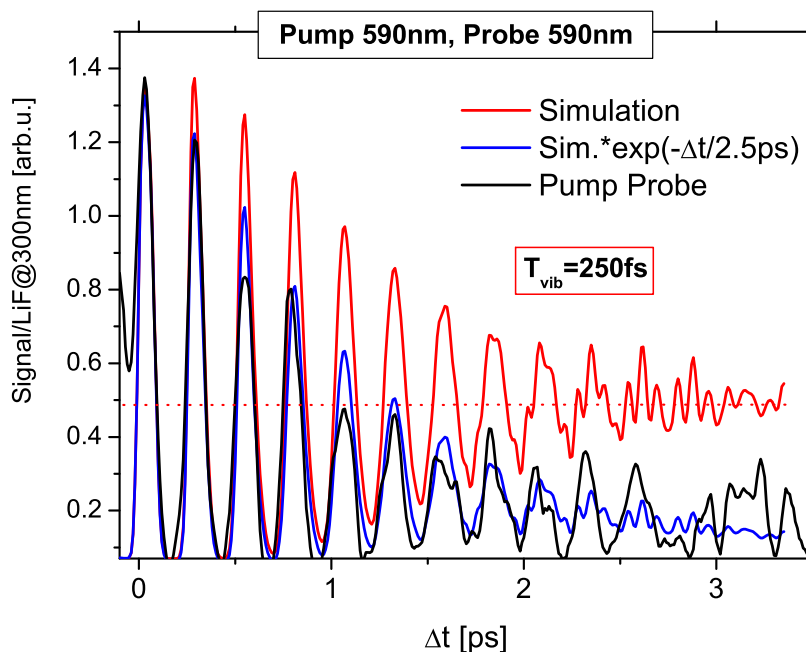
Fig.5.15. Comparison of measured (black, same as in Fig. 5.11) and simulated (red) pump probe spectra excited and probed with pulses centered at 590nm. The blue line shows the simulated spectrum overlaid with a decaying exponential rate function. In all cases pump pulses with t_{FWHM}=75fs and probe pulses of t_{FWHM}=40fs were applied and the excitation pulse energies in the linear regime (see Fig 5.6).

They correspond to a depopulation of the B state by 10% per roundtrip via nonadiabatic population transfer to one or several dissociative states. These predissociation probabilities coincide with those predicted for the consiered energetic region from lifetime arguments, presented in Sec. 2.5.3. The time evolution of the process is thus demonstrated here on a quantitative level. It will be indispensable for the coherent control of this environment induced reaction.

5.4.2   A matter of dissipation

The first pump probe spectra on Br_2:Ar presented in [88] show, that for shorter excitation wavelengths, from 580nm on, a vibrational energy relaxation of the B state wave packet due to the increasing interaction with the matrix atoms are dynamically observable, and a quantitative analysis of vibrational energy relaxation rates has been carried out. In the following, a comparison of simulated and measured spectra in this higher energetic region will be accomplished. A simulated spectrum at a 575nm pump and 590nm probe wavelength is shown in Fig. 5.16 a) in red, together with a pump probe spectrum measured with the same pulse parameters shown in black. Again, a decrease of the mean value is only observable in case of the measured
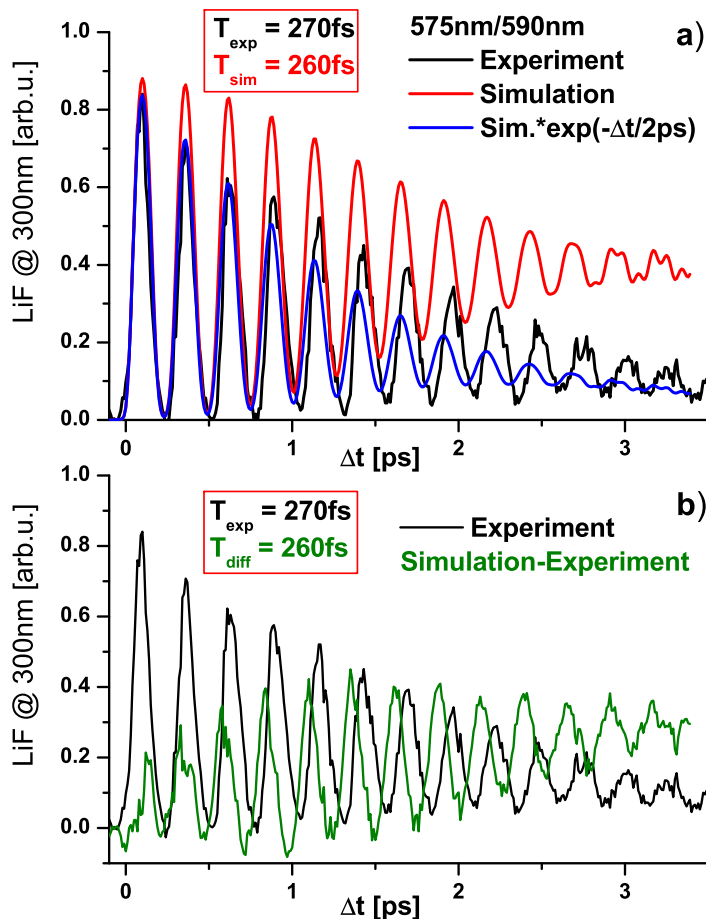
Fig.5.16. a) Comparison of measured (black) and simulated (red) pump probe spectra, pumped at a wavelength of 575nm with (t_{FWHM}=60fs, pulse energy on the sample 0.2μJ) and probed at 590nm (t_{FWHM} =40fs, probe energy 0.3μJ). Multiplication of the simulated spectrum with an exponential decay (blue) reveals a vibrational relaxation timescale of around 2ps. b) The measured pump probe spectrum from a) (black) has been subtracted from the simulated spectrum a) and is shown green (see text for discussion).

spectrum and the simulation only shows the modulation contrast decrease due to dispersion. Similar to the previously presented analysis, the mean value decay can be reproduced well by fitting an exponential decay function to the simulated spectrum (blue line in Fig. 5.16 a). The fitted inverse rate constant of 2ps corresponds to a 13% decrease of the probed population per vibrational period. In a first step, we attribute the exponential decay of the mean value to vibrational energy relaxation of the B wave packet due to kinetic energy transfer to the surrounding matrix atoms (see Sec. 2.3). The relaxation of the wave packet leads to a leaving of the probe window and thus to a successive lowering of the pump probe signal. However, relaxation rates derived in [88] predict a slower dissipation in this energetic region

of the B state. A maximal signal loss of up to 10% per roundtrip can be expected in order to stay within the errorbars of rate constants from [88]. Thus, to explain the faster than expected decrease of the mean value which amounts 13% per roundtrip, the participation of another depopulation process, namely the previously discussed nonadiabatic population transfer to a repulsive states is assumed. This will be confirmed in the following discussion.

We excpect that vibrational energy relaxation of the wave packet proceeds with time and lowers the vibrational energy of the wave packet. Due to the anharmonicity of the B state this should lead to a shortening of vibrational period, as compared to the simulation (see also Fig. 2.7 b). Indeed, in Fig. 5.16 a) simulated and experimental spectra run out of phase. The average vibrational period of the measured B wave packet dynamics is T_{exp}=270fs and T_{sim}=260fs for the simulated spectrum. This is however counterintuitive, since a relaxing vibrational wave packet should propagate with a decreasing vibrational period deeper in the potential well. Actually, the relaxation leads the wave packet closer to the crossing region and a subsequent transfer to the dissociative state occurs. Thus, only the high energetic components are detected for large delay times and the contribution from the lower energetic states decreases. The missing of the low energetic parts is in accordance with the Landau-Zener formula for predissociation, stating highest predissociation probabilities for vibrations close to the crossing (see Sec. 2.3). The spectral narrowing of the wave packet also shows up in a decrease of dispersion during the time evolution: While for the first three maxima, the modulation contrast of the experimental (black) and the fitted simulated (blue) spectrum still agree, for greater delay times a much higher modulation contrast is still present in the experimental case. In order to cross-check the interpretation, a subtraction of the measured spectrum from the simulation is shown in Fig. 5.16 b) in green. Indeed, the "missing" contribution in the measured spectrum shows the vibrational period of T_{diff}=260fs according to the low energetic components dominating in the simulation. Thus, the assumption of an overlaid predissociation is confirmed.

Turning back to the population loss of 13% per roundtrip derived in Fig. 5.16 a), and a maximal energy relaxation caused signal loss of 10% per roundtrip, a minimal predissociation efficiency of 3% per roundtrip for this energetic region can be derived. In Sec. 6.3.2 a maximal efficiency of 5% per roundtrip will be derived from pulse train excited pump probe spectra.

The combined predissociation-relaxation process quantified here with help of gas phase simulations exemplarily for a relatively simple pump probe spectrum monitoring only B state dynamics, will turn out to be essential for a dynamical monitoring of the coherently controlled matrix induced predissociation in Chapter 6.

Chapter 6

Experimental results and discussion

The present chapter contains the results of time resolved experiments monitoring the ultrafast dynamics of Br_2 in solid Ar and its coherent control. In the first part, selected pump probe experiments will be presented and discussed. They will serve as a reference in the analysis of the coherent control experiments which will be presented in the following sections. A decomposition of the wave packet dynamics into A and B state contributions based on polarization sensitive pump probe spectroscopy will be carried out first, followed by the characterization of probe conditions involving charge transfer (CT) states. Afterwards, coherent control experiments carried out in the weak phonon coupling regime will be presented in Sec. 6.2.1. A successful coherent enhancement of B contributions relative to the A state achieved by the excitation with trains of pulses with adapted phases will be shown. Next, in Sec. 6.2.2, a systematic extension of the coherent control to the strong phonon coupling regime will be introduced. The relative weights of contributions from different electronic states which have been determined from single pump probe spectra will be needed for a quantitative analysis of interference phenomena occurring in the coherent excitation process with ultrashort pulse trains. Their discussion is given in Sec. 6.3. The weight factors will turn out to be indispensable also for the identification of predissociated population in Sec. 6.4, allowing for a quantitative analysis of the rational coherent control of matrix induced predissociation, which will be discussed at the end of this chapter.

6.1 Pump probe spectra and their discussion

As already mentioned, the first time resolved experiments on the system Br_2:Ar have been carried out in our working group by M. Gühr [88]. They mainly concentrated on

the high energetic region of the B state potential in order to construct an effective B state potential in the region with strong phonon coupling and to derive vibrational energy relaxation rates [166]. Most of the measurements employed UV pulses in a one-photonic probe step. However, also an extensive set of pump probe spectra with two-photonic probing was recorded by Gühr, which has not been published yet. These measurements were taken as references and served as an orientation for spectra taken in this work [257]. They have been compared with measurements performed in this work with respect to their pump and probe polarization properties. They have been carried out with broad pulses of around 30nm FWHM, correspondingly the pulse durations down to 20fs were achieved. A comparison of the excitation based on the calculations presented in the previous Chapter 5, however, revealed, that the excitation with short pulses leads to a shifting away from spectral weight of the wave packet from the crossing to the blue energy side, due to increasing Franck-Condon factors. Therefore, the pump probe spectra presented here were carried out with pulse durations of around 80fs, corresponding to spectral widths of 10nm to allow for a systematic analysis of the predissociation process. For clarity of presentation, in the following part only pump probe spectra with those two pump photon energies will be discussed, which have been also applied in the coherent control experiments. Other spectra are collected in Appendix B. For a detailed road map describing interpretation of pump probe spectra of chromophores in the condensed phase, the reader is referred to [232].

6.1.1   Polarization dependence

In the early stage of this work, pump probe and coherent control experiments have been carried out with elliptically polarized pulses, leading to a weaker selectivity as expected from the photoselection rules presented in Sec. 4.2.1. First, such a pump probe spectrum will be presented and compared to a corresponding measurement with linear polarizations. In all presented cases the probing took place in a two-photonic probe step with a central probe wavelength of 590nm, as shown in Fig. 6.1 a). The polarization dependence will be exemplified on spectra measured at a central excitation wavelength of 575nm. Then, an excitation deeper in the potential with 585nm will be discussed.

Elliptical polarization

Besides of the relative orientation of the major axis of the polarization ellipse of pump and probe pulses, the fluorescence was detected from two different bands 1 and 2 of the CT states shown in Fig. 2.10 of Sec. 2.5.2 following the pump probe scheme
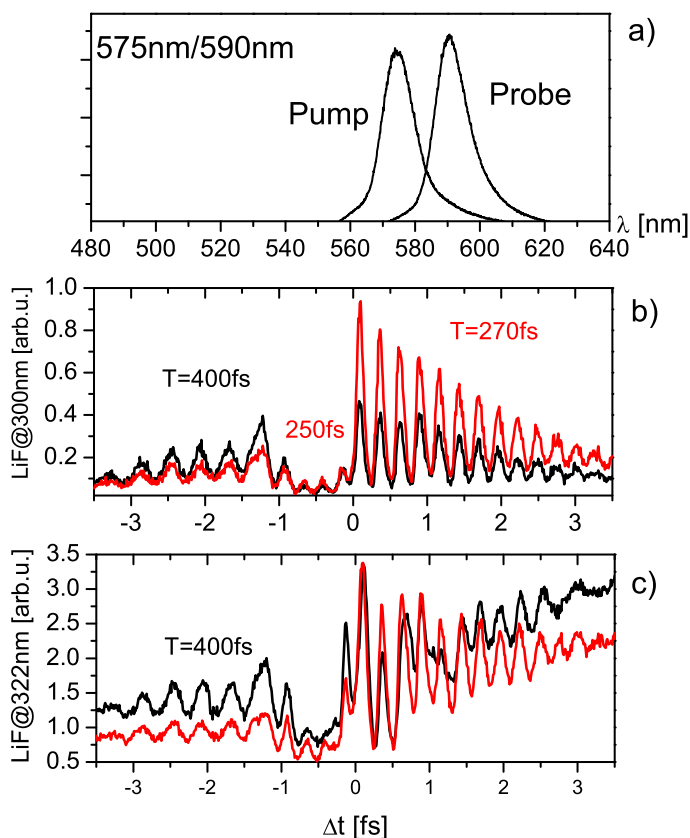
Fig.6.1. a) Measured spectra of elliptically polarized pump and probe pulses with corresponding pulse lengths of t_{FWHM}=60fs (pulse energies on the sample: pump 0.2 μJ, probe 0.3 μJ). b) Corresponding pump probe spectra detected at 300nm with parallel (red) and perpendicular (black) relative polarizations. c) Same as b) recorded at a fluorescence wavelength of 322nm.

introduced in Sec. 3.3.2. The resulting pump probe spectra are shown in Fig. 6.1 b) for 300nm and c) for 322nm fluorescence. In b), for positive delay times a clear B state dynamics with an average vibrational period of T=270fs is observable for parallel (red) and also perpendicular (black) relative orientation of pump and probe polarizations with an intensity ratio of 2:1. For negative delay times, a completely different dynamics is observed. Here, pump and probe pulses change their roles and the 590nm pulse acts as the excitation and the 575nm pulse as the probe pulse. The overall intensity decrease can be attributed to smaller FC factors with decreasing excitation photon energy. In this case, a T=250fs B roundtrip time is observable only for three vibrational periods. From about Δt=-1ps on an oscillation with a 400fs period dominates the spectra. A similar behavior can be registered for the detection of 322nm fluorescence in c). However, here for positive values of Δt, additionally to the B state vibrations an unmodulated, increasing background shows up at about 700fs. In the perpendicular case it dominates the spectrum that much, that the B state signatures get more and more buried and after 2ps they are not discernible anymore. In the parallel case this background shows up, too, however, with a smaller weight. Comparing the perpendicular spectra (black) in b) and c) for $\Delta t > 0$, a much larger signal intensity drop occurs from the first to the second B state maximum in the 322nm case than in the 300nm
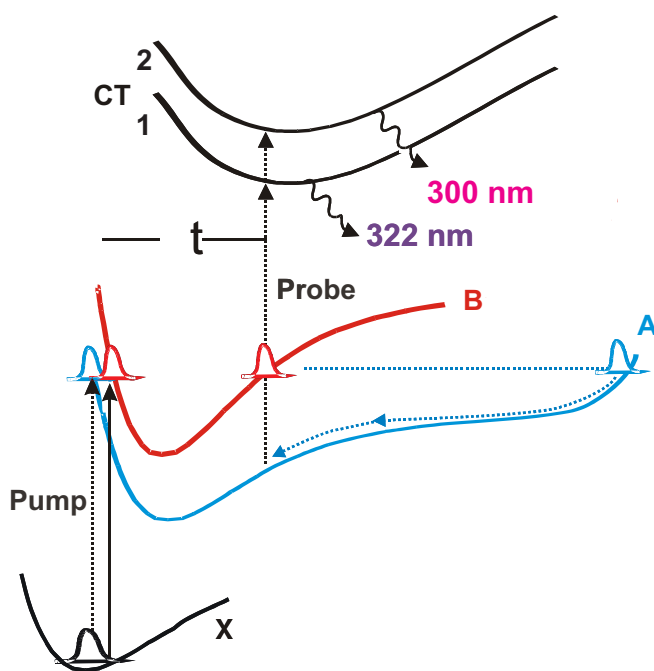
Fig.6.2. Schematic representation of the pump probe mechanism, showing excitation of a B (red) and A (blue) wave packet from the ground state X, subsequent probing to the 1st (CT1) and 2nd (CT2) charge transfer state manifold and corresponding light induced fluorescence at 322nm and 300nm.

spectra. In addition, in c) an unstructured overall background is visible. The just listed observations will be now explained with help of the scheme drawn in Fig. 6.2.

According to the absorption spectrum presented in Sec. 2.5.1 together with the B state also an A state wave packet is excited with an ultrashort pump pulse. Since the A excitation takes place high above the gas phase dissociation limit, the wave packet propagates outwards in the potential without being reflected. It is probed together with the B wave packet in its first excursion and contributes to the first strong peak in the pump probe spectra on the right and left from $\Delta t=0$. The B wave packet is probed around the outer turning point of the B potential. When the B wave packet reaches the probe window in its second recurrence, the A one is just on its way outwards, following a dissociation-like process until it experiences the bending up of the potential's outer wing due to the cage atoms. In an inelastic-like collision it loses a large part of its kinetic energy and slides down the potential wing until it shows up again in a second probe window in the bound part of A. At about 700fs the A state dominates especially the perpendicular pump probe spectra, which is in qualitative agreement with the photoselection rules from Sec. 4.2.1. Since in the parallel case, according to the photoselection rules, the A contribution is weaker than the B part, for positive delay times, besides of the increased background, no strong disturbance of the B dynamics is observable. In the case of 300nm fluorescence detection, any A contribution is hardly recognizable. The reason is that the fluorescence results from a probing to the energetically higher lying second charge transfer manifold (CT2). The probe photon energy is just not sufficiently high to probe an A state

contribution from the relaxed dynamics deep in the A potential well to CT2 states. In that sense, recording the 300nm fluorescence is a spectroscopic trick, allowing to suppress the A contributions in detection even though they dominate in absorption. However, the trick doesn't work for arbitrary pump probe wavelength combinations, as it can be seen on the left side of Δt=0. Here, also for 300nm, and in both, perpendicular and parallel case, after about 1ps, instead of the 250fs B state period, a 400fs period is visible, monitoring the dynamics of the A state in the bound part of the potential, after termination of the strong vibrational energy relaxation. Obviously, the deeper excitation with 590nm in combination with the higher probe photon energy corresponding to 575nm, allows for an efficient probing also deep in the A state. Although, the same A period is observed here for 322nm and 300nm detection, for the 300nm spectra, the amplitude mean value decreases in the 300nm case, whereas it does not for 322nm. Therefore we conclude, that in b) the probing takes place higher in the A state, and attribute the decrease of the mean value to a relaxation out of the probe widow. Correspondingly, we will address the probing of A in the 300nm case to an ionic state belonging to the CT2 manifold (see Sec. 6.1.2), like in the B case. It is also notable, that after experiencing strong scattering with the matrix atoms, the molecule does not lose its vibrational coherence and recombines to a compact localized A wave packet [165]. Also for the B state, a decrease of the mean value amplitude is observable, and its origins have been discussed in combination with the simulations of the free molecular B state wave packet dynamics in Sec. 5.4.

Finally, it shall be emphasized that without the spectroscopic trick applied, the B wave packet dynamics observed in the pump probe spectra are always overlayed with A dynamics. Indeed, for pump probe combinations as chosen for positive time delays, the B wave packet is seen only once in an isolated manner, in its second roundtrip while the first outward motion of the A state and the recombination process take place. In contrast, for combinations similar to that for negative time delays, the B wave packet can be seen isolated for two vibrational periods for the following reasons: (1.) a greater pump wavelength leads to a decreased B period, (2.) with a smaller probe wavelength the A wave packet is probed deeper in the A well, increasing the relaxation time. In the coherent control experiments, a cleaning of the excitation of the B state from the dominant A contributions can be achieved already in excitation as it will be shown later.

Linear polarization

Pump and probe spectra recorded under the same energetic conditions as just presented will be now discussed quantitatively with regard to the polarization sensitivity according to the photoselection rules from Sec. 4.2.1. To this end, instead of
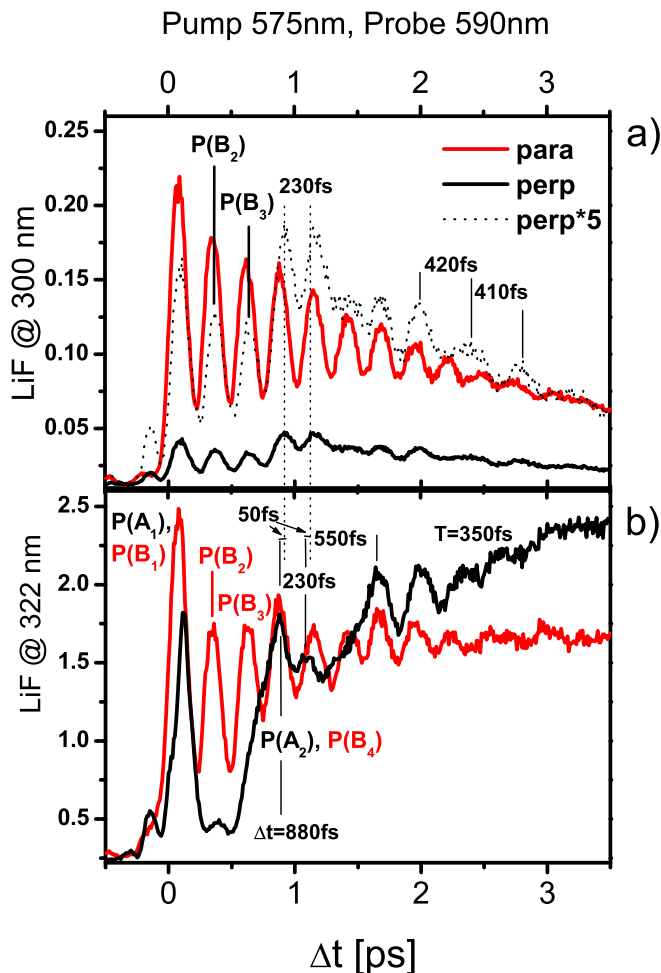
Fig.6.3. Polarization sensitive pump probe spectra with linearly polarized pump and probe pulses of around t_{FWHM}=60fs durations with parallel (red) and perpendicular (black) relative polarizations. Detection of 300nm LiF is shown in a) and 322nm in b). The peaks resulting from the ith passage of the A and B wave packets through their probe windows are denoted $P(A_i)$ and $P(B_i)$, respectively. (Pump energy: 0.2μJ; Probe energy: 0.4μJ)

elliptical, linear polarization was chosen to allow for an experimental verification of the theoretically predicted state selection conditions given for an ideal, non-depolarizing sample with isotropically oriented molecules.

In the spectra depicted in Fig. 6.3 a) parallel (red) and perpendicular (black, solid) relative pump and probe pulse polarizations have been applied and the 300nm fluorescence is detected. As expected, the parallel spectrum shows predominant B state wave packet dynamics with an average period T=270fs. The A state contribution is, also as expected, very weak and only clearly observable in the perpendicular case. However, a much more pronounced $\perp$ to $\parallel$ ratio of about 5:1, as compared to the 2:1 ratio of the elliptical case, is observable here. For convenience, the perpendicular spectrum has been scaled with this factor 5 and is also shown as dotted black line. Again, in this spectrum, two isolated B maxima, labelled $P(B_2)$ and $P(B_2)$, show up during the dissociation-recombination process performed by the A state molecules. Here, the probing of the relaxed A wave packet in the bound part of the potential shows more significantly than for the elliptical case discussed before, that the 300nm A probe window catches the relaxing A wave packet in an energetically
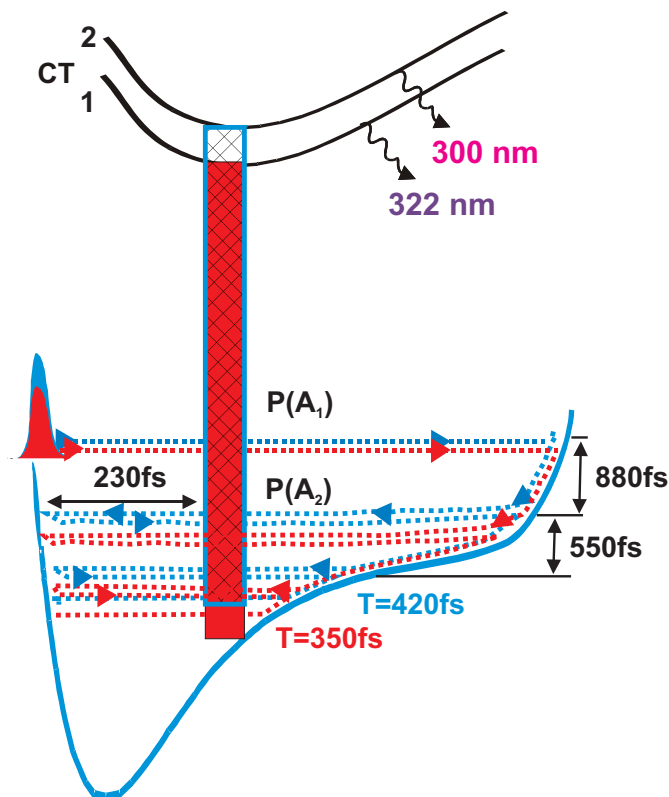
Fig.6.4. Scheme depicting the probing conditions for the vibrational relaxation of the A wave packet showing the CT1 (red) window, catching the low energetic red part of the wave packet and the CT2 (blue crosshatched) window, monitoring the high energetic constituents' vibrational relaxation dynamics. (For labels $P(A_1)$ and $P(A_2)$ see caption of Fig. 6.3)

higher lying part than the 322nm window probing to the CT2 manifold. Indeed, here the relaxation into the window shows up at 1-1.2ps. Then, the continuing fast relaxation leads out of the window, indicated by a strong decrease of the mean value and simultaneously of the vibrational period, also apparent in Fig. 6.3 a). In the 322nm fluorescence shown in b), a completely different view of the A state relaxation process is observable, namely its lower energetic part, as sketched in Fig. 6.4. In both the 322nm and the 300nm case, the second maximum of the A wave packet, labelled $P(A_2)$, shows up after the inelastic collision with the matrix atoms. However, for 322nm the maximum occurs at a delay time of Δt=880fs, whereas for 300nm, only 50fs later, as indicated by the shift between solid and dotted vertical lines in Fig. 6.3. The next maximum is delayed by 230fs, which is the propagation time of the A wave packet to the inner turning point of the potential and back into the probe windows. This time separation is comparable for the blue parts of the wave packet probed to CT2 and the red parts probed to CT1, however, the slower blue parts enter the window 50fs later. A second part of the strong relaxation process takes place for the second outwards propagating A wave packet. This time, it takes only around 550 fs until an A state maximum shows up in the probe window again. For later delay times, the CT2 window only catches the high energetic oscillations with around 420fs period, while the CT1 window monitors the dynamics of the further relaxing red parts with around 350fs period.

This self consistent picture of the A dynamics indicates a large energetic width covered by the A wave packet. Initially excited as a superposition of scattering states, above the gas phase dissociation limit, the redistribution into bound states goes along under preservation of vibrational coherence, although involving a large number of vibrational levels in the newly populated bound superposition state. However, the huge energetic width also goes along with a strong dispersion of the A wave packet when populating the bound part of the anharmonic potential. Therefore, after the first step in the relaxation process (taking around 880fs, see Fig. 6.4), none of the two sketched probe windows is left empty anymore, i.e. the A state signal does not decrease to zero. The structure of the oscillations reflects a refocusing process of the A wave packet during relaxation. A deeper energetic probing, like the one for negative time delays which has been discussed for the spectra of Fig. 6.1, then monitors dispersion-rich, but well-modulated A dynamics.

Turning back to the polarization dependence, the 322nm spectra in Fig. 6.3 b) also show the high electronic state selectivity achieved by the linearly polarized pulses. The isolated B wave packet in its second roundtrip is hardly discernible here in case of the perpendicular polarization. A quantitative discussion will be given within the discussion of the pump probe spectra shown in Fig. 6.5. For these spectra the central wavelength of the probe pulse has been tuned to 585nm. In this energetic region, the coherent control of the matrix induced predissociation will be carried out, and the pump probe spectra, as well as the polarization analysis presented next will be used within a decomposition method in order to identify the matrix induced predissociation dynamics within the coherent control pump probe spectra.

The signals detected at 300nm in Fig. 6.5 a) and 322nm in b) again show the pronounced state selectivity observed in the 575nm pumped spectra before. In the parallel case of a) a pronounced B dynamics with an average period of T=260fs is observed. On the left side of $\Delta t=0$ the 590nm excitation probed with 585nm can be seen. The pronounced intensity drop of one order of magnitude can as well be attributed to the high selection due to linearly polarized pulses. Here, the exponential increase of FC factors in the treated energetic region is reflected (compare Fig. 5.4). The corresponding dynamics is shown in enlarged view in the inserts of Fig. 6.5 a) and b). Qualitatively, again the just discussed type of combined A and B dynamics shows up, here with a B state period of 250fs. The B state dynamics at 590nm excitation has been already discussed in combination with the simulations presented in Sec. 5.4.1. A relatively small B state peak $P(B_2)$ is observed in the perpendicular case of b) and a predominant A dynamics is monitored, showing similar characteristic behavior as explained before.
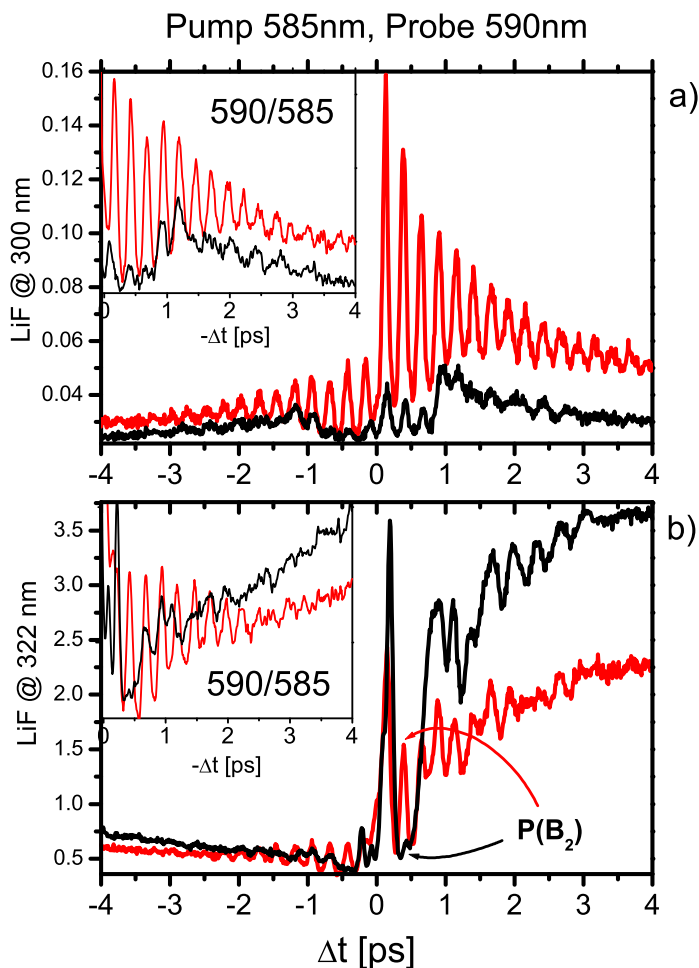
Fig.6.5. Pump probe spectra excited with 585nm pump pulses (t_{FWHM}=80fs, 0.3μJ) and probed at 590nm (t_{FWHM}=50fs, 0.3μJ). Signals detected a) at 300nm, b) at 322nm. The pulses were linearly polarized, with vertical (black) or parallel (red) relative orientations. In the insert, the dynamics pumped at 590nm and probed with 585nm, corresponding to negative Δt, is shown in an enlarged view. $P(B_2)$ in b) denotes the B state maximum detected on the second roundtrip of the B wave packet.

In the following, we concentrate on positive time delays and introduce a method to decompose the signals into A and B state contributions. To this end, the parallel spectrum from Fig. 6.5 a) will serve as a reference for the B dynamics. Indeed, the A dynamics probed here to the CT2 states is quite small already in the perpendicular spectrum, and in the parallel case it is further reduced by a factor 3 according to the photoselection rules for linear pulse polarizations. The decomposition procedure is depicted in Fig. 6.6. In principle, the linear set of equations presented in Sec. 4.2.1 could be solved in order to achieve decomposition. However, then, the probe sensitivity factors would remain undetermined. Therefore, we use the second isolated B peak $P(B_2)$ in the 322nm spectra to define the weight of the B state, by simply scaling the 300nm B dynamics (gray line in Fig. 6.6 a) to match the isolated B maximum. Subtraction of the B dynamics yields the A dynamics seen in parallel configuration (blue line in Fig. 6.6 a). The ratio $B^{322}_{\parallel}/B^{300}_{\parallel}$ from the B state scaling reflects the relative height of the different emission bands shown in Fig. 2.10. In the same way, the B state contribution is subtracted from the perpendicular spectrum shown in Fig. 6.6 b). However, there is not much B (gray) to subtract. In c) the A state dynamics obtained from a) (red line) and
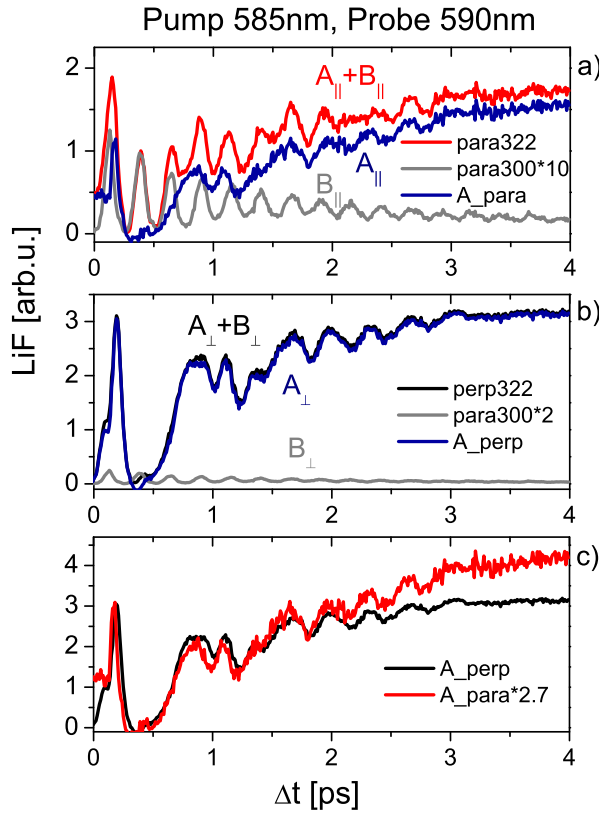
Fig.6.6. Decomposition of pump probe spectra shown in Fig. 6.5 b), recorded at 322nm into contributions from the A and the B state (see text for decomposition method). For pump and probe pulse parameters see caption of Fig. 6.5.

from b) (black line) are replotted for comparison. They differ by about a factor of 2.7, which is collected with the other determined scaling factors in Tab. 6.1. The value for $B_\parallel/B_\perp=5$ (gray lines in A and B) is in excellent agreement with the expectation from photoselection rules discussed in Sec. 4.2.1. The $A_\perp/A_\parallel=2.7$ ratio is also well matching the theoretically expected value of 3 for an ideal, non-depolarizing crystal.

	$B_\parallel^{322}/B_\parallel^{300}$	$A_\perp/A_\parallel$	$B_\parallel/B_\perp$	Reference
theory	-	3	5	eq. (4.1) in Sec. 4.2.1
experiment	10	2.7	5	Fig. 6.6 a), c) and b)
emission	10	-	-	Fig. 2.10 [88]

Tab. 6.1 Relative weights of the B and A state in measurements with varying polarization and detection conditions (see text).

The relative weights for A and B derived here exemplary for the spectra shown in Fig. 6.5 could be reproduced in a number of measurements. The emission band ratios $B_\parallel^{322}/B_\parallel^{300}$, however, turned out to be highly dependent on sample quality, and the clearest, most transparent samples lead to the maximal ratio of $B_\parallel^{322}/B_\parallel^{300} = 10$. For the considered pump and probe conditions the probe sensitivity parameters α and β from eq. (4.2) could be determined to be both close to one.

6.1.2 Probe windows and charge transfer states

The systematic variation of probe and pump wavelength allowed for a characteri-zation of probing conditions, as already discussed in the previous section. In this part, spectra with a fixed pump and a varying probe wavelengths will be presented to exemplary summarize the observed trend and finally provide an overview of the identified probe windows for the A and B states. To follow the trend for other pump and probe wavelength combinations, additional pump probe spectra can be seen in Appendix B.

The spectra shown in Fig. 6.7 allow for the characterization of fine-structured details in the probing process. The excitation was carried out with 590nm pump pulses and probed with 585nm (first column) and 580nm (second column), respec-tively. In the first row, the spectra recorded with parallel relative polarization of pump and probe pulses are shown for 300nm (gray) and 322nm (red) fluorescence. The 300nm spectra have been scaled in order to match the second isolated B state peak in the 322nm spectra. The scaling reveals a fine structure in the composition of the first maximum in the 322nm spectra. In the parallel 300nm spectra the first recursion of the B wave packet is monitored. The first B maximum (gray) advances a side-peak (previously labelled $P(A_1)$) in the combined A and B spectrum (red) for 322nm fluorescence. Since the B state is probed in the outer turning point, the A state wave packet is most likely detected for the first time in the far matrix bound wing of the A potential. The corresponding probe window A1 for the first outwards propagation of the A wave packet is located at around 0.4nm as it is shown in Fig. 6.8. This $P(A_1)$ side-peak in the 322nm spectrum is more pronounced when the dy-namics is probed at 585nm (first column of Fig. 6.7) as in the case of only slightly shifted probe wavelength of 580nm (second column). Obviously, the probing takes place in the right wing of the charge transfer state. A higher probe photon energy (longer blue dotted arrows in Fig. 6.8) would thus lead to a spatial shift of the window to larger internuclear distances which are just not reached by the A wave packet before experiencing strong vibrational energy relaxation due to the matrix interaction.

The less efficient probing of the A state in the A1 window with increasing probe photon energy is also monitored in the perpendicular spectra (black) from 322nm fluorescence in the last row of Fig. 6.7. In the perpendicular spectra, which show almost exclusively A state dynamics, additionally to the $P(A_1)$ peak probed to the A1 window, an A state maximum, corresponding to a third probe window labelled A3, shows up at earlier delay times. It is present in both, 322nm (black) and 300nm (gray) fluorescence. The 300nm spectra have been scaled to match this first A state
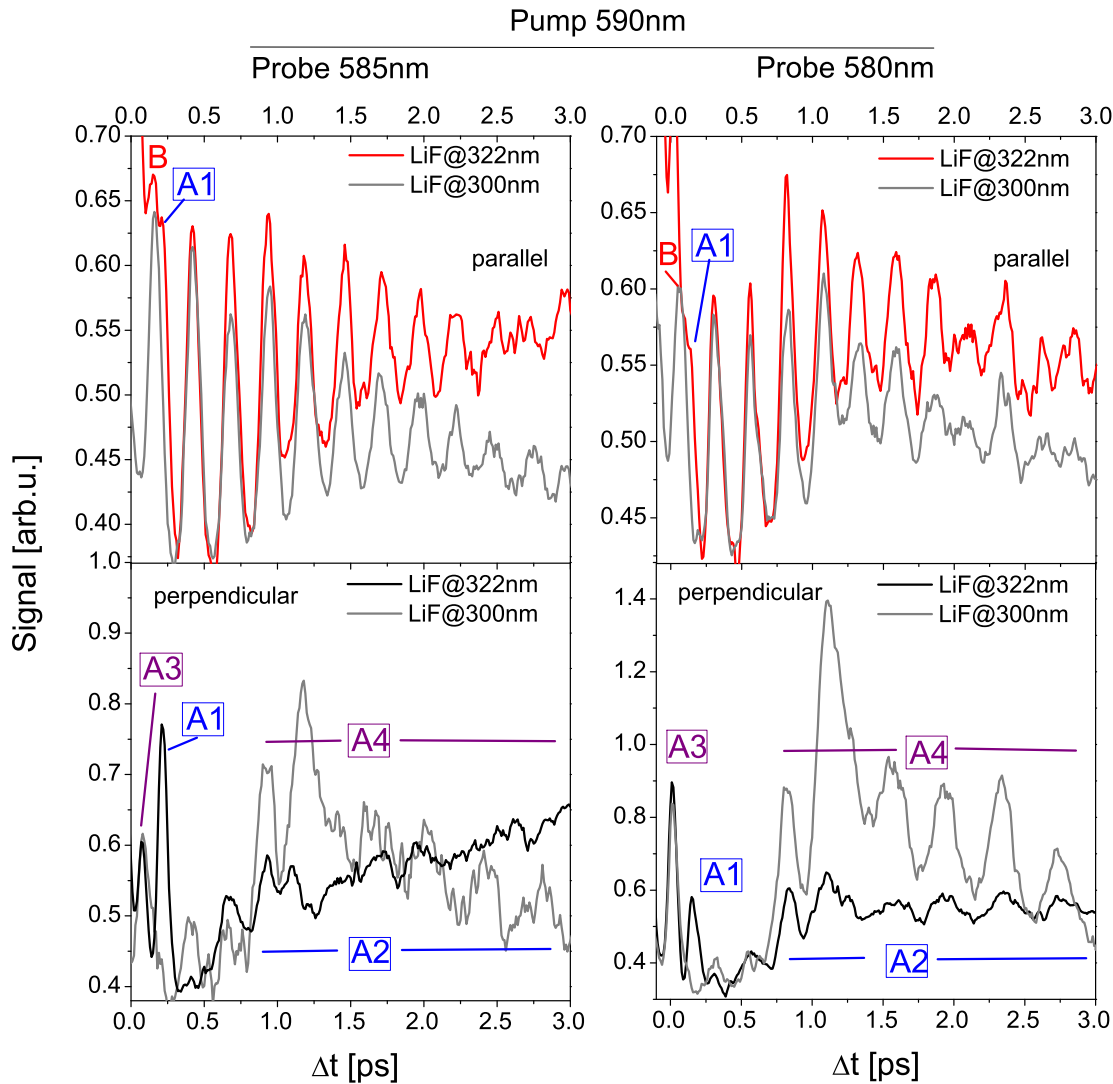
Fig.6.7. Pump probe spectra excited at 590nm (t_{FWHM}=80fs, 0.3μJ) and probed with 585nm (left column) or 580nm (right column) (t_{FWHM}=50fs, 0.3μJ). The spectra collected at 300nm (gray lines) are scaled in order to allow for a comparison with those from 322nm fluorescence (red for parallel and black for perpendicular relative pump and probe polarizations).

peak. The contribution to the pump probe signal from the A1 probe window is not visible at all for 300nm fluorescence (gray lines in second row of Fig. 6.7), which indicates that in this case, the probing to the first charge transfer manifold takes place (see Fig. 6.8). The first peak (A3) can be attributed to a probing of the A state wave packet on its first roundtrip to the CT2 states and the corresponding probe window shown in Fig. 6.8 has been labelled A3. When turning the probe wavelength from 585nm to 580nm, this first A3 peak increases, in contrast to the already discussed peak corresponding to the A1 window. In this case, the A wave packet has not
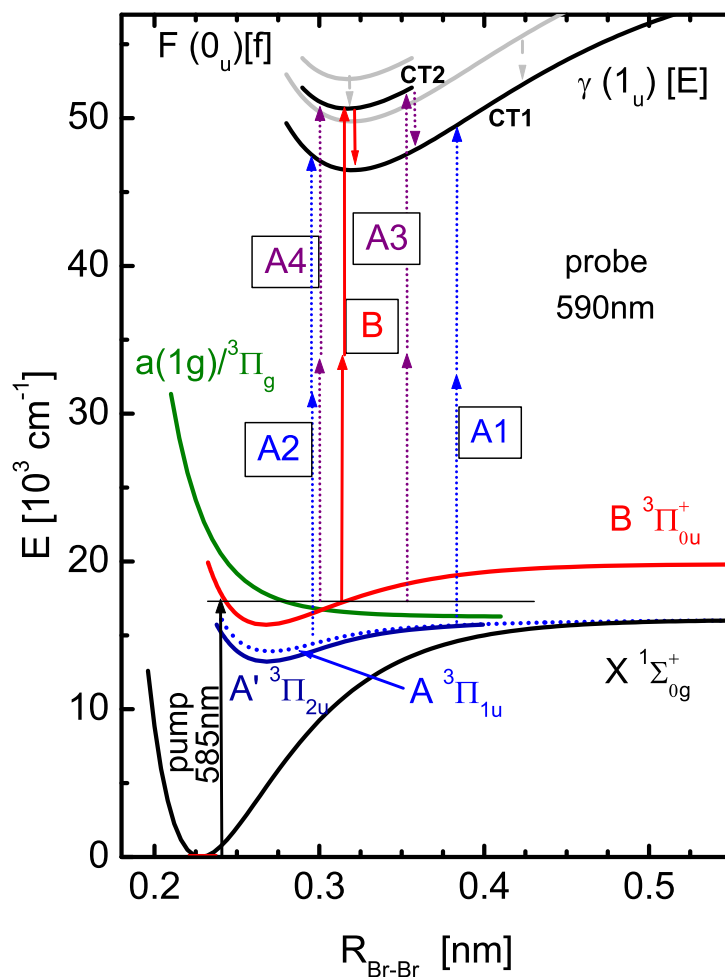
Fig.6.8. Potential scheme illustrating the pump and probe conditions and the involved probe windows for pulse parameters applied in the coherent predissociation control experiments (see text).

reached the matrix interaction region yet and a higher energetic probing leads to an increased signal since the A wave packet decelerates while approaching the inter-action region, thus, it spends a longer time in the A3 window. The appearance of the A3 contribution in the 322nm spectra indicates a radiationless transition from the corresponding CT2 state to a CT1 state and a resulting contribution to the 322nm fluorescence, which is indicated by the downward directed arrow in Fig. 6.8. The monitoring of the vibrationally relaxing A state dynamics in the bound part of the potential at later delay times has been discussed in the Sec. 6.1.1 and the corresponding probe windows labelled A2 for the probing to the CT1 states and A4 for the CT2 states are also shown in the potential scheme of Fig. 6.8. Their contri-bution to the perpendicular spectra is indicated in Fig. 6.7. A similar radiationless relaxation from CT2 states probing the A dynamics in the A4 window to a CT1

state and its contribution to the 322nm fluorescence predominantly monitoring the population in the A2 window, however, cannot be excluded. The presented complexity of the probe conditions in the A state is caused by the complex dynamics of the A state wave packet excited far above the gas phase dissociation limit, in the only matrix bound part of the A potential, thus covering a broad energetic range during the time evolution of the strong energy relaxation process.

This complexity does not show up for the B state excitation deep in the potential well, where only a few vibrational levels contribute to the wave packet dynamics and a slow relaxation does not involve a broad energetic redistribution on the considered timescale. The B state wave packet excited with pulses centered between 590 and 580nm is probed close to the outer turning point with probe pulses in the same wavelength region. The probing here always takes place to the CT2 states, from where a direct fluorescence is detected at 300nm. The B state contribution to the 322nm fluorescence is a result of radiationless transition from CT2 to CT1. The similarity of the B state dynamics observed within the two different fluorescence bands excludes a direct probe transition to CT1. Subtraction of the A contributions to the 322nm spectra, following a photoselection based decomposition scheme like presented in the last section, does not reveal any differences in the B state dynamics detected at 300nm and 322nm fluorescence, respectively.

In summary, the monitoring of the excited wave packet dynamics in the interesting energetic region of a B state crossing with a repulsive state (590nm-585nm), by probing the dynamics around the outer turning point of the potential, also includes the probing of the excited electronic A state in up to 4 additional probe windows belonging to ionic states of the 1st and 2nd CT manifold. The location of the probe windows could be estimated and is summarized on the gas phase potentials in Fig. 6.8. The redshift of the gas phase CT states (gray) due to the reduction of solvation energy in the matrix (black) has been derived in [88] and is indicated by the downwards directed gray arrows. Due to a lack of spectroscopic, as well as theoretical information about the matrix bound CT states, the E potential was used representatively for the CT1 states and f for the CT2 states. The one photonic pump and two photonic probe conditions drawn in Fig. 6.8 will be used for the interpretation of experiments monitoring the coherent control of the matrix induced predissociation in Sec. 6.4 in combination with the single pump probe spectra shown in Fig. 6.5 and Fig. 6.6, respectively.

6.2 Coherent control with polarized pulses

The first rational coherent control experiments with the setup presented in Chapter 4 were carried out in our working group together with and under the supervision of H. Ibrahim, who integrated the pulse shaper in the pump probe setup and passed over the technical know-how about alignment and programming to me. For the first bringing into service, the pulse shaper unit has been aligned to a central wavelength of 590nm, that was also the probe wavelength applied in the initial experiments. In this stage of the project, both, pump and probe pulses originated from one and the same NOPA and were partitioned using a 50:50 beam splitter. Since the results of these joint first control experiments are already presented and extensively discussed in references [89, 188, 190], for reference, only some of them will be presented in the next section 6.2.1. In the first instance, they provide an insight into the coherent processes taking place in the low energetic part of the B state potential which is difficult to access due to the small FC factors. They characterize the dynamics in the weak phonon coupling regime, where the host atoms can be treated as weakly disturbing the molecular B potential and the corresponding vibrational wave packet dynamics, respectively. In the sense of a bottom up approach, the experimental findings in this energetic regime are useful as a reference for the interpretation of control measurements carried out in the moderate up to strong lattice coupling regime. Finally, an overall picture of chromophore-bath coherences on the example of the covalent vibrational wave packet dynamics of Br_2:Ar will be drawn. Furthermore, the polarizations of pump and probe pulses have been mistakenly considered as being linearly polarized. Without being recognized, a birefringent MgF_2 substrate was used for sample deposition, which depolarized the pulses from linear to elliptical. While the pump pulse polarization was not affected strongly and the semimajor axis of the polarization ellipse stayed parallel to the former linear polarization, the mean probe polarization was turned to perpendicular. Therefore, the interpretation of the polarization sensitive measurements has been corrected now (see Sec. 4.2.2) and will be discussed here based on the real polarization conditions [258].

6.2.1 Control in the weak phonon coupling regime

The first goal of the rational control experiments was to find out if it is possible with the pulse trains to amplify the B state with respect to A state already in absorption in order to make a detailed B investigation feasible. We started the measurements in a systematic way with first generating double pulses in the pulse shaper to display the trend, as summarized in Sec. 4.3.1. Next, we switched from the sinusoidal comb (solid red in Fig. 4.9 a) to the spectrally sharper comb of Fig. 4.9 a) (dotted). In
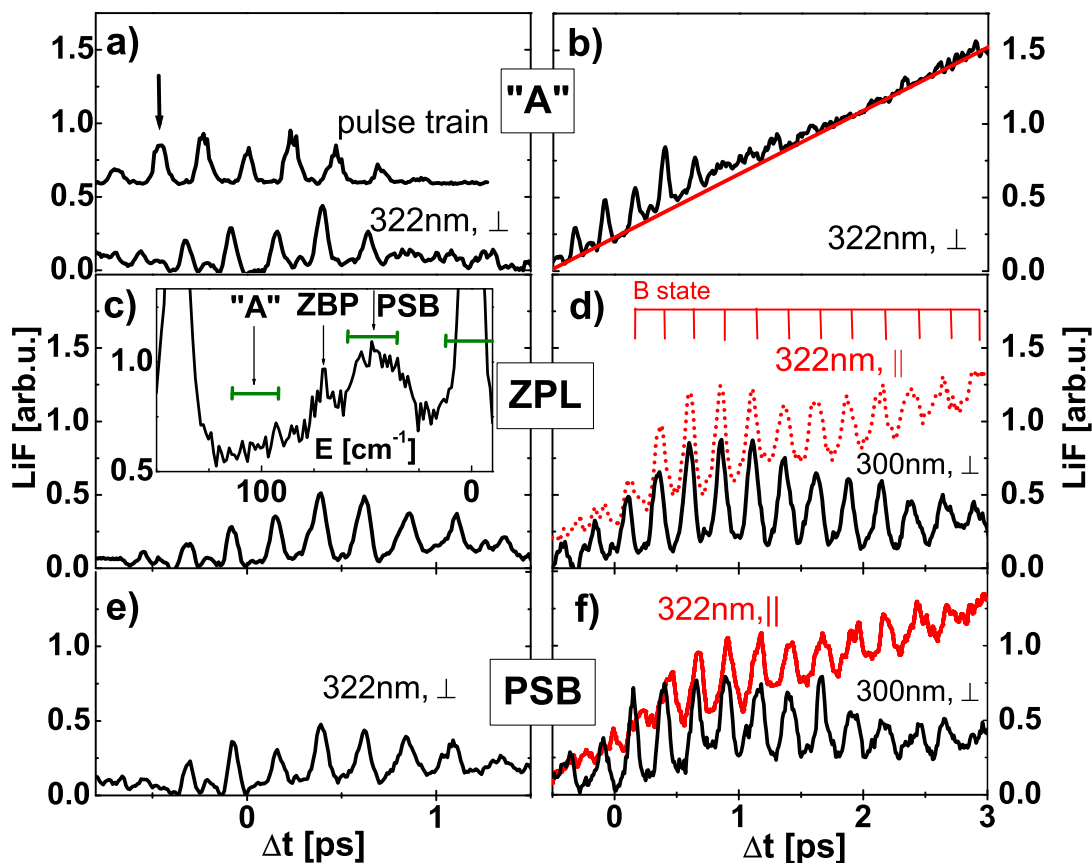
Fig.6.9. Pump probe spectra recorded at 322nm and 300nm fluorescence using a pulse train for excitation with a cross correlation shown in a) (top). a) (bottom) Excitation with comb position labelled "A" with 322nm LIF detection in perpendicular pump probe configuration derived from b) after subtraction of the indicated linear background (red). c) and e) analogous for ZPL and PSB comb. d) and f) compare 322nm parallel configuration fluorescence and 300nm perpendicular configuration without background subtraction. The red vertical sticks in d) indicate a B state vibrational period of T=250fs. Inset in c) displays the "A", PSB and ZPL segments, chosen for the corresponding three rows, on one phonon sideband together with the zone boundary phonon ZBP. The spectra are normalized for better visibility. The PSB spectrum (300nm) is multiplied by 2 with respect to the ZPL (300nm) spectrum. (Corrected polarization conditions as compared to [188], see [258].)

order to illustrate in more detail the relation of the comb to the phonon band structure we zoom in for one tooth of the comb into the three different programmed positions in the insert of Fig. 6.9 c). The spectral interval of 130cm^{-1} between the cut zero phonon lines of v'=8 and v'=9 is displayed and the PSB extends from the ZPL at 0 up to the peak originating from the zone boundary phonon (ZBP) at 70cm^{-1} [135]. Three pixels corresponding to windows of 30cm^{-1} shown in Fig. 6.9

c) are opened for transmission, as indicated by the green bars. They are positioned at "A", PSB and ZPL with the period of the excitation spectrum and within the full envelope shown in Fig. 4.9 a). We recorded the fringe pattern with a spectrometer and checked that it coincides with the attempted comb position relative to the excitation spectrum. Using the X-FROG, the intensity and phase distribution in the resulting pulse train has been determined. All three combs ("A", PSB and ZPL) have the same intensity pattern which is reproduced in Fig. 6.9 a) (top). It consists of five strong subpulses separated by the B state vibrational period. The combs differ however by the chirp within each pulse as discussed in Sec. 4.3.1 and Sec. 5.3, respectively. First, we apply the "A" comb which lies concerning B in the empty region between the termination of the PSB and the next ZPL. There, we catch the full A background according to Fig. 4.9 b). For this case, a smooth background, linearly increasing with time, shows up in Fig. 6.9 b) (red line). On top of it, an oscillatory structure is visible which seems similar to the pulse train itself. Indeed, after subtraction of the red line, a pattern is obtained (Fig. 6.9 a) which is identical within noise with the excitation pulse sequence. No oscillations occur anymore after termination of the pulses. It is just slightly shifted in time due to the propagation to the probe window A1 shown in Fig. 6.8. Evidently, each subpulse generates an A wave packet with an amplitude proportional to the intensity. Each wave packet is seen once as a peak when it passes through window A1 for the first time and all further recursions are relaxed and accumulate to the continuously rising structureless background. This behavior is consistent with the double pulse measurement shown in Fig. 4.10 b) and shows that only the A1 feature survived with the pulse train. All further A2 and later contributions merge to the background which rises by the addition of pulses together with the improved detection efficiency. Next, the ZPL comb was employed. A similar background is observed. When it is subtracted in the same way, an oscillatory structure is observed (Fig. 6.9 c) which differs from Fig. 6.9 a) significantly. The peak intensity grows continuously with the number of pulses until termination of the train. Thus, a clear accumulation occurs which does not reproduce the intensity drops in the train. The modulation proceeds with the same period and initially full amplitude after termination of the train. For the PSB comb (Fig. 6.9 e) we obtain qualitatively the same behavior as for ZPL. Obviously for the ZPL and PSB combs, the oscillatory structure corresponds nearly exclusively to a B state wave packet which accumulates by constructive interference within the pulse sequence.

We dwell on the ZPL and PSB combs in more detail in Fig. 6.9 d) and f). In addition, we change the fluorescence detection from 322nm to 300nm and thus suppress already in the recording the relaxed A state background, as already discussed in the
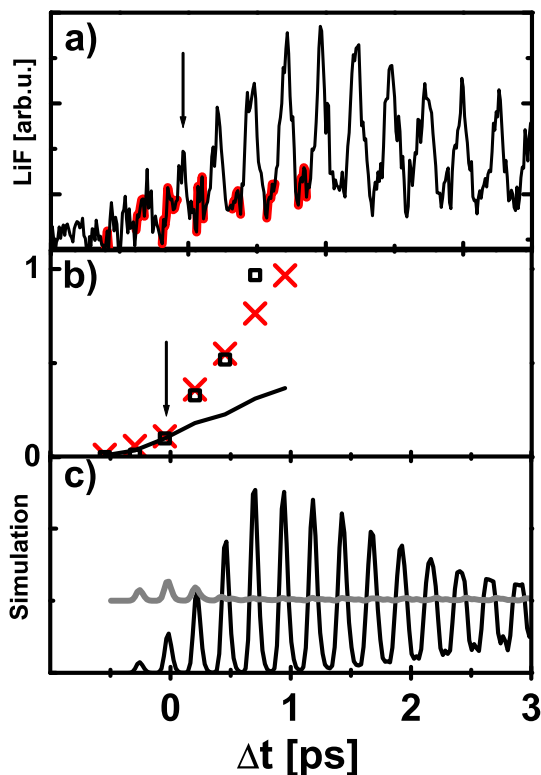
Fig.6.10. a) Fluorescence from the 300nm band showing pronounced B vibrational dynamics and a weak A contribution marked red in between the strong B peaks. b) Integrated LiF area from solid line in a) (crosses), integrated peak intensity from Fig. 6.9 a) (solid line) and squared integrated peak intensity (open squares). All data are normalized to the peak marked with the arrow (see also Fig. 6.9 a). c) Simulation of the free molecule for constructive (black) and destructive (gray with offset) B excitation (see text) [188].

previous Sec. 6.1.1. Now, we obtain for ZPL and PSB high quality spectra (solid lines) which reflect the coherent preparation of B state wave packets and their dynamics after pulse termination for in total 14 periods. PSB dynamics is very similar to that of ZPL. The intensity is reduced by about a factor of two, which will be explained later on.

The pulse train and probe pulse used in the experiments had an elliptical polarization due to a birefringent substrate, with the semimajor axis being oriented parallel to the optical table for the pulse trains and vertically for the probe pulse. A further confirmation of the results is obtained from 322nm spectra in parallel polarization which are also included in Fig. 6.9 d) and Fig. 6.9 f). By switching from perpendicular to parallel relative polarization of pump and probe, the B contributions are enhanced in 322nm detection, according to the photoselection rules presented in Sec. 4.2.1. At the same time, the accumulated A signal is suppressed as compared to Fig. 6.9 b) by the performed photoselection and has not been subtracted. Already this qualitative comparison demonstrates that the goal of separating A and B contributions and enhancing B to an extent that ZPL and PSB can be addressed individually has been fully reached with the pulse train excitation.

The ZPL spectrum for 300nm fluorescence from Fig. 6.9 d) has been repeated in Fig. 6.10 a). The increase of integrated intensity from peak to peak in this spectrum is shown by the crosses in Fig. 6.10 b). For the duration of the underlying

pulse train in Fig. 6.9 a), the integrated intensity in the subpulses themselves follow the solid line in Fig. 6.10 b) which is normalized to the crosses for the first strong peak indicated by the arrow in Fig. 6.9 a). The stronger than linear increase with number of pulses is evident. The train consists of five pulses with comparable intensity and if we square the intensity in the solid line we obtain the square dots in Fig. 6.10 b). Thus, the ZPL contribution of the B state signal accumulation preserves coherence for the overall duration of the pulse train of 1 to 1.5ps. This holds however only for the B state contribution. The A state continuum lies below the ZPL (Fig. 4.9 b) and an A state contribution should be present also in the ZPL comb excitation. Indeed, there is a weak red shaded contribution in Fig. 6.10 a) which can be identified with the A part. For the first pulses up to the arrow it is comparable in amplitude to the B part. For later pulses the B part rockets upwards according to the square dependence of the population dynamics on the number of subpulses in case of constructive interference (see eq. (4.4) in Sec. 4.3), while the A part stays at low amplitude. This illustrates in a direct comparison the coherent accumulation of B and the incoherent one of A. The A part represents a linear replica of the intensity pattern like that one observed for the "A" comb in Fig. 6.9 a) due to energy relaxation and mismatch in timing. Simulations of the coherent B dynamics for constructive and destructive interference for pulse trains are shown in 6.10 c) (black and gray line), including experimental X and B-state parameters and appropriate probe window conditions, but no depopulation and decoherence, analogue to those presented in Sec. 5.4 [198, 208]. The black line in Fig. 6.10 c) shows the simulated result for the ZPL configuration and the agreement with the experiment in Fig. 6.10 a) is convincing.

Finally, we treat the 300nm fluorescence for the programmed PSB comb (Fig. 4.9 b) as depicted in Fig. 6.9 f) as solid line. We observe once more a progressive increase in the beginning. The intensity stays however constant after the center of the pulse sequence and the final signal is lower by a factor of 2 to 2.5 compared to Fig. 6.9 d), which is explained now. After coherent superposition of the full pulse train the spectral sharpness of the frequency comb covers the full ZPL and even the most stringent interference of the last pulses do not cut into it. This is different for the broad PSB. Thus, the destructive part of the interference conditions cuts more and more of the PSB and the progressive constructive part has to compensate for this loss. The spectral weight of the PSB included within the chosen bandwidth of 30cm^{-1} is about half of that of the ZPL. If we multiply the plot of Fig. 6.9 f) with these weight factors we come close to the coherent result in Fig. 6.9 d). This consideration shows the lasting coherence properties of the PSB. A quantitative analysis of the destructive interference dynamics for the PSB comb excitation will be

carried out in the following section 6.3.1 by decomposing the signal into accumulated contributions and interference terms.

To emphasize the coherence even throughout the whole PSB, we turn back to excitation in the "A" position in Fig. 6.9 a) (bottom). The power spectra for all three excitation positions ZPL, PSB and "A" (Fig. 6.9 a) top) are identical and only the phases determine the selection of the favored comb position by interference. Every ultrashort subpulse covers the full spectrum (see also Fig. 4.9 a) and in an incoherent accumulation with statistical phase we would observe B wave packets linearly increasing with deposited intensity. The long lasting vibrational coherence in B would preserve this contribution also at long times. There is however, no discernible B contribution in Fig. 6.9 a) and this can only be explained by a destructive interference of new wave packets with the former ones in B. The destructive interference with the full phonon contribution (ZPL and PSB) requires that also PSB wave packets preserve the phase memory for several roundtrips. The gray line in Fig. 6.10 c) shows the result of the simulation for the pulse sequence at comb position "A". An offset is added for better visibility. The first pulses generate some population in B. However, the more pulses are added, the more efficiently population is depleted because destructive interference becomes more stringent as illustrated in the spectral representation in Fig. 5.14. At the termination of the pulse train no discernible population survives, in full agreement with the experiment in Fig. 6.9 a). This emphasizes the high phase stability for ZPL and PSB wave packets in this low energetic region of the B state. For ZPL it is consistent with the narrow spectral width yielding a lifetime of 1.5ps while a conversion of the full PSB would only correspond to about 100fs. Obviously, the PSB represents a distribution of phonon modes with long living individual components. Phonons originate from an expanding electronic wave function in the B → X transition (displacive excitation of coherent phonons, DECP) and also the intra-molecular vibrations couple to the matrix, according to the spectroscopic evidence [135]. The PSB shape resembles the Ar phonon density of states [83] and the maximum around $70cm^{-1}$ in the inset of Fig. 6.9 c) can be attributed to the zone boundary phonon (see also Sec. 2.2) [259]. Scrambling within the phonon modes and even only a propagation of the phonon part in the excitation from the chromophore into the surrounding bulk changes the transition energy and thus the very sensitive electronic coherence. Coherent zone boundary phonons coupled for several ps to the chromophore were observed in the DECP process and the weak damping was attributed to its vanishing group velocity [259]. For the PSB comb (Fig. 4.9 a) we cut out a $30cm^{-1}$ broad band in the middle part around $40cm^{-1}$ shown in Fig. 6.9 c). It is remarkable that electronic and vibrational coherence extend into the picosecond regime also for all those modes being resonant with

delocalized matrix phonons. Additionally, the extinction of B-state contributions in Fig. 6.9 a) by destructive interference for excitation in the "A" comb situation indicates that the major part of the phonon modes preserves electronic coherence during the full pulse sequence. In the following section a new exploration of these coherence properties in the presence of even stronger chromophore-bath coupling will be presented. The duration of the electronic coherence will be shown to extend up to the lifetime limit of the sharp zero phonon lines, despite of the stronger influence of the cage, when going to higher excitation energies. This lasting coherence in a rather large volume containing several hundred atoms provides the prerequisite for the coherent control of the matrix induced and phonon supported predissocation [85], which will be proven experimentally in the last sections.

6.2.2   Control in the strong phonon coupling regime

To provide the performance of two color experiments with varying photon energies of the excitation and probe pulse, a second NOPA shown in Fig. 4.1 has been reinstalled and aligned together with L. M. Krocker during her work for her diploma thesis. In order to profit from higher FC factors and to exploit the possibility of enhancing the B contribution relative to the incoherent, dominating A part, we switched the central excitation wavelength from 590nm to around 580nm. To allow for a systematic comparison of the measurements performed with one NOPA, and the new ones with pump and probe pulses originating from two NOPAs, reference measurements with 580nm pump and probe wavelengths have been carried out with the one NOPA setup and will be presented in this section [260].

The spectral combs are shown in Fig. 6.11. In the selected energetic region, the excitation pulses cover a part of the unstructured increasing background attributed to the creation of multiphonons with increasing matrix coupling (see section 2.5). It will be shown that vibronic coherence allows for a selective excitation of specific phonon modes also in this part of the excitation spectrum. To this end, coherent control spectra recorded at 300nm fluorescence will be presented. Especially, the dependence on the probe pulse's intensity will be discussed.

Probe pulse intensity dependence

The combined detection of the fluorescence at 322nm from the 1st CT manifold and the additional monitoring of the excited wave packet dynamics at a fluorescence wavelength of 300nm from the 2nd CT manifold allows for a suppression of the A state in detection. It also turned out to be indispensable to decompose the pump probe spectra into the contributions of the different electronic states
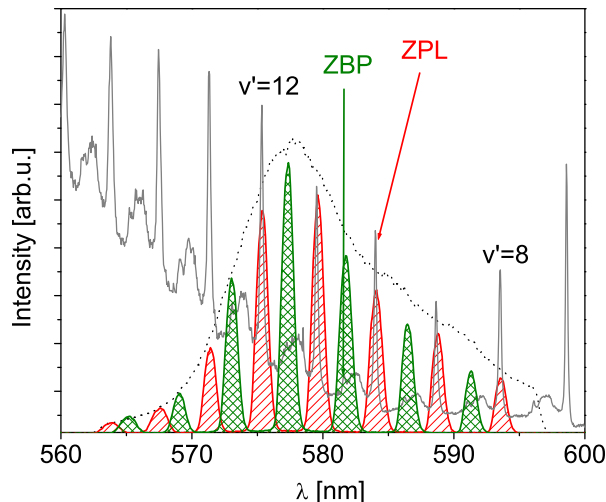
Fig.6.11. Spectral combs in the strong phonon coupling regime centered at 578nm shown together with the B state excitation spectrum. The pulse spectral envelope (dotted line) covers a wavelength range of 15nm FWHM, and includes 4 vibrational quanta v'= 9-12. Two different comb positions are shown: ZPL (red) and zone boundary phonon ZBP (green), the peak on the high energy side of the PSB.

involved. However, in order to exclude a higher order than two photonic probe step and thus, a contribution to the fluorescence signal from even higher lying ionic molecular states or even Rydberg states, further considerations are required [89]. Higher order processes involving higher than $\chi^{(3)}$ terms in the sample's polarizability depend in a peculiar way on the probe field intensity. Therefore, a probe field energy region has been experimentally identified with high signal to noise ratio, however, well below the onset of such critical processes. Fig. 6.12 shows a systematic variation of the probe pulse's field energy, from the largest value of $6\mu J$ going down to $1.7\mu J$ by using a gray wedge filter. The pulse energies are given in terms of directly measured NOPA output powers and on the sample around 10% of the NOPA output arrived after an optical path of nearly 10m and was focussed to a diameter of around $100\mu m$ on the sample. The intensity dependent measurement has been carried out for a parallel and perpendicular relative orientation of the semimajor axis' of elliptically polarized pump pulse trains and probe pulses. Due to the elliptical polarization, only small differences between parallel (red) and perpendicular (black) spectra can be noticed. In the left column of Fig. 6.12 the excitation comb was positioned at the ZPL and in the right column on ZBP as shown in Fig. 6.11. For both comb positions a pronounced B state dynamics is observable for in total 13 vibrational periods of 260fs duration, however with modulation contrasts depending on the probe pulse intensity. We definine a signal to noise ratio as the ratio of maximal modulation contrast divided by non modulated background, which is the sum of the signals induced by the pump pulse and the probe pulse, each separately
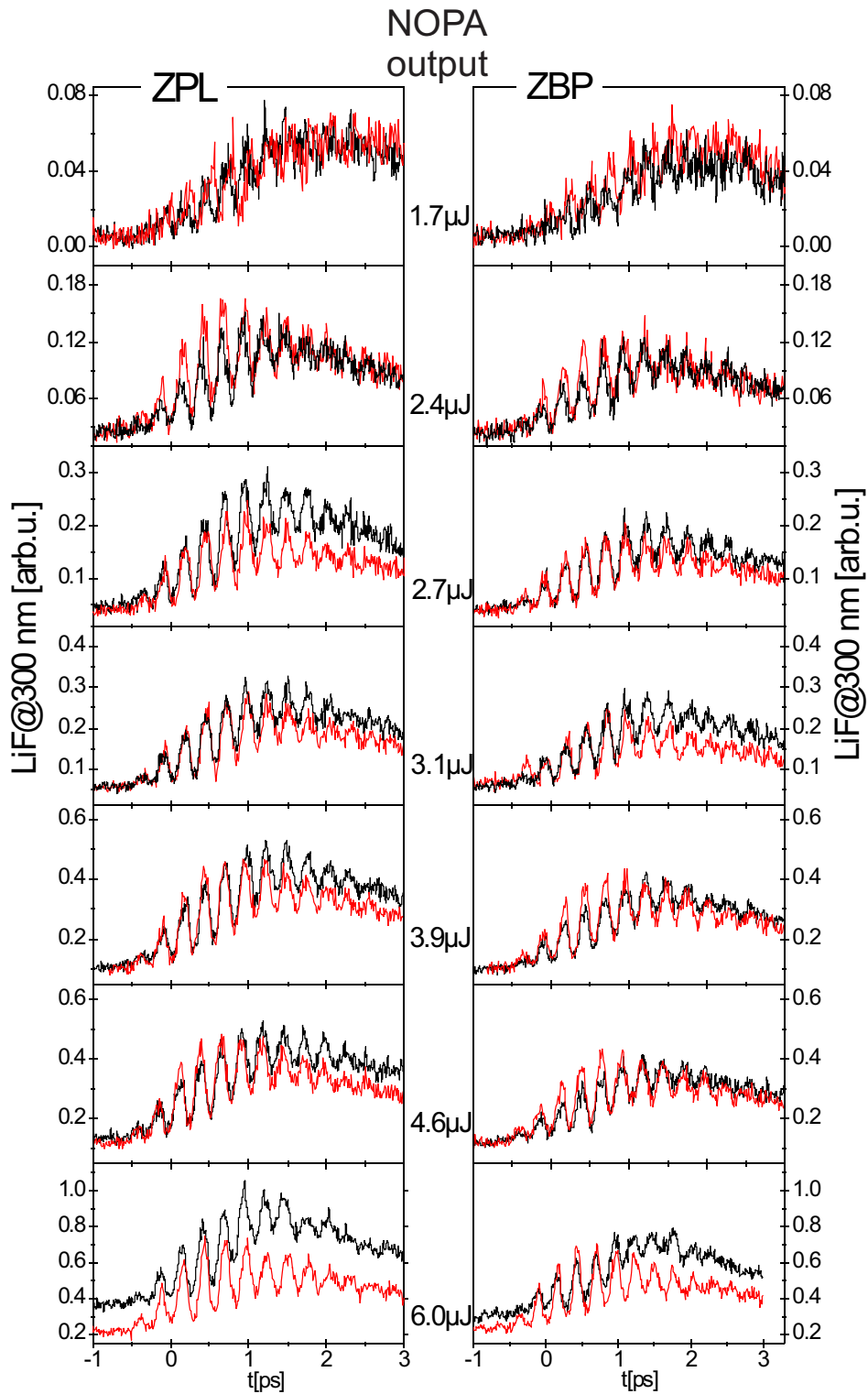
Fig.6.12. Pulse train pump probe spectra recorded at 300nm fluorescence wavelength for the spectral comb positioned on the zero phonon lines (left column) or the zone boundary phonon (right column) for parallel (red) and perpendicular (black) relative pump and probe polarization (semimajor axis of polarization ellipse) with varying probe pulse field energies from $1.7\mu J$ (first row) up to $6\mu J$ (last row). Corresponding spectral combs are shown in Fig. 6.11. (Note that here, direct NOPA outputs were measured. Around 10% of the field energies arrived at the sample.)

and therefore not including the time dependent, modulated part. The field energy dependent signal to noise ratios have been collected in Tab.6.2.

Energy [μJ]	1.7	2.4	2.7	3.1	3.9	4.6	6.0
ZPL	4.0:1	4.3:1	5.0:1	6.0:1	4.0:1	3.3:1	2.0:1
ZBP	3.0:1	4.0:1	4.0:1	4.4:1	3.5:1	2.9:1	1.9:1

Tab. 6.2 Probe field energy dependent signal to noise ratios from Fig. 6.12. Spectral combs corresponding to the excitation pulse trains are shown in Fig. 6.11.

With increasing NOPA power an increasing signal with also increasing signal to noise ratio is observable up to 3.1μJ field energy for both comb positions. A decreasing trend shows up for higher field energies, although the scattering of data points still decreases. Obviously, one observes here a saturation process in the probing, degrading the modulation contrast with increasing probe field energy. Therefore, in the experiments presented in the following sections, probe pulse intensities have been controlled in order to maximize the modulation contrast in the control pump probe spectra. Now what is the origin of this saturation process? When comparing parallel and perpendicular spectra, one can observe a trend to higher overall signals with increasing field energy for the perpendicular spectra as compared to parallel ones. For 2.4μJ still the parallel spectra, which contain more B state dynamics, dominates. At 2.7μJ however, the perpendicular signals, containing more A state contributions probed to the 2nd CT manifold, start to dominate the signal. For the maximal probe energy of 6μJ the deviation also shows up in the time independent background at early times, resulting from higher than second order excitations performed by the probe and pump pulses, independently, also contributing to the 300nm fluorescence. Most likely, these time independent higher order processes involve the A state as an intermediate state, why the saturation process is most pronounced in the perpendicular case.

In order to crosscheck the order of the probe process, for the ZPL measurements, the signal intensities of the first maximum following Δt=0 have been plotted versus the probe field energy and are shown in Fig 6.13 on a linear b) and double logarithmic scale a). In a) a quadratic dependence on the energy can be read off, proving the two photonic character of the excitation.

We now turn back to the signal to noise ratios collected in Tab. 6.2 for the ZBP and ZPL comb. Although the trend is the same for both comb positions, the modulation contrast, monitoring B wave packet dynamics, always dominates in the ZPL comb case. Indeed, the coherent enhancement of the B state wave packet also works
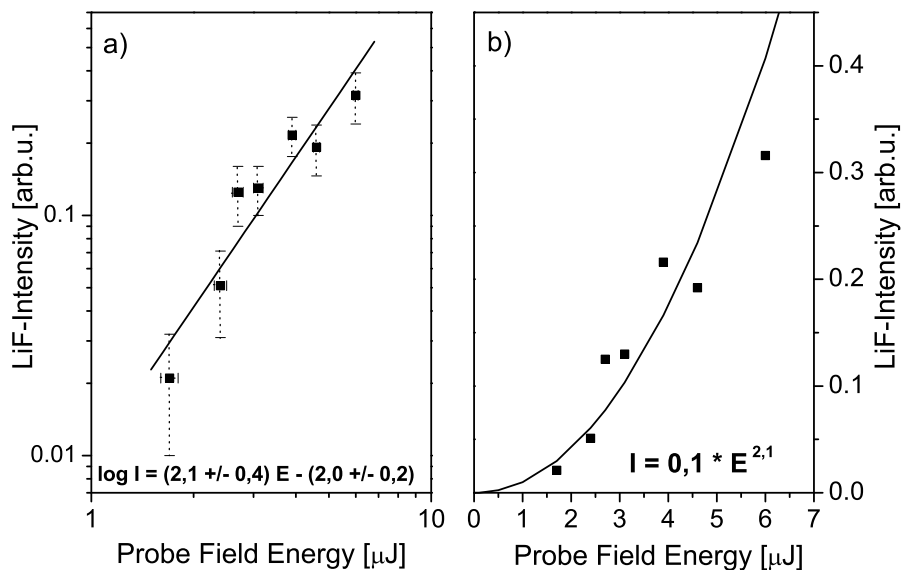
Fig.6.13. Probe field energy dependent pump probe signal intensities from first column of Fig. 6.12. a) double logarithmic scale, b) linear scale. Spectral combs corresponding to the excitation pulse trains are shown in Fig. 6.11. (For detailed discussion see text.)

in this high energetic multiphonon dominated region with the ZPL comb. To which extent, will be answered in a more quantitative analysis in section 6.3.2. Here, it shall be noted, that the choice of the right probe field energy is not only important for optimal modulation contrast in individual measurements, but especially in order to allow for identification of state selective effects contained in the spectra. To this end a good compromise between possibly low level scattering of subsequent data points and possibly high spectral selectivity monitoring is given by probe field energies of 2.7-3μJ.

6.2.3   Rational control with linearly polarized pulses

From the discussion of pump probe experiments performed with different polarization properties of the pulses it is obvious, that the linear polarization is crucial for achieving highest possible state selectivity, which is required for a proper decomposition into contributions from different electronic states involved in the pump probe spectra. On the other hand, the high selectivity leads to even smaller excitation cross sections in the interesting energetic regime of nonadiabatic crossings. Since no control experiments with reasonable signal to noise ratios could be made in the energetic region around 590nm when working with linearly polarized pulse trains, the

central excitation wavelength has been tuned to 584.25nm (see Fig. 6.14), which lies
in between v'=9 and v'=10. Taking into account the spectral blueshift due to the
Franck-Condon spectrum discussed in detail in the theory Chapter 5, the excitation
leads for the narrow spectral width of $\Delta\lambda$=9nm and correspondingly long pulses of
t_{FWHM}=80fs, to B state wave packets, which are expected to be centered around
v'=10. They are composed of the superposition of two additional vibrational states
v'=9 and v'=11.[1]

Besides of avoiding a strong spectral blueshift, the spectral narrowness of the
combs' envelope provides a number of other advantages for our purpose. First, it
facilitates the spectral selectivity between different electronic states involved in the
spectra. Second, which will turn out in the following section, it allows to resolve
phonon modes of different orders in the excitation with the different comb positions
and shapes. Especially, for the identification of predissociated population in the
quantum control pump probe spectra, the spectrally narrow excitation is inevitable.
The spectral sharpness of the nonadiabatic transfer process has been already pointed
out in Sec. 2.5.3 within the discussion of the frequency resolved spectra [83].

Playing "excitation piano" with spectral combs

Already in the last section, a fine tuning of the spectral comb within the phonon
sideband has been indicated, by performing additionally to the spectral comb po-
sitioned in the middle of the sideband, excitation of the zone boundary phonon
structure. In the experiments, which will be presented next, not only a fine tuning
of the comb position has been carried out, but also the number of teeth has been
varied. Fig. 6.14 a) shows the applied spectral combs in this energetic region, with
the already introduced comb positions PSB (olive) and "A" (blue). The ZPL (red)
and ZBP (green) combs which have been introduced previously are depicted in b).
The corresponding pulse train is shown in Fig. 6.14 c). In Fig. 6.14 b) the new
spectral comb with teeth positioned additionally to the ZPL also on the ZBP, is
introduced (violet) with the corresponding pulse train shown in Fig. 6.14 d). In the
following discussions it will be called the ZBP&ZPL comb[2]. In order to preserve
the overall spectral intensity, the number of open pixels per tooth has been reduced
from four open pixels (1.32nm) (for the ZPL and ZBP combs and the combs in a) to
two (0.66nm) for the ZBP&ZPL comb. The spectral sharpness of the teeth, gained

---

[1]It is worth to note, that in this case the loss of modulation contrast due to dispersion of the
wave packet is very small. Indeed, in order to observe the anharmonicity of the potential, at least
three vibrational states have to be superimposed. The superposition of only two vibrational states
would monitor dispersion-free wave packet dynamics analogous to the dynamics observed for a
harmonic oscillator with equidistant energy level spacings.

[2]Thanks to Prof. Ara Apkarian for having the idea during an inspiring discussion.
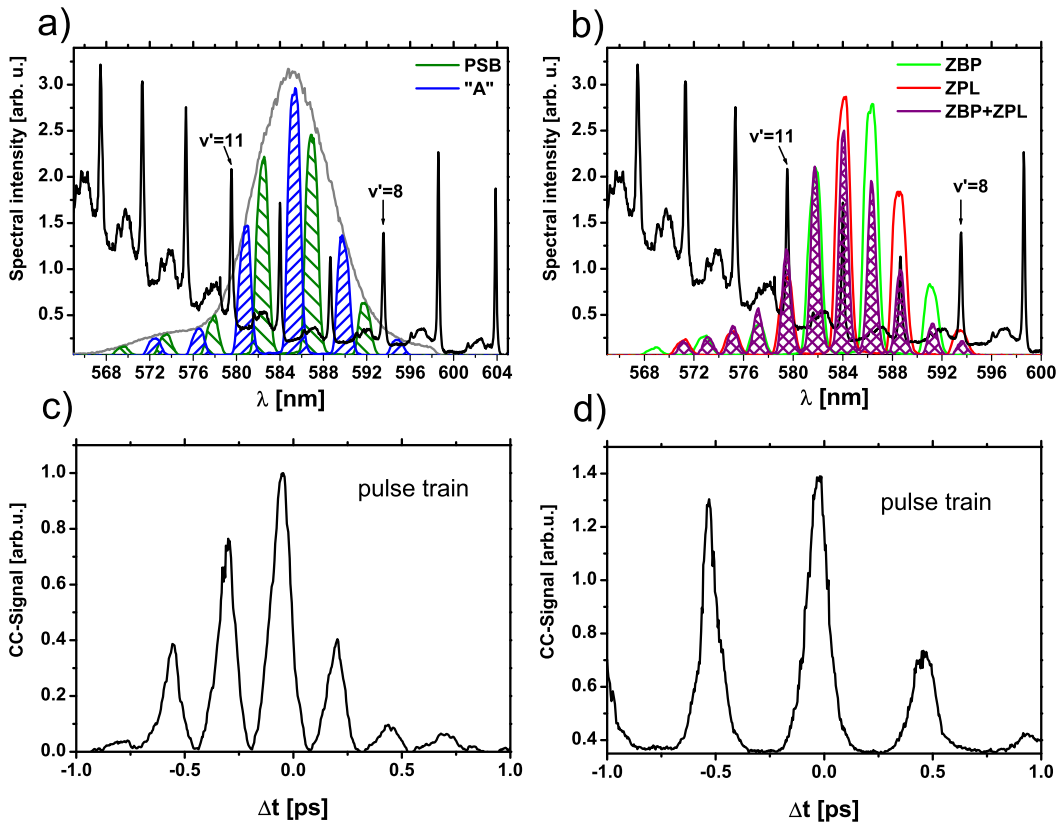
Fig.6.14. Spectral combs generated from the pulse with a 10nm spectral envelope (gray) and positioned on the ZPL (red line in b) positions in the excitation spectrum (black), or shifted to the ZBP (green line in b) position, in the middle of the broad PSB (olive line in a) or in the region labelled "A" (blue line in a). The corresponding cross correlation of the pulse train with the probe pulse (centered at 590nm) is shown in c). b) Spectral comb with simultaneous ZBP and ZPL excitation (violet), having half of the spectral separation of the teeth as in the ZPL or ZBP comb and the PSB and "A" combs shown a). Correspondingly, the subpulse separation in the time dependent structure of the pulse train intensity in d) has been doubled, as compared to c).

in this way is best visible when comparing the ZPL tooth (red) lying at v'=9 and the corresponding ZBP&ZPL tooth (violet), or the energetically next lower and higher lying ZBP tooth (green teeth) with the corresponding ones. According to the Fourier transformation, the spectral sharpening of the teeth shows up in the overall duration of the pulse train increased from 1ps in c) to 1.7ps in d). The number of strong subpulses remained the same, just like in c), four strong subpulses are visible in d), too[3]. Having the same spectral envelope, the duration of individual

---

[3]The rising part of the first subpulse was unintentionally missed in the FROG-measurement, thus, it is missing in Fig. 6.14 d). For a comparable, complete pulse train see Fig. 6.26.

ZPL&ZBP
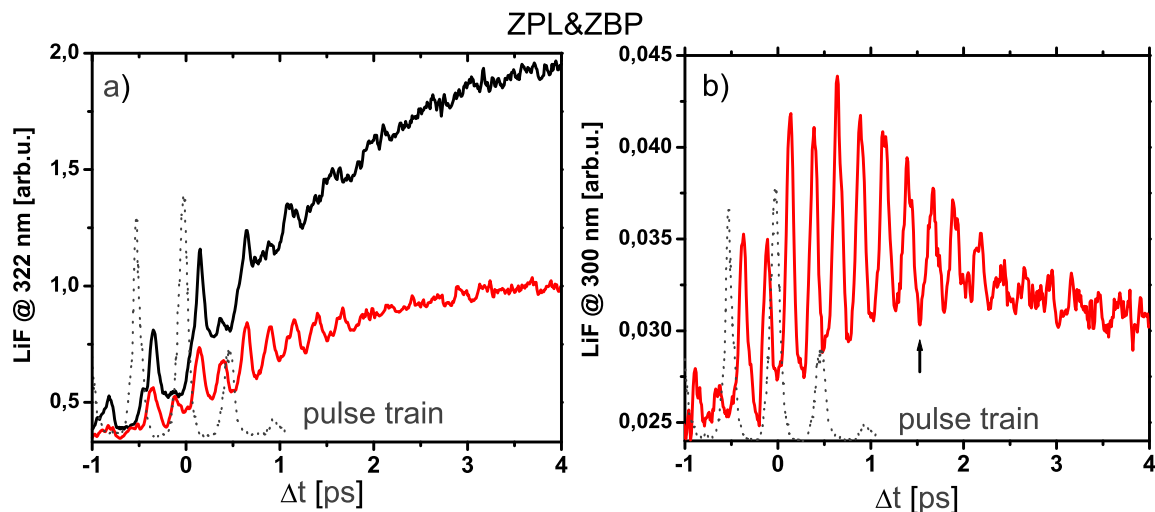
Fig.6.15. a) Pump probe signals of the ZBP&ZPL comb excitation for parallel (red line) and perpendicular (black line) relative polarization between pump pulse train (gray dotted line) and probe pulse, A (gray, c) and d)) from 322nm fluorescence (b) parallel case detected at 300nm (description see text).

subpulses remained constant. The doubling of the number of teeth corresponds to halving of the frequency interval and thus doubling of the time separation between subpulses. Indeed, the separation is now given by twice the vibrational period of the excited B wave packet. Interferences occur with only every second roundtrip. This means, that the wave packet excited by the first subpulse has no newly excited interference partners after propagation times equal to odd multiples of the vibrational period. The response of the sample to the excitation with the ZBP&ZPL comb is shown in Fig. 6.15 a) for fluorescence detected at 322nm, with a parallel (red) and perpendicular (black) relative polarization of the pulse train with respect to the probe pulse. The parallel case detected at 300nm is shown in b). The 300nm case again shows predominantly B state vibrational dynamics. As a response to the pulse train structure (gray dotted), the B wave packet rockets upwards with every second roundtrip. To which extent the whole pulse train with its increased duration is absorbed coherently will be analyzed quantitatively in the following section 6.3.1. However, it is already visible, that even the last tiny subpulse ending at about 1ps leaves its fingerprint on the signal in Fig. 6.15 b). Although the following modulation maximum at 1.1ps is decreased, as compared to the former maximum, the signal drop at 1.5 ps (marked by the arrow) indicates, that the excitation process has just been completed. It monitors the increase of nonmodulated background due to the excitation of the A state contribution with the last subpulse. For the 322nm fluorescence in a) for both polarizations the increasing
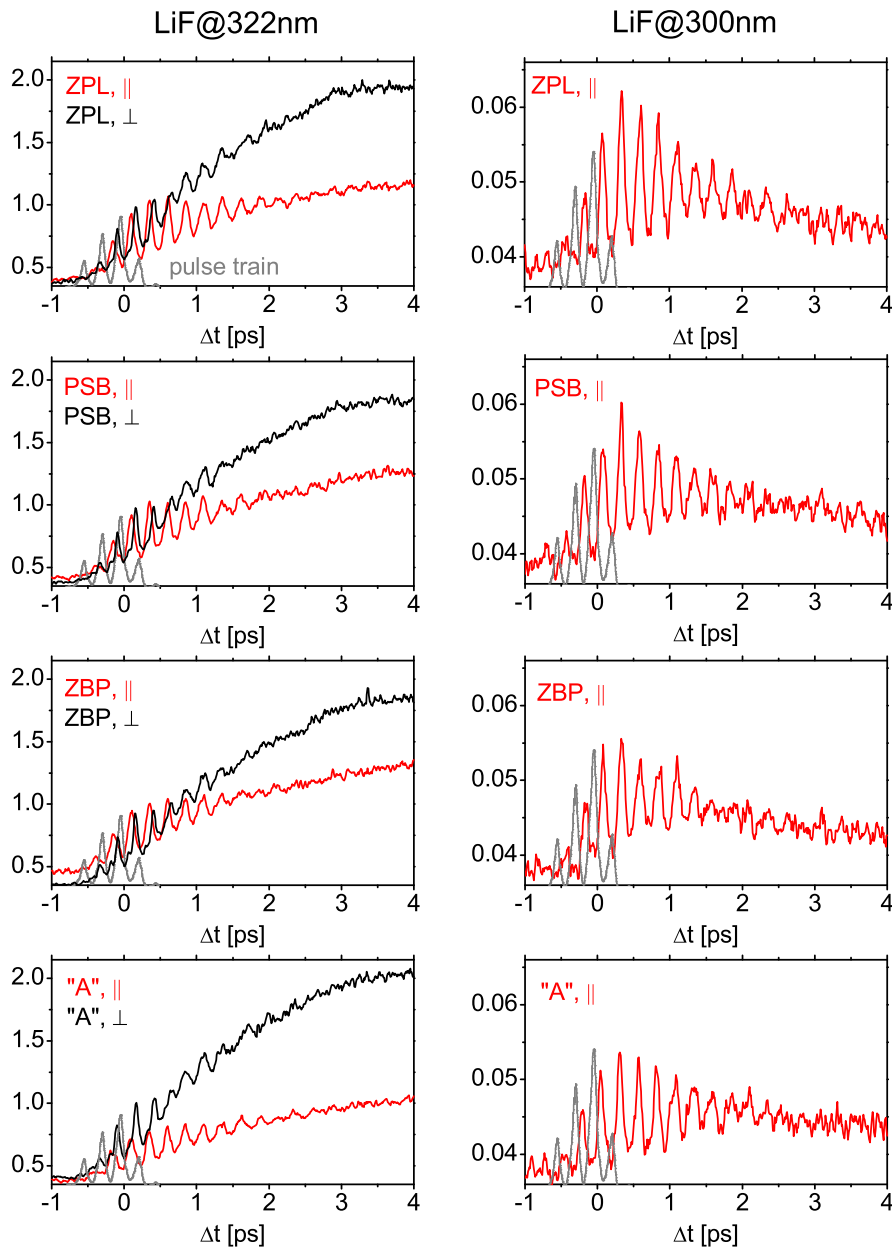
Fig.6.16. Pump probe signals of the ZPL, PSB, ZBP and "A" comb excitation for parallel (red lines) and perpendicular (black lines) relative polarization between pump pulse train (gray lines) and probe pulse. The first column collects spectra detected at 322nm fluorescence wavelength, the last column the 300nm case (description see text).

unstructured background shows up, originating from relaxation of the incoherent A parts into the A2 probe window, as explained in previous sections. The increase converges towards a maximum at 4ps. With the linearly polarized pulses a ratio

of 2:1 for the $\perp$:$\parallel$ signals is achieved, significantly overruling the selection achieved with the elliptical polarization discussed in the last section. In the left column of Fig. 6.16, the pump probe spectra performed with ZPL, PSB, ZBP and "A" comb positions recorded at 322nm are collected. In principle all of them show comparable qualitative behavior. However, it is immediately observable, that the exact $\perp$:$\parallel$ ratio is strongly comb dependent. The reason is the performed spectral phonon state selection achieved by excitation with the pulse trains corresponding to the different comb positions. The largest ratio is observed for the "A" comb, according to the expectation, since here, the incoherent A state absorption dominates and the phase distribution in the pulse train does not support constructive interference for the B state wave packet. In comparison, the ZPL comb excitation shows a decreased $\perp$:$\parallel$ ratio, which is mainly caused by the enhancement of the B contribution in the parallel spectrum. Indeed, the 300nm fluorescence detection with suppressed A state probing, shown in the right column of Fig. 6.16 in red, clearly denotes most intense B state dynamics with largest modulation contrast for the ZPL comb, least for the "A" comb.

It will turn out, that the set of high quality data, presented here, which at the first glance look quite the same, contains a rich insight into the quantum mechanical character of the Br_2:Ar system. Entanglement between phonons and molecular vibrational wave packets will be discovered based on the analysis of the interference terms contained in the data. This will be topic of the next section. Furthermore, the dynamics of predissociated population will be shown to be contained in these measurements consisting not only of coherently enhanced B population and linearly added incoherent A parts. In the last section, a decomposition method for the different electronic state contributions will be presented. The differences in predissociation dynamics will be shown to be highly dependent on the excitation comb position.

6.3 Wave packet interferences in action

In the previous sections and especially in Sec. 6.2.1 it has been pointed out, that a prerequisite for a dynamical coherent control of matrix induced predissociation is the coherent enhancement of B vibrations relative to the incoherent A contribution dominating the absorption. In Fig. 6.10 the coherent enhancement of the B wave packet was demonstrated by a higher than linear increase of the B population with accumulating pulse train intensity. In the following section an alternative method will be introduced, which allows a dynamical separation of the additive, i.e. linear constituents of the B wave packet and the coherent parts resulting from interferences.

Furthermore, the time evolution of the interferences will be analyzed in a moderate (excitation centered around 585nm) and in the strong (excitation centered around 575nm) phonon coupling regime. In addition, the dependence of the interferences on up to five different spectral comb structures will be discussed and related to environment induced effects which are steered by the spectral selection.

6.3.1 Interferences in the moderate phonon coupling limit

A shift of the central excitation wavelength from 590nm to 585nm was made inevitable when increasing the excitation selectivity by changing the polarization of the excitation and probe pulses from elliptical to linear in order to record stable, reproducible B state dynamics, despite the small FC factors. This energetic region marks the limit of lowest phonon coupling strength accessible for an experimental rational control analysis and provides high electronic state selectivity. The generated spectral combs and pulse trains and corresponding quantum control spectra have just been presented in Fig. 6.14 and Fig. 6.16, respectively. In the following analysis, the spectra recorded at 300nm fluorescence wavelength with parallel relative polarizations of probe pulse and pulses train will be considered. They contain almost only B wave packet dynamics. The additional A contribution probed to the 2nd CT manifold is very small and does not disturb the structured part of the spectra (see Sec. 6.1). In order to decompose the B wave packet's dynamics into contributions responding linearly to the pulse train intensity and those resulting from interference, the single pump probe spectra presented in Fig. 6.5, recorded with parallel polarization at 300nm, have been scaled by the relative intensities of subpulses in the train and added up after being displaced in time by the time separation of subpulses, that is the B wave packet's average vibrational period. In column A) of Fig. 6.17 the measured pulse train spectra (black lines) for the five different spectral combs from Fig. 6.14 are shown together with the shifted and scaled single pump probe spectra (gray) according to the pulse trains' temporal shapes (red thick lines). The accumulative sum of single pump pulse contributions is shown in blue. By subtracting this sum from the coherent control spectra the interference terms of the B state excitation can be extracted. They are depicted in column B) as red lines. The signal base line is marked with blue. It displays the border between positive interference terms resulting from constructive enhancement of the B wave packet with subsequent subpulses of the train and negative terms corresponding to destructive interference of the considered vibrational modes of the chromophore. The interference terms are plotted together with the pulse train (dotted) and the measured B state spectra from A) which have been scaled by a factor 0.25 to allow
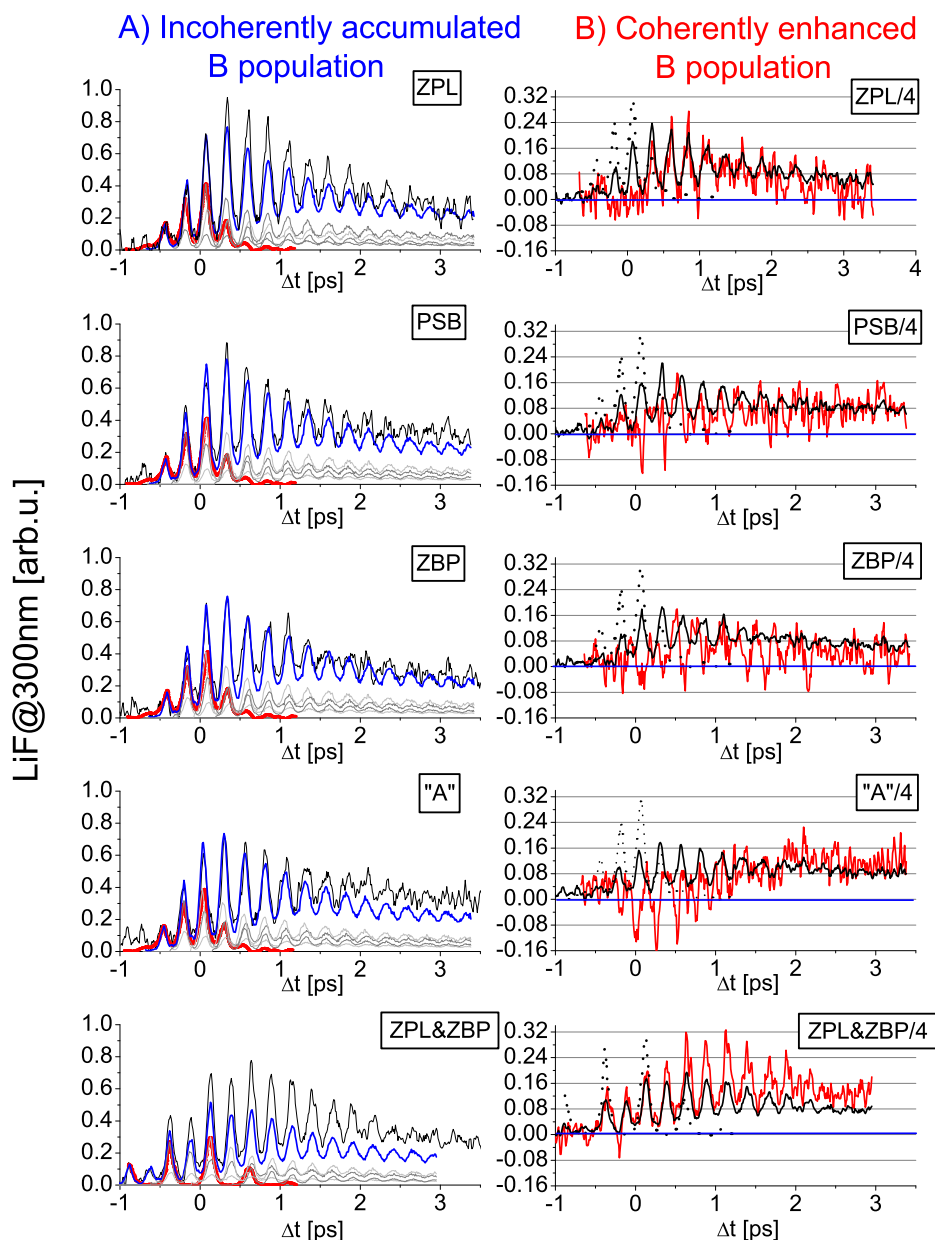
Fig.6.17. Pulse train pump probe spectra detected at a fluorescence wavelength of 300nm in the parallel polarization configuration (left column black lines) for different comb structures centered at 585nm (see also Figs. 6.14 and 6.16 (right column)) together with accumulated single pulse pump probe spectra (single spectra in gray, their sum in blue) representing the incoherently accumulated parts of the B wavepacket. The leftover signal is shown in the right column (red), representing the dynamics of the nonlinear and coherent terms in the B excitation. For comparison, the black spectra from the right are repeated, scaled with a factor 0.25 (see text). The pulse trains have been shifted by half a vibrational B period to match the B structures and are depicted as thick red lines in A) and black dotted lines in B). The envelopes of the pulse trains in the first four rows are the same and only the relative phases of the subpulses differ (see discussion of Fig. 4.11).

also graphically for a quantitative comparison. A detailed discussion of the dynamics of the interference terms for the five different excitation combs will be given now. They have been replotted together with the pulse trains in Fig. 6.18 a) - e).

In case of the ZPL comb in Fig. 6.18 a), the interference sets in after the fourth subpulse, following the subpulse having maximal intensity at $\Delta t=0$ps. This coherent part contains almost 25% of the highest B state signal, which is just reached with the inset of the first significant interference term. In the next two B roundtrips the interference term further increases despite of the weakness of the last subpulses. This behavior indicates the necessity of at least four subpulses transferring their coherence properties to the system in order to build up sharp spectral features, like the B vibrational progressions represented in absorption by the sharp zero phonon lines. After the vibronic interference of vibrational B wave packets with subsequently excited ones has been completed at $\Delta t=1$ps, the interference terms follow the same decaying behavior as predetermined for the B wave packet. The anharmonicity of the potential causes the modulation weakening by dispersion, and the nonadiabatic crossing with the repulsive state leads to the decay of the mean value, as discussed in Sec. 5.4.1. The noise in the data cannot be avoided, since they result from a subtraction of strongly modulated sharp structures.

A very different dynamics is observable for the excitation with the PSB in Fig. 6.18 b). Here, significant interference sets in already with the third subpulse. It is however, destructive with respect to the B vibrational wave packet and generates the sharp minima below the base line. About 15% of the maximally excited B wave packet experiences destructive interference after excitation of the third and the fourth subpulse for the PSB comb. The advanced inset of the destructive interference is again due to the spectral sharpness of the zero phonon lines, but now in an opposite sense: In order not to match them, the whole spectral range in between the sharp ZPL line is available. It covers the broad phonon sideband and a non structured area being in total about five times broader than the sharp ZPL lines. Therefore, already a broad spectral selection is sufficient for destructive interference, which can be achieved already with three (two of which are strong) pulses. After termination of the pulse train also positive interference terms are monitored, reflecting the surviving coupling of the selected phonon modes to the molecular vibration. In case of the ZBP excitation shown in Fig. 6.18 c), a 10% loss is observable after excitation with the most intense third subpulse. The interference term oscillates for further 8 vibrational periods between this negative value and positive values reaching up to 20%. The also sharp zone boundary phonon has a vibrational period corresponding to nearly twice the B period in this energetic region. Having zero group velocity, the zone boundary phonon amplitude remains at the molecule and the coupled motion oscillates between
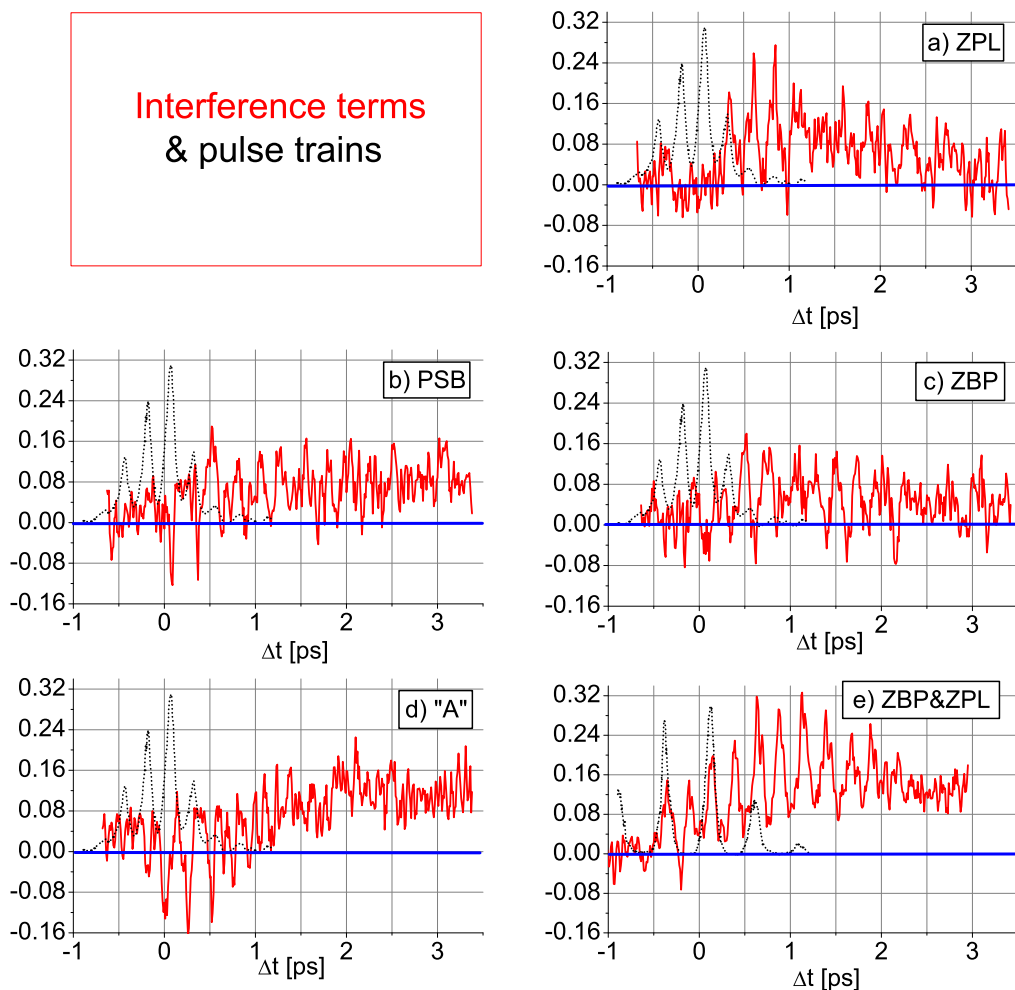
Fig.6.18. Enlarged view of the interference terms (solid lines) shown in Fig. 6.17 together with pulse trains (dotted lines, shifted by half a vibrational period). Spectral combs corresponding to the excitation pulse trains are shown in Fig. 6.14.

in phase and out of phase motion showing the typical behavior of two superimposed vibrations with different frequencies and amplitudes: While for the ZPL excitation the interference terms oscillate with the B vibrational period, here, a time dependent frequency shifts interference maxima and minima out of phase with the B vibrations, according to the superimposed molecular and local phonon vibrations. The reason why the interference beat pattern is not that pronounced in the PSB case is, that a great number of individual, correlated phonon modes propagating away from the chromophore is involved in the interference process, thus leaving as a fingerprint on the molecular wave packet less distinct disturbances.

The excitation with the "A" comb (see Fig. 6.18 d) leads to the most dramatic destructive interference of the B wave packet. Already with the second subpulse the first negative interference term shows up and increases with the following subpulse,

extinguishing one fourth of the overall remaining B wave packet. The early inset of the destructive interference with the second subpulse is again due to the great spectral width of the structureless part characterizing the "A"-region covering on average 2nm. In principle one could already achieve destructive interference of the phonon parts in a double-pulse experiment using alternatively to the pulse shaper, a Michelson interferometer [76, 186, 188]. However, in case of four strong pulses like here, the building up of the interference can be monitored for five vibrational periods. Due to the coupled molecular-lattice motion discussed for the ZBP and PSB comb excitations, the efficiency of the interference again underlines the coherence of both, Br_2 vibrations and phonons, which have to be extinguished all together. The destructive intereference observed here for an excitation with a spectral comb centered around 585nm is in qualitative agreement with the results of the "A" comb excitation centered at 590nm presented in Fig. 6.9 b) and a) and discussed in Sec. 6.2.1, respectively. However, here, the phonon contributions are not extinguished completely since on the high energetic part of the combs shown in Fig. 6.14, between v'=10 and v'=11 the increase of the multiphonon background sets in in the excitation spectrum. In that case, on this high energetic side of the excitation region, the "A" comb positions also contain phonon contributions. Thus, no complete extinction of the zero and coupled higher order phonons and therefore, no exclusive A state excitation can be achieved.

Finally, the excitation with comb positioned on both, ZBP and ZPL marks the other extreme, a surprisingly efficient constructive interference structure shown in Fig. 6.18 e). Besides of noise contributions at early times, the interference term does not fall below the zero level. On the contrary, the B wave packet excited with the second subpulse, now coinciding with the second recurrence of the firstly excited B portion in the excitation region, interferes constructively to an extent that leads to a relative amount of additionally generated B population on the order of that in the ZPL comb case after termination of the entire interference process. The interference term further increases with every following subpulse and only after termination of the even weakest structure of the pulse train at 1.2ps, it reaches a maximum holding 42% of the overall B population. That comes close to the ideal situation, which one can maximally achieve in a double-slit interference experiment, where the maximum value of the interference term just matches the value of the additive term of squared amplitudes. The reason for this great efficiency is given by the pulse structure. The ZPL comb contains in the stabilized temporal phase structure the vibrational progression and a chirp structure compensating for the anharmonicity dispersion, provided the required constructive interference conditions (of course, preconditioned the coherent absorption). In this way, it includes information about host induced

changes in the spectral structure of the chromophore vibrations with respect to the gas phase structure, according to the excitation spectra (see Fig. 2.12). It does, however, not account explicitly for the phonon dynamics in the time separation structure of the subpulses. The pulse train corresponding to the ZBP&ZPL comb includes the phonon dynamics in the following sense: The separation of two vibrational periods incidentally coincides with one vibrational period of the zone boundary phonon. Due to their strong entanglement, the synchronized excitation being tailored to the in-phase vibration of chromophore and local phonon, provides optimal constructive interference conditions. Complementary to these studies, on the theoretical side, A. Borowski found by projecting nonadiabatic B-to-C state coupling matrix elements onto the phonon spectrum, that a phonon mode having a similar vibrational period is responsible for the efficient matrix induced predissociation and that the coincidence of this phonon's amplitude and the B wave packet in the crossing region opens the predissociation channel, which will be proven experimentally in Sec. 6.4 [84,85].

6.3.2   Interferences in the multiphonon regime

The following questions have been investigated and will be discussed in the present part of this work: How high can we go in excitation photon energy in order to carry out coherent control experiments? To which extent are the required coherence properties present in the multiphonon regime? Does the unstructured background originating from multiphonon contributions in the B state's excitation spectrum reflect electronic decoherence? Can in that sense, unstructured chromophore:matrix excitation spectra in general be interpreted as due to a lack of long lasting electronic coherence? In order to study the spectral selection achievable by the pulse train excitation and the coherence properties of Br_2:Ar in that regime of the excitation spectra where the multiphonon background dominates, the spectral comb has been centered around 575nm which corresponds to v'=12. Control experiments have been carried out for the ZPL (red), PSB (green) and ZBP (violet) combs, which are shown together with the B state excitation spectrum in Fig. 6.20 a). Although having a full width at half maximum of again 10nm, like in the experiments carried out in the moderate phonon coupling regime, the spectrum covers here 5 vibrational quanta due to the anharmonicity of the B potential, which are coherently superimposed in the wave packet excitation.

The pump probe spectra for the comb excitation detected at 300nm fluorescence wavelength are plotted in Fig. 6.19 for parallel (red lines, first column) and perpendicular (black lines, last column) relative pump and probe polarizations together with the cross correlation measurement of the pulse train (gray, dotted). On the
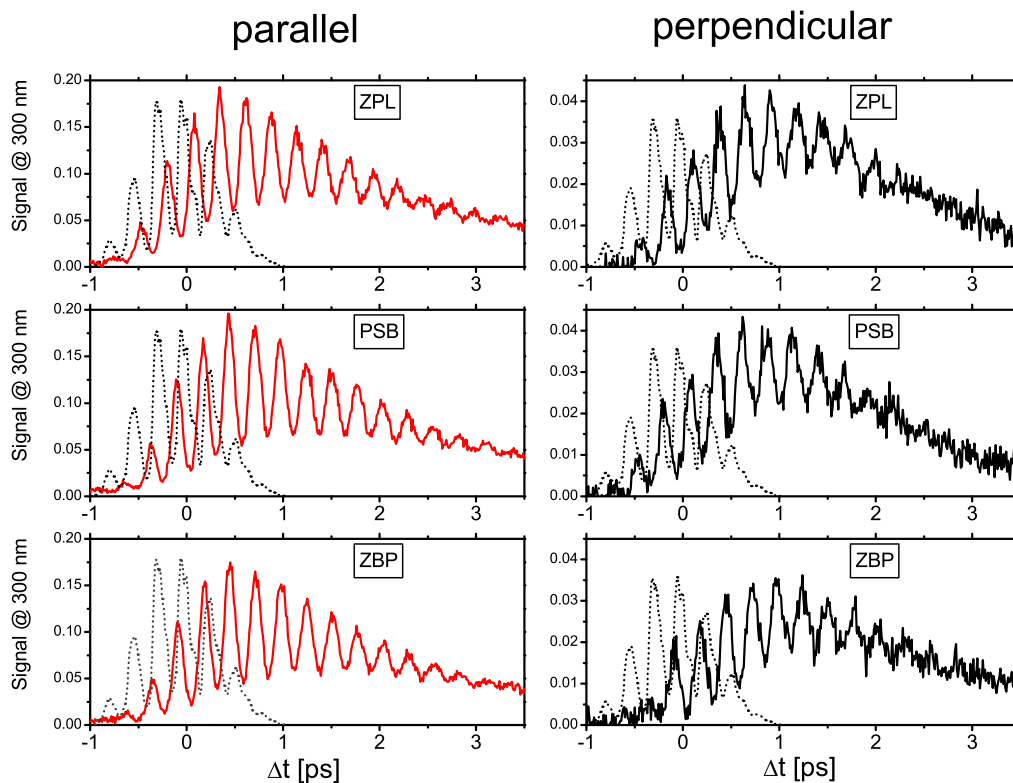
Fig.6.19. Pump Probe spectra detected at 300nm fluorescence with excitation pulse trains (gray dotted) corresponding to the ZPL (first row), PSB (second row) and ZBP(last row) comb positions shown in Fig. 6.20 a) centered at 575nm. Parallel relative polarizations of pulse train and probe pulse (first column, red) and perpendicular ones (last column, black) have been applied.

first sight any difference for the three employed comb positions is hardly discernible. Both, parallel and perpendicular spectra show highly modulated B wave packet dynamics. The perpendicular to parallel ratio is 1:5, as already observed in single pump probe spectra. It matches amazingly well the theoretical expectations from photoselection rules valid for an ideally non-depolarizing, isotropic sample. The perpendicular spectra include additionally to the B structures an up to 1ps rapidly increasing and afterwards decreasing unstructured background due to the probing of the electronically incoherent A contributions into the probe window A3 (see Sec. 6.1.2), which is only slightly suppressed with parallel polarization. After termination of the pulse train excitation, the modulation contrast decreases due to the dispersion of the superimposed 5 vibrational states. In addition, the mean value decreases by a factor 2 after ten vibrational periods which corresponds to a decrease of 5% per roundtrip. Furthermore, a decrease of the vibrational period of 270fs down to 260 fs during the propagation is observable for each comb excitation. However, the
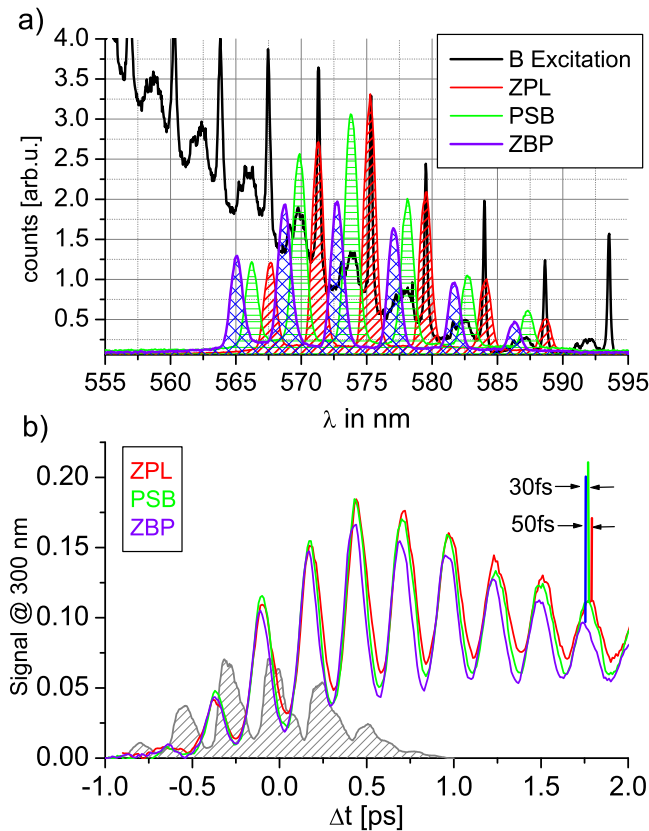
Fig.6.20. a) Spectral combs positioned on ZPL (red), PSB (green) and ZBP (violet) of the excitation spectrum (black), centered at 575nm. b) Response of the sample to the corresponding pulse train (gray) excitation detected at 300nm (same as Fig.6.19 red lines).

reduction sets in with different velocities. It indicates vibrational relaxation and a faster oscillating contribution at later times, deeper in the anharmonic potential. The mean value decay can therefore be attributed partly to the vibrational energy relaxation and to predissociation. Thus, the predissociation efficiency has to be smaller than 5% per roundtrip. The low efficiency in this energy region, being in agreement with the spectroscopic information, is not favorable for its dynamical monitoring and coherent manipulation.

Now, do we see any signatures of spectral selection in this excitation region at all? Yes, they are however subtle. They appear when directly comparing the measurements, like it has been done in Fig. 6.20 b). For the ZPL comb an average vibrational period of T=270fs can be observed, while for the PSB comb it reduces to T=265fs and to T=260fs in ZBP case. With an applied step of 10fs for the stepping motor and a probe pulse duration of t_{FWHM}=60fs, this difference is visible only after several periods. A direct comparison of the spectra shows the accumulated difference

at late delay times. In Fig. 6.20 b) at a delay time of 1.8ps an accumulated difference of 30fs for the PSB spectrum (green) and of 50fs for the ZBP spectrum (blue) with respect to the ZPL spectrum (red) can be observed. The question remains, where this difference comes from. A shifting of the spectral comb has been carried out in high energy direction when switching from the ZPL comb to the PSB and the ZBP. The observed vibrational period is, however, lowered, therefore it cannot be attributed to the selection of high vibrational levels. A satisfactory explanation for the lowering would be, that the spectral combs positioned in the middle (PSB) part or the high energetic (ZBP) part of the phonon sidebands lead to an enhanced vibrational relaxation, like it has been observed for Cl_2:Ar with double pulses from a Michelson interferometer [186]. However, no corresponding enhancement of the decrease of the mean value is observed for the PSB and ZBP comb as compared to the ZPL comb excitation. A faster decay would be expected for an increased vibrational relaxation and as it was the case in the Cl_2:Ar measurements. The reason for the period decrease has to be different and it results from coherent phonons, as it will be shown now. The origin of the multiphonon background has been simulated by H. Ibrahim by adding up individual phonon modes modeled as Lorentzian functions. This way, the increase of the structureless multiphonon background with increased chromophore-bath coupling, which was given in the configuration coordinate model in terms of the Huang-Rhys coupling constant S (see [89] and Sec. 2.5, respectively) could be explained. It goes along with a broadening of individual phonon modes belonging to a specific molecular vibrational level and a shifting away from spectral weight from the zero phonons to the lattice phonons. These can have a spectral weight even completely burying the next higher lying zero phonon vibration, which finally leads to the structureless background on the high energetic but still chemically bound part of the spectrum, beyond v'=18. In the case considered here the value of the Huang-Rhys coupling constant is S=2 (see Fig. 2.12 b). Here, phonons belonging to a lower energetic vibrational level v'_i spectrally overlap with the next higher lying vibration v'_{i+1}. Therefore, the successful spectral selection of such a phonon, contributing to the multiphonon background, belonging to a lower lying chromophore vibration v'_i , automatically causes destructive interference of the zero phonon lines for v'_{i+1}. The spectral selection performed here proves, that only those faster v'_i vibrations being coupled to the coherently selected phonon survive. This is the reason for the period decrease observed in Fig. 6.20 b).

In order to complement this interpretation, suggesting the presence of coherent multiphonons in this strong coupling region, an analysis of the interference terms has been carried out. The terms have been extracted from the control spectra shown in Fig. 6.19 by applying the same decomposition scheme as already presented in the
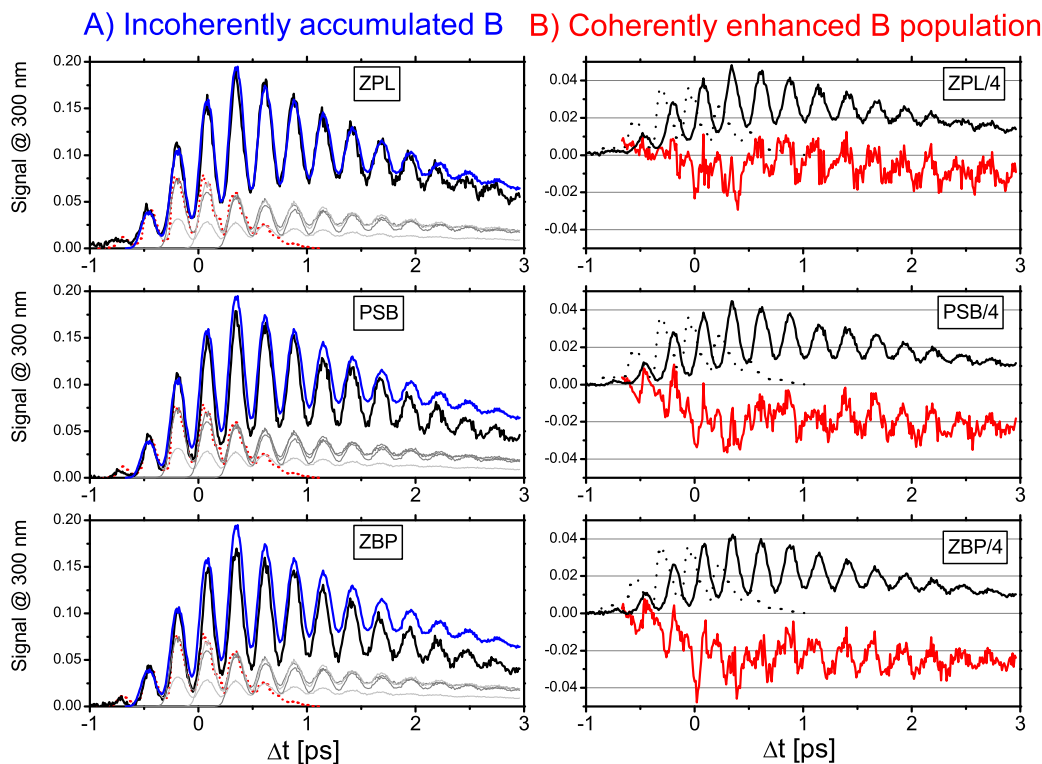
Fig.6.21. Same as Fig. 6.17 with excitation combs positioned at ZPL, PSB and ZBP, centered at 575nm. The excitation pulse (shifted by half a vibrational period in a) is shown with dotted lines (see text for discussion).

previous section for the moderate coupling regime. The results are shown in Fig. 6.21. Again, the interference terms are shown in the right column B) as red lines. In all cases, they monitor destructive interference, therefore supporting the interpretation given above. Additionally, as expected, the destructive interference takes least effect in the ZPL case, where 10% of the B wave packet is extinguished, and most for the PSB and ZBP with a loss of 17% and 23%, respectively. For the ZPL case the interference is completed after the fourth subpulse, for the phonon combs already after the third. Obviously, the electronic coherence doesn't live longer than 1ps. Decoherence experiments based on interferometric measurements often have an additional structure blurring source, like anharmonicity causing dispersion. Or the number of interference slits is not sufficiently high in order to provide maximally achievable spectral resolution, which for our type of experiments would correspond in the time domain to pulse train durations smaller than the coherence time. Therefore, derived coherence times are often restricted to predict a lowest value. Here, an exact value could be derived. Coming back to the introductory questions of this part: Vibronic coherence times are reduced in the multiphonon region to 1ps. In general, the unstructured background cannot be attributed straightforwardly to
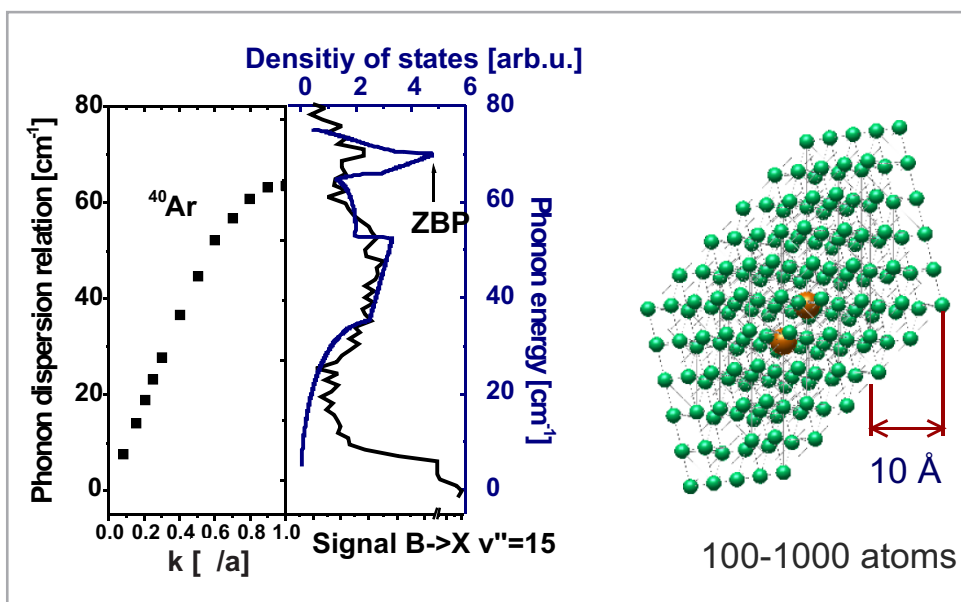
Fig.6.22. On the left, the phonon dispersion relation of Ar and the phonon density of states measured in [130] is shown together with a phonon sideband from the excitation spectrum is shown. The slope in the linear regime of the dispersion relation, covering the hole phonon sideband area, with exception of the zone boundary phonon with zero group velocity, leads to group velocities around 10Å/ps. On the right, a box containing atoms being involved in the coherent excitation process are sketched (see text).

vanishing electronic coherence. The fact that it holds for 1ps gives intriguing insight in the coupled chromophore-lattice motion. As can be viewed from the slope of the phonon dispersion relation of Ar shown in Fig. 6.22 together with the phonon density of states, reflecting the phonon structure in the excitation spectra, the involved phonons have group velocities exceeding $10Å/ps$. Apart from the zone boundary phonon, these phonons spread out during the excitation pulse train over a volume containing several hundreds of atoms (sketched on the right), as also predicted by classical trajectory calculations [149]. Still, they preserve quantum mechanical phase information and their spectral decomposition can be steered.

6.4   Control of matrix induced predissociation

In this final section, the results of the rational coherent control experiments performed in the moderate phonon coupling regime with central excitation photon wavelengths around 585nm and probed with 590nm pulses will be analyzed with respect to the predissociation dynamics they contain. In a first part, the dynamical

signatures of matrix induced predissociation will be introduced, followed by an evaluation scheme allowing for reconstruction of the overall predissociated population. Finally, the experimental proof for the possibility of coherently controlling the predissociation efficiency will be given and the astonishingly good agreement with the theoretical predictions will be emphasized.

### 6.4.1   Vibrationally relaxing predissociated population

In order to decompose the control spectra recorded at 322nm fluorescence wavelength into its incoherently accumulated A state contributions and coherently enhanced B part, in a first step, the spectra measured with perpendicular relative polarization of the excitation pulse train and the probe pulses have been analyzed. As discussed in section 6.1.1, they monitor almost only A state dynamics probed to the first CT manifold. The A state wave packets cannot be enhanced by constructive interference, on the one hand due to a missing synchronization of the A wave packet's recurrence time and separation period of subpulses in the train, on the other hand because of the energetic redshift experienced by the wave packets in their first excursion due to strong energy relaxation. Therefore, the perpendicular spectra should consist of an incoherent linear superposition of A state contributions excited which each subpulse, as it has been discussed in detail for the "A"-comb excitation at 590nm in Sec. 6.2.1. To crosscheck this assumption, the single pump probe spectra recorded with perpendicular relative pump and probe polarization presented in Fig. 6.5 have been scaled with the relative weights of subsequent subpulse intensities and added with a time separation of subsequent subpulses of about 260fs similar to the analysis of the B interferences performed in Sec. 6.3. In the left column of Fig. 6.23 this summation of scaled and time shifted single pump probe spectra (gray lines) according to the pulse train's intensity distributions (red lines) is shown as blue lines. The pulse trains have been shifted in time by the delay of 200fs, the A state wave packet needs to propagate into the first probe window A1 after its excitation in the inner turning point of the A potential (see Sec. 6.1.2). The black lines are the measured spectra for the 5 different spectral combs ZBP&ZPL, ZPL, "A", ZBP and PSB as plotted in Fig. 6.14. Except for the ZBP&ZPL comb, where the additional teeth in the comb lead to a doubling in the time separation of subpulses, the temporal shape of the pulse trains measured in the cross-correlation look the same (see also discussion of Fig. 6.14 in Sec. 6.2.3). The differences in the sums are due to different scaling, which was chosen such, as to match the response of the sample (black lines) to the first subpulse. Contrary to the expectation, measured (black) and simulated (blue) lines are not identical for all propagation times.
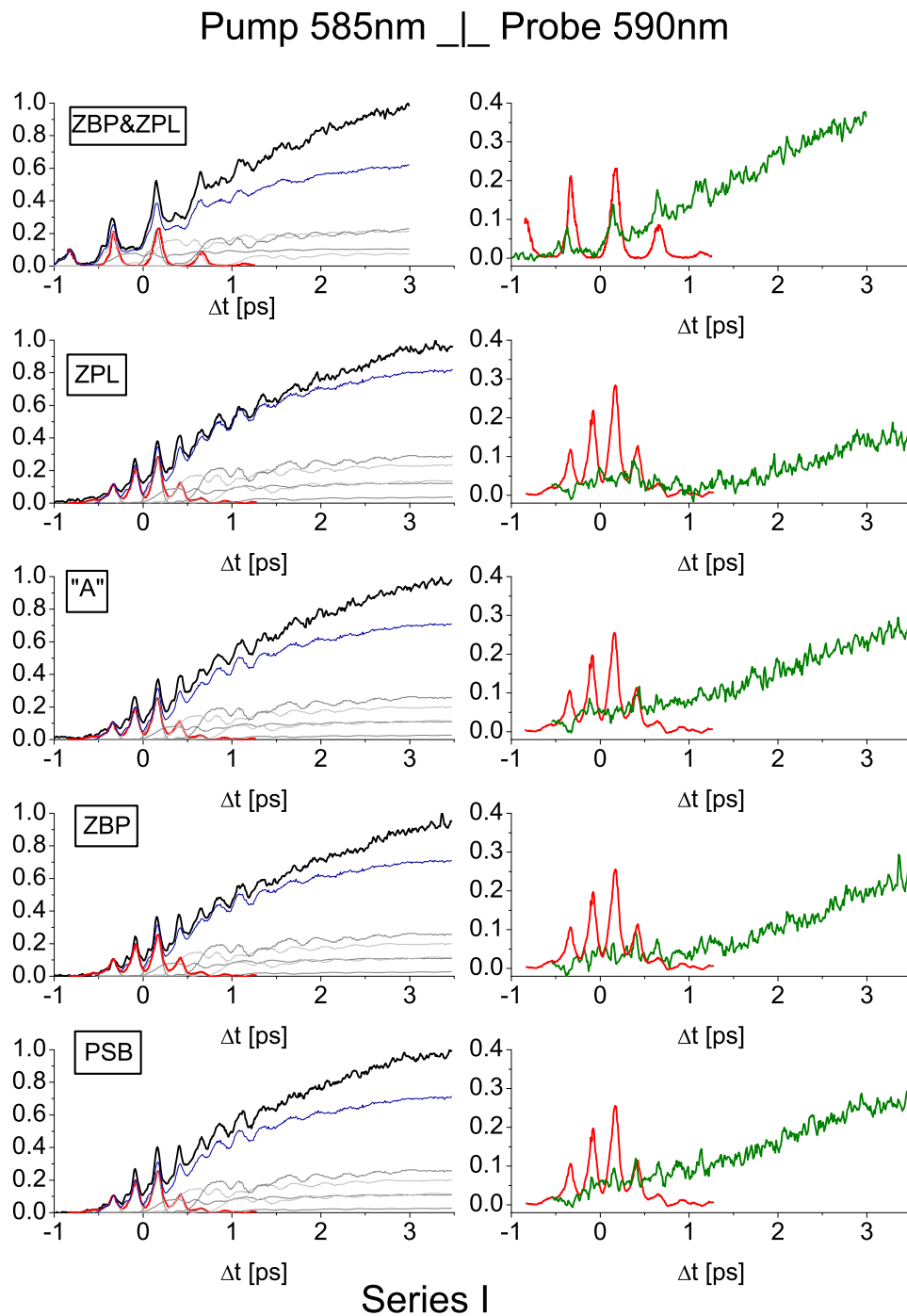
Fig.6.23. Left: control experiments with perpendicular polarization of the excitation pulse train with respect to the probe pulse (black lines) together with summed (blue lines) single pump probe spectra (gray lines) for five different spectral comb positions (see text) together with corresponding pulse trains (red). Right: Pulse trains replotted together with the difference of control spectra and summed pump probe spectra (green) from the left.

The measured control spectra show for times greater than the pulse train duration a growing excess intensity compared to summation of single pulse spectra for all comb positions. For the ZBP&ZPL comb the deviation already sets in after the second strong subpulse and reaches a maximal deviation of 35% of the population detected in the control experiment, at a delay time of 3ps. At this time the A state wave packet reached its maximum during its relaxation into the probe window A2 located in the chemically bound part of the A potential (see Fig. 6.24). For excitation with the PSB and "A" comb, the inset of the deviation with the second strong subpulse is comparable, however, it does not exceed 25%. For the relatively sharp ZBP the difference of accumulated spectra and control spectrum becomes significant only after termination of the pulse train, but reaches 20% at 3ps, while for the comb positioned at the sharp ZPL, the difference builds up only after about 2ps and doesn't exceed 12.5% at all. Now, what is the origin of this significant amount of additional population in the control spectra? The absorption conditions allow only two possibilities: A or B state. The A state contribution is, however, completely contained in the incoherent sum, and A state interferences have been ruled out above. The B state contribution to the 322nm fluorescence with linear, perpendicular polarization has been determined to be negligibly small in this energy region, and the incoherent part is already included in the accumulated sum. As it has been shown and explained previously in Sec. 6.2.3 for excitation combs centered at 585nm and in Sec. 6.3.1 for pulses of 590nm, for the ZPL comb, the B state enhancement by constructive interference significantly exceeds the amount achieved by PSB, ZBP or "A" combs. However, the leftover signal (green lines in Fig. 6.23) is minimal for the ZPL comb. Furthermore, the leftover signal does not show any B state structure. Therefore it can be definitely excluded, that it originates from a direct probing of coherently enhanced B state wave packets. In addition, the dynamics reflects the signatures of the A state's vibrational relaxation process into the second probe window A2. Hence, the only reasonable interpretation, being consistent with our knowledge about the dynamical behavior of the system collected in the previous chapters, as well as the information provided by the corresponding frequency resolved B and A'-state excitation spectra, is, that we handle predissociated population from the B state. It is transferred via an intermediate crossing state a or Π, being located in the considered energetic region (see Fig. 2.13), into the A or A' state. The proposed propagation scheme is sketched in Fig. 6.24. The population transfer process from the repulsive a or Π state to the A or A' state, most probably involves a Rosen-Zener-type crossing [124] which was also treated in the DIM-potentials calculated in [84]. One cannot distinguish A and A' because of their very similar potential structures in this energy region.
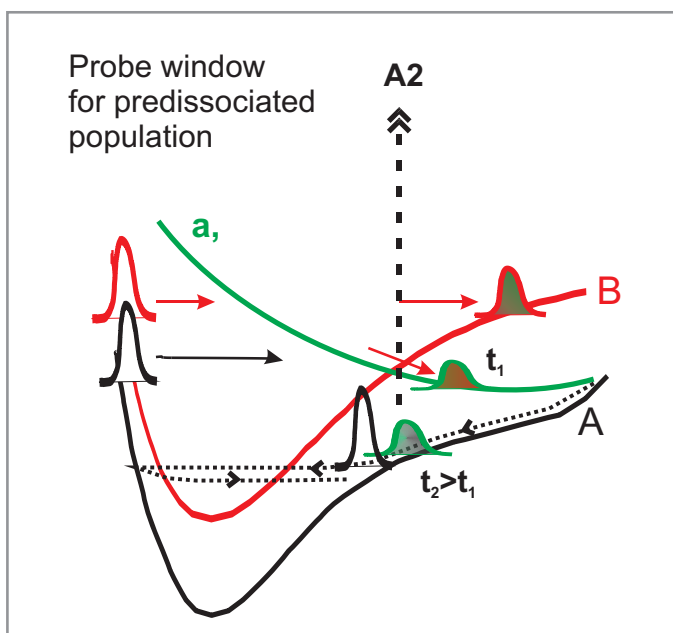
Fig.6.24. Sketch of the predissociation dynamics: Parts of the excited B wave packet (red) are transferred via a crossing intermediate repulsive state a or Π (green) into the A state (black), from where they relax into the A probe window A2, where they are detected together with the A state wave packet (black). For an extension regarding the involved probe windows see Fig. 6.30.

The requirements concerning experimental conditions will be discussed first, before the complexity of the dynamics involved in these pulse train pump probe spectra and their decomposition into A, B and predissociated contributions will be presented.

Stability requirements and reproducibility

In order to confirm the interpretation given above, in a first step, the reproducibility has been verified. The Figs. 6.25 and 6.26 show two additional series of data sets analyzed by following the same procedure as in Fig. 6.23. Qualitatively, they show the same behavior as the spectra of series I. In all cases a positive difference between control signals and accumulated signals remains with final relative weights of around 30% for the ZBP&ZPL combs and around 10% for ZPL combs and for other comb positions values lying in between. The final relative values of differences for the three measurement series are collected in Tab. 6.3. Although the qualitative behavior could be reproduced, the number of runaway values, like for the A position in series II and the comparably low values for the PSB combs, doesn't allow for a statistical evaluation of the data series. Therefore, in following sections, more quantitative considerations will be restricted to the results of the measurement series I.

Pump 583nm _|_ Probe 590nm
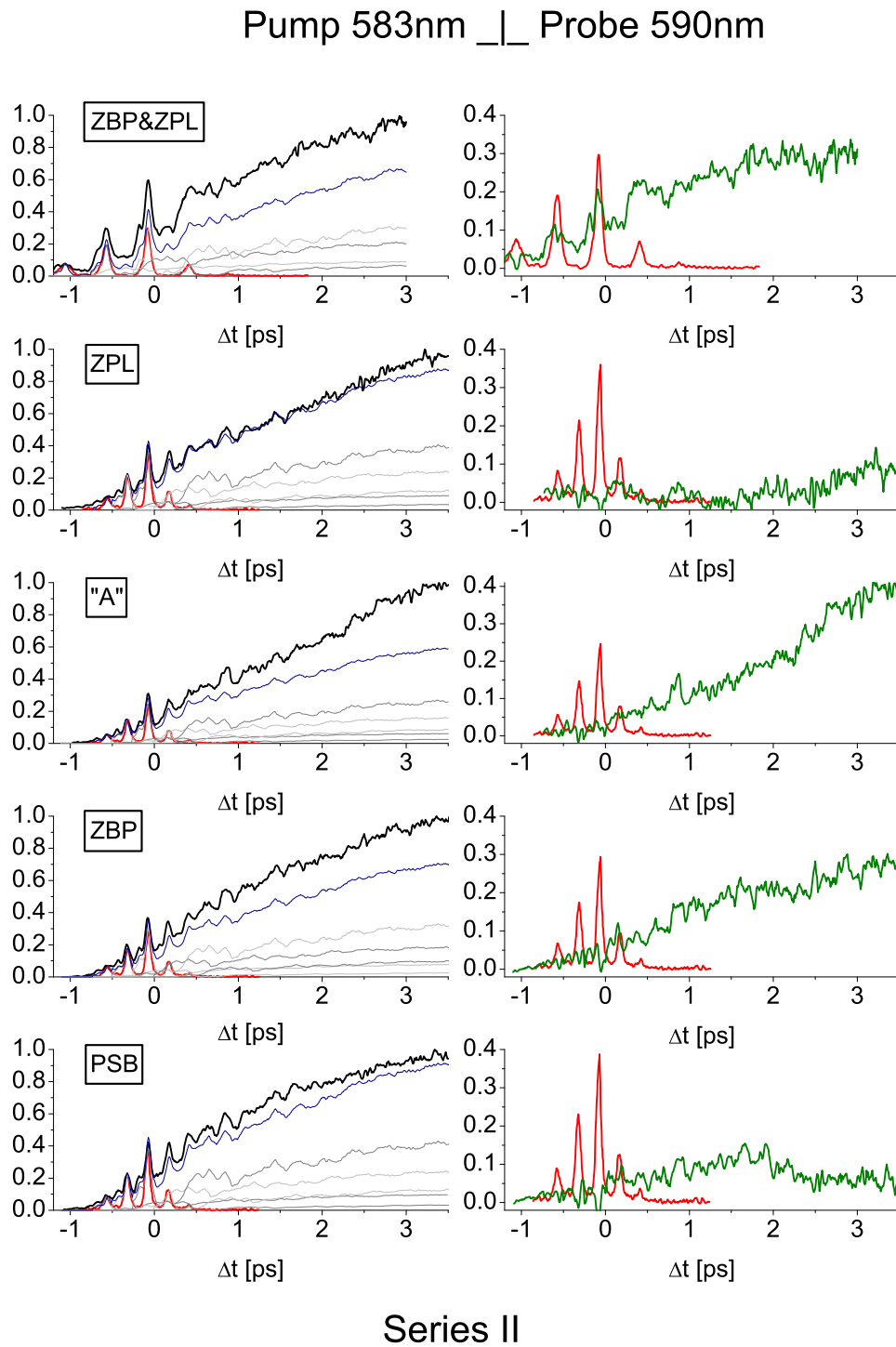
Fig.6.25. Same as Fig. 6.23 in order to check reproducibility (see text).
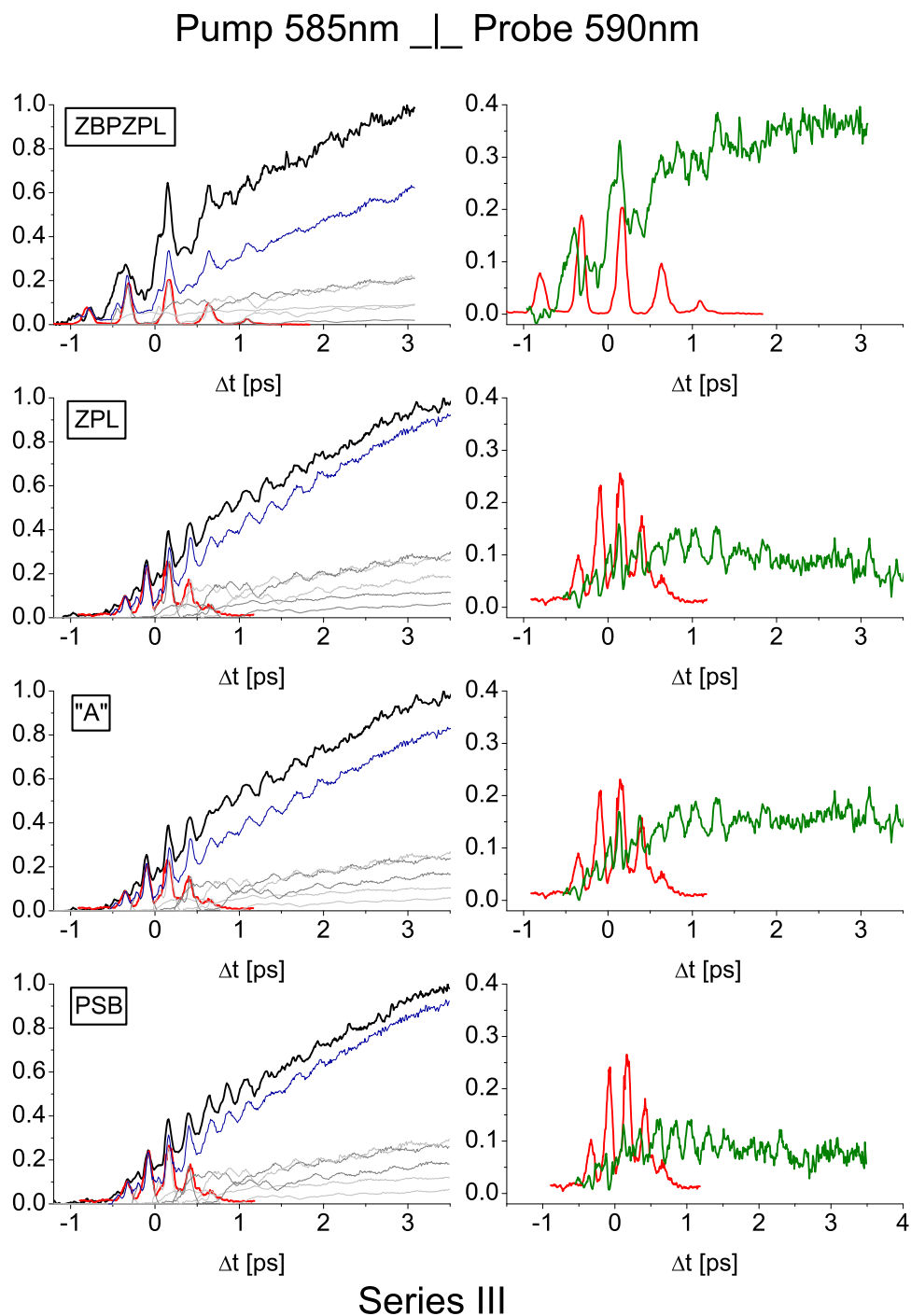
Fig.6.26. Same as Fig. 6.23 and Fig. 6.25, respectively, in order to verify reproducibility (see text).

Reasons for the quantitative reproducibility difficulties shall be, however, discussed in the following in order to provide further insight into the nature of measurements performed in this work. In general, in order to record a complete data series with single pump probe and pulse train pump probe spectra for the five different comb positions, parallel and perpendicular polarization, at the fluorescence wavelength of 322nm and 300nm, the sample has to be kept under identical conditions at a stable temperature of 6K for at least 40hours, depending on the success in finding and optimizing the time dependent fluorescence signal. In the course of subsequent measurements, a bleaching of the sample sets in, as investigated and discussed in [89]. To this end, during the experiments, the sample position has to be changed and eventually measurements repeated, to bypass the bleaching. Therefore, only highly homogeneous samples can guarantee for quantitatively evaluable data sets, especially concerning not only the time structures but also relative signal intensities.

While the deposition and bleaching problems could be solved as a result of systematic experimental studies of optimal conditions (see also Sec. 4.2.2), a second, more challenging problem concerns the stability of the laser system during this long time period of measurement. Already small intensity fluctuations of a few percent of the CPA-fundamental beam may dramatically change the excitation process and probe conditions. On their more than 10m long way to the sample, each of the pulses passes nonlinear optical elements including 2nd and higher order processes in the NOPA setups, amplifying the fluctuations, as well, in a higher than linear way. During the experiments, slow spectral drifts, of about 1nm/3hours have been also observed, and complete measurement series had to be repeated several times. Last but not least, phase instabilities, especially of the excitation pulse trains, could easily remain undiscovered during the experiments. They would destroy the coherent character of the control process.

| Series	ZBP&ZPL	ZPL	"A"	ZBP	PSB	reference
I	35	12.5	25	20	25	Fig. 6.23
II	30	7	37	25	5	Fig. 6.25
III	35	7	15	-	7	Fig. 6.26

Tab. 6.3 Relative deviations in % of overall measured A state population at Δt=3ps for measurement series I, II and III and the five different spectral combs and perpendicular polarization of pulse trains and probe pulses (see text).

## 6.4.2   Evaluation scheme for predissociation dynamics

The final results presented in Sec. 6.2.3 monitoring coherently controlled vibronic molecular dynamics coupled to the phonon environment will be analyzed in the following with respect to the phonon induced predissociation dynamics they contain. In order to retrieve the information about predissociation rates for the different excitation pulse-trains corresponding to different spectral comb positions a data analysis scheme has been developed which is based on the polarization selective electronic state decomposition scheme presented in 6.1.1 combined with the fluorescence band selective detection. The evaluation scheme is sketched in a diagram in Fig. 6.27. In order to be able to identify all contributions, a number of independent measurements being equal to or greater than the number of parameters has to be carried out, as already discussed in the previous chapters. A complete data set recorded at stable conditions includes:

A) Single pump probe spectra with linearly polarized pulses with parallel and perpendicular relative pump and probe polarization, monitored by detecting the 322nm fluorescence. For the 300nm fluorescence band the detection of the parallel case is sufficient since it will be applied as a reference for the pure B dynamics. To this end, the probe wavelength has been chosen in such a way, as to minimize the A contribution probed to the 2nd CT manifold by maximizing the B contribution at the same time (probing in outer turning point). A comparison of the 300nm spectra with the 322nm-parallel case allows for a determination of the ratio $B_{322}^{\parallel}/B_{300}^{\parallel}$ by simply comparing the spectra for the second isolated B peak (see 6.1.1). In the same way the B-state-ratio $B_{322}^{\parallel}/B_{322}^{\perp}$ has been determined to check the applicability of polarization selection rules. It matches surprisingly well the theoretically expected values. Finally, after subtracting the B contribution from the 322nm spectra, the A-state-ratio $A_{322}^{\parallel}/A_{322}^{\perp}$ can be read out. The values have been collected in Tab. 6.1 and will be now needed for the decomposition of the coherent control spectra.

B) For the excitation with a specific spectral comb profile XXX in a first step the B contributions have been eliminated from the parallel polarized pulse train spectra. To this end, the parallel, 300nm spectra excited with the pulse train have been scaled with parameter 1 from A) and simply subtracted. Scaling this B contribution with parameter 2 from A) allows for an analogous subtraction of the B contribution, which are however very small (see previous part) from the perpendicular spectra. Since the 300nm spectra excited with the pulse train corresponding to the specific comb position XXX, contain both, accumulated B contributions and those amplified by constructive or canceled by destructive interferences, we can be sure, that all B parts have been removed, without touching any other parts at this
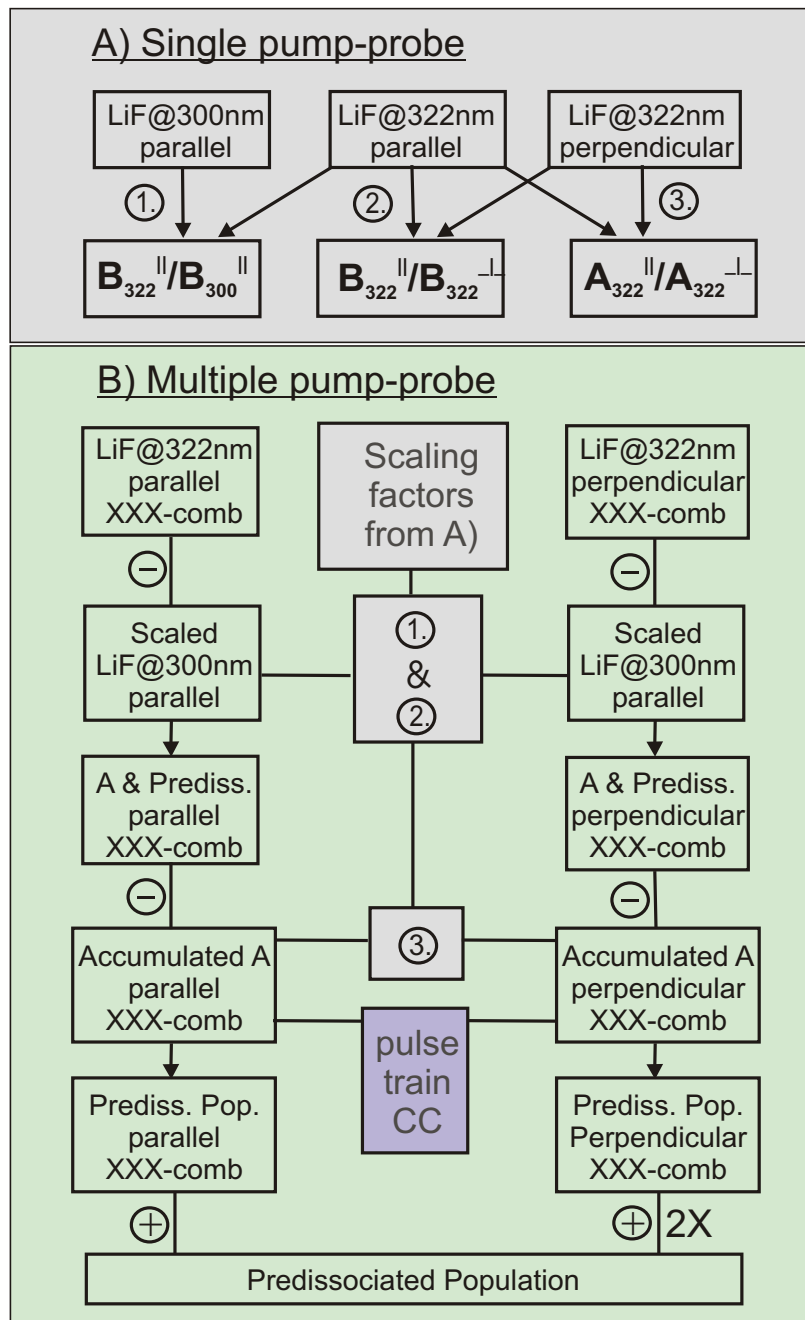
Fig.6.27. Evaluation scheme for A) decomposition into A and B state contributions of the single pump pulse - probe spectra recorded at 322nm fluorescence wavelength, using the LiF at 300nm, that monitors (almost) only B dynamics. The parameters (1), (2) and (3) are used for B) analysis of the multiple pump pulse - probe spectra in order to subtract the coherently enhanced B and accumulated A contributions. The remaining signal monitors predissociated population.
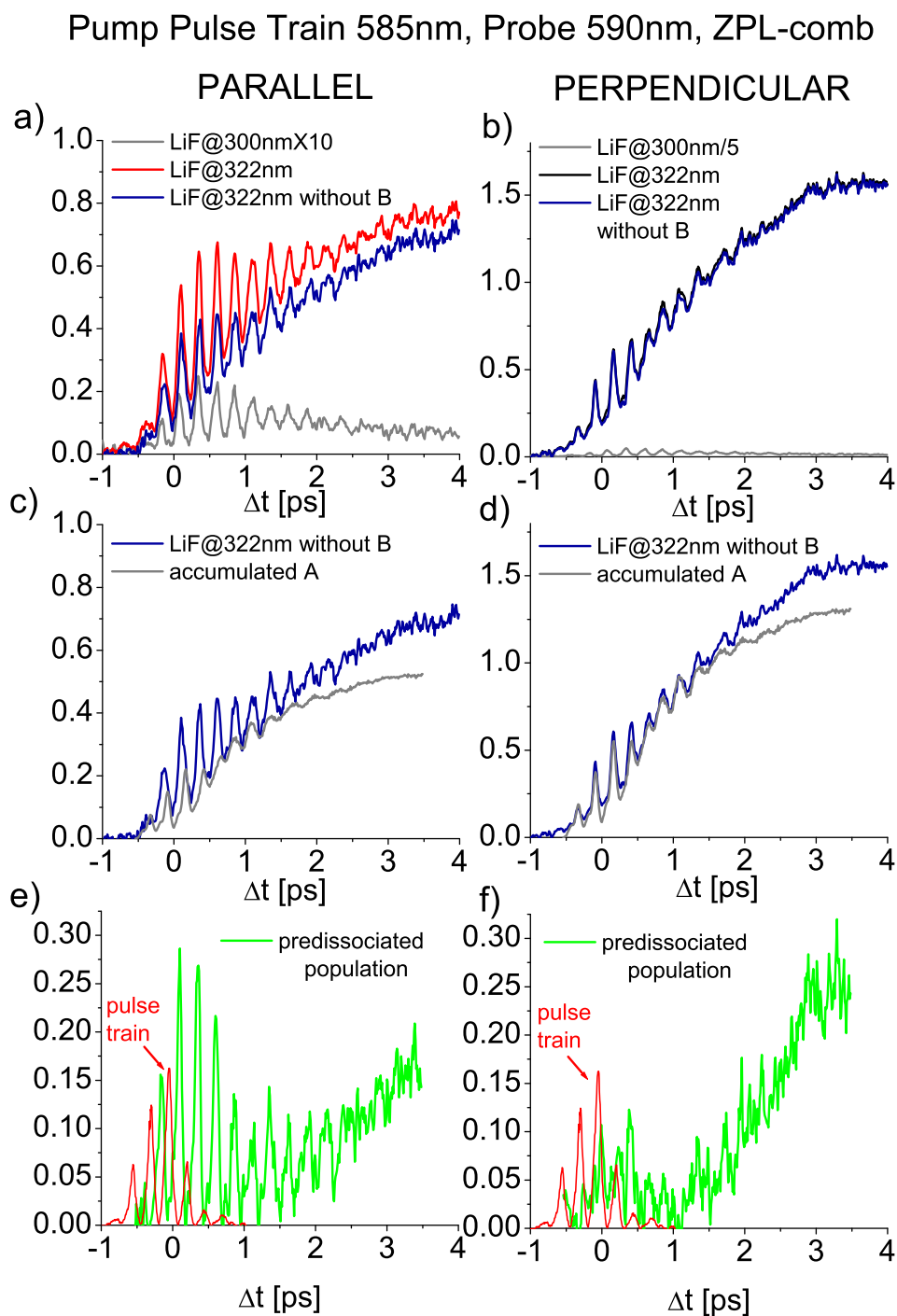
Fig.6.28. Pump probe signals of the ZPL comb excitation for parallel (left column) and perpendicular (right column) relative polarization between pump pulse trains and probe pulses have been decomposed into B (gray, a) and b)), A (gray, c) and d)) and predissociated (green, e) and f)) contributions following the decomposition scheme sketched in Fig. 6.27 (description see text). The excitation pulse train already shown in Fig. 6.14 c) is scaled and replotted in e) and f) (red lines) for reference.
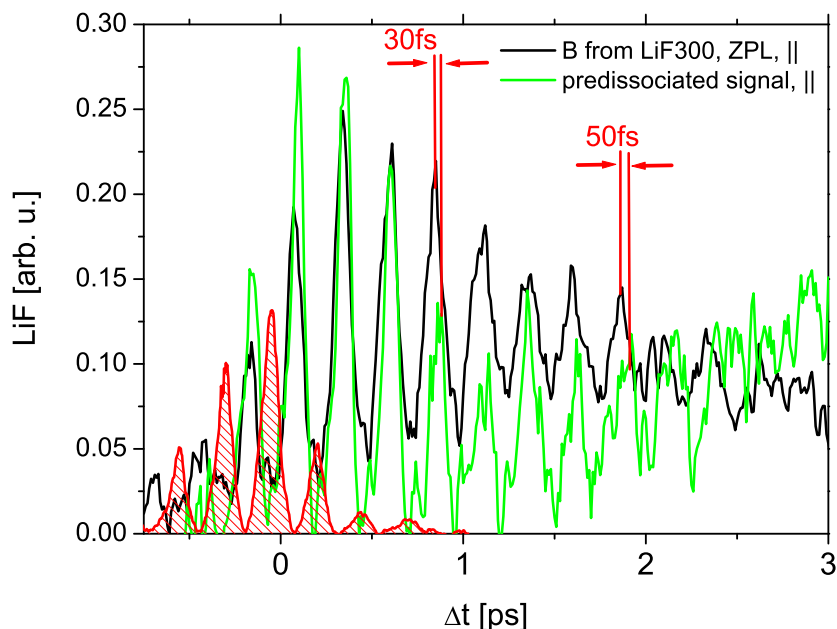
Fig.6.29. Pump probe signal of the ZPL comb excitation for parallel relative polarization from Fig. 6.28 a) (black) together with the predissociated population from Fig. 6.28 e)(green). The vertical lines indicate the time shift between the probing on the B and the repulsive state. The (scaled) excitation pulse train from Fig. 6.14 c) is depicted in red.

point. The subtraction process is shown exemplary for the ZPL comb excitation of series I in the first row of Fig. 6.28. The left column contains the evaluation for the parallel relative polarization and the right column treats the perpendicular case according to the scheme structure of Fig. 6.27. While the red and black lines in Fig. 6.28 a) and b) show the measured spectra, the blue ones depict the contributions not being B, resulting from the subtraction of the properly scaled, time shifted and summed up 300nm spectra (gray lines). In a next step, the accumulated A state contributions will be removed. For the perpendicular case, the procedure has been already presented in the previous part 6.4.1. The accumulated A contribution has been constructed, using the pulse train intensity and subpulse separation time structure to sum up the perpendicular single pump probe spectra (gray lines in Fig. 6.28 c) and d)[4]. For the parallel situation in c) the same procedure has been applied, scaling with parameter 3 from the single pump data. In both cases, perpendicular and parallel, after subtraction a significant signal remains (green lines in e) and f)). This is the predissociated contribution we search for. For parallel

---

[4]At this point it should be noted, that the cross correlation measurement used for the temporal pulse characterization is just the adequate experimental characterization method to be used for the evaluation presented here. Autocorrelation methods would not be appropriate (see Sec. 4.3.2)!
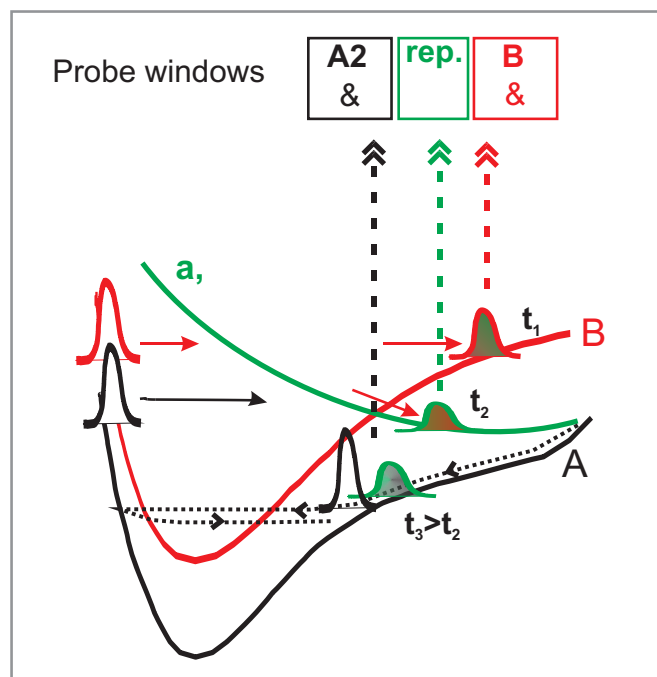
Fig.6.30. Sketch of the predissociation dynamics (extended as compared to Fig. 6.24): Parts of the excited B wave packet (red) are transferred via a crossing intermediate repulsive state a or Π (green) into the A state, where they relax into the A probe window A2 and are probed together withe the A state (black) preferably with perpendicular relative polarization. An additional probing of the predissociated population takes place on the intermediate state with parallel probe polarization at times t_1 before they reach the A2 window at t_2, as shown in Sec. 6.4.2. The corresponding dynamics is very similar to the B state dynamics probed on the outer turning point of the B potential with preferred parallel polarization.

probing, a pronounced additional modulation structure reflecting the B state vibrational period can be observed, remaining for 2.5ps, long after termination of the last subpulse at 0.75ps (compare Fig. 6.14), until the modulations become buried in the structureless part relaxing in probe window A2. Did we forget to remove some B parts? No we did not. Careful comparison of the B wave packet's dynamics from the 300nm fluorescence with this leftover signal, as shown in Fig. 6.29 reveals a small time shift. For early delay times it is not even resolvable with the applied time resolution, however, for the maximum at 800fs, the time difference accumulates to 30fs and at about 1.9ps it reaches a shift of 50fs. Obviously, another probe window comes into play here, monitoring the B state population being predissociated with every single roundtrip of the B wave packet in the nonadiabatic crossing region to an intermediate repulsive state. A possible location of this probe window

is indicated in Fig. 6.30 with the green double arrow (rep., ∥). The small time shift between the probing on the B state and the repulsive state allows the conclusion, that the new probe window is located at an internuclear distance very close to the B potential's outer turning point, where the B state is probed (red double arrow in Fig. 6.30). The direction of the position shift, however, cannot be determined uniquely. A reliable knowledge of the potential structures and corresponding simulations of the wave packet splitting process would be required to gain additional information. In any case we know the following: The splitting takes place before the B wave packet has reached its outer turning point since it is excited above the crossing. Therefore, the corresponding classical position-momentum phase space trajectories of the B and repulsive potential cross at smaller internuclear distances as readable from the potential schemes in Fig. 6.30. This would in principle allow a repulsive probe window position left from the B probe window. After the splitting off from the B potential, however, the predissociated wave packet propagates faster, with a larger kinetic energy than the B wave packet, experiencing immediately after the population transfer to the repulsive wing of the only matrix bound repulsive potential curve, while the B wave packet just approaches the turning point of the attractive wing of the B potential. Hence, a repulsive probe window position on the right side of the B window cannot be excluded either based on these qualitative considerations. Therefore, the exact knowledge of the splitting time and the subsequent wave packet kinetic energy are required for a finer positioning of the parallel probe windows. Finally, the most surprising conclusion concerns the great efficiency of probing on the intermediate state. The intensity is on the order of the B state contribution. At the same time, the predissociation rates predicted by spectroscopy are around 10% per roundtrip in this energetic region. This indicates about one order of magnitude larger transition probability for the probe excitation from the repulsive state to the corresponding CT state. Most likely, the predissociated part is also included in the spectra recorded at 300nm, which have been, however, subtracted. We can assume, that the overall predissociated contribution to the spectra is even larger than determined based on this simple evaluation scheme. Hence, a complete, quantitatively correct determination of the wave packet split-off originating from the B excitation cannot be provided here. The application of the presented evaluation scheme to all applied comb position, will however provide an interesting insight into the challenging coherence properties leading to quantum control of the efficiency of the predissociation process. Predissociation rates will be derived, which will represent lower limits and be quantitatively comparable as relative values for the different comb structures and corresponding state selection, respectively. Before presenting these final results, another self-evident question shall be addressed:

Why does the probing of the predissociated population on the intermediate repulsive state not show up in the single pump probe spectra? In the first instance, it may very well be included, is however hardly discernible from the B state dynamics due to the small time shift and identical periodic structure, in this sense the split-off wave packet is a "twin wave packet" of the one remaining on B. Second, inspecting the comb-structure-dependent outcome of the B state interferences in Fig. 6.17 of Sec. 6.3.1, revealed, that the B state, being the feeding channel of the predissociation, increases to a significant amount only for the ZPL comb and the comb positioned on both ZBP&ZPL. The repulsive probe window is only active in the parallel case, obviously the predissociated population propagates on the intermediate state with B polarization. The repulsive probe window doesn't monitor the velocity of the predissociation, it much more reflects the dynamical development of B state population being potentially available for the reaction. To gain information about the predissociation velocities and rates, the predissociation dynamics has to be analyzed on a larger timescale, which will be done in the following section. When excitation is carried out with a single pump pulse, no coherent enhancement of the B state relative to the A state contribution takes place, hence, despite of the effective probing conditions, the contribution from the repulsive state cannot be isolated from the dominant A part. Finally, in order to construct the overall predissociated population's dynamics according to the evaluation scheme sketched in Fig. 6.27 we have to add parallely and perpendicularly probed contributions. The perpendicular contributions have a double weight as compared to the parallel parts and the overall fluorescence intensity covering the full solid angle 4π is given by $S^{pred} = S_{\parallel}{}^{pred} + 2\,S_{\perp}{}^{pred}$.

6.4.3 Detection scheme for predissociated population

In the following, the overall predissociated populations derived from the pulse train pump probe spectra of series I, following the previously presented procedure, will be presented and explained with help of a simple model. In Fig. 6.31 the overall predissociated signals S^{pred} are shown (green lines) as they are composed of the parallel (red) and double weighted perpendicular (black) contributions in the first column (a-e). In the second column (f-j) the same signals are plotted together with the B dynamics from the 300nm spectra which were used for the decomposition of 322nm-fluorescence parallel spectra for all comb positions, like the one shown in Fig. 6.28 for the ZPL comb excitation. They are scaled with a factor 3 for better comparability. The relative overall predissociation efficiency for the five different comb positions will be quantified by means of three criteria which are marked and

labelled in the first row of Fig. 6.31 (two of them only exemplary for the ZPL comb data). The three quantification parameters are:

- The final values (FV) for the overall predissociated population signal intensities at 3ps (marked by the green curved arrow in Fig. 6.31)

- The crossing times (CT) of the predissociated dynamics and their "mirror" B dynamics (marked by the blue curved arrow)

- The slopes κ of linearly increasing predissociated population after the pulse train excitation is completed and the signal is probed on the A/A' state (the linear fits are depicted as red lines)

Their values are collected in Tab. 6.4 and will be discussed in the following.

First we consider the right column of Fig. 6.31 and compare the decay in the B state dynamics with the rise in predissociation dynamics. For early delay times, up to 1.2ps, for all five comb positions, the predissociation dynamics monitors the B state's "twin wave packet" dynamics on the dissociative state, until the transfer to the A/A' state and the relaxation process of the predissociated part starts to dominate the spectra. If it was not overlayed with the dissipation process, the predissociated population would monitor in this second time interval, after termination of the pulse train excitation, a "mirror wave packet" dynamics of the B state. The population loss process in B would be mirrored in the corresponding gain process of the reaction channel. However, due to the relaxation the positive slope of the predissociated population is steeper than the decrease in the B wave packet's mean value time evolution. Nevertheless, the crossing times (CT) of the B dynamics and the predissociated dynamics (blue vertical arrows) can be used to compare the relative efficiency of the process for the different spectral comb positions concerning its velocity. The relative intensities have been already treated in the previous section and are collected in Tab. 6.3 for the measurements with perpendicular pulse polarizations.

According to the crossing times (CT) at 3ps, the ZPL position leads to the slowest predissociation, immediately followed by the "A" comb, while the PSB and the ZBP comb spectra cross their mirror states 1/3 of the considered time interval earlier. For the simultaneous selection of the ZBP&ZPL the process is three times faster than in the slowest ZPL case (see also Tab. 6.4). The final value of the overall population is also doubled for this comb, as compared to the ZPL case. Indeed, the population increase follows a linear behavior fitted in the left column of Fig. 6.31 with red lines.
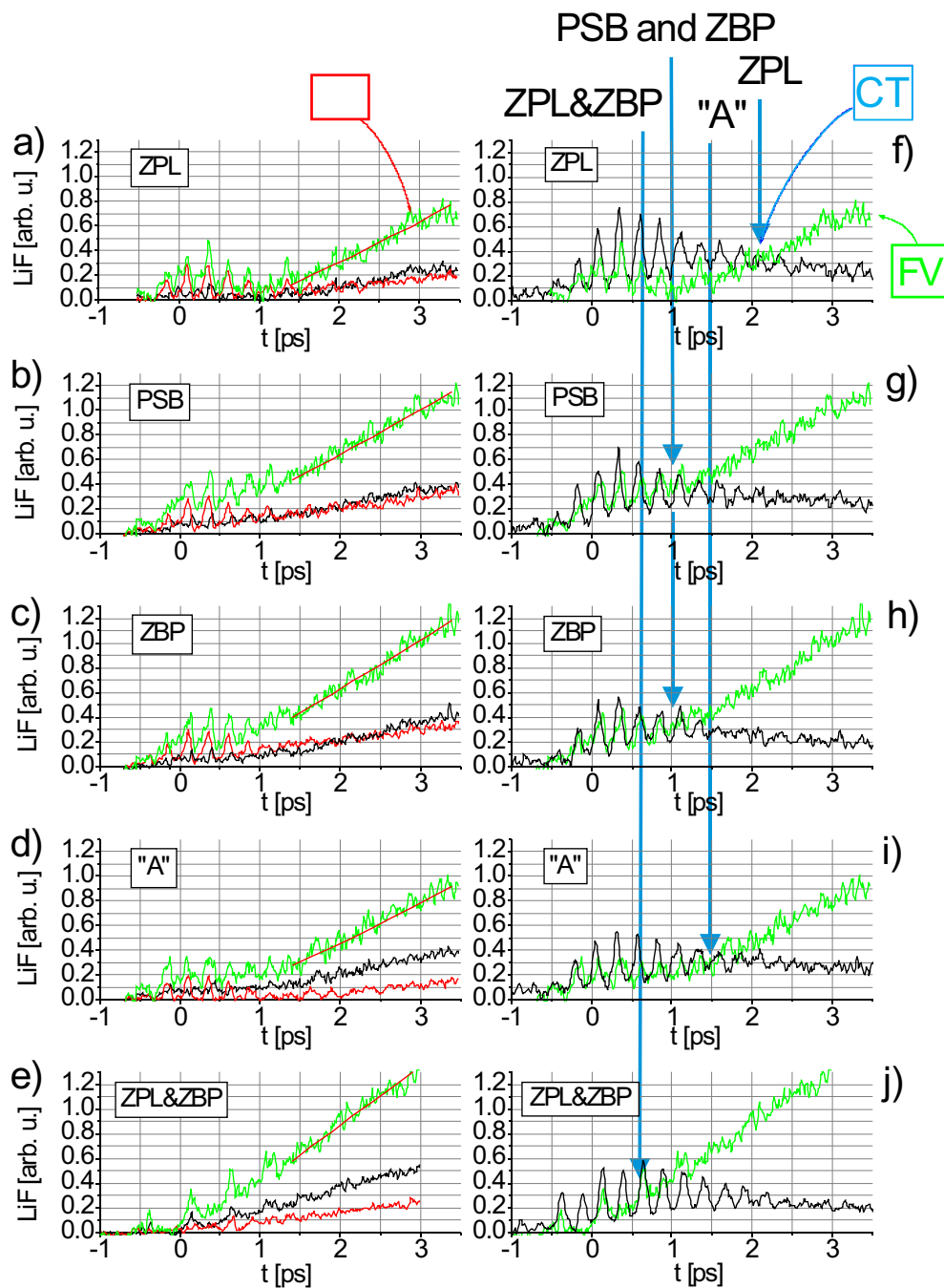
Fig.6.31. The overall predissociated signals (green in left and right column) as an anisotropy corrected sum (see text) of the predissociated signals derived from pump probe spectra with relative to the excitation pulse train parallel (left column, red) and perpendicular (left column, black) polarized probe pulses shown together with calculated values based on a simple model for the accumulating population vibrationally relaxing on the A state (red squares, see text). The right column compares the corresponding B state dynamics (black, LiF@300nm, scaled) to the predissociation dynamics for the five different spectral comb positions (five rows). CT denotes the crossing times of predissociated and B wave packet dynamics, FV stands for the final values and κ for the slopes of the predissociated signals (see text for discussion). Excitation pulse trains and corresponding spectral combs are shown in Fig. 6.14.

comb	ZPL	PSB	ZBP	"A"	ZPL&ZBP
κ [ps^{-1}]	0.32	0.36	0.40	0.32	0.48
CT [ps]	2.00	0.90	0.90	1.62	0.63
FV [arb.u.]	0.7	1.1	1.2	0.9	1.3
From Fig. 6.31	a) and f)	b) and g)	c) and h)	d) and i)	e) and j)

Tab. 6.4 The first row collects the slopes κ of the linear increase of the predissociated population from 6.31 a) - e). The second row collects the temporal position of the crossing (CT) with the B state signal shown in Fig. 6.31 f) - j). In the last row the final value (FV) of the overall predissociated signal at $\Delta t=3$ps is given.

In the following, the results for the different comb positions will be compared and attributed to the chosen spectral selection. Like already indicated by the crossing times of decreasing B and increasing predissociated contributions, the slowest predissociation is observed for the excitation comb positioned on the ZPL. Although, the available B state contributions have been enhanced by constructive interference (see Sec. 6.3.1), thus, in principle a large amount of potentially predissociating population is available, the predissociated population arriving in the A2 probe window and the slope κ are minimal for this comb position. Obviously, the coherent selection of the zero phonon lines goes along with a destructive interference of all phonon contributions. They are responsible for the symmetry breaking in the cage geometry and the weakening of selection rules, thus, for the enhancement of transition probabilities between B and repulsive states, as compared to the gas phase [84]. The decisive importance of the phonon modes and their entanglement to the vibronic states of the molecule for the predissociation process is further supplemented by the final values of predissociated population for the ZBP and PSB comb positions. Although, according to Fig. 6.17 (in Sec. 6.3.1) no significant amount of B population can be gained by excitation with these comb positions, the predissociated population exceeds that of the ZPL position by nearly 40%. The corresponding larger slopes κ and earlier crossing times (CT) for the phonon combs ZBP and PSB as compared to the ZPL comb values, further emphasize the much more stringent relevance of matrix phonons for the predissociation efficiency as compared to the available B population. In addition, the slope κ and the final value FV of the predissociated population in the ZBP case are slightly larger than the corresponding PSB parameters. This observation also supports the theoretical predictions, where the specific phonon modes, which are responsible for the large predissociation efficiency, were

found on the high energetic side of the phonon spectrum [84, 85], where the zone boundary phonons are located, too [5]. For the "A" comb the minimal slope value also observed in the ZPL case is obtained. However, the characteristic values CT and FV lie just in between the ZPL and ZBP/PSB values. Since in that case, besides the contributions from the multiphonon background on the high energy side of the excitation spectrum, all one-phonon modes experience destructive interference, one would intuitively expect the worst conditions for matrix induced predissociation. Far from it! The final predissociated population beats the ZPL value by 22%. Obviously, the phonon contribution in the multiphonon regime contains the relevant phonon modes coupled to the chromophore vibrations, thus, opening the predissociation channel[6]. Although the enhanced predissociation efficiency compared to the ZPL is not reflected in the κ parameter, the advanced crossing time of B and its "mirror wave packet" at 1.62ps, which is 380fs earlier than for the ZPL comb, hold the relevance of coherent multiphonons for the predissociation process. This finding gives evidence for a coherent phonon-phonon-coupling in at least this low energetic part of the multiphonon regime, which supplements the interpretation of the measurements carried out in the strong phonon coupling regime in Sec. 6.3.2. Finally, a doubling of the predissociated population with the value of a κ enhanced by 50% of the ZPL value and a crossing happening 1.37ps earlier than for the ZPL case, is achieved, when selecting a simultaneous ZPL and ZBP excitation. In these types of measurements with the ZPL&ZBP comb, supplementary to the phonon selections, the reaction feeding B state vibrations are constructively enhanced (see Fig. 6.18 in Sec. 6.3.1) even surpassing by far the ZPL case. To this end, the highest predissociation efficiency is obtained, according to the intuitive expectation, when both, chromophore and relevant bath modes are excited with large spectral weights, as compared to the other contributions of the wave packet. The previous considerations of the 4 other comb positions have proven, that the presence of the matrix phonons is a sine qua non in allowing the coherently enhanced B vibrations to influence the predissociation efficiency. The ZPL&ZBP comb measurements even go one step further. The corresponding subpulse separation is adapted to a double period of the B vibrational wave packet of 2·T=500fs. As it can be read off from the phonon density of states of Ar (compare for example Fig. 6.22), this is just the vibrational period of the highest energetic phonon structure attributed to the zone boundary phonon. This is the reason why the ZPL&ZBP comb allows for an in-phase coherent enhancement of both phonon structures.

---

[5]Compare for example Fig. 6.22 in Sec. 6.3.2

[6]See also discussion of the "A" comb excitation shown in Fig. 6.18 d) in Sec. 6.3.1.

Now, besides of being happy about a significant enhancement of the reaction product population, we can learn about the system and the origin of the nonadiabatic transfer process. Not only the presence of specific phonon amplitudes is a sine qua non for the solvent induced predissociation, its dynamical evolution is much more dependent on and dictated by the entanglement between phonon modes themselves just as well as a coherent vibron-phonon-coupling. This allows to create vibrational wave packets with different weights of excitation coefficients belonging to specific phonon modes of the crystal or zero phonon vibrations of Br_2. The success of these spectral selections within the wave packet excitation process is directly reflected in the comb-dependent behavior of the predissociation process. We emphaseize again, that the imprint of the spectral combs into the absorption of the Ar matrix surrounded Br_2 molecules, the whole pulse trains have been absorbed coherently, containing the relevant phase information characterizing the different combs. We can conclude: the goal of controlling solvent induced predissociation in the condensed phase has been achieved with a pulse train being synchronized with every second roundtrip of the B wave packet and the vibrational period of the zone boundary phonon. The experimental realization of the predissociation enhancement is in stimulating good agreement with the theoretical findings, which predict a doubling of predissociation efficiency in presence of the relevant high energetic phonon modes [84,85,177]. These theoretical results also predict a population transfer to the dissociative C state with only every second passage of the B wave packet through the crossing, due to the in-phase motion with the high energetic phonon. Signatures of this behavior observed in the simulations can be also observed experimentally, in the dynamics of the predissociated population for the ZBP&ZPL comb excitation, especially that contained in the early time behavior of the parallel spectra, which is shown in Fig. 6.32. In its early time evolution, the predissociation is predominantly monitored on the intermediate repulsive state, immediately after the splitting off from the B wave packet occurred and the dynamical structure of the process can be resolved (compare Fig. 6.30). At later times, when probing on the A state, due to the previously experienced strong vibrational relaxation and the accumulation of subsequently predissociated portions in the probe window, the compactness and localization of the predissociated wave packet, as it was given in the B state, cannot be expected to be preserved anymore. However, for the probe window of the repulsive state, experimental observations accompany the theoretical ones. Although, in this work, not the crossing with the C state but another crossing has been studied experimentally, which is accessible with FC factors, the theoretically revealed mechanism [84, 85, 177] could be confirmed by means of polarization sensitive rational coherent control with adapted ultrashort pulse trains.
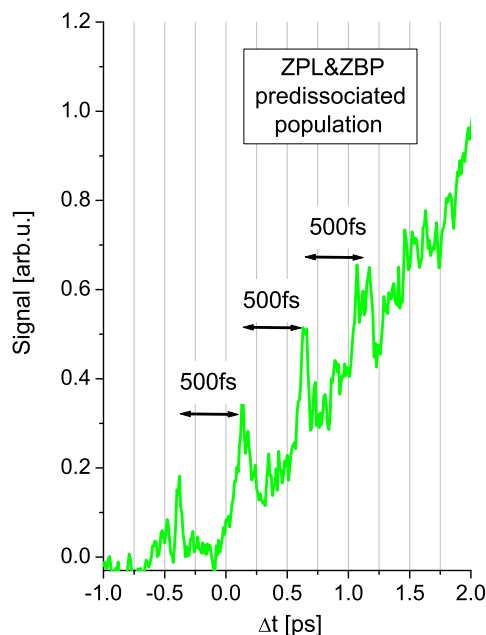
Fig.6.32. Predissociated population for the ZPL&ZBP comb excitation replotted from Fig. 6.30 a). The population probed on the repulsive state in the delay time range between -0.5ps and 1.2ps shows an oscillatory behavior with a period of 500fs, belonging to the oscillation period of the zone boundary phonon.

Hence, it can be concluded, that the phonon induced nature of the reaction is not restricted to a crossing of B and a specific repulsive state but is most likely uniform for all present Landau-Zener type crossings.

Before closing the discussion, we develop an argument for the observed linear behavior of the predissociated population probed on the A/A' states for delay times greater than Δt=1.4ps (see Fig. 6.30 a-f). The relaxation of the predissociated population into the probe window A2 will be explained in two steps. In the first step, we analyze the pure relaxation process in the A state. Afterwards the model will be complemented by the predissociation process. For the first step, the dynamics of a single A wave packet will play the role of a test wave packet. Fig. 6.33 repeats the single pump probe spectrum from series I recorded with perpendicular relative polarizations. It shows the A dynamics with negligibly small B contribution. The relaxation process in the pump probe signal sets in at 700fs with the first recurrence and reaches a maximal value in the probe intensity at 3.25ps. The subsequent relaxation out of the probe window is not relevant in the considered time range. The relaxation towards the probe window leads to a linear increase of the mean value of the oscillations with slope $1/m$, as indicated in Fig. 6.33. The modulation structure has been discussed at the beginning of this chapter. The velocity of the relaxation of this A state test wave packet will be used to model the building up of the predissociated
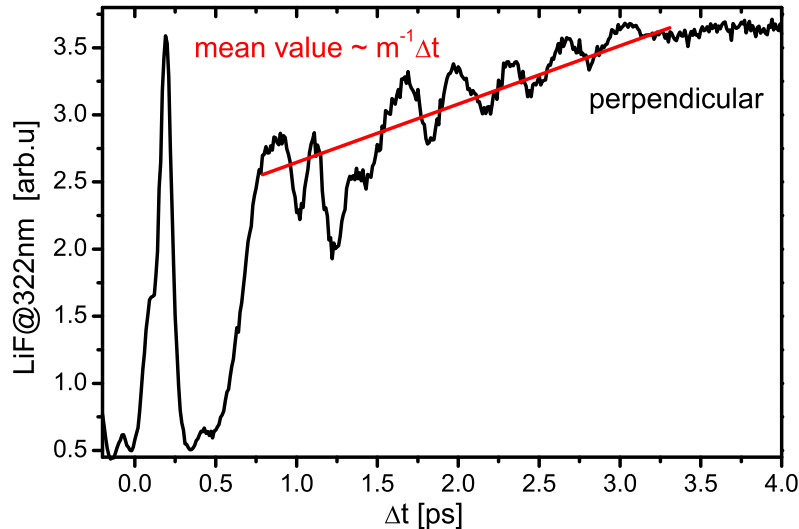
Fig.6.33. Vibrational relaxation of the A state into the probe window A2 (see text).

signal S^{pred}. The second step is the empirical modelling of the additional increase of the signal due to the predissociation process after the coherent excitation process with the pulse train has been completed. Thus, we start signal modelling at a delay time of T_{offset}=1.4ps, assuming that the first portion of predissociated population after termination of the pulse train at Δt=700fs takes additional 700fs in order to appear in the probe window A2, because it performs an A-like dynamics (see Fig. 6.33). After the settling time T_{offset}, parts of the B state wave packet are transferred to the repulsive state in the crossing region with a period denoted ΔT. Between the $(j-1)$-th and the j-th roundtrip the amount of transferred B state population is $\Delta N_j = N_j - N_{j-1}$, where N_j is supposed to evolve according to the process $N_j = N_{j-1} e^{-\alpha \Delta T}$. This model simply assumes, that in each roundtrip, the same percentage of the actual B state population is transferred via the repulsive state in A/A'. We emphasize that this model is applied only for propagation times after the coherent excitation process has been completed. By combining the two steps, the process building up the whole signal S^{pred} will be constructed. Its time evolution is sketched in Fig. 6.34. The signal is formed by a part containing the cumulative sum of all former increments (black dashed) which was assumed to increase linearly in ΔT according to the observed relaxation process and by an additional increment due to the periodic feeding from the repulsive state (red dotted). According to Fig. 6.34 the combined signal for all future times $T_j = T_{offset} + j \cdot \Delta T$ reads:

$$S_j{}^{pred} = S_{j-1}{}^{pred} + \frac{\Delta T}{m} \cdot \sum_{i=1}^{j-1} \Delta N_i + \Delta N_j. \qquad (6.1)$$
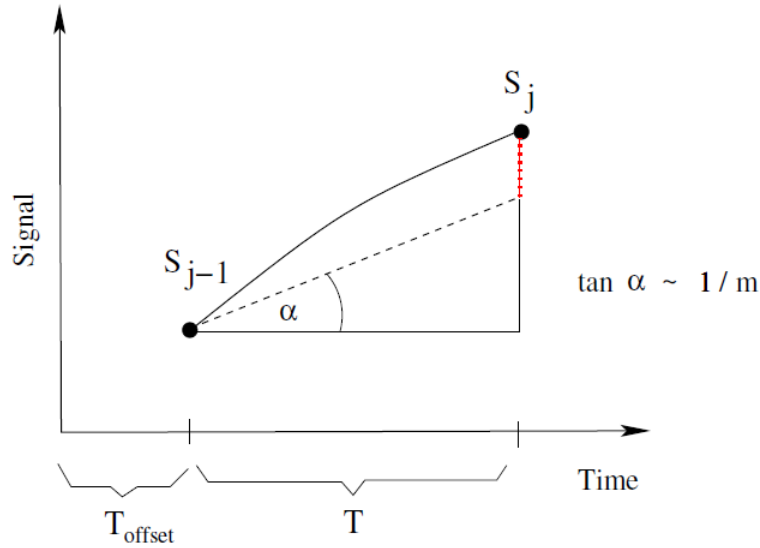
Fig.6.34. Sketch of the model describing the predissociated signal during its energy relaxation into the A state probe window (see text). The model is restricted to times larger than T_{offset}, after termination of the pulse train and an additional time the predissociated population takes to first appear in the probe window. ΔT denotes the period with which population is transferred from B to the repulsive state and finally to the A/A' states. (See text for further explanation.)

The j-th increment is proportional to the first increment ΔN_1 which is the first amount of predissociated population appearing in the A state probe window after T_{offset} and will be therefore denoted $S_1{}^{pred}$ in the following. It reads

$$\Delta N_j \;=\; S_1{}^{pred} \cdot e^{-(j-1)\,\alpha\,\Delta T}\,. \tag{6.2}$$

Inserting equations (6.2) in eq. (6.1) leads to:

$$
\begin{aligned}
S_j{}^{pred} \;&=\; S_{j-1}{}^{pred} \;+\; S_1{}^{pred}\, e^{-(j-1)\,\alpha\,\Delta T} \;+\; S_1{}^{pred} \cdot \frac{\Delta T}{m} \cdot \sum_{i=1}^{j-1} \left(e^{-\alpha\,\Delta T} \right)^{i-1} \\[2mm]
&=\; S_{j-1}{}^{pred} \;+\; S_1{}^{pred}\, e^{-(j-1)\,\alpha\,\Delta T} \;+\; S_1{}^{pred} \cdot \frac{\Delta T}{m} \cdot \sum_{i=0}^{j-2} \left(e^{-\alpha\,\Delta T} \right)^{i} \\[2mm]
&=\; S_{j-1}{}^{pred} \;+\; S_1{}^{pred}\, e^{-(j-1)\,\alpha\,\Delta T} \;+\; S_1{}^{pred} \cdot \frac{\Delta T}{m} \cdot \frac{e^{-(j-1)\,\alpha\,\Delta T} - 1}{e^{-\alpha\,\Delta T} - 1}
\end{aligned}
$$

where in the first step just an index shift has been carried out in order to get the usual form of the geometric series visible and to solve it in the second step. Reorganizing the equation now leads to a definition of the slope of the signal sketched in Fig. 6.34

and observed in Fig. 6.31 a) - e) for the measured data:

$$\frac{S_j{}^{pred} - S_{j-1}{}^{pred}}{\Delta T} = S_1{}^{pred} \cdot \left(\frac{e^{-(j-1)\,\alpha\,\Delta T}}{\Delta T} + \frac{1}{m} \cdot \frac{e^{-(j-1)\,\alpha\,\Delta T} - 1}{e^{-\alpha\,\Delta T} - 1} \right) . \quad (6.3)$$

For sufficient large j the slope reduces to a constant because the exponential function $e^{-(j-1)\,\alpha\,\Delta T}$ decays very fast to zero, hence:

$$\frac{S_j{}^{pred} - S_{j-1}{}^{pred}}{\Delta T} \sim S_1{}^{pred} \cdot \frac{1}{m} \cdot \frac{1}{1 - e^{-\alpha T}} = \kappa . \quad (6.4)$$

Thus, this simple empirical model allows to explain the linear late time behavior of the predissociated signal observed in the experiments for times greater than the electronic coherence times.

Chapter 7

Summary

The goal of this work has been already set in 1998, in the proposal for the first funding period of the collaborative research center SFB 450, "Analysis and Control of Ultrafast Photoinduced Reactions". It comprises the coherent control of phonon induced predissociation in a system built up by dihalogen molecules isolated in a rare gas matrix. The aim was finally achieved in the framework of this PhD thesis on Br_2 embedded in an Ar-matrix environment. This success required the systematic studies carried out during four PhD-generations in our working group. Important milestones were for example the integration of home built NOPAs into the fs-laser setup followed by coherent control experiments with chirped pulses and double pulses from Michelson interferometers, applied to exploit vibrational and electronic coherences in several dihalogen:rare-gas-matrix combinations. Detailed references can be found in the course of the previously presented chapters. In all cases, ultrafast studies were guided and accompanied by conventional wavelength resolved spectroscopic characterization of the systems under consideration.

The choice of Br_2:Ar for the coherent control of predissociation was finally motivated by the well structured excitation spectra, promising sufficiently long vibronic coherence times and dynamically well accessible predissociation efficiencies needed for the quantum control experiments. Combined information from the first pump probe spectra of Br_2:Ar from [88] and the high resolution excitation spectra from [89] revealed appropriate central wavelength regions for pump and probe pulses in the relevant excitation region near nonadiabatic crossings of the electronic B state with repulsive states.

High quality quantum mechanical studies of our theoretical collaboration partners predicted the importance of specific high energetic phonon modes for the efficient predissociation. This finding has been confirmed from an experimental point of view in this thesis.

Footing on the previously mentioned expertise, the systematic experimental and accompanying numerical studies of this work include the following steps and findings:

- First, the optimal duration of excitation pulses for the predissociation studies was determined to be around 80fs by means of a numerical study of the vibronic excitation process for gas phase molecular Br_2 in the spectral domain. The spectral decompositions used field free vibrational states of an effective Morse potential fitted to the B state vibrations in the matrix, determined from excitation spectra in [89]. The spectral representation of B wave packet dynamics was implemented in first order perturbation theory and compared to results of a numerically exact propagation performed with the "WavePacket"-software from [211]. An analytical expression for the spectral coefficients was also derived within first order perturbation theory.

- We had to deal with small Franck Condon factors in the interesting energetic region of nonadiabatic crossings of the B state with repulsive states. Therefore, specific spectral domain effects occurring in case of an ultrashort excitation process with small Franck-Condon factors in the far falling wing of the B state absorption spectrum were characterized numerically. The simulations revealed, how the excitation with spectrally broad ultrashort pulses leads to a blueshift of spectral weight of wave packets with respect to the pump pulses' central photon energy. That could be explained by the underlying interference processes dictated by the phase relations between ground and excited vibrational states and phases of the exciting electric field. It has been elucidated, that sufficiently long pulses, containing a large number of optical cycles are necessary to force the excited wave packet close to the energetic region selected by the central excitation wavelength.

- The numerical spectral domain investigations have been extended to excitations with ultrashort pulse trains and corresponding wave packet interferometric methods. Destructive and constructive wave packet interferences have been simulated in a combined spectral-time domain representation. They illustrate for the simplified gas phase molecule the guiding ideas of our rational coherent control scheme. They especially emphasize the decisive role of both, appropriate relative phase differences between subpulses as well as appropriate linear chirp parameters, in order to establish optimal constructive or destructive interference conditions.

- A comparison of simulated pump probe spectra for gas phase Br_2 with spectra measured in the matrix allowed to identify the signatures of matrix induced predissociation in pump probe spectra and to derive predissociation rates.

- In the experiments pump probe spectra were measured in a polarization sensitive manner. Fluorescence from two different emission bands was detected. This way, sets of measurements with varying parameters were recorded under otherwise identical conditions, allowing for a systematic decomposition of excited vibrational wave packets into their contributions from the different electronic states A and B. The decomposition method tested for conventional single pulse pump probe spectra was cross-checked by the expectation from photoselection rules and afterwards applied to coherent control measurements using trains of five phase-stablized ultrashort excitation pulses. This way, a remaining amount of population, not being addressable to the absorbing B or A state, has been identified. Its dynamics could be interpreted as that of intermediate population predissociated from the B state to a crossing repulsive state and subsequently transferred to the A state. This dynamics also supports the energetic picture of the population flow in the matrix induced predissociation process drawn by the evaluation of excitation spectra in [83].

- Experimentally, spectral combs were generated in a liquid crystal pulse shaper, which lead to the excitation pulse trains in time domain after optical Fourier transformation, according to the setup first introduced in [89, 188, 190]. The B state excitation spectra were directly written in the spectrum of ultrashort laser pulses by pure amplitude filtering. However, the tuning of the spectral combs between spectral positions belonging to zero phonons or phonon sidebands corresponds to a fine tuning of temporal phases of subpulses with a sub-femtosecond accuracy. It allowed to prepare vibrational superposition states of molecular and specific groups of spectrally selected phonon vibrations.

- The possible efficiency of matrix induced predissociation could be enhanced by selecting high energetic phonon modes in the excitation. A combined selection of B state zero phonon vibrations with the highest energetic zone boundary phonon that stays localized at the chromophore led to a doubling of predissociation efficiency, in accordance with the theoretical predictions [84, 85, 177]. The early time dynamics of the predissociated population could be directly monitored on the crossing repulsive state. Its late time dynamics was monitored after transfer to the A/A' states during its vibrational relaxation into an A/A' probe window.

- Finally, systematic variations of pump and probe wavelengths allowed to completely characterize the involved probing conditions on the first and second charge transfer state manifolds (CT1 and CT2) of Br_2. One probe window going to CT2 for the B state could be shown to contribute to two emission

bands, partly radiating directly from CT2 and partly fluorescing after radiationless transition to CT1. Four probe windows (two to CT1, two to CT2) were shown to be involved in the probing of the A state, one of which also undergoes radiationless transition from CT2 to CT1 before emission. Another probe window monitoring predissociated B population on the intermediate repulsive state could be identified. It records the predissociated fragments with each passage of the B wave packet through the nonadiabatic crossing and is located close to the B state window.

- A combination of single pump probe spectra and cross-correlation measurements of the time structure of excitation pulse trains allowed to separate incoherent accumulations in the interferometric wave packet excitations from nonlinear coherence terms. The nonvanishing coherence terms reflect the success in the experimental implementation of our control scheme, revealing vibronic coherence times of up to 1.7ps (longest excitation pulse trains) in the weak phonon coupling regime. Spectral combs positioned on zero phonon lines led to constructive interference terms in the corresponding B state vibrations. They could be optimally amplified interferometrically by additionally selecting spectrally the synchronized zone boundary phonon.

- The wave packet interferometric measurements have been extended to spectral regions with strong phonon coupling. Also in this energetic region, where multiphonons dominate the excitation spectrum, coherently coupled chromophore-lattice dynamics lasting for 1ps could be revealed. The long lasting vibronic coherence shows up here in destructive interference of zero phonon lines observed for spectral combs positioned in the multiphonon background region.

- Finally, the success in experimentally controlling the phonon induced nonadiabatic population transfer process from a chemically bound to an only matrix bound state of the chromophore relies on long lasting vibronic coherences in the coupled chromophore:solid-state-system. It involves coherently synchronized motion of several hundreds of atoms.

Meanwhile, decoherence studies have been extended by other groups to biologically relevant systems. They reveal the importance of coherences for example for light harvesting systems being part of photosynthetic processes [21, 24, 261]. They also stimulate numerous efforts for theoretical exploration of coherences which occur at the ultrafast timescale in many-body systems at the border between quantum and classical mechanics. The methods developed in this work can contribute to resolve the underlying processes on molecular scales.

Appendix A

Calculation of the Morse oscillator eigenstates

The spectral problem of the Morse oscillator has attracted constant interest since the early days of quantum mechanics. Soon after its solution was published by P. M. Morse [212], its generalizations to rovibrational problems have been studied in [262–264] and reviewed in [265, 266]. Further generalizations comprise for example the modelling of stretching modes of methane and similar molecules [267]. Furthermore, coherent states of the Morse oscillator have been investigated in [268–270]. Phase space properties and problems concerning a stable numerical implementation of the Morse oscillator eigenstates can be found in [271].

In this appendix we record for the convenience of the reader the derivation of the eigenstates for the Schrödinger equation with a Morse potential as it has been implemented in this work. The starting point is the Schrödinger equation below,

$$\left[-\frac{\hbar^2}{2m} \frac{\partial^2}{\partial R^2} + V(R) \right] \psi(R) = E \psi(R), \tag{7.1}$$

where the functional shape of the Morse-Potential from eq. (7.2) and as depicted in Fig. 3.3 will be used

$$V(R) = D \cdot \left[1 - e^{-\beta (R - R_0)} \right]^2. \tag{7.2}$$

For further consideration it is reasonable to eliminate all irrelevant parameters, which leads to following scaling:

$$D = \frac{\hbar^2 k_0^2}{2m}, \qquad E = \frac{\hbar^2 \beta^2}{2m} \varepsilon \tag{7.3}$$

and to the coordinate shift

$$\xi = R - R_0 \quad \Rightarrow \quad \frac{\partial}{\partial R} = \frac{\partial}{\partial \xi} \cdot \frac{\partial \xi}{\partial R} = \frac{\partial}{\partial \xi}. \tag{7.4}$$

In these coordinates the Schrödinger equation (7.1) takes the following form:

$$\left[-\frac{\partial^2}{\partial \xi^2} + k_0^2 \cdot \left[1 - e^{-\beta \xi} \right]^2 \right] \psi(\xi) = \beta^2 \varepsilon \psi(\xi) . \tag{7.5}$$

Another variable transformation, which was chosen in such a way, that the new variable appears in the transformed Schrödinger equation only polynomially,

$$y = 2\frac{k_0}{\beta} e^{-\beta \xi} \quad \Rightarrow \quad \frac{\partial}{\partial \xi} = \frac{\partial}{\partial y} \cdot \frac{\partial y}{\partial \xi} = -\beta y \frac{\partial}{\partial y} , \tag{7.6}$$

leads to

$$\left[-\beta y \frac{\partial}{\partial y} \left(\beta y \frac{\partial \psi}{\partial y} \right) + k_0^2 \cdot \left[1 - \frac{\beta y}{2 k_0} \right]^2 \psi(y) \right] = \beta^2 \varepsilon \psi(y) \tag{7.7}$$

and can be finally written as

$$\left[\frac{\partial^2}{\partial y^2} + \frac{1}{y} \frac{\partial}{\partial y} - \frac{1}{4} + \frac{k_0}{\beta y} + \frac{\varepsilon - k_0^2/\beta^2}{y^2} \right] \psi(y) = 0 . \tag{7.8}$$

Asymptotic form of the solution

One obtains the asymptotic shape of the solution for $y \to \infty$ from the solution of following differential equation (DE), which arises by neglecting terms which disappear for $y \to \infty$:

$$\left[\frac{\partial^2}{\partial y^2} - \frac{1}{4} \right] \psi(y) = 0 . \tag{7.9}$$

The two linearly independent solutions are

$$\psi(y) = c_1 e^{-y/2} + c_2 e^{y/2} . \tag{7.10}$$

The request of regularity of the wave function for $y \to \infty$ leads to the choice $c_2 = 0$. In an analogue way the asymptotic form of the DE in the limes $y \to 0$ becomes

$$\left[\frac{\partial^2}{\partial y^2} + \frac{1}{y} \frac{\partial}{\partial y} + \frac{\varepsilon - k_0^2/\beta^2}{y^2} \right] \psi(y) = 0 . \tag{7.11}$$

One deals with an Euler DE. Inserting the Ansatz $\psi(y) = y^\lambda$ in equation (7.11)

leads to

$$0 \;=\; \lambda\,(\lambda-1)\,y^{\lambda-2} + \lambda\,y^{\lambda-2} + \left(\varepsilon - \frac{k_0^2}{\beta^2}\right)y^{\lambda-2}\,, \tag{7.12}$$

i.e.:

$$\lambda^2 \;=\; \frac{k_0^2}{\beta^2} - \varepsilon \quad\Leftrightarrow\quad \lambda \;=\; \pm\sqrt{\frac{k_0^2}{\beta^2} - \varepsilon}\,. \tag{7.13}$$

Only the positive sign remains of interest since the wave function has to be regular in the origin.

Constructing the solutions:

From the asymptotic analysis following Ansatz for the wave function $\psi(y)$ can be derived

$$\psi(y) \;=\; y^\lambda\, e^{-y/2}\, \varphi(y)\,, \tag{7.14}$$

where $\varphi(y)$ is regular for $y \to 0$ and falls stronger than $e^{-y/2}$ for $y \to \infty$.
In order to reformulate the DE (7.8) with help of the Ansatz from eq. (7.14) to the unknown function $\varphi(y)$ we need the first and second derivative of $\psi(y)$:

$$\psi' \;=\; \frac{\lambda}{y}\,\psi - \frac{1}{2}\,\psi + y^\lambda\, e^{-y/2}\,\varphi' \tag{7.15}$$

$$\psi'' \;=\; -\frac{\lambda}{y^2}\,\psi + \frac{\lambda}{y}\,\psi' - \frac{1}{2}\,\psi' + \lambda\, y^{\lambda-1}\, e^{-y/2}\,\varphi'$$
$$-\frac{1}{2}\,y^\lambda\, e^{-y/2}\,\varphi' + y^\lambda\, e^{-y/2}\,\varphi''\,. \tag{7.16}$$

Inserted in eq. (7.8) one receives

$$y^\lambda\, e^{-y/2}\left[\varphi'' + \left(\frac{\lambda}{y} - \frac{1}{2}\right)\varphi' + \left(\frac{\lambda}{y} - \frac{1}{2}\right)\frac{\psi'}{y^\lambda\, e^{-y/2}} - \frac{\lambda}{y^2}\,\varphi \right.$$
$$\left. +\frac{1}{y}\frac{\psi'}{y^\lambda\, e^{-y/2}} - \frac{1}{4}\,\varphi + \left(\frac{k_0/\beta}{y} - \frac{\lambda^2}{y^2}\right)\varphi\right] \;=\; 0\,,$$

what can be summarized into:

$$0 \;=\; y\,\varphi'' + [2\,\lambda + 1 - y]\,\varphi' + \left[\underbrace{\frac{k_0}{\beta} - \frac{2\lambda+1}{2}}_{\stackrel{!}{=}n}\right]\varphi\,. \tag{7.17}$$

where n at this point is only an abbreviation and will turn out to be is the integer valued vibrational quantum number. The underbraced expression in eq. (7.17) expresses λ in terms of n as:

$$\lambda \;=\; \frac{k_0}{\beta} - \frac{2n+1}{2} \tag{7.18}$$

and due to eq. (7.13) we receive the known eigenenergies

$$\varepsilon \;=\; \frac{k_0^2}{\beta^2} - \lambda^2 \tag{7.19}$$

$$\;=\; \frac{k_0^2}{\beta^2} - \left(\frac{k_0}{\beta} - \frac{2n+1}{2} \right)^2 . \tag{7.20}$$

The greatest quantum number n belonging to the highest energetic bound state is:

$$\frac{k_0}{\beta} - \frac{2n+1}{2} \;\geq\; 0 \quad \Leftrightarrow \quad n \leq \frac{k_0}{\beta} - \frac{1}{2} . \tag{7.21}$$

For further calculation of the analytical form of the corresponding eigenstates we recognize that eq. (7.17) is a special case of the confluent hypergeometric DE

$$y\varphi'' + (b - y)\varphi' - a\varphi \;=\; 0 . \tag{7.22}$$

The regular solution of the confluent hypergeometric DE at $y = 0$ reads [266, 272]

$$_1F_1(a, b; y) \;=\; \sum_{k=0}^{\infty} \frac{(a)_k}{(b)_k} \frac{y^k}{k!} \tag{7.23}$$

where $(a)_n = \frac{\Gamma(a+n)}{\Gamma(a)}$ is the Pochhammer symbol. In eq. (7.17) the parameters a and b take the values $-n$ and $2\lambda + 1$, respectively. Since we are interested in polynomial solutions of eq. (7.17) only, the confluent hypergeometric DE simplifies to the Laguerre DE which assumes integer valued n [252]. Then, the solutions simplify to the generalized Laguerre polynomials which read [273]

$$L_n^{2\lambda}(y) \;=\; \frac{\Gamma(n + 2\lambda + 2)}{n! \cdot \Gamma(2\lambda + 2)} \cdot {}_1F_1(-n, 2\lambda + 1, y) . \tag{7.24}$$

They obey the orthogonality relation

$$< L_n^{2\lambda} | L_m^{2\lambda} > \;=\; \int_0^{\infty} y^{2\lambda} e^{-y} L_n^{2\lambda}(y) L_m^{2\lambda}(y) \, dy \;=\; \frac{\Gamma(n + 2\lambda + 1)}{n!} \cdot \delta_{nm} . \tag{7.25}$$

It is particularly useful to determine the normalization constant of the eigenstates. They read:

$$\psi_n(y) \;=\; \sqrt{\frac{2\,\lambda\,\beta\,n!}{\Gamma(n+2\lambda+1)}}\, y^\lambda\, e^{-y/2}\, L_n^{2\lambda}(y)\,. \tag{7.26}$$

Now, the eigenenergies from eq. (7.19) will be also given in the physical units. Combination with eq. (7.3) leads to the expression:

$$E \;=\; \frac{\hbar^2\beta^2}{2m}\left[\frac{k_0^2}{\beta^2} - \left(\frac{k_0}{\beta} - \frac{2n+1}{2}\right)^2\right]$$

$$=\; \frac{\hbar^2\beta^2}{2m}\left[2\frac{k_0}{\beta}\left(n+\frac{1}{2}\right) - \left(n+\frac{1}{2}\right)^2\right]$$

$$\overset{!}{=}\; \hbar\,\omega_e\left(n+\frac{1}{2}\right) - \hbar\,\omega_e\,x_e\left(n+\frac{1}{2}\right)^2$$

where

$$\omega_e \;=\; \frac{\hbar\beta k_0}{m} \quad\text{and}\quad x_e\,\omega_e \;=\; \frac{\hbar\beta^2}{2m}\,. \tag{7.27}$$

Inserting for D the expression from eq. (7.3) leads to

$$\omega_e \;=\; \frac{\sqrt{2}\beta\sqrt{D}}{\sqrt{m}}, \quad x_e\,\omega_e \;=\; \frac{\hbar\beta^2}{2m} \tag{7.28}$$

or the well known expressions

$$D \;=\; \frac{\hbar\,\omega_e}{4\,x_e}, \quad \beta \;=\; \sqrt{\frac{2\,m\,x_e\,\omega_e}{\hbar}} \tag{7.29}$$

The harmonic frequency then builds up from the product of D and β^2:

$$\omega_e^2 \;=\; \frac{2\,D\,\beta^2}{m}\,. \tag{7.30}$$

Appendix B

Gallery of pump probe spectra

The pump probe spectra collected in this gallery were recorded with elliptically polarized pulses, with parallel (red) and perpendicular (black) relative orientation of the polarization ellipses of pump and probe pulses. The experiments were carried out according to the setup from Fig. 4.1, where NOPAII provided the probe and NOPAIII the pump pulses. The variation of excitation and probe wavelengths allowed to identify the probe windows collected in Fig. 6.8.

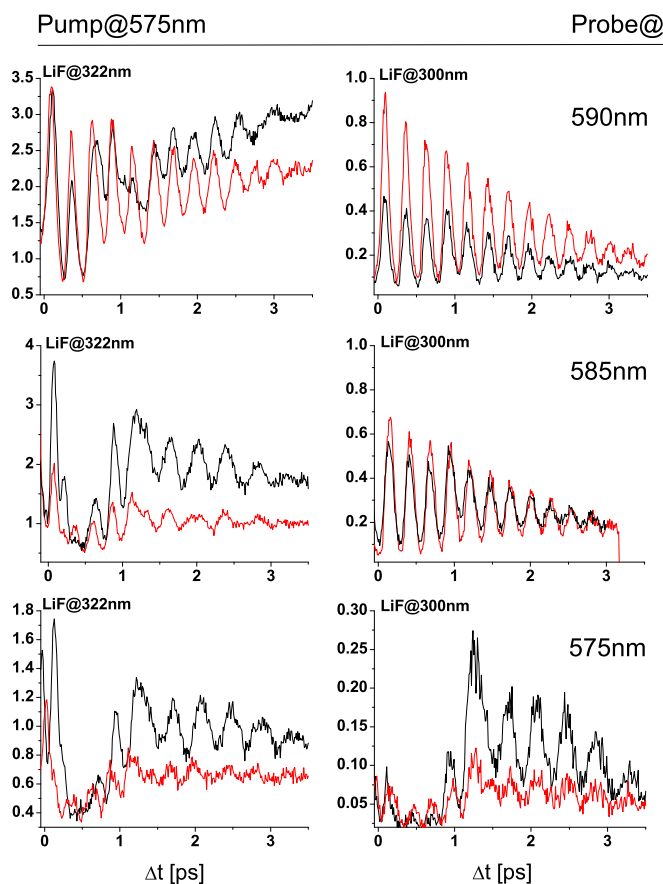Figure showing pump probe spectra excited with 575nm pulses and probed with 590nm (first row), 585nm (second row) and 575nm (last row). Fluorescence recorded at 322nm wavelength is shown in the first column, at 300nm in the second one.

Pump probe spectra with elliptically polarized pulses with parallel and **perpendicular** relative orientations of pump and probe polarizations for varying pump and probe wavelengths
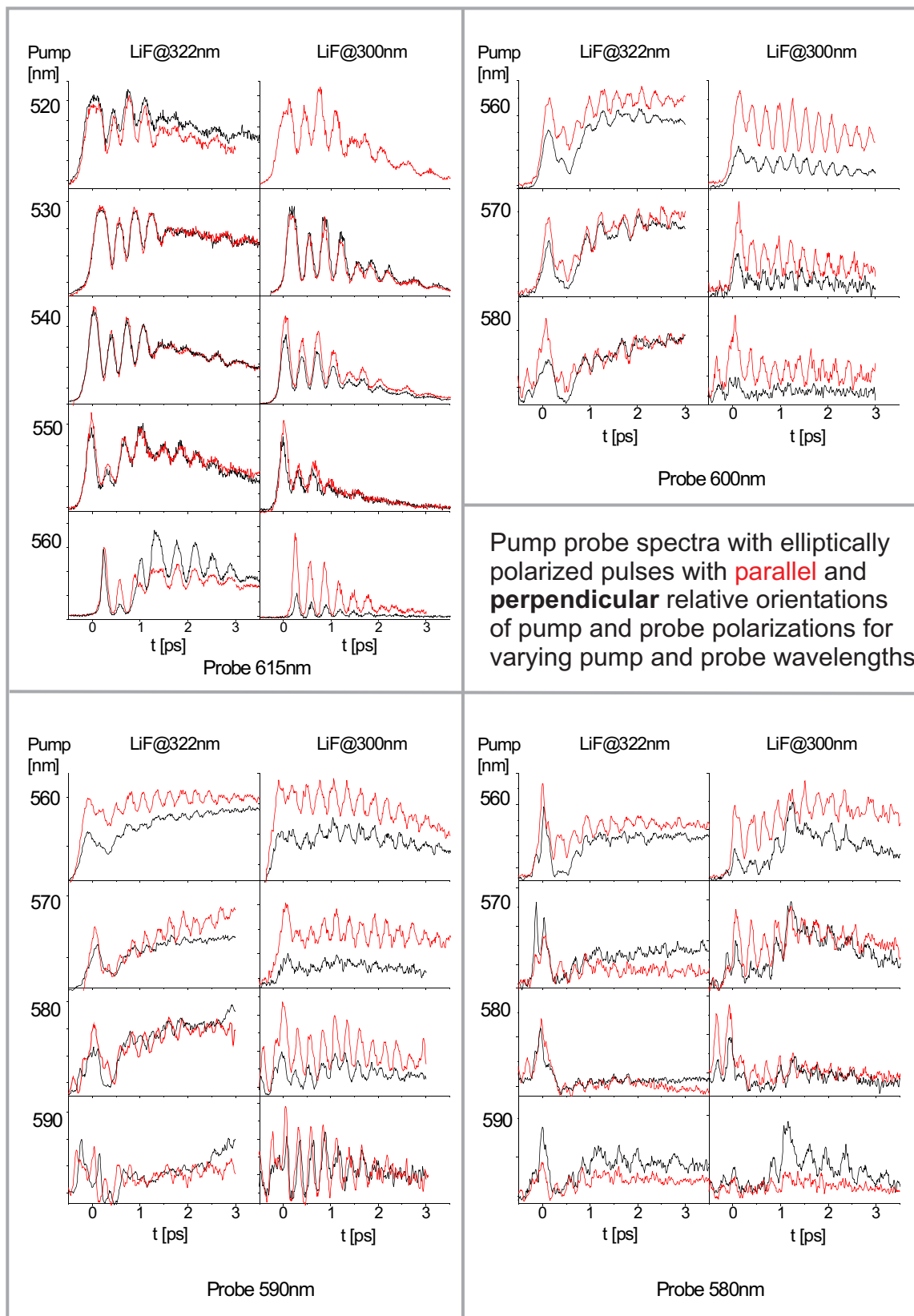
Bibliography

[1] E. Schrödinger, "Die gegenwärtige Situation in der Quantenmechanik," *Naturwissenschaften* **23** (1935) 807–812, 823–828, 844–849.

[2] E. Schrödinger, "Discussion of probability relations between separated systems," *Proc. Cambridge Philos. Soc.* **31** (1935) 555–563.

[3] E. Schrödinger, "Probability relations between separated systems," *Proc. Cambridge Philos. Soc.* **32** (1936) 446–452.

[4] M. Born and R. Oppenheimer, "Zur Quantentheorie der Molekeln," *Annalen der Physik* **389** (1927) 457–484.

[5] D. J. Tannor, *Introduction to Quantum Mechanics, A Time-Dependent Perspective.* University Science Books, Sausalito, first ed., 2007.

[6] E. Joos, H. D. Zeh, C. Kiefer, D. Giulini, J. Kupsch, and I.-O. Stamatescu, *Decoherence and the Appearance of a Classical World in Quantum Theory.* Springer, Berlin Heidelberg, first ed., 1996.

[7] W. H. Zurek, "Decoherence and the Transition from Quantum to Classical - Revisited," *Los Alamos Science* **27** (2002) 86–109.

[8] W. H. Zurek, "Quantum Darwinism," *Nature Physics* **5** (2009) 181 – 188.

[9] M. Schlosshauer, *Decoherence and the Quantum to Classical Transition.* Springer, Berlin Heidelberg, first ed., 2007.

[10] D. Segale, M. Karavitis, E. Fredj, and V. A. Apkarian, "Quantum coherent dissipation: A glimpse of the 'cat'," *J. Chem. Phys.* **122** 111104 (2005) (5 pages).

[11] A. Mari, K. Kieling, B. M. Nielsen, E. Polzik, and J. Eisert, "Most quantum states are too entangled to be useful as computational resources," *Phys. Rev. Lett.* **106** 10403 (2011) (4 pages).

[12] D. Segale and V. A. Apkarian, "Dissipative quantum coherent dynamics probed in phase-space: Electronically resonant 5-color 4-wave mixing on I_2(B) in solid Kr," *J. Chem. Phys* **135** 024203 (2011) (12 pages).

[13] W. H. Zurek, "Environment-induced superselection rules," *Phys. Rev. D* **26** (1982) 1862–1880.

[14] E. Joos and H. D. Zeh, "The emergence of classical properties through interaction with the environment," *Z. Phys. B* **59** (1985) 223–243.

[15] C. Monroe, D. M. Meekhof, B. E. King, and D. J. A. Wineland, "'Schrödinger cat' superposition state of an atom," *Science* **272** (1996) 1131–1136.

[16] E. Schrödinger, "Der stetige Übergang von der Mikro- zur Makromechanik," *Naturwissenschaften* **28** (1926) 664–666.

[17] R. J. Glauber, "Coherent and incoherent states of the radiation field," *Phys. Rev.* **131** (1963) 2766–2788.

[18] R. J. Glauber, "Nobel Lecture: One hundred years of light quanta," *Rev. Mod. Phys.* **78** (2006) 1267–1278.

[19] M. Brune, E. Hagley, J. Dreyer, X. Maître, A. Maali, C. Wunderlich, J. M. Raimond, and S. Haroche, "Observing the progressive decoherence of the 'meter' in a quantum measurement," *Phys. Rev. Lett.* **77** (1996) 4887–4890.

[20] J. M. Raimond, M. Brune, and S. Haroche, "Manipulating quantum entanglement with atoms and photons in a cavity," *Rev. Mod. Phys.* **73** (2001) 565–582.

[21] G. S. Engel, T. R. Calhoun, E. L. Read, T.-K. Ahn, T. Mancal, Y.-C. Cheng, R. E. Blankenship, and G. R. Fleming, "Evidence for wavelike energy transfer: Quantum coherence in photosynthetic systems," *Nature* **446** (2007) 782–786.

[22] H. Lee, Y.-C. Cheng, and G. R. Fleming, "Coherence dynamics in photosynthesis: Protein protection of excitonic coherence," *Science* **316** (2007) 1462–1465.

[23] T. K. Ahn, T. J. Avenson, G. Peers, Z. Li, L. DallOsto, R. Bassi, K. K. Niyogi, and G. R. Fleming, "Investigating energy partitioning during photosynthesis using an expanded quantum yield convention," *Chem. Phys.* **357** (2009) 151–158.

[24] E. L. Read, G. S. Schlau-Cohen, G. S. Engel, T. Georgiou, M. Z. Papiz, and G. R. Fleming, "Pigment organization and energy level structure in light-harvesting complex 4: Insights from two-dimensional electronic spectroscopy," *J. Phys. Chem. B* **113** (2009) 6495–6504.

[25] J. L. Herek, W. Wohlleben, R. J. Cogdell, D. Zeidler, and M. Motzkus, "Quantum control of energy flow in light harvesting," *Nature* **417** (2002) 533–535.

[26] A. Einstein, B. Podolsky, and N. Rosen, "Can quantum-mechanical description of physical reality be considered complete?," *Phys. Rev.* **47** (1935) 777–780.

[27] A. A. P. Grangier and G. Roger, "Experimental Realization of Einstein-Podolsky-Rosen-Bohm Gedankenexperiment: A New Violation of Bell's Inequalities," *Phys. Rev. Lett.* **49** (1982) 91–94.

[28] P. G. Kwiat, K. Mattle, H. Weinfurter, A. Zeilinger, A. V. Sergienko, and Y. H. Shih, "New High-Intensity Source of Polarization-Entangled Photon Pairs," *Phys. Rev. Lett.* **75** (1995) 4337–4341.

[29] M. O. Scully and M. S. Subairy, *Quantum Optics*. Cambridge University Press, Cambridge, first ed., 1997.

[30] W. P. Schleich, *Quantum Optics in Phase Space*. Wiley VCH, Berlin, first ed., 2001.

[31] D. Goswami, "Decoherence control in quantum computing with simple chirped pulses," *PRAMA-Journal of Phys.* **59** (2002) 235–242.

[32] P. Shor, "Scheme for reducing decoherence in quantum computer memory," *Phys. Rev. A.* **52** (1995) 2493–2496.

[33] L. K. Grover, "Quantum mechanics helps in searching for a needle in a haystack," *Phys. Rev. Lett.* **79** (1997) 325–328.

[34] C. Miquel, J. P. Paz, and W. H. Zurek, "Quantum computation with phase drift errors," *Phys. Rev. Lett.* **78** (1997) 3971–3974.

[35] E. Knill, R. Laflamme, and G. J. Milburn, "A scheme for efficient quantum computation with linear optics," *Nature* **409** (2001) 46–52.

[36] H. Katsuki, K. Hosaka, H. Chiba, and K. Ohmori, "Read and write amplitude and phase information by using high-precision molecular wave-packet interferometry," *Phys. Rev. A.* **76** 013403 (2007) (13 pages).

[37] D. Gross, S. Flammia, and J. Eisert, "Directly measuring non-classicality," *Phys. Rev. Lett.* **102** 190501 (2009) (4 pages).

[38] L. Hackermüller, S. Uttenthaler, K. Hornberger, E. Reiger, B. Brezger, A. Zeilinger, and M. Arndt, "The wave nature of biomolecules and fluorofullerenes," *Phys. Rev. Lett.* **91** 090408 (2003) (4 pages).

[39] L. Hackermüller, K. Hornberger, B. Brezger, A. Zeilinger, and M. Arndt, "Decoherence of matter waves by thermal emission of radiation," *Nature* **427** (2004) 711–714.

[40] L. Hackermüller, K. Hornberger, B. Brezger, A. Zeilinger, and M. Arndt, "Decoherence in a Talbot Lau interferometer: the influence of molecular scattering," *Appl. Phys. B* **77** (2003) 781–787.

[41] A. H. Zewail, *Femtochemistry, Ultrafast Dynamics of the Chemical Bond Vol. I + II.* World Scientific, Singapore, 1994.

[42] A. H. Zewail, "Femtochemistry: atomic-scale dynamics of the chemical bond," *J. Phys. Chem. A* **104** (2000) 5660–5694.

[43] A. H. Zewail, "Femtochemistry: Atomic-Scale Dynamics of the Chemical Bond Using Ultrafast Lasers (Nobel Lecture)," *Angewandte Chemie International Edition* **39** (2000) 2586–2631.

[44] J. Manz and J. A. Castleman, "Special issue on femtochemistry," *J. Phys. Chem.* **97** (1993) 12423–12644.

[45] J. Manz and L. Wöste, *Femtosecond Chemistry Vol. I + II.* VCH Verlagsgesellschaft, Weinheim, 1995.

[46] M. Chergui, "Structural dynamics in quantum solids," in *Trends in femtosecond lasers and spectroscopy*, pp. 1453–1467. Academie des sciences Paris, 2001.

[47] P. H. Bucksbaum, "The future of attosecond spectroscopy," *Science* **317** (2007) 766–769.

[48] F. Krausz and M. Y. Ivanov, "Attosecond physics," *Rev. Mod. Phys.* **81** (2009) 163–234.

[49] E. Goulielmakis, Z. Loh, A. Wirth, R. Santra, N. Rohringer, V. Yakovlev, S. Zherebtsov, T. Pfeifer, A. M. Azzeer, M. F. Kling, S. R. Leone, and F. Krausz, "Real-time observation of valence electron motion," *Nature* **466** (2010) 739–744.

[50] I. Barth and J. Manz, "Quantum switching of magnetic fields by circularly polarized re-optimized π laser pulses: From one-electron atomic ions to molecules," in *Progress in Ultrafast Intense Laser Science VI* (K. Yamanouchi, A. D. Bandrauk, and G. Gerber, eds.), no. 99 in Springer Series in Chemical Physics, pp. 21–44. Springer, Berlin, 2010.

[51] M. F. Kling and M. J. J. Vrakking, "Elektronen unter Kontrolle," *Physik Journal* **01/2012** 25–30.

[52] P. Brumer and M. Shapiro, "Control of unimolecular reactions using coherent light," *Chem. Phys. Lett.* **126** (1986) 541–546.

[53] P. Brumer and M. Shapiro, "Laser control of molecular processes," *Ann. Rev. Phys. Chem.* **43** (1992) 257–282.

[54] M. Shapiro, C. Zhidang, and P. Brumer, "Simultaneous control of selectivity and yield of molecular dissociation: pulsed incoherent interference control," *Chem. Phys.* **217** (1997) 325–340.

[55] R. S. Judson and H. Rabitz, "Teaching lasers to control molecules," *Phys. Rev. Lett.* **68** (1992) 1500–1503.

[56] W. S. Warren, H. Rabitz, and M. Dahleh, "Coherent control of quantum dynamics: The dream is alive," *Science* **259** (1993) 1581–1589.

[57] H. Rabitz, R. de Vivie-Riedle, M. Motzkus, and K. L. Kompa, "Whither the future of controlling quantum phenomena?," *Science* **288** (2000) 824–828.

[58] S. A. Rice and M. Zhao, *Optical Control of Molecular Dynamics*. John Wiley and Sons, New York, 2000.

[59] M. Shapiro and P. Brumer, *Principles of the Quantum Control of Molecular Processes*. Wiley, New York, 2003.

[60] Z. Amitay, A. Gandman, L. Chuntonov, and L. Rybak, "Multichannel selective femtosecond coherent control based on symmetry properties," *Phys. Rev. Lett.* **100** 193002 (2008) (4 pages).

[61] M. de Groot, R. W. Field, and W. J. Buma, "Interference in acetylene intersystem crossing acts as the molecular analog of young's double-slit experiment," *PNAS* **106** (2009) 2510–2514.

[62] D. J. Tannor and S. A. Rice, "Control of selectivity of chemical reaction via control of wavepacket evolution," *J. Chem. Phys.* **83** (1985) 5013–5018.

[63] D. J. Tannor, R. Kosloff, and S. A. Rice, "Coherent pulse sequence induced control selectivity of reactions: Exact quantum mechanical calculations," *J. Chem. Phys.* **85** (1986) 5805–5820.

[64] D. Goswami, "Optical pulse shaping approaches to coherent control," *Phys. Rep.* **374** (2003) 385–481.

[65] T. Brixner and G. Gerber, "Femtosecond polarization pulse shaping," *Opt. Lett.* **26** (2000) 557–559.

[66] T. Brixner, G. Krampert, T. Pfeifer, R. Selle, G. Gerber, M. Wollenhaupt, O. Graefe, C. Horn, D. Liese, and T. Baumert, "Quantum control by ultrafast polarization shaping," *Phys. Rev. Lett.* **92** 208301 (2004) (4 pages).

[67] S. M. Weber, A. Lindinger, M. Plewicki, C. Lupulescu, F. Vetter, and L.Wöste, "Temporal and spectral optimization course analysis of coherent control experiments," *Chem. Phys.* **306** (2004) 287–293.

[68] A. Lindinger, S. M. Weber, C. Lupulescu, F. Vetter, M. Plewicki, A. Merli, L. Wöste, A. F. Bartelt, and H. Rabitz, "Revealing spectral field features and mechanistic insights by control pulse cleaning," *Phys. Rev. A* **71** 013419 (2005) (7 pages).

[69] M. Plewicki, F. Weise, S. M. Weber, and A. Lindinger, "Phase, amplitude and polarization shaping with a pulse shaper in a mach-zehnder interferometer," *Appl. Opt* **45** (2006) 8354–8359.

[70] M. Plewicki, S. M. Weber, F. Weise, and A. Lindinger, "Independent control over the amplitude, phase and polarization of femtosecond pulses," *Appl. Phys. B* **86** (2007) 259–263.

[71] S. M. Weber, F. Sauer, M. Plewicki, A. Merli, L. Wöste, and A. Lindinger, "Multi-objective optimization on alkali dimers," *J. Mod. Opt.* **54** (2007) 2659–2666.

[72] F. Weise, S. M. Weber, M. Plewicki, and A. Lindinger, "Application of phase, amplitude and polarization shaped pulses for optimal control on molecules," *Chem. Phys.* **332** (2007) 313–317.

[73] P. Nürnberger, D. Wolpert, H. Weiss, and G. Gerber, "Initiation and control of catalytic surface reactions with shaped femtosecond laser pulses," *Phys. Chem. Chem. Phys* **14** (2012) 1185–1199.

[74] U. Weiss, *Quantum Dissipative Systems*. World Scientific, Singapore, 1993.

[75] Z. Bihary, M. Karavitis, and V. A. Apkarian, "Onset of decoherence: Six-wave mixing measurements of vibrational decoherence on the excited state of I_2 in solid argon," *J. Chem. Phys.* **120** (2004) 8144–8156.

[76] M. Fushitani, M. Bargheer, M. Gühr, and N. Schwentner, "Pump-probe spectroscopy with phase-locked pulses in the condensed phase: decoherence and control of vibrational wavepackets," *Phys. Chem. Chem. Phys.* **7** (2005) 3143–3149.

[77] P. Nürnberger, G. Vogt, T. Brixner, and G. Gerber, "Femtosecond quantum control of molecular dynamics in the condensed phase," *Phys. Chem. Chem. Phys* **9** (2007) 2470–2497.

[78] J. Hauer, T. Buckup, and M. Motzkus, "Enhancement of molecular modes by electronically resonant multipulse excitation: Further progress towards mode selective chemistry," *J. Chem. Phys.* **125** 061101 (2006) (3 pages).

[79] L. G. Rego, L. F. Santos, and V. S. Batista, "Coherent control of quantum dynamics with sequences of unitary phase-kick pulses," *Annu. Rev. Phys. Chem.* **60** (2009) 293–320.

[80] S. Fechner, F. Dimler, T. Brixner, G. Gerber, and D. J. Tannor, "The von Neumann picture: a new representation for ultrashort laser pulses," *Opt. Express* **15** (2007) 15387–15401.

[81] A. Rodenberg, S. Fechner, F. Dimler, D. J. Tannor, and T. Brixner, "Experimental implementation of ultrashort laser pulses in the von Neumann picture," *Appl. Phys. B* **93** (2008) 763–772.

[82] S. Rützel, C. Stolzenberger, F. Dimler, D. J. Tannor, and T. Brixner, "Adaptive coherent control using the von Neumann basis," *Phys. Chem. Chem. Phys.* **13** (2011) 8627–8636.

[83] H. Ibrahim, M. Gühr, and N. Schwentner, "Valence transitions of Br_2 in Ar matrices: Interaction with the lattice and predissociation," *J. Chem. Phys.* **128** 064504 (2008) (13 pages).

[84] A. Borowski, *Non-Adiabatic Multi-Dimensional Quantum Dynamics of Br_2 in Solid Argon.* PhD thesis, Freie Universität Berlin, 2008.

[85] A. Borowski and O. Kühn, "Nonadiabatic quantum dynamics of Br_2 in solid Ar: A four-dimensional study of the B to C state predissociation," *Chem. Phys.* **347** (2008) 523–530.

[86] G. Herzberg, *Molecular Spectra and Molecular Structure I. Spectra of Diatomic Molecules.* Van Nostrand Reinhold Company Inc., New York, 1950.

[87] M. L. Klein and J. A. Venables, *Rare Gas Solids Vol. I + II.* Academic Press, London, 1976.

[88] M. Gühr, *Coherent Dynamics of Small Molecules in Rare Gas Crystals.* PhD-Thesis, FU-Berlin, Cuvillier Verlag, Göttingen, 2005.

[89] H. Ibrahim, *Tracking coherences in a dissipative ocean: Analysing and controlling Br_2/Ar matrix.* PhD-Thesis, FU-Berlin, Cuvillier Verlag, Göttingen, 2008.

[90] N. Schwentner and V. A. Apkarian, "A solid state rare gas halide laser: XeF in crystalline Argon," *Chem. Phys. Lett.* **154** (1989) 413–419.

[91] G. Zerza, G. Sliwinski, N. Schwentner, G. J. Hoffman, D. G. Imre, and V. A. Apkarian, "Spectroscopy of XeF in Ar and Ne matrices," *J. Chem. Phys.* **99** (1993) 8414–8423.

[92] R. Zadoyan, N. Schwentner, and V. A. Apkarian, "Wavepacket diagnosis with chirped probe pulses," *Chem. Phys.* **233** (1998) 353–363.

[93] V. A. Apkarian and N. Schwentner, "Moleular photodynamics in rare gas solids," *Chem. Rev.* **99** (1999) 1481–1514.

[94] R. Alimi, R. B. Gerber, and V. A. Apkarian, "Dynamics of molecular reactions in solids - photodissociation of F_2 in crystalline Ar," *J. Chem. Phys.* **92** (1990) 3551–3558.

[95] R. B. Gerber, M. V. Korolkov, J. Manz, M. Y. Niv, and B. Schmidt, "A reflection principle for the control of molecular photodissociation in solids: Model simulation for F_2 in Ar," *Chem. Phys. Lett.* **327** (2000) 76–84.

[96] G. Chaban, R. B. Gerber, M. V. Korolkov, J. Manz, M. Y. Niv, and B. Schmidt, "Photodissociation dynamics of molecular fluorine in an argon matrix induced by ultrashort laser pulses," *J. Phys. Chem. A* **105** (2001) 2770–2782.

[97] M. V. Korolkov and J. Manz, "Initial processes of laser induced diatomic molecular photodissociation in matrices: Quantum simulations for F_2 in Ar in reduced dimensionality," *Z. Phys. Chem.* **217** (2003) 115–131.

[98] M. V. Korolkov and J. Manz, "Design of UV laser pulses for the preparation of matrix isolated homonuclear diatomic molecules in selective vibrational superposition states," *J. Chem. Phys.* **126** 174306 (2007) (11 pages).

[99] M. Bargheer, R. B. Gerber, M. V. Korolkov, O. Kühn, J. Manz, M. Schröder, and N. Schwentner, "Subpicosecond spin-flip induced by the photodissociation dynamics of ClF in an Ar matrix," *Phys. Chem. Chem. Phys.* **4** (2002) 5554–5562.

[100] M. Bargheer, A. Cohen, R. B. Gerber, M. Gühr, M. V. Korolkov, J. Manz, M. Y. Niv, M. Schröder, and N. Schwentner, "Dynamics of electronic states and spin-flip for photodissociation of dihalogens in matrices: Experiment and semiclassical surface-hopping and quantum model simulations for F_2 and ClF in solid Ar," *J. Phys. Chem. A* **111** (2007) 9573–9585.

[101] M. Bargheer, A. Borowski, A. Cohen, M. Fushitani, R. Gerber, M. Gühr, P. Hamm, H. Ibrahim, T. Kiljunen, M. Korolkov, O. Kühn, J. Manz, B. Schmidt, M. Schröder, and N. Schwentner, "Coherence and control of molecular dynamics in rare gas matrices," in *Analysis and Control of Ultrafast Photoinduced Reactions* (O. Kühn and L. Wöste, eds.), no. 87 in Springer Series in Chemical Physics, pp. 257–385. Springer, Heidelberg, 2007.

[102] V. S. Batista and D. F. Coker, "Nonadiabatic molecular dynamics simulation of photodissociation and geminate recombination of I_2 in liquid xenon," *J. Chem. Phys.* **105** (1996) 4033–4054.

[103] V. S. Batista and D. F. Coker, "Nonadiabatic molecular dynamics simulation of ultrafast pump-probe experiments on I_2 in solid rare gases," *J. Chem. Phys.* **106** (1997) 6923–6941.

[104] R. B. Gerber, "Formation of novel rare-gas molecules in low-temperature matrices," *Ann. Rev. Phys. Chem.* **55** (2004) 55–78.

[105] L. Sheng and R. B. Gerber, "Predicted stability and structure of $(HXeCCH)_n$ (n=2 or 4) and clusters of crystalline HXeCCH," *J. Chem. Phys.* **126** 021108 (2007) (3 pages).

[106] Merck AG, Sicherheitsdatenblatt Br_2, www.chemdat.de.

[107] *Gas Encyclopedia.* L'Air Liquide Scientific Division, Elsevier, 1976.

[108] Deutsche Gesetzliche Unfallversicherung, www.dguv.de/bgia/stoffdatenbank.

[109] R. F. Barrow, T. C. Clark, J. A. Coxon, and K. K. Yee, "The $B^3\Pi 0_u^+ - X^1\Sigma_g^+$ system of Br_2: Rotational analysis, Franck-Condon factors and long range potential in the $B^3\Pi 0_u^+$ state," *J. Mol. Spectrosc.* **51** (1974) 428–449.

[110] A. Sur and J. Tellinghuisen, "The D'→A' Transition in Br_2," *J. Mol. Spectrosc.* **88** (1981) 323–346.

[111] G. Capelle, K. Sakurai, and H. P. Broida, "Lifetime and self-quenching cross sections of vibrational levels in the B state of bromine excited by a tunable dye laser," *J. Chem. Phys.* **54** (1971) 1728–1730.

[112] J. A. Coxon, "$B^3\Pi 0_u^+ - X^1\Sigma_g^+$ system of $^{79}Br^{79}Br$," *J. Mol. Spectr.* **37** (1971) 39–62.

[113] J. A. Coxon, "Franck-Condon factors and r-centroids for halogen molecules - II. the $B^3\Pi(0_u^+)$–$X^1\Sigma_g^+$ system of $^{79}Br^{81}Br$.," *J. Quant. Spectrosc. Radiat. Transfer.* **12** (1972) 639–650.

[114] J. A. Coxon, "The Extreme Red Absorption Spectrum of Br_2, $A^3\Pi(1_u) \leftarrow X^1\Sigma_u^+$," *J. Mol. Spectrosc.* **41** (1972) 548–565.

[115] J. Coxon, *Chapt. 4: Low-lying electronic states of diatomic halogen molecules.* Molecular Spectroscopy, Volume 1. The Chemical Society, Burlington House, London, W1V 0BN, 1973.

[116] E. Hwang, P. J. Dagdigan, and J. Tellinghuisen, "Spectroscopy of metastable species in a free-jet expansion: The $\beta \leftarrow A$ transition in Br_2," *J. Mol. Spectrosc.* **181** (1997) 297–306.

[117] P. Berwanger, K. S. Viswanathan, and J. Tellinghuisen, "The E→B transition (3000–3140 Å) in Br_2," *J. Mol. Spectrosc.* **91** (1982) 275–285.

[118] S. Yabushita, "unpublished ab-initio potentials for Br_2.".

[119] Y. Asano and S. Yabushita, "Theoretical study of nonadiabatic transitions in the photodissociation of Cl_2 and Br_2," *Chem. Phys. Lett.* **372** (2003) 348–354.

[120] L. D. Landau, "On the theory of transfer of energy at collisions," *Phys. Z. Sov.* **2** (1932) 46–51.

[121] C. Zener, "Non-adiabatic crossing of energy levels," *Proc. R. Soc.* **137** (1932) 696–702.

[122] E. C. G. Stückelberg, "Theorie der unelastischen Stösse zwischen Atomen," *Helvetica Physica* **5** (1932) 369–422.

[123] E. Majorana, "Atomi orientati in campo magnetico variabile," *Nuovo Cimento* **9** (1932) 43–50.

[124] N. Rosen and C. Zener, "Double Stern-Gerlach experiment and related collision phenomena," *Phys. Rev.* **40** (1932) 502–507.

[125] K. B. McAfee, R. M. Lum, and R. S. Hozack, "Excited state bromine atom and molecule reactions," *J. Chem. Phys.* **64** (1976) 5073–5076.

[126] K. B. McAfee and R. S. Hozack, "Lifetimes and energy transfer near the dissociation limit in bromine," *J. Chem. Phys.* **64** (1976) 2491–2495.

[127] M. S. Child, "Analytical interpretation of predissociation rates: the $B^3\Pi_{0u+}$ state of Br_2," *J. Phys. B* **13** (1980) 2557–2563.

[128] R. S. Hozack, A. P. Kennedy, and K. B. McAfee, "Krypton ion laser-excited fluorescence in bromine," *J. Mol. Spectr.* **80** (1980) 239–243.

[129] M. A. A. Clyne and M. C. Heaven, "Theoretical treatment of the spontaneous predissociation of Br_2, $B^3\Pi(0_u^+)$," *J. Chem. Phys.* **76** (1982) 5341–5349.

[130] Y. Fujii, N. A. Lurie, R. Pynn, and G. Shirane, "Inelastic neutron scattering from solid ^{36}Ar," *Phys. Rev. B* **10** (1974) 3647–3659.

[131] B. M. Axilrod and E. Teller, "Interaction of the van der Waals type between three atoms," *J. Chem. Phys.* **11** (1943) 299–300.

[132] V. F. Lotrich and K. Szalewicz, "Three-body contribution to binding energy of solid argon and analysis of crystal structure," *Phys. Rev. Lett.* **79** (1997) 1301–1304.

[133] M. Karavitis, R. Zadoyan, and V. A. Apkarian, "Time resolved coherent anti-Stokes Raman scattering of I_2 isolated in matrix argon: Vibrational dynamics on the ground electronic state," *J. Chem. Phys.* **114** (2001) 4131–4140.

[134] M. Karavitis, D. Segale, Z. Bihary, M. Pettersson, and V. A. Apkarian, "Time-resolved CARS measurements of the vibrational decoherence of I_2 isolated in an Ar matrix," *Low Temp. Phys.* **29** (2003) 814–821.

[135] M. Gühr, M. Bargheer, and N. Schwentner, "Generation of coherent zone boundary phonons by impulsive excitation of molecules," *Phys. Rev. Lett.* **91** 085504 (2003) (4 pages).

[136] T. K. Cheng, S. D. Brorson, A. S. Kazretoonian, J. S. Moodera, G. Dresselhaus, M. S. Dresselhaus, and E. P. Ippen, "Impulsive Excitation of Coherent Phonons Observed in Reflection in Bismuth and Antimony," *Appl. Phys. Lett.* **57** (1990) 1004–1006.

[137] T. K. Cheng, J. Vidal, H. J. Zeiger, G. Dresselhaus, M. S. Dresselhaus, and E. P. Ippen, "Mechanism for displacive excitation of coherent phonons in Sb, Bi, Te, and Ti_2O_3," *Appl. Phys. Lett.* **59** (1991) 1923–1925.

[138] H. J. Zeiger, J. Vidal, T. K. Cheng, E. P. Ippen, G. Dresselhaus, and M. S. Dresselhaus, "Theory for displacive excitation of coherent phonons," *Phys. Rev. B* **45** (1992) 768–778.

[139] A. V. Kuznetsov and C. J. Stanton, "Theory of coherent phonon oscillations in semiconductors," *Phys. Rev. Lett.* **73** (1994) 3243–3246.

[140] G. A. Garrett, T. F. Albrecht, J. F. Whitaker, and R. Merlin, "Coherent THz phonons driven by light pulses and the sb problem: What is the mechanism?," *Phys. Rev. Lett.* **77** (1996) 3661–3664.

[141] M. Hase, M. Kitajima, S. Nakashima, and K. Mizoguchi, "Dynamics of coherent anharmonic phonons in bismuth using high density photoexcitation," *Phys. Rev. Lett.* **88** 067401 (2002) (4 pages).

[142] M. Hase, I. Ishioka, M. Kitajima, S. Hishita, and K. Ushida, "Dephasing of coherent THz phonons in bismuth studied by femtosecond pump-probe technique," *Appl. Surf. Science* **197-198** (2002) 710–714.

[143] K. Sokolowski-Tinten, C. Blome, J. Blums, A. Cavalleri, C. Dietrich, A. Tarasevitch, I. Uschmann, E. Förster, M. Kammler, M. Horn-von-Hoegen,

and D. von der Linde, "Femtosecond X-ray measurement of coherent lattice vibrations near the Lindemann stability limit," *Nature* **422** (2003) 287–289.

[144] K. K. Rebane, *Impurity Spectra of Solids.* Plenum Press, New York, 1970.

[145] S. H. Lin, *Radiationless Transitions.* Academic Press, New York, 1980.

[146] B. S. Ault, W. F. Howard, and L. Andrews, "Laser-Induced Fluorescence and Raman Spectra of Chlorine and Bromine Molecules Isolated in Inert Matrices," *J. Mol. Spectrosc.* **55** (1975) 217–228.

[147] M. Gühr, M. Bargheer, M. Fushitani, T. Kiljunen, and N. Schwentner, "Ultrafast dynamics of halogens in rare gas solids," *Phys. Chem. Chem. Phys.* **9** (2007) 779–801.

[148] M. Bargheer, M. Gühr, P. Dietrich, and N. Schwentner, "Femtosecond spectroscopy of fragment-cage dynamics: I_2 in Kr," *Phys. Chem. Chem. Phys.* **4** (2002) 78–81.

[149] T. Kiljunen, M. Bargheer, M. Gühr, and N. Schwentner, "A potential energy surface and a trajectory study of photodynamics and strong field alignment of ClF molecule in rare gas (Ar,Kr) solids," *Phys. Chem. Chem. Phys.* **6** (2004) 2185–2197.

[150] T. Kiljunen, M. Bargheer, M. Gühr, N. Schwentner, and B. Schmidt, "Photodynamics and ground state librational states of ClF molecule in solid Ar. Comparison of experiment and theory," *Phys. Chem. Chem. Phys.* **6** (2004) 2932–2939.

[151] T. Kiljunen, B. Schmidt, and N. Schwentner, "Intense-field alignment of molecules confined in octahedral fields," *Phys. Rev. Lett.* **94** 123003 (2005) (4 pages).

[152] T. Kiljunen, B. Schmidt, and N. Schwentner, "Aligning and orienting molecules trapped in octahedral crystal fields," *Phys. Rev. A* **72** 053415 (2005) (11 pages).

[153] T. Kiljunen, B. Schmidt, and N. Schwentner, "Time-dependent alignment of molecules trapped in octahedral crystal fields," *J. Chem. Phys.* **124** 164502 (2006) (13 pages).

[154] A. Borowski and O. Kühn, "Towards a quantum mechanical description of the photochemistry of dihalogens in rare gas matrices," *J. Photochemistry and Photobiology A* **190** (2007) 169–176.

[155] R. Fraenkel and Y. Haas, "Molecular dynamics simulations of rare gas matrix deposition," *Chem. Phys.* **186** (1994) 185–204.

[156] X.-J. Ning and Q.-Z. Qing, "A new molecular dynamics method for simulating trapping site structures in cryogenic matrices," *J. Chem. Phys.* **110** (1999) 4920–4928.

[157] P. Casavecchia, G. He, R. K. Sparks, and Y. T. Lee, "Interaction potentials for Br(^{2}P)+Ar, Kr and Xe(^{1}S) by the crossed molecular beams method," *J. Chem. Phys.* **75** (1981) 710–721.

[158] R. A. Aziz, "A highly accurate interaction potential for argon," *J. Chem. Phys.* **99** (1993) 4518–4524.

[159] R. A. Aziz, M. J. Slaman, and A. R. Janzen, "Critique of interatomic potentials obtained from neutron diffraction," *Phys. Rev. E* **49** (1994) 5310–5315.

[160] P. Casavecchia, G. He, R. K. Sparks, and Y. T. Lee, "Rare gas-halogen atom interaction potentials from crossed molecular beams experiments: I($^2P_{3/2}$)+Kr, Xe($^1S_0$)," *J. Chem. Phys.* **77** (1982) 1878–1885.

[161] M. P. Allen and D. J. Tildesley, *Computer Simulations of Liquids.* Oxford University Press Inc., New York, 1987.

[162] J. Helbing and M. Chergui, "Solvation of ion-pair states in nonpolar media: I_2 in solid neon, argon and krypton," *J. Chem. Phys.* **115** 6158 (2001) (15 pages).

[163] N. Yu and D. F. Coker, "Ion pair state emission from I_2 in rare gas matrices: effects of solvent induced symmetry breaking," *Mol. Phys.* **102** (2004) 1031–1044.

[164] J. Franck and E. Rabinowitch, "Some remarks about free radicals and the photochemistry of solutions," *Trans. Faraday Soc.* **30** (1934) 120–131.

[165] M. Bargheer, M. Gühr, and N. Schwentner, "Collisions transfer coherence," *Israel J. Chem.* **44** (2004) 9–17.

[166] M. Gühr and N. Schwentner, "Effective chromophore potential, dissipative trajectories and vibrational energy relaxation: Br_2 in Ar matrix.," *J. Chem. Phys.* **123** 244506 (2005) (12 pages).

[167] L. D. Landau and E. M. Lifschitz, *Lehrbuch der theoretischen Physik.* Vol. III: Quantenmechanik, Akademie-Verlag, Berlin, 1979.

[168] C. Zhu and H. Nakamura, "Theory of nonadiabatic transition for general two-state curve crossing problems. I. Nonadiabatic tunneling case," *J. Chem. Phys* **101** (1994) 10630–10647.

[169] C. Zhu and H. Nakamura, "Theory of nonadiabatic transition for general two-state curve crossing problems. II. Landau-Zener case," *J. Chem. Phys* **102** (1995) 7448–7461.

[170] H. Lefebvre-Brion and R. W. Field, *Perturbations in the Spectra of Diatomic Molecules.* Academic Press, London, 1986.

[171] Q. Liu, C. Wan, and A. H. Zewail, "Solvation ultrafast dynamics of reactions. 13. Theoretical and experimental studies of wave packet reaction coherence and its density dependence," *J. Phys. Chem.* **100** (1996) 18666–18682.

[172] N. F. Scherer, L. D. Ziegler, and G. R. Fleming, "Heterodyne-detected time-domain measurement of I_2 predissociation and vibrational dynamics in solution," *J. Chem. Phys.* **96** (1992) 5544–5547.

[173] R. Zadoyan, M. Sterling, and V. A. Apkarian, "Dynamical spectroscopy of many body interactions, coherent vibrations and predissociation of $I_2(B)$ in solid Kr," *J. Chem. Soc., Faraday. Trans.* **92** (1996) 1821–1829.

[174] R. Zadoyan, J. Almy, and V. A. Apkarian, "Lattice dynamics from the 'eyes' of the chromophore, real-time studies of I_2 isolated in rare gas matrices," *Faraday Discuss.* **108** (1997) 255–269.

[175] O. Roncero, N. Halberstadt, and J. A. Beswick, "A wave-packet study of Ar...$I_2(B) \rightarrow$ Ar+I+I electronic predissociation," *Chem. Phys. Lett.* **226** (1994) 82–87.

[176] O. Roncero, N. Halberstadt, and J. A. Beswick, "A three-dimensional wave packet study of Ar...$I_2(B) \rightarrow$ Ar+I+I electronic predissociation," *J. Chem. Phys.* **104** (1996) 7554 – 7560.

[177] A. Accardi, A. Borowski, and O. Kühn, "Nonadiabatic quantum dynamics and laser control of Br_2 in solid Argon," *J. Phys. Chem. A* **113** (2009) 7491–7498.

[178] M. Gühr, M. Bargheer, P. Dietrich, and N. Schwentner, "Predissociation and vibrational relaxation in the B state of I_2 in a Kr matrix," *J. Phys. Chem. A* **106** (2002) 12002–12011.

[179] M. Fushitani, N. Schwentner, M. Schröder, and O. Kühn, "Cage motions induced by electronic and vibrational excitations: Cl_2 in Ar," *J. Chem. Phys.* **124** 024505 (2006) (7 pages).

[180] M. Bargheer, M. Y. Niv, R. B. Gerber, and N. Schwentner, "Ultrafast solvent-induced spin-flip and nonadiabatic coupling: ClF in argon solids," *Phys. Rev. Lett.* **89** 108301 (2002) (4 pages).

[181] M. V. Korolkov and J. Manz, "Cage exit supported by spin-orbit coupling: Quantum model simulations for ClF in an Ar matrix," *Chem. Phys. Lett.* **393** (2004) 44–50.

[182] M. V. Korolkov and J. Manz, "Coherent spin control of matrix isolated molecules by IR+UV laser pulses: Quantum simulations for ClF in Ar," *J. Chem. Phys.* **120** 11522 (2004) (10 pages).

[183] A. B. Alekseyev, M. V. Korolkov, O. Kühn, J. Manz, and M. Schröder, "Model simulation of coherent laser control of the ultrafast spin-flip dynamics of matrix-isolated Cl_2," *J. Photochem. Photobiol. A: Chem.* **180** (2006) 262–270.

[184] N. F. Scherer, A. J. Ruggiero, M. Du, and G. R. Fleming, "Time resolved dynamics of isolated molecular systems studied with phase-locked femtosecond pulse pairs," *J. Chem. Phys.* **93** (1990) 856–857.

[185] N. F. Scherer, R. J. Carlson, A. Matro, M. Du, A. J. Ruggiero, V. Romero-Rochin, J. A. Cina, and G. R. Fleming, "Fluorescence-detected wave packet interferometry: Time resolved molecular spectroscopy with sequences of femtosecond phase locked pulses," *J. Chem. Phys.* **95** (1991) 1487–1511.

[186] M. Fushitani, M. Bargheer, M. Gühr, H. Ibrahim, and N. Schwentner, "Control of chromophore to bath coupling by interferometry: Cl_2 vibrational wave packets in solid Ar," *J. Phys. B: At. Mol. Opt. Phys.* **41** 074013 (2008).

[187] V. E. Bondybey, S. S. Bearder, and C. Fletcher, "Br_2 $B^3\Pi(0_u^+)$ excitation spectra and radiative lifetimes in rare gas solids," *J. Chem. Phys.* **64** (1976) 5243–5246.

[188] H. Ibrahim, M. Héjjas, M. Fushitani, and N. Schwentner, "Phase sensitive control of vibronic guesthost interaction: Br_2 in Ar matrix," *J. Phys. Chem. A.* **113** (2009) 7439–7450.

[189] A. Borowski and O. Kühn, "Tailoring model hamiltonians for dihalogen - rare gas matrix problems," *Theor. Chem. Acc.* **117** (2007) 521–533.

[190] H. Ibrahim, M. Héjjas, and N. Schwentner, "Tracing, amplifying, and steering chromophore-bath coherences by ultrashort pulse trains," *Phys. Rev. Lett.* **102** 088301 (2009) (4 pages).

[191] A. A. Passchier, J. D. Christian, and N. W. Gregory, "The ultraviolet-visible absorption spectrum of bromine between room temperature and 440C," *J. Phys. Chem.* **71** (1967) 937–942.

[192] L. Andrews, "Optical spectra of the dibromide and diiodide ions in the matrix-isolated $M^+Br_2^-$ and $M^+I_2^-$," *J. Am. Chem. Soc.* **98** (1976) 2152–2156.

[193] R. Schinke, *Photodissociation Dynamics.* Cambridge University Press, Cambridge / England, 1993.

[194] R. J. L. Roy, R. G. Macdonald, and G. Burns, "Diatom potential curves and transition moment functions from continuum absorption coefficients: Br_2^*," *J. Chem. Phys.* **65** (1976) 1485–1500.

[195] D. B. Fitchen, *Physics of Color Centers, Ed. W. B. Fowler, Ch. 5: Zero Phonon Transitions.* Academic Press, New York, 1968.

[196] N. Schwentner, E.-E. Koch, and J. Jortner, *Electronic Excitations in Condensed Rare Gases.* Springer Verlag, Berlin, Heidelberg, 1985.

[197] K. Huang and A. Rhys, "Theory of light absorption and non-radiative transitions in F-centres," *Proc. Roy. Soc. London A* **204** (1950) 406–423.

[198] M. Gühr, H. Ibrahim, and N. Schwentner, "Controlling vibrational wave packet revivals in condensed phase: Dispersion and coherence for Br_2:Ar," *Phys. Chem. Chem. Phys.* **6** (2004) 5353–5361.

[199] A. G. Redfield, "On the theory of relaxation processes," *IBM J. Res. Dev.* **1** (1957) 19–31.

[200] G. Lindblad, "Generators of quantum dynamical semigroups," *Commun. Math. Phys.* **48** (1976) 119–130.

[201] G. Lindblad, "Brownian motion of a quantum harmonic oscillator," *Rep. Math. Phys.* **10** (1976) 393–406.

[202] N. Owschimikow, F. Königsmann, J. Maurer, P. Giese, A. Ott, B. Schmidt, and N. Schwentner, "Cross Sections for Rotational Decoherence of Perturbed Nitrogen Measured via Decay of Laser-Induced Alignment," *J. Chem. Phys.* **133** 044311 (2010) (13 pages).

[203] B. Kohler, V. V. Yakovlev, J. Che, J. L. Krause, M. Messina, K. Wilson, N. Schwentner, R. M. Whitnell, and Y. Yan, "Quantum control of wave packet evolution with tailored femtosecond pulses," *Phys. Rev. Lett.* **74** (1995) 3360–3363.

[204] M. D. Feit, J. A. Fleck, and A. Steiger, "Solution of the Schrödinger-equation by a spectral method," *J. Comput. Phys.* **47** (1982) 412–432.

[205] D. Kosloff and R. Kosloff, "A Fourier Method Solution for the Time Dependent Schrödinger equation as a Tool in Molecular Dynamics," *J. Comp. Phys.* **52** (1983) 35–53.

[206] R. Kosloff and D. Kosloff, "A Fourier Method Solution for the Time Dependent Schrödinger equation: Study of the Reaction H^++H_2, D^++D_2 and $D^+ + H_2$," *J. Chem. Phys.* **79** (1983) 1823–1833.

[207] H. Goto, H. Katsuki, H. Ibrahim, H. Chiba, and K. Ohmori, "Strong-Laser-Induced Quantum Interference," *Nature Physics* **7** (2011) 383–385.

[208] D. Tannor, "Homepage http://www.weizmann.ac.il/chemphys/tannor/home.html."

[209] J. C. Light, I. P. Hamilton, and J. V. Lill, "Generalized discrete variable approximation in quantum-mechanics," *J. Chem. Phys.* **82** (1985) 1400–1409.

[210] J. C. Light and T. Carrington, "Discrete-variable representations and their utilization," *Adv. Chem. Phys.* **114** (2000) 263–310.

[211] B. Schmidt, "Homepage http://page.mi.fu-berlin.de/bsch63/Software/WavePacket.html."

[212] P. M. Morse, "Diatomic molecules according to the wave mechanics. II. vibrational levels," *Phys. Rev* **34** (1929) 57–64.

[213] M. Dantus, M. J. Rosker, and A. H. Zewail, "Real-time femtosecond probing of 'transition states' in chemical reactions," *J. Chem. Phys.* **87** (1987) 2395–2397.

[214] M. Dantus, M. J. Rosker, and A. H. Zewail, "Femtosecond real-time probing of reactions. II. The dissociation reaction of ICN," *J. Chem. Phys.* **89** (1988) 6128–6140.

[215] E. Treacy, "Optical pulse compression with diffraction gratings," *IEEE J. Quantum Eletron.* **QE-5** (1969) 454–460.

[216] R. Fork, O. E. Martinez, and J. P. Gordon, "Negative dispersion using pairs of prisms," *Opt. Lett.* **9** (1984) 150–152.

[217] R. Trebino, K. W. DeLong, D. N. Fittinghoff, J. N. Sweetser, M. A. Krumbügel, B. A. Richman, and D. Kane, "Measuring ultrashort laser pulses in the time-frequency domain using frequency-resolved optical gating," *Rev. Sci. Instrum.* **68** (1997) 3277–3295.

[218] S. Linden, H. Giessen, and J. Kuhl, "XFROG – a new method for amplitude and phase characterization of weak ultrashort pulses," *Physica Status Solidi (B)* **206** (1998) 119–124.

[219] B. E. A. Saleh and M. C. Teich, *Grundlagen der Photonik.* Wiley VCH, Weinheim, 2008.

[220] P. M. W. French, "The generation of ultrashort laser pulses," *Rep. Prog. Phys.* **58** (1995) 169–267.

[221] J.-C. Diels and W. Rudolph, *Ultrashort Laser Pulse Phenomena.* Academic Press, San Diego, California, 1996.

[222] C. Rullière, *Femtosecond Laser Pulses.* Springer Verlag, Berlin, Heidelberg, 1998.

[223] T. Wilhelm, J. Piel, and E. Riedle, "Sub-20-Fs Pulses Tunable Across the Visible from a Blue-Pumped Single-Pass Noncollinear Parametric Converter," *Opt. Lett.* **22** (1997) 1494–1496.

[224] G. Cerullo, M. Nisoli, S. Stagira, and S. D. Silvestri, "Sub-8-fs pulses from an ultrabroadband optical parametric amplifier in the visible," *Opt. Lett.* **23** (1998) 1283–1285.

[225] A. Shirakawa and T. Kobayashi, "Noncollinearly phase-matched femtosecond optical parameteric amplification with a 2000 cm^{-1} bandwidth," *Appl. Phys. Lett.* **72** (1998) 147–149.

[226] S. Lochbrunner, J. Piel, S. Schenkl, S. Spörlein, W. Zinth, E. Riedle, and M. Beuttner, "Generation of 10 to 50 fs pulses tunable through all the visible and the NIR," *Appl. Phys. B* **71** (2000) 457–465.

[227] G. Cheriaux, P. Rousseau, F. Salin, J. P. Chamaret, B. Walker, and L. F. Dimauro, "Abberation-free stretcher design for ultrashort-pulse amplification," *Opt. Lett.* **21** (1996) 414–416.

[228] P. Maine, D. Strickland, P. Bado, M. Pessot, and G. Mourou, "Generation of ultrahigh peak power pulses by chirped pulse amplification," *IEEE J. Quantum Electron* **24** (1988) 398–403.

[229] I. Walmsley, L. Waxer, and C. Dorrerl, "The role of dispersion in ultrafast optics," *Rev. Sci. Instrum.* **72** (2001) 1–29.

[230] R. W. Boyd, *Nonlinear Optics.* Academic Press, London, 2003.

[231] G. Cerullo and S. D. Silvestri, "Ultrafast optical parametric amplifiers," *Rev. Sci. Instr.* **74** (2003) 1–18.

[232] M. Bargheer, *Ultrafast Photodynamics in Condensed Phase: ClF, Cl$_2$ and I$_2$ in Solid Rare Gases.* PhD-Thesis, FU-Berlin, Shaker Verlag, Aachen, 2002.

[233] A. Weiner, J. Heritage, and E. M. Kirschner, "High-resolution femtosecond pulse shaping," *J. Opt. Soc. Am. B* **5** (1988) 1563–1572.

[234] A. M. Weiner, "Femtosecond pulse shaping using spatial light modulators," *Rev. Sci. Instr.* **71** (2000) 1929–1960.

[235] Spatial light modulator system, *User's manual.* Cambridge Research & Instrumentation, Inc., 2003.

[236] O. E. Martínez, "Grating and prism compressor in the case of finite beam size," *J. Opt. Soc. Am. B* **3** (1986) 929–934.

[237] A. C. Albrecht, "Polarization and assignments of transitions: The method of photoselection," *J. Mol. Spectrosc.* **6** (1961) 84–108.

[238] J. Michl and E. Thulstrup, *Spectroscopy with polarized light.* VCH Publishers, New York, 1986.

[239] D. S. Kliger, J. W. Lewis, and C. E. Randall, *Polarized Light in Optics and Spectroscopy.* Academic Press, Boston, 1990.

[240] M. Bargheer, M. Gühr, and N. Schwentner, "Depolarization as a probe for ultrafast reorientation of diatomics in condensed phase: ClF vs I_2 in rare gas solids," *J. Chem. Phys.* **117** (2002) 5–8.

[241] C. Chen, Y. Yin, and D. Elliott, "Interference between optical transitions," *Phys. Rev. Lett.* **64** (1990) 507–510.

[242] T. Baumert, M. Grosser, R. Thalweiser, and G. Gerber, "Femtosecond time-resolved molecular multiphoton ionization: The Na_2 system," *Phys. Rev. Lett.* **67** (1991) 3753–3756.

[243] E. Potter, J. L. Herek, S. Pedersen, Q. Liu, and A. Zewail, "Femtosecond laser control of a chemical reaction," *Nature* **355** (1992) 66–68.

[244] S. Ruhman and R. Kosloff, "Coherent Molecular Vibrational Motion Observed in the Time Domain Trough Impulsive Stimulated Raman Scattering," *J. Opt. Soc. Am. B* **7** (1990) 1748–1751.

[245] M. Sterling, R. Zadoyan, and V. A. Apkarian, "Interrogation and control of condensed phase chemical dynamics with lineary chirped pulses: I_2 in solid Kr," *J. Chem. Phys.* **104** (1996) 6497–6506.

[246] S. Shi, A. Woody, and H. Rabitz, "Optimal control of selective vibrational excitation in harmonic linear chain molecules," *J. Chem. Phys.* **88** (1988) 6870–6883.

[247] J. A. Wheeler, "Franck-Condon effect and squeezed-state physics as double-source interference phenomena," *Lett. Math. Phys.* **10** (1985) 201–206.

[248] J. P. Dowling, W. P. Schleich, and J. A. Wheeler, "Interference in phase space," *Ann. Phys.* **48** (1991) 423–502.

[249] P. Backhaus and B. Schmidt, "Femtosecond quantum dynamics of photoassociation reactions: the exciplex formation of mercury," *Chem. Phys.* **217** (1996) 131–143.

[250] J. Tellinghuisen, "Transition strength and potential curves for the valence transitions in Br_2 from reanalysis of the ultraviolet-visible absorption at low resolution," *J. Chem. Phys.* **115** (2001) 10417–10424.

[251] J. Tellinghuisen, "Erratum: "Transition strength and potential curves for the valence transitions in Br_2 from reanalysis of the ultraviolet-visible absorption at low resolution"," *J. Chem. Phys.* **118** (2003) 1573–1574.

[252] I. N. Bronstein, K. A. Semendjajew, G. Musiol, and H. Mühlig, *Taschenbuch der Mathematik*. Verlag Harri Deutsch, Frankfurt am Main, 1999.

[253] B. Hartke, R. Kosloff, and S. Ruhman, "Large-amplitude ground-state vibrational coherence induced by impulsive absorption in CsI - a computer-simulation," *Chem. Phys. Lett.* **158** (1989) 238–244.

[254] U. Banin, A. Bartana, S. Ruhman, and R. Kosloff, "Impulsive excitation of coherent vibrational motion ground surface dynamics induced by intense short pulses," *J. Chem. Phys.* **101** (1994) 8461–8481.

[255] G. Ashkenazi, U. Banin, A. Bartana, R. Kosloff, and S. Ruhman, "Quantum Description of the Impulsive Photodissociation Dynamics of I_3^- in Solution," *Adv. Chem. Phys.* **100** (1997) 229–315.

[256] E. Luc-Koenig, F. Masnou-Seeuws, and R. Kosloff, "Dynamical hole in ultrafast photoassociation: Analysis of the compression effect," *Phys. Rev. A* **76** (2007) 53415–53428.

[257] M. Gühr, "unpublished results." 2004.

[258] H. Ibrahim, M. Héjjas, M. Fushitani, and N. Schwentner, "Correction to "phase sensitive control of vibronic guesthost interaction: Br_2 in Ar matrix"," *J. Phys. Chem. A.* (2012) available online: http://dx.doi.org/10.1021/jp301367j.

[259] M. Gühr and N. Schwentner, "Coherent phonon dynamics: Br_2 in solid Ar," *Phys. Chem. Chem. Phys.* **6** (2005) 760–767.

[260] L.-M. Krocker, "Prädissoziation in der Wellenpaketdynamik von Br_2 in Ar induziert mit ultrakurzen Pulszügen," Master's thesis, FU-Berlin, 2008.

[261] G. Panitchayangkoon, D. Hayes, K. Fransted, J. Caram, E. Harel, J. Wen, R. Blankenship, and G. Engel, "Long-Lived Quantum Coherence in Photosynthetic Complexes at Physiological Temperature," *PNAS* **107** (2010) 12766–12770.

[262] J. L. Dunham, "The Energy Levels of a Rotating Vibrator," *Phys. Rev.* **41** (1932) 721–731.

[263] N. Rosen, "Lifetimes of Unstable Molecules," *J. Chem. Phys.* **1** (1933) 319–326.

[264] C. I. Pekeris, "The Rotation-Vibration Coupling in Diatomic Molecules," *Phys. Rev.* **45** (1934) 98–103.

[265] J. Rundgren, "The rotating Morse oscillator," *Arkiv för Fysik* **30** (1965) 61–90.

[266] S. Flügge, *Practical quantum mechanics.* Springer, Berlin, 1974.

[267] L. Halonen and M. Child, "A local mode model for tetrahedral molecules," *Molec. Phys.* **46** (1982) 239–255.

[268] M. M. Nieto and L. M. Simmons, "Eigenstates, coherent states, and uncertainty products for the Morse oscillator," *Phys. Rev. A* **19** (1979) 438–444.

[269] S. Kais and R. D. Levine, "Coherent states for the Morse oscillator," *Phys. Rev. A* **41** (1990) 2301–2305.

[270] I. L. Cooper, "A simple algebraic approach to coherent states for the Morse oscillator," *J. Phys. A: Math. Gen.* **25** (1992) 1671–1683.

[271] J. P. Dahl and M. Springborg, "The Morse oscillator in position space, momentum space, and phase space," *J. Chem. Phys.* **88** (1988) 4535–4543.

[272] W. Walter, *Gewöhnliche Differentialgleichungen.* Springer Verlag, Berlin, 1990.

[273] R. Courant and D. Hilbert, *Methoden der Mathematischen Physik I,II.* Springer-Verlag, Berlin Heidelberg New York, 1968.

Publikationsliste

- B. Esser und M. Héjjas, **Wellenpaketaufspaltungen auf gekoppelten Phasenbahnen**, in T. Pöschel, H. Malchow, L. Schimansky-Geier, "Irreversible Prozesse und Selbstorganisation", Logos-Verlag, (2006), ISBN 978-3-8325-1350-4

IM RAHMEN DIESER ARBEIT:

- H. Ibrahim, M. Héjjas, N. Schwentner, **Tracing, Amplifying, and Steering Chromophore-Bath Coherences by Ultrashort Pulse Trains**, Phys. Rev. Lett., (2009), **102**, 88301

- H. Ibrahim, M. Héjjas, M. Fushitani, N. Schwentner, **Phase Sensitive Control of Vibronic Guest - Host Interaction: Br_2 in Ar Matrix**, J. Phys. Chem. A (2009), **113 (26)**, 7439

- H. Ibrahim, M. Héjjas, M. Fushitani, N. Schwentner, **Correction to "Phase Sensitive Control of Vibronic Guest - Host Interaction: Br_2 in Ar Matrix"**, J. Phys. Chem. A (2012), online: http://dx.doi.org/10.1021/jp301367j

Präsentationen auf Konferenzen

- M. Héjjas und B. Esser, **Quantendynamik von Wellenpaketen auf gekoppelten adiabatischen Potentialen**, Frühjahrstagung der DPG, März 2005, Berlin (Vortrag)

- M. Héjjas, H. Ibrahim, M. Gühr und N. Schwentner, **Schwingungsrelaxation und Prädissoziation, Dephasierung und Dispersion: Br_2 in festem Argon**, Frühjahrstagung der DPG, März 2007, Düsseldorf (Poster)

- M. Héjjas, L. M. Krocker, H. Ibrahim, M. Gühr und N. Schwentner, **Coherent control of environment induced predissociation dynamics by pulse train pump-probe spectroscopy (Br_2 in Ar matrix)**, Gordon Research Conference on Molecular Energy Transfer, January 2009, Ventura CA, USA (Poster Präsentation)

- M. Héjjas, L. M. Krocker, H. Ibrahim und N. Schwentner, **A rational coherent control scheme applied to the solvent induced predissociation of Br_2 in solid Ar**, ICP 2009 - XXIV International Conference on Photochemistry, July 2009, Toledo, Spain (Vortrag)